Models of Causal Inference in the Elasmobranch Electrosensory System: How Sharks Find Food

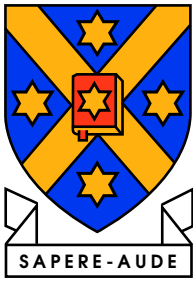

Kiri Pullar

Department of Zoology

A thesis submitted for the degree of

Doctor of Philosophy

at the University Otago, Dunedin,

New Zealand.

January 4th 2017

"It was supposed that electroreception should be unusually simple in converting a stimulus in the form of an electrical potential difference across a receptor cell membrane into a physiological response in the same form."
Bullock [1993]

Abstract

We develop a theory of how the functional design of the electrosensory system in sharks reflects the inevitability of noise in high-precision measurements, and how the Central Nervous System may have developed an efficient solution to the problem of inferring parameters of stimulus sources, such as their location, via Bayesian neural computation.

We use Finite Element Method to examine how the electrical properties of shark tissues and the geometrical configuration of both the shark body and the electrosensory array, act to focus weak electric fields in the aquatic environment, so that the majority of the voltage drop is signalled across the electrosensory cells. We analyse snapshots of two ethologically relevant stimuli: localized prey-like dipole electric sources, and uniform electric fields resembling motion-induced and other fields encountered in the ocean. We demonstrated that self movement (or self state) not only affects the measured field, by perturbing the self field, but also affects the external field.

Electrosensory cells provide input to central brain regions via primary afferent nerves. Inspection of elasmobranch electrosensory afferent spike trains and inter-spike interval distributions indicates that they typically have fairly regular spontaneous inter-spike intervals with skewed Gaussian-like variability.

However, because electrosensory afferent neurons converge onto secondary neurons, we consider the convergent input a "super afferent" with the pulse train received by a target neuron approaching a Poisson process with shorter mean intervals as the number of independent convergent spike trains increases.

We implement a spiking neural particle filter which takes simulated electrosensory "super afferent" spike trains and can successfully infer the fixed Poisson parameter, or the equivalent real world state, distance to a source. The circuit obtained by converting the mathematical model to a network structure bears a striking resemblance to the cerebellar-like hindbrain circuits of the dorsal octavolateral nucleus.

The elasmobranchs' ability to sense electric fields down to a limit imposed by thermodynamics seems extraordinary. However we predict that the theories presented here generalize to other sensory systems, particularly the other octavolateralis senses which share cerebellar-like circuitry, suggesting that the cerebellum itself also plays a role in dynamic state estimation.

Acknowledgements

Firstly, I would like to acknowledge the support and advice provided by my primary supervisor, Associate Professor Mike Paulin. He developed the neural models presented in this thesis and provided me with the opportunity to explore these theories in the elasmobranch electric sense. He has supported me in my advancement from an undergraduate student with countless hours of advice. I am also grateful to the graduate students who went before me in the Paulin lab, in particular Dr Rachel Berquist and Dr Travis Monk for providing me a framework to build on for my research.

Many thanks to Associate Professor Sarah Wakes in the Centre for Materials Science and Technology for her support and encouragement when it was most needed. Sarah offered feedback from a different perspective and constantly reminded me that all models are wrong, what's important is what you can learn from them.

I grateful to Professor David Bodznick, Wesleyan University for providing me with electrosensory afferent recordings, these were invaluable in developing and testing our model predictions. Additionally, I am appreciative to the many other academics who took time to respond to my emails through the duration of my thesis, either on my search for data or requests for papers.

Many thanks to the University of Otago and the Department of Zoology for financially supporting this thesis by awarding me a generous scholarship. Thank you to the staff and fellow students in the Department of Zoology and the Centre for Materials Science and Technology who provided friendship, support and opportunities.

Finally, thank you to my friends and family who endured this thesis with me. In particular, I am truly grateful to my parents and partner Joshua for their patience, constant encouragement and support in all stages of my studies.

Contents

List of Tables

List of Figures

Chapter 1

Introduction

The brain receives a continual stream of data from a variety of sensory modalities. In order to maximize their chances of survival, animals must extract information from these noisy sensory observations and produce appropriately coordinated responses. Accumulating evidence suggests the brain combines this information in a Bayes' optimal (or nearly optimal) manner to make inferences about behaviourally relevant world states [Bobrowski *et al.*, 2008; Fischer & Pena, 2011; Ganguli & Simoncelli, 2014; Hoyer & Hyvarinen, 2003; Karmali & Merfeld, 2012; Lochmann & Deneve, 2008, 2011; MacNeilage *et al.*, 2008; Paulin, 2005, 2015; Rich *et al.*, 2015], although this field is not without controversy [Bowers & Davis, 2012a,b; Jones & Love, 2011].

The elasmobranch electrosensory system provides a simple model to examine the mechanisms underlying causal inference in the vertebrate brain. The electric sense belongs to the octavolateral system and hence shows similarities to the vestibular, lateral line and auditory systems [Bodznick & Montgomery, 2005]. Transduction in elasmobranch electroreceptors is mediated by sensory hair cells, thus comparative analysis may provide insight into hair cell mechanisms elsewhere. Electroreception allow us to examine the flow of information from peripheral sensory structures, to the destination brain centres [Bullock, 1993]. Whereas hair cells in the vestibular, lateral line and auditory systems all receive feedback from the brain, electroreceptors lack any sign of such efferents [Bodznick, 1989]. In ampullary electroreception measurements are passive, with the stimulus strength falling off predictably as a function of distance. Given the lack of efferents, sensors encode the measurement process undistorted by feedback from the brain.

In early electrosensors, the scenario is further simplified as the only other sources of electric fields would have been other slowly moving living things. The electrosensory signal would therefore reliably indicate the distance and direction of other animals. Early

sensory neurons likely evolved as simple threshold detectors, therefore we can begin with a simple one dimensional model in which the state variable of interest is distance to source. Such a sensor would provide late pre-Cambrian animals with a means to detect proximity to other animals and therefore react in ethologically meaningful ways, such as striking or fleeing [Monk & Paulin, 2014]. Indeed, the onset of carnivory has been hypothesised to be the driving force behind the evolution of neurons [Monk, 2014]. Therefore understanding how the modern day elasmobranch brain infers predator/prey location may provide insights into general principles of brain evolution.

This thesis demonstrates that there is a "cheap trick" for performing Bayesian inference using spiking neurons. This mechanism makes quantitative predictions about electrosensory afferent firing patterns and neural circuitry in the electrosensory brainstem.

1.1 Electrosensory systems

In passive electrosensory systems animals respond to nearby objects that emit electric fields stimulating the electrosensory organs, whereas with active electrosensory systems animal generate their own electric field and sense perturbations caused by nearby objects. Sharks, skates and rays use their ampullary electrosensory system passively, although skates possess an electric organ rendering them capable of active electroreception. Here we focus on the processes involved with transduction in the passive electric sense.

The electrosensory system has been implicated in a variety of behaviours. Kalmijn [1971] identified the electric sense as the dominant modality used in locating prey at close range when compared to visual, chemical and mechanical cues. Collectively, experiments examining the responses of sharks and rays to natural and artificial dipole fields demonstrate that while the behavioural responses may differ between species, Elasmobranchs rely heavily on their electrosense to locate and strike at prey [Blonder & Alevizon, 1988; Kajiura & Fitzgerald, 2009; Kajiura & Holland, 2002; Tricas, 1982]. The electric sense also appears to play a role in other other biological interactions including communication [Sisneros *et al.*, 1998], detection of mates [Tricas *et al.*, 1995] and predator avoidance [Peters & Evers, 1985; Sisneros & Tricas, 2002a]. Additionally, it has been hypothesized that elasmobranchs may be able to use their electric sense for navigational purposes. If ampullae are sensitive enough, they will respond to the electric field induced when either the fish or water moves through the Earth's magnetic field [Kalmijn, 1974; Murray, 1962; Paulin, 1995]

Detection threshold have been estimated from both nerve recordings and behavioural

experiments. Originally the threshold gradient for the most sensitive primary afferent units was estimated to be in the order of $1\,\mu V\,cm^{-1}$ [Murray, 1962]. More recent experiments extend this range, with units responding to gradients of $20\,nV\,cm^{-1}$ [Tricas & New, 1998]. This is still an order of magnitude larger than reported minimum behavioural response threshold values as low as $<1\,nV\,cm^{-1}$ [Kajiura & Holland, 2002]. If such a gradient were applied directly to the sensory cells the stimulus is minuscule, particularly in the presence of much larger background noise sources. Theories have been put forward to account for this remarkable sensitivity. The enhancement of the signal can generally be categorised into three key steps [Pickard, 1988]. Anatomical and biophysical properties of the animal and sensory structures combine to *focus* the stimulus onto receptor cells. The receptors are tonically active, so that changes to the focussed stimulus *modulate* the activity of afferent fibres. Fibres then *converge* to the same area in the Central Nervous System (CNS), which acts to *integrate* the output of a large number of receptor cells.

Briefly, the processes involved in the transduction of the signal are: an external electric field creates a transdermal potential in the ampullae of Lorenzini, which convert the electric signal to action potentials. The afferent nerves associated with the ampullae of Lorenzini are spontaneously active, information is encoded by either an increase or decrease in the rate of action potentials in response to the stimuli. The CNS is responsible for deciphering the signals and noise in the spike trains, thus allowing the animal to adjust its behaviours accordingly. These processes will be described in more detail in the following sections.

1.2 Anatomy and physiology of detectors

Electroreception appears to have been lost and re-established independently several times over the course of evolutionary history [Bullock *et al.*, 1983]. Despite many similarities, it was originally proposed that ampullary organs in cartilaginous fish were derived from the neural crest, unlike bony fish which possess ampullary organs derived embryonically from lateral line placodes. However recent research has confirmed that both ampullary electroreceptors and mechanosensory neuromasts form from lateral line placodes in elasmobranchs [Gillis *et al.*, 2012]. The homology of these organs between cartilaginous and non-teleost bony fishes suggests that an electrosensory system was already present in the last common ancestor of vertebrates [Gillis *et al.*, 2012].

1.2.1 Ampullae of Lorenzini

Elasmobranchs possess groups of specialized electroreceptive organs called the ampullae of Lorenzini. Each ampulla consists of two main parts: the ampulla proper, formed by alveoli and the jelly filled canal, which opens to the skin at pores (Figure 1.1). Because each pore leads to an internal ampulla they provide information about the count and distribution of internal organs without the need for dissection. Pores are distributed bilaterally, with distinct patterns of up to five different clusters [Norris, 1929]. The number and distribution of ampullary pores has been described across a variety of species [Atkinson & Bottaro, 2006; Berquist, 2003; Camilieri-Asch *et al.*, 2013; Egeberg *et al.*, 2014; Jordan, 2008; Kajiura, 2001; Kempster *et al.*, 2012; Mello, 2009; Moore & McCarthy, 2014; Norris, 1929; Raschi, 1986; Raschi & Adams, 1988; Theiss *et al.*, 2011; Tricas, 2001; Wueringer & Tibbetts, 2008; Wueringer, 2012]. While there are significant differences between species, within species the number and distribution of pores is relatively conserved and is not dependent of the age of the animal [Kajiura, 2001].

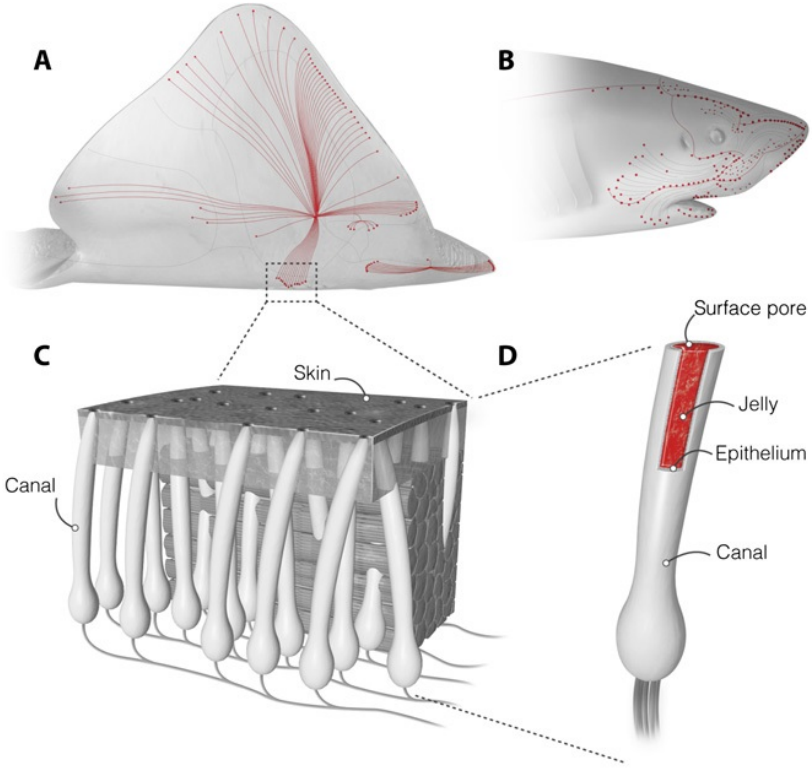

Figure 1.1: (A and B) Skates and sharks locate their prey by detecting the weak electric fields naturally generated by biomechanical activity. (C) A network of electrosensory organs called the AoL is responsible for this sense. (D) An individual ampulla consists of a surface pore connected to a set of electrosensory cells by a long jelly-filled canal. Sharks and skate can sense fields as small as 5 nV/cm despite canals travelling through up to 25 cm of noisy biological tissue. Reprinted from Josberger *et al.* [2016], under terms of the Creative Commons Attribution License.

The canals have a diameter of about 0.1 cm and range in length from 1 to 25 cm for marine elasmobranchs [Brown *et al.*, 2005]. Waltman [1966] likened these canals to a submarine cable, noting that the transduction of potential or current depends not only on the resistivity of the core but also the surrounding insulation. He observed that the canal walls were thick and their electrical resistance, averaging 6 MΩ cm, was "uniquely high". Conversely, the glycoprotein based gel filling these canals is highly conductive with similar properties to seawater, almost double the conductivity (inverse of resistivity) of body fluids [Murray & Potts, 1961]. Kalmijn [1974] queried whether it was primarily the voltage across or the current through the receptor or a combination of both that stimulated these receptive organs. Based on observations relating the properties of an ampulla to an ideal voltmeter or current-meter, it was concluded that the canals were likely signalling voltage down to receptor cells rather than channelling current.

More recently, there has been debate over whether the gel acts as a thermoelectric semiconductor allowing sharks to follow temperature gradients. Brown [2003] measured the strength of the electric field generated by an applied temperature gradient (thermopower) for the gel of two species of shark. Results suggested that ampullae may be sensitive enough to respond to temperature gradients of tiny magnitude (<0.001 °C). Fields *et al.* [2007] question these extraordinary claims, suggesting a measurement artefact resulting from the use of metallic electrodes. Experiments found that measuring ordinary seawater with silver electrodes reproduced the same effect as ampulla gel and when gel measurements were conducted with carbon or salt bridges no response was found. The controversy has yet to be resolved, but it was suggested in a review by Brown [2010] that future measurements with "small, single-material, well-characterized carbon electrodes" and electrophysiological examination where a temperature gradient is induced between the ampulla and some point along the canal should help to clarify matters.

1.2.2 Sensory cells

The receptor epithelium found in the alveoli (Figure 1.2a) consists of sensory and support cells joined by tight junctions. This creates an electrical barrier between the apical and basal surfaces of the epithelium [Tricas, 2001]. Receptor cells (Figure 1.2a) have a single kinocilium on their apical surface and form synapses with primary afferent nerve fibres (AFF) on their basal surface [Waltman, 1966]. The potential difference between these surfaces modulates the rate of release of neurotransmitter from within vesicles clustered about the synaptic ribbon (Figure 1.2b), located at the basal surface of receptor cells [Fields & Ellisman, 1988].

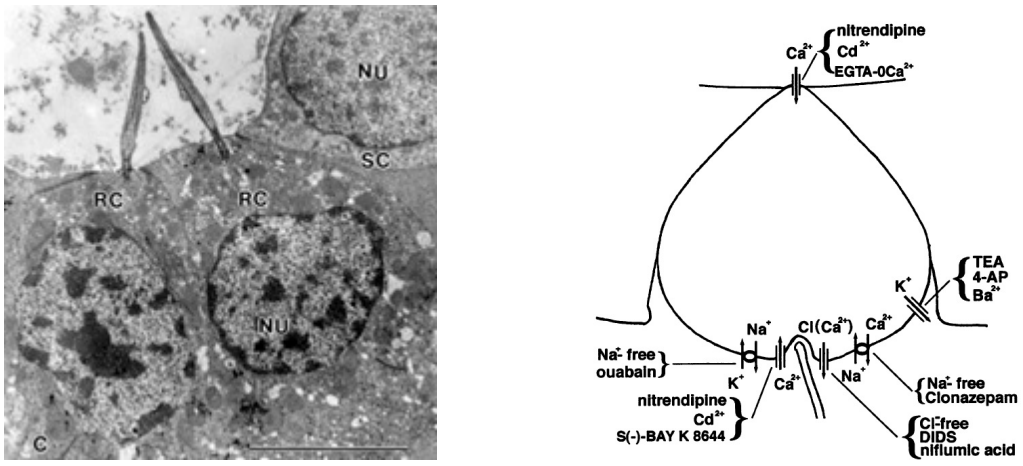

(a) Receptor cell section **(b)** Ion channels and transporters

Figure 1.2: Sensory cell of the ampulla of Lorenzini. a) Transverse section through sensory epithelium showing two adjacent receptor cells (RC) with their central nuclei (NU) and a supportive cell (SC) with an apically positioned nucleus (NU). TEM. Scale bar = 5 µm. Reprinted from Whitehead *et al.* [2015], with permission from John Wiley & Sons Inc. b) Diagram summarizing the ion channels and transporters in the ampullary epithelium identified by the effect of specific antagonists, agonists, or ion substitutions (in brackets) on the negative conductance and the oscillation, as interpreted from admittance spectra of isolated organs. Reprinted from Lu & Fishman [1995], with permission from Elsevier.

Most nervous system synapses respond to potentials in the order of tens of millivolts, several orders of magnitude greater than electroreceptor limits [Broun & Govardovskii, 1983]. It has been suggested that interactions between both positive and negative conductances, in apical and basal membranes, act to amplify signals [Lu & Fishman, 1994].

The morphology and biophysical properties of the peripheral electrosensory organs, and their associated sensory cells, play an important role in how an animal perceives stimuli. However, to comprehensively understand the function of the electrosensory system, it is also important to examine the circuitry that connects these sensors to the CNS.

1.3 Anatomy and physiology of the afferent nerves

A typical ampulla may contain 10,000 receptor cells, which are innervated by five to twenty primary afferent nerve fibres [Antipin *et al.*, 1984; Metcalf, 1915; Peabody, 1897]. These afferents (AFF) transmit sensory impulses from the periphery to the CNS via the dorsal branch of the Anterior Lateral Line Nerve (ALLN).

AFF are spontaneously active, their rate of discharge is modulated by the potential difference across the epithelium. Stimuli which make the apical surface more negative (relative to the basal surface) are depolarizing, resulting in excitation of nerve activity

(↑ in spike rate). Conversely, stimuli which make the apical surface more positive are hyperpolarizing, resulting in inhibitory nerve activity (↓ in spike rate) [Lu & Fishman, 1994].

Unlike mechanosensory hair cells in the lateral line, ampullary electroreceptors lack efferent innervation. Efferent innervation of hair cells has been implicated as playing an important role in the suppression of self stimulation, caused by the fishes own movement [Bodznick, 1989]. While reafference is still problematic for electrosensors, noise cancelling mechanisms appear to act within the CNS rather than at the receptors.

1.4 Central processing of stimuli

Like the mechanoreceptive lateral line system, the ampullae of Lorenzini are associated with cerebellar-like specialized hindbrain circuitry (Figure 1.3a). The AFF terminate in the Dorsal Octavolateral Nucleus (DON) in a somatotopically organised manner [Bell & Maler, 2005], this forms a map like representation of the spatial arrangement of electroreceptors within the brain. In skates, the DON is divided into regions corresponding to the ampullary clusters, with the volume of each division being proportional to the number of ampullae, rather than the body surface area served by these receptors [Bodznick & Northcutt, 1984]. Likewise, somatotopy of electrosensory receptive fields is evident in both the mediolateral and rostral-caudal axes in rays [Schweitzer, 1986]. Similar patterns of termination exist in other Chondrichthyes [Bodznick & Boord, 1986].

Immediately below the molecular layer, AFF contact with ascending efferent neurons (AEN), which are the principal output of the DON (Figure 1.3a). While the animals own ventilatory movements appear to be mainly responsible for the activity of AFFs, the second-order AENs appear to effectively learn to cancel out the effects of this much larger stimuli and extract biologically relevant signals (Figure 1.3b; Montgomery & Bodznick [1999]). The neural mechanisms behind this signal processing appear to be the combination of common mode rejection and adaptive filtering [Nelson & Paulin, 1995]. This effect can be explained by an adaptive filter model in which the self-generated component of sensory input is predicted by parallel fibre activity and subtracted from the sensory input in the DON [Montgomery & Bodznick, 1999; Nelson & Paulin, 1995]. However, parallel fibre activity seems to have non-linear effects on AEN responses to afferent input, at variance with predictions of this model [Rotem *et al.*, 2007, 2014].

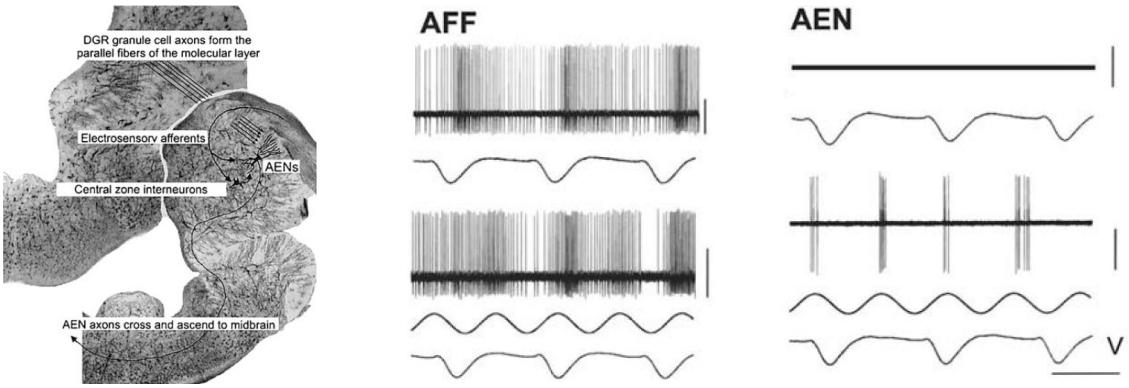

(a) Hindbrain circuits **(b)** Reafference comparison between AFF and AEN

Figure 1.3: Hindbrain circuitry associated with suppression of reafference. a) Principal neuron (AEN-ascending efferent neuron) and circuits of the dorsal octavolateralis nucleus (DON) are shown overlaying Golgi stained transverse sections. Reprinted from Bodznick *et al.* [2003], with permission from Springer. b) Comparison of afferent (AFF) and AEN activity in relation to the animal's own ventilation and an extrinsic electrosensory stimulus. Top two traces for both AFF and AEN represent spontaneous spike activity and record of the animal's ventilation respectively. Note that the AFF is strongly spontaneously active and strongly driven by the animal's ventilation. The AEN is silent and unaffected by ventilation. The lower three traces for AFF and AEN represent the spike activity in response to a 1 Hz, 2 µV extrinsic electrosensory stimulus, the representation of the stimulus itself, and the record of ventilation. Reprinted from Bodznick & Montgomery [2005], with permission from Springer.

1.5 Environmental adaptations

Both peripheral anatomy and CNS structures associated with electroreception have been examined in terms of sensory adaptation to an animal's given environment. However, such investigations have several difficulties. Firstly, phylogeny also has to be taken into account, as similarities and differences may due to evolutionary history rather than ecological adaptations. Secondly, it's often difficult to classify some species into a single particular habitat as there can be some overlap. Despite this, Kajiura *et al.* [2010] noticed several broad trends in the data. Oceanic pelagic and deep water species have fewer pores than coastal pelagic species, suggesting a reduced role of electroreception in predatory iterations. Deep water species showed the greatest range of both total pore number and ratio of dorsal to ventral pores. These results suggest utilization of different feeding strategies, with some species likely feeding off the sea floor and others using alternative strategies, such as ambush predation or benthic invertebrate specialists. The relative roles of different sensory cues was also supported by differences in brain morphology, with deep water species showing enlargement of cerebellar-like structures and a reduction of the telencephalon compared to coastal species [Kajiura *et al.*, 2010].

1.6 Inference in nervous systems

It has been hypothesised that utilization of different feeding strategies was also the selection pressure driving the origin of nervous systems. When pre-Cambrian animals transitioned from passive filter-feeding, or substrate grazing, to animal-on-animal predation it became advantageous to have a nervous system in spite of its energetic cost [Monk *et al.*, 2015]. Even a rudimentary threshold sensor is beneficial in predator-prey interactions, allowing for precisely timed actions, such as striking or fleeing, in response to a particular world state reaching a critical level [Monk & Paulin, 2014]. As such a trigger becomes more sensitive it also becomes less reliable. An unreliable threshold trigger may be useful, but at a certain point it is more useful to treat its responses as information relevant to deciding how to act rather than as instructions to act per se. At this point it is necessary to make inferences from the observed events, and it is necessary to evolve a brain. The question then becomes how to extract the maximum amount of information about behaviourally relevant states of the world based on dynamic, potentially noisy, measurements.

Bayesian inference provides a optimal framework for updating beliefs about the state of the world based on uncertain measurements. Paulin [2005] constructed a simple model of the electrosensory system where individual spikes of AFF are noisy measurements of prey location and the spatial distribution of spikes in the AEN provides a Monte Carlo approximation of the posterior (belief about prey location given sense data). Recently it has been demonstrated that properties of real neurons and their circuitry emerge naturally from using principles of probability theory, without the need for additional biological constraints [Paulin, 2015]. The structure of the Bayesian lattice, used for inference given observations from a Poisson process, is remarkably similar to the anatomy of cerebellar-like structures [Paulin, 2015], such as the electrosensory filtering structures in the shark hindbrain depicted in Figure 1.3a.

The elasmobranch electric sense is relatively primitive in structure. However, it has many similarities to more complex vertebrate senses and provides a good model system for examining general principles of brain structure and function.

1.7 Models of passive electroreception

Computational models of electroreception can serve neuroethological research in multiple ways:

1) they allow complex hypotheses on central nervous systems to be tested

in silico. The ampullae of Lorenzini detect electric fields and provide the CNS spatial and temporal information about the stimuli. From this information the brain constructs a representation of the external world. In order to investigate models of neural processing in sharks' brains, we first need to construct a realistic representations of spatial and temporal information acquisition by the electrosensory periphery. The potential difference experienced by receptor cells depends on numerous factors, including the location of the pore, canal length and orientation. These spatial factors, along with pore abundance, have been measured for certain species. However, quantitative evaluation of how the biophysical properties of the ampulla, and supporting structures, shape the stimulus is somewhat lacking. A theoretical analysis of electrosensory observations will complement previous experimental studies and attempt to predict the electrosensory stimulus with acceptable accuracy. If we can mimic the spatial and temporal response of primary afferent neurons, this will allow a realistic environment for testing hypotheses of sensory processing in the cerebellar-like circuits of the DON.

2) they can provide new ideas for experimental measurement and manipulation. Models represent simplified versions of reality, as it is often impossible to achieve an exact representation of the entire system under all conditions. A model can be interpreted as a hypothesis about a given system: it includes only the parameters and interactions considered biologically relevant. Model development is a continuous task, allowing the examination of the role of different parameters in the sensory processing. We aim to investigate the morphological and biophysical properties that shape the stimulus received by the CNS, through doing so we may identify parameters of the model that require further experimental analysis.

3) they can provide biological inspiration for engineers. Electrosensory imaging offers many interesting areas to explore. The ampullary system of elasmobranchs is capable of sensing electric fields often with greater sensitivity and at spatial and temporal resolutions exceeding conventional engineering instrumentation. Of particular interest is even though electroreceptors are extremely sensitive, animals successfully use electroreception in the presence of noise far exceeding the stimulus. Through studying the ampullae of Lorenzini we may be able to identify fundamental principles concerning the design and function of passive electosensing systems. This is especially relevant now that researchers are starting to develop artificial electrosensors as a means of underwater detection, localization and classification of objects [Friedman *et al.*, 2010].

Modelling efforts to date can be divided into two parts: 1) response of electrosensory periphery to naturalistic stimuli; and 2) sensory processing in the DON.

1.7.1 Response of electrosensory periphery to naturalistic stimuli

This study of the response of electrosensory periphery builds on the work of Berquist [2003] and overcomes several of the limitations of previous modelling attempts. A summary of the mathematical studies of sensorimotor strategies in electroreception is presented in Table 1.1. For the clarity of comparison, studies are described using five criteria: model stimulus, morphological and biophysical properties of ampullae, the biophysical properties of body tissue, motion through the environment, and response of AFF (Table 1.1).

Table 1.1: Mathematical studies on the response of electrosensory periphery

Study	Stimulus	Body	Ampulla	Approach	AFF
Gusev *et al.* [1986, 1985]	Dipole	Cylinder shaped ray	2D	None	None
Pickard [1988]	Uniform	Spherical fish	None	None	Linear model relating lumen V to firing rate
Adair *et al.* [1998]	Uniform	Spherical fish	None	None	Firing rate modulated via voltage gated sensory cells
Brown [2002]	Dipole	None	2D 36 fixed length canals, 2 geometries corresponding to roundhead and hammerhead	Unchanged, Direct, Field line	None
Berquist [2003]	Dipole, Monopole, Uniform	None	3D morphologically accurate dogfish	Unchanged, Direct, Field line, Sinusoidal movement	Decay function used to mimic published data Δ V to firing rate
Camperi *et al.* [2007]	Dipole	None	Simplified 2D ray. Only dorsal hyoid cluster (132 ampullae). Clusters are treated as a single point	Parallel swim-by (same as unchanged in other models) Non-parallel swim-by (direction 45° angle to source)	Sigmoidal gain function fitted to published data
Kim [2007]	Dipole	None	2D simplification of shark 50 ampullae 15 clusters	Field line Sinusoidal movement	None
Present study	Dipole, Uniform	2D accurate, 2D and 3D simplified	2D projections, 3D simplified	Unchanged, Direct, Field line	Examination of afferent spontaneous activity

Models have been used to investigate the spatial and temporal mechanisms responsible for elasmobranch electro-sensitivity The ampullae of Lorenzini consists of structurally

independent groups of ampullae, with canals of differing lengths and orientations. Models have shown that these spatial features are responsible for the functional differences between responses of individual receptors to electric stimuli [Berquist, 2003; Brown, 2002; Camperi *et al.*, 2007; Kim, 2007].

Models illustrated the body of the fish distorts the electric field, altering the sensitivity of the receptors to the stimulus [Adair *et al.*, 1998; Gusev *et al.*, 1986, 1985; Pickard, 1988]. Therefore body tissues can be regarded as accessory structures of the electroreceptors and should be accounted.

Dynamic models suggest that the stimulus pattern depends not only on the distance between the sensors and the source, but also the rotational movements of the animal within the electric field [Berquist, 2003].

From the potential drops in ampullary sensors models of neural activity of AFF have been examined. These range in complexity from simple models which qualitatively look like published data [Berquist, 2003; Camperi *et al.*, 2007; Pickard, 1988], to models where firing rate is dependent on voltage gated sensory cells and their interactions [Adair *et al.*, 1998].

Previous studies have illustrated key concepts in electroreception, but none of them have included sufficient detail to examine the complex interactions between the stimulus, the movements and shaping of the signal by the animal and its sensory receptors (Table 1.1). The model presented here builds on the framework created by Berquist [2003] and uses the virtual dogfish [Berquist, 2003; Berquist & Paulin, 2001] to create a morphologically realistic FEM model to examine shark electroreception. This thesis investigates the effects of different fish body geometries and electrical properties tissue on the spatial and temporal pattern of voltage drops within canals under differing behaviourally relevant stimuli. The statistical organization of spontaneous spiking activity in the electrosensory periphery is examined, along with how it converges centrally onto secondary neurons.

1.7.2 Sensory processing in the DON

Models of the canal voltage drops allow for computational models of the AFF neurons, which in turn allow us to investigate the CNS circuitry involved in sensory processing in the DON. The DON has been implicated as playing a vital role in learning to cancel out the effects of the fish's own movements, acting as an adaptive filter [Montgomery & Bodznick, 1994]. The noise component in the signal is suppressed in the cerebellar-like circuitry, where the parallel fibres in the molecular layer adjust the strength of their synapses onto the AEN [Montgomery & Bodznick, 1999]. Using known anatomical circuitry in con-

junction with accurate representations of neuron response properties, modelling by Nelson & Paulin [1995] demonstrated that the combination of common-mode rejection and adaptive cancellation were sufficient to suppress ventilatory reafference. Whereas previous modelling studies take a network-level, phenomenological approach, recently the adaptive filter has been implemented using a conductance-based neuron model which demonstrates suppression of reafferent signals based only electrophysiological neuron dynamics [Bratby *et al.*, 2014].

However, some experimental results are inconsistent with the adaptive cancellation models of the DON proposed above. Rotem *et al.* [2007, 2014] suggest that filtering may be mediated by parallel fibres adjusting the AEN sensitivity to AFF input. Similar to the descending gain control observed in the teleost electrosensory brainstem [Bastian, 1986; Mehaffey *et al.*, 2005; Nelson, 1994]. As an alternative to adaptive filter models, recent advances have been made suggesting the cerebellar-like circuits of the hindbrain act as a Bayesian estimator [Paulin, 2005].

1.8 Thesis objectives

This thesis investigates electroreception as dynamic state estimation (Figure 1.4) and hypothesises how the neural circuitry of the DON may apply Bayes' rule. To a Bayesian, a measurement is a sample from a probability distribution whose parameters include state variables of interest (e.g. distance to prey). The measurement distribution is called the *likelihood* function or generative model. The objective for a Bayesian brain is to compute the *posterior* density of relevant state variables from sensory data. This must be done by continuously modifying a *prior* distribution, as new observations become available.

Accurate, realistic generative models are a key pre-requisite for discovering if and how elasmobranchs' brains compute Bayesian posterior probability distributions from electrosensory data. This thesis examines two fundamental processes involved in the generative model. First, the physics governing the interaction between the electrosensory system and weak electrical stimuli in the aquatic environment. Second, the spontaneous activity of electrosensory afferents, which is related to how these neurons fire in response to small stimuli.

This thesis aims to implement a spiking neural particle filter, which takes simulated electrosensory spike trains (based on the generative model developed here) and infers relevant state variables.

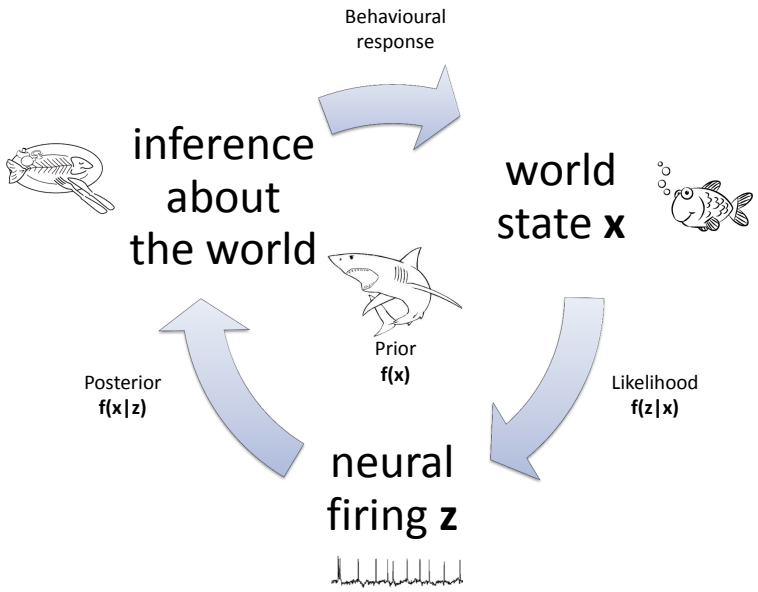

Figure 1.4: Schematic of Bayesian inference in the elasmobranch electrosensory system. A generative model (*likelihood*) maps the state of the world **x** to sensory spikes **z**, the brain combines this with existing beliefs (*priors*) to compute the *posterior*. The *posterior* is continuously updated as new observations become available, allowing the shark to make inferences about the state of the world.

1.9 Thesis overview

Electrosensory processing of external stimuli by the central nervous system depends on the extraction of information that is shaped by pre-receptor, receptor and neuron circuitry mechanisms. This thesis investigates several key issues of sensory acquisition in elasmobranchs, including:

- Biological physics governing the interaction between the electrosensory system and the environment surrounding it and the use of numerical models to characterize such interactions (Chapter 2).
- How the morphology and electrical properties of shark tissue distort the stimulus received by the ampullae of Lorenzini (Chapter 3).
- The statistical organization of spontaneous spiking activity in the electrosensory periphery and how this may reflect a trade-off between sensitivity, noise and energetic efficiency (Chapter 4).
- Convergence of afferent input onto the hindbrain and how a network of spiking neurons with similar circuitry can construct and represent the Bayesian posterior density (Chapter 5).

We predict that the statistical organization of spiking activity in the electrosensory periphery and anatomy of the CNS may reflect an efficient solution for maximizing sensory system sensitivity in the presence of noise, via Bayesian neural computation.

Part I

Characterising the stimulus received by the electrosensory system

Chapter 2

Methodology

2.1 Introduction

The key motivation behind this section is to improve our current understanding of the biological physics governing the interaction between the elasmobranch ampullary electrosensory system and the water surrounding it. This will be done by applying and solving Maxwell's equations and in this way clarifying the signal received by individual ampulla, for subsequent neural processing. Modelling allows investigations into hypotheses that may be difficult, or impossible, to undertake; such as from live animals undergoing naturalistic behaviour. Modelling also allows parameters to be manipulated under controlled circumstances.

There already exists several models of the peripheral electroreceptive organs in elasmobranchs. To date these models have all either neglected the presence of body tissues, or approximated the animal as a sphere or cylinder (Table 1.1). Numerical approaches are gaining popularity, largely due to the decreasing costs and increasing processing power available in modern computers. Thus, numerical techniques have been applied, by researchers in a variety of fields, to examine scenarios of greater complexity than analytical approaches previously allowed. This chapter will briefly describe the different methods used in electric field modelling and their application to electric imaging in weakly electric fish. We then provide more detail on the numerical approach used in our research, Finite Element Method (FEM), COMSOL the software and some of the assumptions required to make the model tractable.

2.2 Approaches to electric field modelling

2.2.1 Maxwell's equations of Electromagnetics

We begin with the fundamental equations for electric fields and various simplifying assumptions, then describe some of the approaches used to solve these equations. Electromagnetic propagation in any media can be characterised by Maxwell's equations for time varying fields, we use the differential form presented in COMSOL's AC/DC Module User Guide:

$$\nabla \times \vec{H} = \vec{J} + \frac{\partial \vec{D}}{\partial t} \tag{2.1a}$$

$$\nabla \times \vec{E} = -\frac{\partial \vec{B}}{\partial t} \tag{2.1b}$$

$$\nabla \cdot \vec{D} = \rho \tag{2.1c}$$

$$\nabla \cdot \vec{B} = 0 \tag{2.1d}$$

where $\vec{E}$ and $\vec{H}$ are the electric and magnetic field intensities, $\vec{D}$ is the electric displacement (or electric flux density) and $\vec{B}$ is the the magnetic flux density. Additionally $\vec{J}$ and ρ denote the current and electric charge densities respectively. By combining Equation (2.1c) with the divergence of Equation (2.1a) we obtain the equation of continuity:

$$\nabla \cdot \vec{J} = -\frac{\partial \rho}{\partial t} \tag{2.2}$$

Solving Maxwell's equations requires additional equations (constitutive relations) describing the electrical properties of the materials in which the fields and currents are produced. These may be very complex in biological tissues, but we simplify by assuming that the media are linear and isotropic. In this case we have:

$$\vec{D} = \epsilon \vec{E} \tag{2.3a}$$

$$\vec{B} = \mu \vec{H} \tag{2.3b}$$

$$\vec{J} = \sigma \vec{E} + \vec{J}_e \tag{2.3c}$$

where μ is the magnetic permeability, ϵ the electric permittivity. In a medium with electric conductivity σ the electric field induces a current additional to any externally generated current $\vec{J}_e$.

It is these equations from which the electromagnetic fields generated by a given source

$\vec{J_e}$ in a medium are derived. It can also be useful to formulate these problems in terms of the electric potential (V) and magnetic potential ($\vec{A}$). These are described by:

$$\vec{B} = \nabla \times \vec{A} \tag{2.4a}$$

$$\vec{E} = -\nabla V - \frac{\partial \vec{A}}{\partial t} \tag{2.4b}$$

2.2.2 Modelling Maxwell's equations

While the basic physical laws of electromagnetics are well known, it can be difficult to solve the partial differential equations (PDE). Thus analytical approaches are generally only used in highly simplified models, for more realistic geometrical and biophysical properties numerical approaches are often employed. Here we will briefly discuss some of the more commonly used methods, before describing how they have been applied to modelling active electroreception in weakly electric fish.

Numerical solvers are based on discretising the PDEs, which are continuous, based on either domain or boundary discretisation techniques. The most commonly used approaches in biological electromagetics are Finite Difference Method (FDM), Finite Element Method (FEM) and Boundary Element Method (BEM). The specific properties of the problem at hand determine which of these techniques is most advantageous (Table 2.1).

Table 2.1: A comparison of the different methods for solving the forward problem of a source in conductive medium. Modified from Hallez *et al.* [2007], under terms of the Creative Commons Attribution License.

	FDM	**FEM**	**BEM**
Position of computational points	volume	volume	surface
Free choice of computational points	no	yes	yes
System matrix	sparse	sparse	full
Solvers	iterative	iterative	direct
Number of compartments	large	large	small
Requires tessellation	yes	yes	no
Handles anisotropy	yes	yes	no

FDM models discretise the space-time domain onto a grid (Figure 2.1(B)). The PDEs are then approximated using finite difference equations, describing the relationships between neighbouring nodes, which can be derived by truncating Taylor expansions [Pruis

et al., 1993]. However this technique lacks geometrical flexibility, meaning it cannot deal with complex geometries.

Another powerful numerical approach for solving domain discretised PDEs is FEM. In this case elements are usually, but not limited to, triangles in 2D or tetrahedra in 3D (Figure 2.1(C)). The solution is then determined by approximating the true PDE in each element. The original problem is represented by a set of local basis functions, which are combined to obtain a system of equations for the final calculation of the global solution [Pruis *et al.*, 1993]. The resulting matrix is sparse, thus it can be tackled with efficient numerical techniques. FEM is sometimes advantageous over other numerical approaches, as elements can have different shapes, which can be used to handle complex geometries and material heterogeneities. However, as the complexity of the problem increases so does the size of the system of equations, which can have a high computational cost.

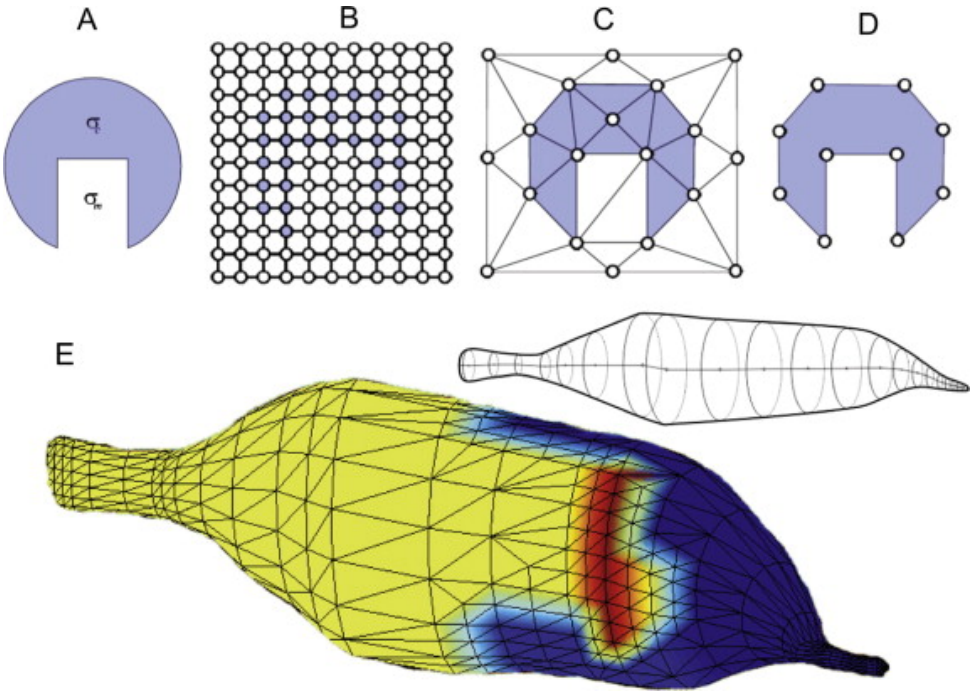

Figure 2.1: The first row of figures shows strategies of different numerical methods used to discretise a two-dimensional geometry problem: (A) Shows a 2D scene composed by an arbitrary object c (pale violet) in a medium m (pale yellow), with their respective internal conductivities σ_c and σ_m. (B) In the Finite Difference Method (FDM) the nodes are distributed uniformly throughout space to reconstruct the scene in A using a regular grid, (C) in the Finite Element Method (FEM) elements are triangles and there are only nodes at their vertices, (D) in the Boundary Element Method (BEM) elements are segments and nodes are at the end of the segments defining the boundary surface. In the second row it is shown how the methodology applies to the 3D fish problem: (E) Use of the BEM in 3D scenes: *G. petersii*, the skin of the fish was approximated by triangles; different colors represents different conductivities of the skin. Reprinted from Gomez-Sena *et al.* [2014], with permission from Elsevier.

BEM is similar to FEM, except instead of domains only boundaries are discretised (Figure 2.1(D)). The resulting surface integral equations can be computed using the Barnard formula [Pruis *et al.*, 1993]. Solutions require that boundaries are closed and separate regions must be homogeneous and isotropic in nature. On each boundary element the PDE is approximated either using truncated Taylor expansion (as with FDM) or using a set of local basis functions (as with FEM) [Pruis *et al.*, 1993]. Unlike FDM and FEM where matrices are sparse, the matrix representing BEM is dense, making it difficult to solve. However, due to only discretising boundaries rather than domains it generally reduces the number of points required significantly.

To our knowledge numerical techniques have yet to be applied to the study of passive electroreception. This is not limited to elasmobranchs, Gomez-Sena *et al.* [2014] stated "Passive electroreception has been poorly studied through modelling approaches to the point that we did not find simulation results in the bibliography of weakly electric fish". On the other hand, modelling studies of active electroreception in weakly electric fish span the past four decades and many research groups [Gomez-Sena *et al.*, 2014]. We briefly describe some of the different approaches used, for a detailed overview see Gomez-Sena *et al.* [2014].

2.2.3 Modelling of active electroreception in weakly electric fish

Whereas passive electroreception refers to the detection of weak electric fields generated by animals and other sources in the environment, active electroreception refers to detecting the distortions to a self-generated electric field caused by the presence of objects. Like the passive sense, active electroreception has evolved independently multiple times and has been implicated as playing a role in object location, orientation and communication [Lavoue *et al.*, 2012].

Analytical methods have been used to characterize the electric fields generated by weakly electric fish based on variations of Maxwell's equations (section 2.2.1). Bacher [1983] reduced the three-dimensional (3D) problem to a two-dimensional (2D) one by assuming cylindrical symmetry. The electric field generated by the fish was represented by the superposition of line charges and an object perturbing this field was modelled by a dipole. It was demonstrated how various parameters such as size, shape and position affected the electric image of an object. Analytical approaches lack the precision required when geometries and/or sources are complex. They do not consider how the properties of the fish body shape the stimulus received [Gomez-Sena *et al.*, 2014]. However, in spite of lack of explicit representation of the high-resistance skin and low-resistance internal body

of the fish, Chen *et al.* [2004] were able to estimate key features of empirically measured signal and background components across the electroreceptor array of fish during natural behaviours. While analytical approaches are fast, numerical approaches provide greater accuracy by allowing more complex geometries and/or physics to be examined. However, there generally is a trade off between model complexity and computation time.

Initial efforts in finite difference models also relied on a 2D approach. Heiligenberg [1975] solved Laplace's equation in 2D describing the electric field in the mid-horizontal plane of the animal's body, this approximation was expected to accurately model the animal's near field becoming less accurate at larger distances from the animal. Using this model not only was he able to simulate electric images, but he also made predictions of the ranges of parameters such as interior body and skin resistances prior to any direct measurement. More recently, 3D FDM was applied to studying the images of capacitive objects [Budelli & Caputi, 2000]. Results were qualitatively similar to those previously obtained using a 2D model [Caputi *et al.*, 1998] and provided a realistic model which was able to reproduce experimental data.

Likewise the first FEM model was also based on solving Laplace's equation in 2D. The main advantage of this FEM approach over the previous FDM simulation was this simulation had a heterogeneous mesh, allowing a higher mesh resolution near the surface of the fish [Hoshimiya *et al.*, 1980]. Results demonstrated that skin resistance plays an important role in shaping the electric image, with skin resistivity being higher at head than tail. The majority of FEM models have been limited to 2D representations of the horizontal mid plane of the fish. These models can easily be adapted to a 3D state, but the cost in terms of computation needs increases significantly. Recently Ahn & Kim [2012] created a 3D FEM model which examined the electric field perturbation for arbitrary shaped target objects. The potential applicability of such a FEM model to examining the relative resistivity of fish's internal body, fish skin, and water was also discussed.

In order to avoid the large number of elements required by FEM to accurately represent thin layers, such as skin, BEM has often been applied because only the solution at boundaries is required. BEM has been successfully applied to the 3D study of 1) the fields generated by weakly electric fish, 2) the voltage and current across the skin in the presence and absence of objects and 3) the effect of position and electrical properties of objects on electric images [Gomez-Sena *et al.*, 2014]. While BEM has been the most commonly applied approach in modelling weakly electric fish, it is not without its drawbacks. BEM requires additional calculations to determine the electric potential and field in non-boundary regions, whereas FDM and FEM calculate these quantities directly.

After considering the advantages and disadvantages of the methods discussed above,

a decision was made to create a FEM shark model to examine passive electroreception. Realistic models of the measurement process are necessary for determining if and how sharks' brains perform Bayesian inference.

2.3 Finite Element Method

FEM provides a numerical approach for finding solutions of the spatial distribution of one (or more) dependent variables. In our work we seek to find the distribution of the electric field (or equivalently electric potential) in a shark and surrounding medium. Mathematically, this problem is expressed by the differential equations described in Section 2.2.1. The region of interest is digitized in small elements Figure 2.1(C). An approximate solution is associated with each element, it allows only simple spatial variation and support is local (i.e. the solution is non vanishing inside the given element and zero elsewhere) [Lehner, 2008]. The global solution consists of a system of equations that is formed from this set of linearly independent basis functions, a corresponding number of initially undetermined parameters and the boundary conditions [Lehner, 2008]. Galerkin's method of weighted residuals is usually used to determine the value of the parameters at the nodal points [Lehner, 2008]. In general this system of equations is very big, hence software such as COMSOL that incorporates methods to reduce the computational burden and increase efficiency is useful.

2.4 COMSOL Multiphysics

COMSOL Multiphysics is software that lets the user model and simulate physics-based systems using FEM. The user can either define their own PDEs or can choose from one of the predefined physics modules. The user first specifies the physics, spatial and temporal dimensions of the model. Then the geometry of the problem must be defined. For simple geometries, this can be achieved by using the geometry primitives in COMSOL to create a geometry union or assembly, more complicated geometries may require using external computer-aided design tools and importing the resulting entities. Domains, boundaries, edges and points are then assigned relevant material properties and physical constraints. Finally, the geometry is meshed, the model is solved and the solution can be either examined in COMSOL or exported for post-processing. The electronic supplementary material (Appendix A) includes a description and simple example of how to implement models via the COMSOL user interface and how generate .m files in COMSOL for use in

MATLAB. The electronic supplementary material (Appendix A) also includes copies of COMSOL/MATLAB generated figures for high resolution viewing.

Our modelling makes use of the predefined AC/DC module, which allows for simulating electric, magnetic and electromagnetic fields in static and low-frequency applications. In particular, we use the electric currents interface to compute electric field, current and potential distributions in conducting media. This physics interface solves a current conservation equation based on Ohm's law using the scalar electric potential as the dependent variable (Equation (2.4b)). The specific equations and boundary conditions will be discussed in section 2.5.

Additionally, COMSOL offers a variety of algorithms which solve the system of equations. There are two fundamental classes that are used: direct and iterative methods. All of the direct solvers are based on lower-upper decomposition, whereas iterative solvers are essentially similar to a conjugate gradient method. Direct methods are both memory and CPU time intensive so are suited to smaller problems, whereas iterative solvers are generally used for larger problems and approach the solution gradually to within a given convergence tolerance. COMSOL automatically detects the best solver for the defined system of equations without requiring any user interaction.

2.5 Modelling considerations

Humphries [2010] warns modellers "The validity of code results depends more on the identification of the relevant physical processes and the soundness of approximations than on the sophistication of the numerical methods or the capabilities of the computer". Here we identify the relevant physical processes and approximations required for the model to be computationally tractable.

2.5.1 Sources of electric fields in the ocean and behavioural experiments

Sea water acts as a highly conductive medium, presenting a wealth of electromagnetic features to animals possessing sensory systems with detective capabilities. These signals, varying in waveform and strength, are briefly described in the following subsections.

2.5.1.1 Near-field dipole sources

Aquatic animals emit electric fields through three main mechanisms. Firstly, direct current fields are associated with differences in potential distribution across certain areas, in particular mucous membranes and gill epithelia. Wounded animals, even with minor skin abrasions can often have significantly increased potentials [Kalmijn, 1972]. Interestingly, Kalmijn [1972] discovered that the direct current (DC) fields emitted by elasmobranchs were generally ten fold smaller than those of teleosts, which was suggested to be a mechanism for reducing self-stimulation. Secondly, the DC field is modulated by alternating contractions and expansions of body cavities producing low frequency alternating current (AC) fields [Kalmijn, 1972]. Finally, high frequency AC fields were immediately recognised as resulting from muscle action potentials (e.g. heart, gill and motor muscles; Kalmijn [1972]). While high frequency AC fields do exist in the ocean, these are of less interest, as they are outside of the range of elasmobranch detection capabilities.

Prey bioelectric fields are typically described mathematically as a multipole expansion. In seawater higher-order components rapidly decay leading to sources being primarily monopolar or dipolar fields, which have been the primary focus of most studies [Kalmijn, 2000]. In behavioural experiments response thresholds are often quantified using a dipole electric field generator designed to mimic prey fields. However there was little data on the field characteristics of prey items to validate the accuracy of experimental design.

Recently Bedore & Kajiura [2013] quantified the voltage and frequency characteristics of eleven families of marine organism, as well as an experimental dipole stimulus generator. As predicted, the largest voltage sources were at the mucous membranes and gill epithelia. Supporting previous studies larger potentials were found in teleost species than elasmobranch and invertebrate species [Bedore & Kajiura, 2013]. All species examined produced both voltage and frequency characteristics that would be detectable by elasmobranchs within a sufficient distance (Table 2.2).

The stimulus generator was found capable of reproducing the DC voltages characteristic of the species examined, but AC voltages were not examined. As expected from an ideal dipole, the stimulator voltage decayed proportionally to an inverse square, and electric field inverse cube of the distance from the source [Bedore & Kajiura, 2013]. However while the dipole stimulator decayed as expected, all prey sources decayed at a slower rate than the ideal dipole prediction (Table 2.2). Bedore & Kajiura [2013] hypothesised that this may be due to the complex multipolar nature of actual prey items, with higher order terms actually contributing significant components to the source. It is unclear how important these higher order terms are to fish behaviour as foraging choice experiments

demonstrated while the small-spotted catshark (*Scyliorhinus canicula*) is able to distinguish between DC magnitude and preferred AC over DC, they were either unable to discriminate between or had no preference between a natural (crab) and similar magnitude artificial dipole [Kimber *et al.*, 2011].

Table 2.2: Point source voltage and electric field decay equations and theoretical elasmobranch detection distance from electric potential decay measurements, with a median sensitivity of $35\,\mathrm{nV\,cm^{-1}}$ for elasmobranchs. Reprinted from Bedore & Kajiura [2013], with permission from University of Chicago Press.

Family	Point source voltage	Electric field	Detection distance (cm)
Ariidae	$y = 15.98\,\mathrm{x}^{-.48}$	$y = 7.62\,\mathrm{x}^{-1.48}$	38
Diodontidae	$y = 76.55\,\mathrm{x}^{-1.19}$	$y = 90.72\,\mathrm{x}^{-2.19}$	36
Gerreidae	$y = 74.39\,\mathrm{x}^{-1.27}$	$y = 94.77\,\mathrm{x}^{-2.27}$	32
Haemulidae	$y = 32.65\,\mathrm{x}^{-.67}$	$y = 21.78\,\mathrm{x}^{-1.67}$	47
Lutjanidae	$y = 127.74\,\mathrm{x}^{-.97}$	$y = 124.30\,\mathrm{x}^{-1.97}$	63
Sphyraenidae	$y = 197.58\,\mathrm{x}^{-1.02}$	$y = 201.33\,\mathrm{x}^{-2.02}$	73
Prey simulating	$y = 118.59\,\mathrm{x}^{-1.95}$	$y = 231.49\,\mathrm{x}^{-2.95}$	20

2.5.1.2 Modelling dipole sources in COMSOL

An ideal DC dipole field can be described analytically in 3D by [Griffiths, 1999]:

$$\vec{E}_{dip}(\vec{r}) = \frac{1}{4\pi\sigma}\frac{1}{r^3}[3(\vec{p}\cdot\hat{r})\hat{r} - \vec{p}] \tag{2.5}$$

where $\hat{r} = \frac{\vec{r}}{|\vec{r}|}$ is the unit vector in the direction of $\vec{r}$ and $\hat{r} = |\vec{r}|$ is the magnitude of the separation vector between the origin and a point in space. This represents the limiting case of zero separation distance between two equal and opposite point sources $+q$ and $-q$ separated a short distance d. The electric current dipole moment is given by $\vec{p} = q\vec{d}$, where $\vec{d}$ is a vector going from $-q$ to $+q$.

In COMSOL point sources have a finite but mesh-dependent potential value. In general, using volume or boundary sources is more flexible than using point sources but the meshing of the source domains becomes more expensive.

2.5.1.3 Far-field and geomagnetically induced uniform electric fields

Whereas during prey detection electroreception is used to detect localized fields relating to nearby dipole-like sources, at distances sources become more uniform in nature. Additionally aquatic animals also encounter localized uniform electric fields resulting from

movement of seawater through the Earth's geomagnetic field. The horizontal component of the ocean current induced field reaches values in the order of $0.1\,\mu V\,cm^{-1}$ toward the poles and is weaker near the equator [Tyler *et al.*, 1997]. Conversely, the vertical component tends to be slightly higher and is greatest near the equator and weaker near the poles [Tyler *et al.*, 1997]. Peak tidal flows can induce electric fields as large as $1\,\mu V\,cm^{-1}$ [Kuvshinov *et al.*, 2006], while magnetic anomalies can induce fields that are larger still [Kuvshinov, 2008].

Prompted by the findings that electric fish use their electric sense for navigation, Murray [1962] hypothesized electromagnetic induction may be used for this purpose in elasmobranchs. While he was sceptical that ampullae had the required sensitivity, he identified the horizontal component of the Earth's field as the relevant stimulus for potential navigation. Kalmijn [1974] suggested two possible modes of electromagnetic orientation: passive mode where fish detect the fields induced by ocean currents, or active mode where the fields result from the animals' own swimming activity.

The active mode hypothesis has been revisited, with Paulin [1995] clarifying the physical laws involved and proposing that sharks could compute a heading by comparing information encoded by the vestibular and electrosensory systems. Building on this framework, analysis was conducted on the amplitudes of electrosensory signals at harmonics of the vestibular signals [Molteno & Kennedy, 2009]. This paper also refuted the claims that behavioural experiments using attached magnets should be expected to impair magnetite based magnetoreception, but leave induction based magnetoreception unaffected. Using a simple model for a swimming fish, it was found that relative motion between the magnet and electrosensory system as small as 100 μm is sufficient to induce a detectable electric field [Molteno & Kennedy, 2009]. This highlights one of the difficulties involved with such experiments, which is possibly why direct evidence supporting or refuting this mode of navigation does not yet exist.

Electrophysiological experiments confirm that elasmobranchs are sensitive to magnetic fields with strengths similar to that of earth. The response of primary afferents to stimulation with a magnetic field was examined in Black Sea skates (*Raja clavata* and *Trygon pastinaca*). Measurements taken from a stationary animal in motionless water, required a change in magnetic field to solicit a response and the intensity of the response was dependant on the rate of change in the field strength [Brown & Ilyinsky, 1978; Brown *et al.*, 1974]. When conditions were altered so that the magnetic field remained constant and either the fish was moved in the water, or the water was moved with respect to the fish, ampullae again responded and in this case intensity was roughly proportional to magnetic field or velocity [Brown & Ilyinsky, 1978].

Perhaps the most compelling behavioural evidence comes from tracking of the migratory trajectory and potential cues in hammerhead sharks. Klimley [1993] concluded sharks used the local magnetic field (consisting of the geomagnetic field and underwater anomalies, such as magnetized rocks) to orientate. The above findings illustrate that elasmobranchs can clearly sense earth strength magnetic stimuli. Whether this is via geomagnetic induction, or an alternative mechanism, and the role the earth's magnetic field plays in navigation remains unclear. However, the stingray (*Urolophus halleri*) was successfully conditioned to detect and orientate relative to uniform electric fields similar to those produced by ocean currents [Kalmijn, 1982]. Furthermore, sandbar (*Carcharhinus plumbeus*) and scalloped hammerhead (*Sphyrna lewini*) sharks have been conditioned to respond directly to changes in the magnetic field [Meyer *et al.*, 2005].

2.5.1.4 Modelling uniform sources in COMSOL

In the shark's reference frame, the electric field induced by swimming in the Earth's horizontal magnetic field is virtually uniform in nature [Paulin, 1995]. Rather than dealing with the full electromagnetic interactions we choose to model this situation as a uniform electric field. As well as simplifying the model, uniform electric fields have frequently been used as a stimulus in behavioural and electrophysiological experiments quantifying sensitivity.

Potential difference in a uniform electric field varies linearly with distance. Therefore, uniform electric fields can be approximated in COMSOL by fixing the potential values on boundaries, with the magnitude controlled by the separation distance. This is similar to experimental set ups, where the electric field stimuli are generally delivered along either the transverse or longitudinal axis of the tank (animal/individual ampulla) via plate/needle or point electrodes.

2.5.2 Morphology and physical properties of shark electroreceptors and tissues

As mentioned in chapter 1, the anatomical arrangement of the ampullae of Lorenzini has been examined for a variety of species. Differences in electroreceptor size, number, location, pore distribution and projection patterns have been described, leading to the functional subunit hypothesis. This states that ampullae are divided into morphologically distinct groups, which serve different primary functions e.g. prey detection and orientation to horizontal uniform fields [Tricas, 2001]. We have access to an accurate 3D representation of the spiny dogfish (*Squalus acanthias*) electrosensory organ array, based

on digital reconstruction of plastinated cross-sectional tissue slices [Berquist, 2003] and will use its anatomy as the basis for our morphological considerations.

Conversely, data on the electrical properties of various elasmobranch tissues is lacking, but there exists some details in the literature and we will use these values to approximate the correct order of magnitude of parameters (Table 2.3).

Table 2.3: Tissue resistances in elasmobranchs.

Genus	**Tissue**	**Resistivity** ($\Omega\,\mathrm{cm}$)	**Resistance** ($\Omega\mathrm{cm}^2$)	**References**
Raja	Ampulla jelly	24-25		Murray & Potts [1961]
		31		Waltman [1966]
	Cranial fluids	48		Murray & Potts [1961]
	Muscle			
	-longitudinal	110-200		Murray [1967]
	-transverse	250-800		Murray [1967]
	Cartilage	47-66		Murray [1967]
	Skin		400-2800	Waltman [1966]
	-dorsal		75-125	Murray [1967]
	-ventral		75-150	Murray [1967]
	Ampulla wall		6×10^6	Waltman [1966]
Squalus	Skin		370	Bennett *et al.* [1961]
Triaenodon	Ampulla jelly	31.5		Brown *et al.* [2002]
Carcharinus	Ampulla jelly	20.7		Brown *et al.* [2002]
Carcharodon	Ampulla jelly	28.3		Brown *et al.* [2002]

2.5.3 Boundary conditions and spatial dimensions

In 3D simulations of electromagnetic signals, it is intuitive to model the electric field or potential of point/boundary/volume sources in 3D space. However, the application of such approaches is limited due to the computational resource and time requirements associated with discretising the PDEs associated with geometry of interest. Two dimensional modelling is often used as it reduces the number of elements required, thus reducing the time and resource demands. Additionally, boundary conditions are required to specify interfaces between sub-domains of different media and truncate the domain of interest.

The electric currents interface solves a current conservation equation based on Ohm's law, using electric potential as the dependent variable. We use the stationary study, all variables depend on space only, which is appropriate for static electric fields and direct

currents. The form of Ohm's law which is solved is:

$$-\nabla \cdot (\sigma \nabla V - \vec{J}_e) = Q_j \tag{2.6}$$

where σ is the electrical conductivity ($\mathrm{S\,m^{-1}}$), $\vec{J}_e$ is an externally generated current density ($\mathrm{A\,m^{-2}}$) and Q_j is the current source ($\mathrm{A\,m^{-3}}$).

COMSOL allows the user to specify traditional boundary conditions used in FEM such as electric potential, electric insulation, zero charge, and field and current values. In addition, COMSOL provides a range of specialized formulations for efficient electromagnetic simulations where thin structures in the geometry model need not be meshed (requiring a large number of small elements) but can instead be represented with a boundary condition. Infinite elements are also available for modelling unbounded or large domains. By meshing a layer outside the modelling domain with infinite elements, the field equations are automatically scaled. These elements allow the representation of an infinite domain with a finite-sized model and reduce the truncation effects due to model boundaries.

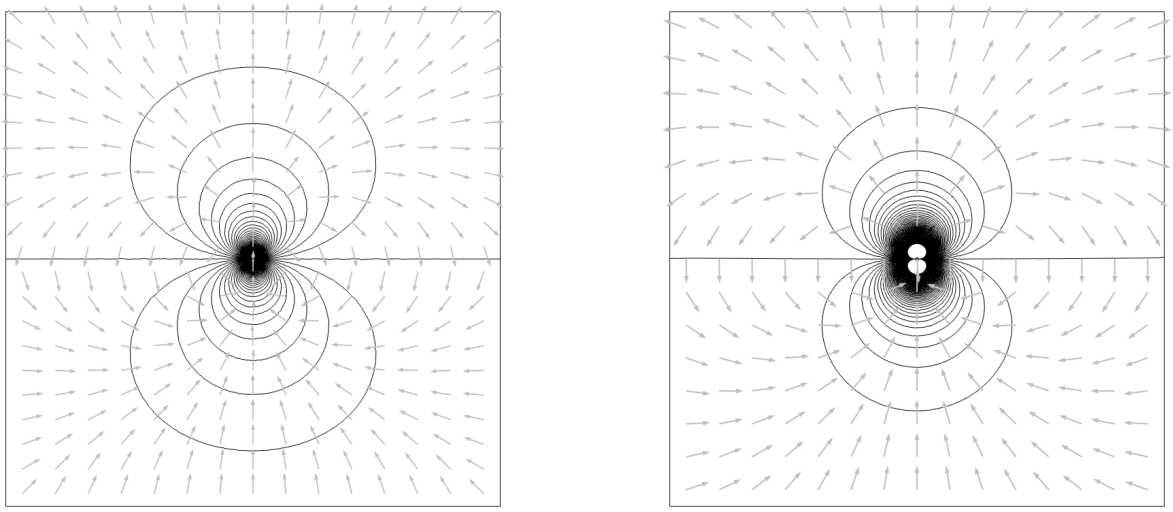

(a) 2D **(b)** 3D

Figure 2.2: Equipotential contours (black) and electric fields (grey arrows) due to a dipole pointing in the positive direction of the y axis.

In the 2D case, the electric currents interface assumes that the model has a symmetry, where the electric potential varies only in the x and y directions and is constant in the z direction. Essentially the model in the 2D plane is extruded along the z axis. This assumption is not too problematic for modelling uniform electric field stimuli but causes issues with the representation of point sources, which are then equivalent to line sources in 3D. The fundamental solution (or Green's function) is used to solve Equation (2.6).

In 3D this gives point source decay proportional to $\frac{1}{4\pi r}$, where r is the distance from the source, whereas in 2D decay is proportional to $-\frac{1}{2\pi} ln(r)$. While the results in Figure 2.2 look qualitatively similar the magnitudes of the potentials differ significantly, meaning we cannot interpret values obtained for 2D dipoles in terms of experimentally described electroreceptor sensitivities.

This is by nature a 3D problem, and only 3D studies will adequately capture the relevant electric field information. However because 2D models are easier to modify and solve much faster, we still begin with 2D representations of both localized and uniform electric fields. The challenge then is to utilize 2D simulations to illustrate which morphological and physical properties have the greatest impact on the stimulus received and might merit further investigation in the 3D.

2.6 Verification of meshing, boundary considerations and overall accuracy of COMSOL

Before investigating the role of body parts in shaping the stimulus in the vicinity of the shark, we first examine meshing, boundary considerations, and overall accuracy of COMSOL. To achieve this the numerical results are compared with simplistic problems for which analytical results are known.

2.6.1 2D conducting cylinder in a uniform electric field

To test the accuracy of modelling the uniform electric field stimulus, we compare the analytical solution to numerical results obtained from an infinite conducting cylinder kept between two parallel plates (Figure 2.3). The electric potential depends on both the original electric field E_0 and the potential superimposed due to the induced charges on the cylinder.

This example involves boundary conditions at both the exterior and at the interface between of the surrounding medium and the cylinder. In order to achieve a uniform electric field at the centre of cylinder, separation between plates and width of the plates need to be chosen to be large compared to the radius of cylinder.

2.6.1.1 Numerical vs. analytical solutions

The analytical solution for the electric potential in the neighbourhood of an infinite cylinder of radius a, placed in an initially uniform electric field E_o, is given by the following

equations [Haus & Melcher, 1989]:

$$\begin{aligned} V(r \leq a, \theta) &= -\frac{2\sigma_e}{\sigma_i + \sigma_e} E_0 r cos\theta \\ V(r > a, \theta) &= -aE_0 cos\theta \left[\left(\frac{r}{a}\right) - \left(\frac{a}{r}\right) \left(\frac{\sigma_i - \sigma_e}{\sigma_i + \sigma_e}\right) \right] \end{aligned} \tag{2.7}$$

where (r, θ) is the coordinate of interest, σ_i and σ_e are the conductivity of the cylinder and external medium respectively.

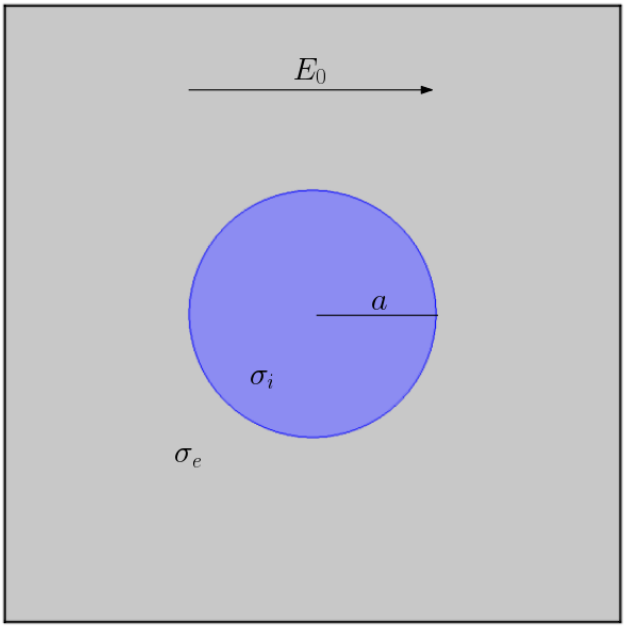

Figure 2.3: Infinite conducting cylinder of radius a and conductivity σ_i immersed in a medium of conductivity σ_e exposed to a uniform electric field of strength E_0.

The numerical solution was found using COMSOL and compared to the analytical solution which was calculated using a MATLAB function. To assess the goodness of fit a Root Mean Square (RMS) error was calculated, comparing the analytical and numerical values at specific points in the geometry. This percent error is used along with qualitative comparisons to investigate the location of the outer boundary and the degree of precision for the mesh (both of these impact computation time and thus constrain our choices particularly when we extend these models to 3D).

2.6.1.2 Location of the exterior boundary

In experimental analyses of electroreception involving uniform electric fields, tanks range between approximately 2 m [Kalmijn, 1982] and 7 m [Meyer *et al.*, 2005] in diameter. Kalmijn [1982] stated inside the smaller, fenced off region used for behavioural experiments, the field was uniform to within 5 percent. We examine diameters (separation distance between the two parallel plates, using a square geometry) from 2 to 40 m. Because we are predominately interested in the accuracy of the field inside and near the "fish", in this example we assess the RMS % error for 100 points between r = 0.01 m and r = 1.0 m ($\theta = 0$ and the fish is a cylinder at the origin, with radius 0.4 m). Our analyses suggest that while 7m was sufficient for electric potential to be visually indistinguishable from the analytical solution (Figure 2.4c), RMS was still approximately 1% and continued to decrease with increasing ROI (Figure 2.4a). Therefore 20m was selected as our region of interest for 2D uniform electric field models.

2.6.1.3 Mesh density

COMSOL offers both the ability to use predefined meshing options, or create custom meshes based on specifying a variety of element size parameters. If the physics-controlled mesh is selected, COMSOL creates a mesh that is adapted to the current physics settings in the model. There are nine predefined element sizes, which generate meshes ranging from extremely fine to extremely coarse. Having already examined the effect of location of the outer boundary, we are now more concerned that the mesh is sufficiently detailed for fields at the fish-water interface. Therefore, we assess the RMS % error for 100 points between $\theta = 0$ and $\theta = \pi$ (along the fish water interface, r = 0.4 m) for each of the default mesh sizes. Our analysis of mesh resolution suggested that for this simple geometry meshing with the 'normal' resolution was sufficient and little advantage was gained by having a finer mesh (Figure 2.5). Therefore for 2D uniform electric field models, the normal mesh was used for the seawater exterior, and 'finer' resolution was selected for the electroreceptors in order to get them to successfully mesh.

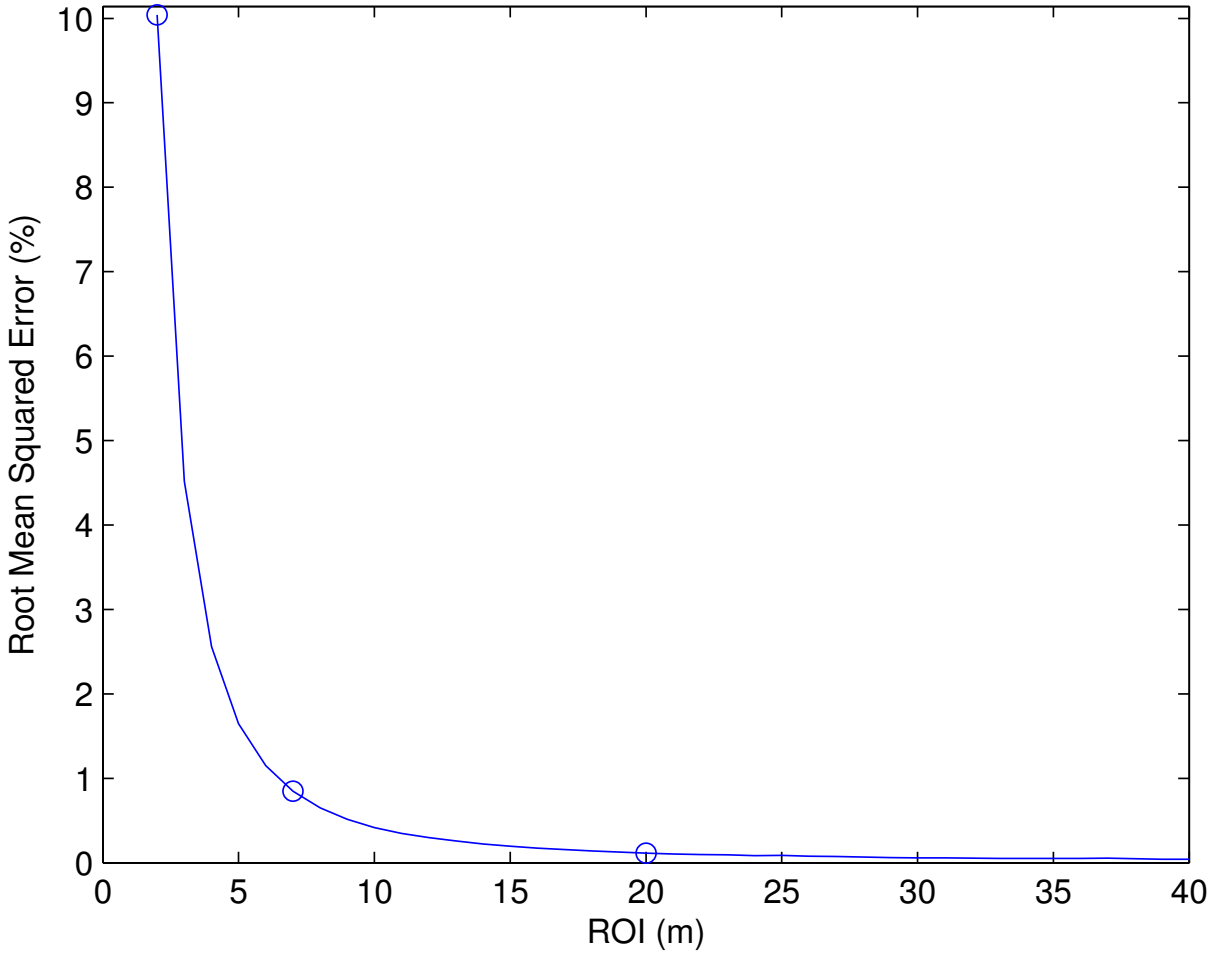

(a) Root Mean Squared error (%) versus Region Of Interest (ROI)

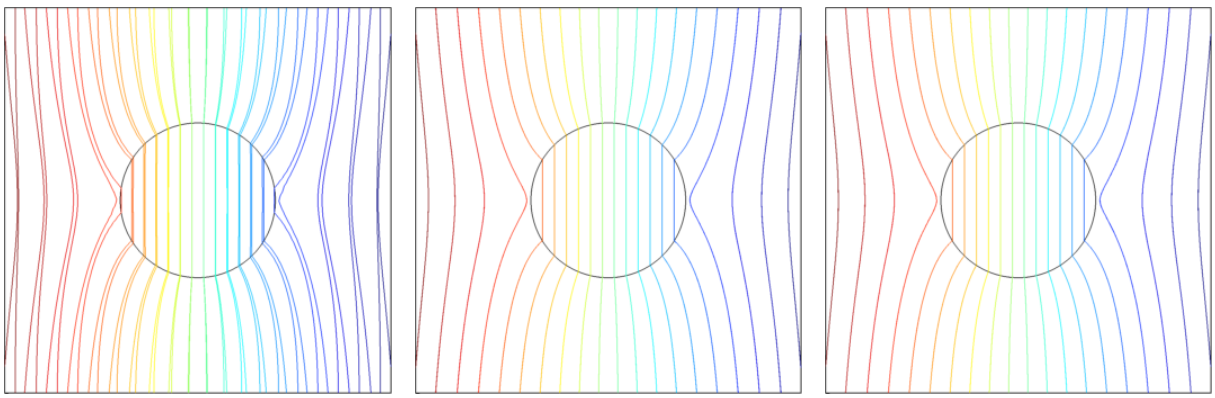

(b) ROI=2m **(c)** ROI=7m **(d)** ROI=20m

Figure 2.4: 2D outer boundary calibration: Uniform stimulus. Comparison between numerical (COMSOL) and analytical solutions for the electric potential in the neighbourhood of an infinite cylinder, in a uniform electric field. Figure 2.4a shows the RMS error (in %) for 100 points between r = 0.01 and r = 1.0 m (along $\theta = 0$), with the outer boundary at various locations. Circles in Figure 2.4a mark the ROI's displayed in Figures 2.4b to 2.4d, which show the numerical and analytical solutions overlaid.

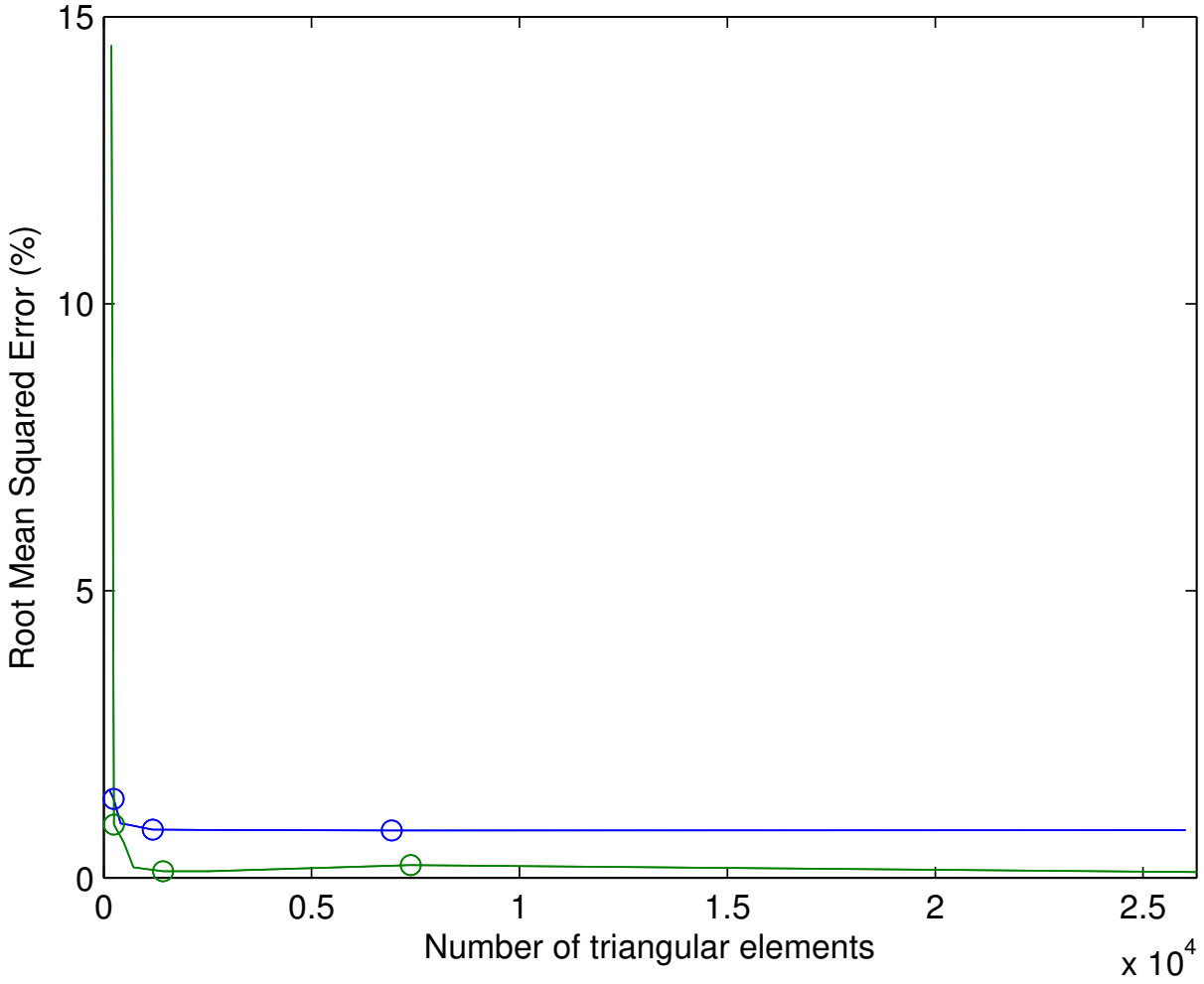

(a) Root Mean Squared error (%) versus number of triangular elements. Blue line shows ROI=7m and green shows ROI=20m.

ROI=7m

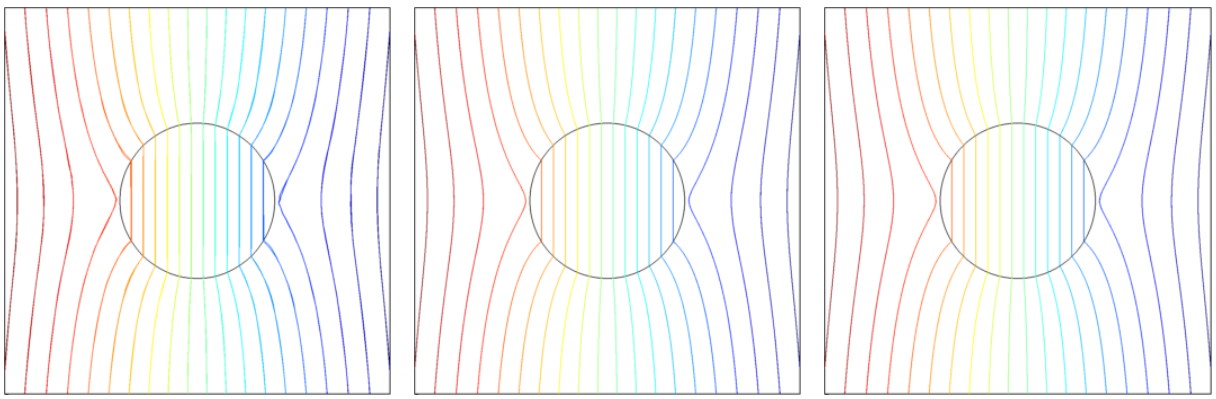

(b) extra coarse (236 tri.) **(c)** normal (1182 tri.) **(d)** extra fine (6926 tri.)

Figure 2.5: (Continued on the following page.)

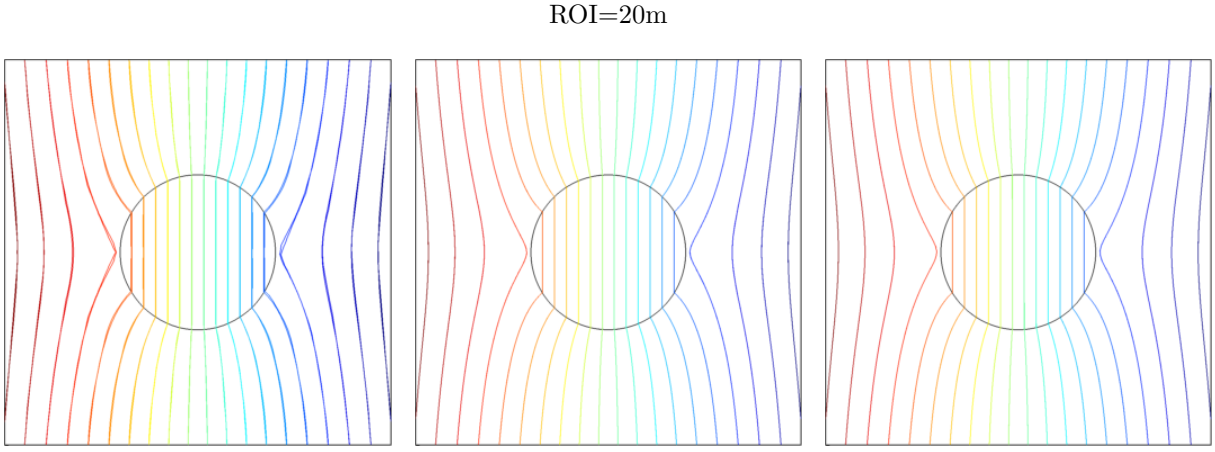

(e) extra coarse (246 tri.) **(f)** normal (1426 tri.) **(g)** extra fine (7382 tri.)

Figure 2.5: 2D mesh density calibration: Uniform stimulus. Comparison between numerical (COMSOL) and analytical solutions for the electric potential in the neighbourhood of an infinite cylinder, in a uniform electric field. Figure 2.5a shows the RMS error (in %) for 100 points between $\theta = 0$ and $\theta = \pi$ (along the fish water interface $r = a$) with different COMSOL default mesh densities. Circles in Figure 2.5a mark the mesh densities displayed in Figures 2.5b to 2.5g, which show the numerical and analytical solutions overlaid.

2.6.2 2D line dipole

Whereas in 3D the fundamental solution tends toward zero as the distance from the source approaches infinity, this is not the case in 2D (see Section 2.5.3). Analytical solutions in 2D are complicated by the fact that at infinity the field must be uniform (therefore solutions include an arbitrary coefficient which must be specified [Haus & Melcher, 1989]). We are unaware of an analytical solution for the line dipole adjacent to a cylinder. Therefore, to test the accuracy of modelling the localised electric field stimulus, we first compare the analytical solution to numerical results obtained from a pair of infinite, oppositely charged, parallel cylinders (Figure 2.6). This example involves boundary conditions at both the exterior and between the cylindrical sources and the surrounding medium.

2.6.2.1 Numerical vs. analytical solutions

The analytical solution for pair of infinite, oppositely charged, parallel cylinders immersed in a medium of conductivity σ_e, can be derived by replacing the cylinders with equivalent line charges [Paul, 2008]. The voltage at point $\vec{P}$, shown in Figure 2.6, due to the line

charges $\pm q$,separated by distance d along the x axis, is expressed as

$$V(x,y) = \frac{q}{2\pi\sigma_e} \ln\left(\frac{R^-}{R^+}\right) \tag{2.8}$$

where

$$R^+ = \sqrt{(x + d/2)^2 + y^2}$$

and

$$R^- = \sqrt{(x - d/2)^2 + y^2}$$

We specify this source numerically in COMSOL using floating potential boundary conditions, where an unknown potential depends on a fixed total current $\pm q$. Simulations use cylinders of radius 1 mm, separated by 5 cm.

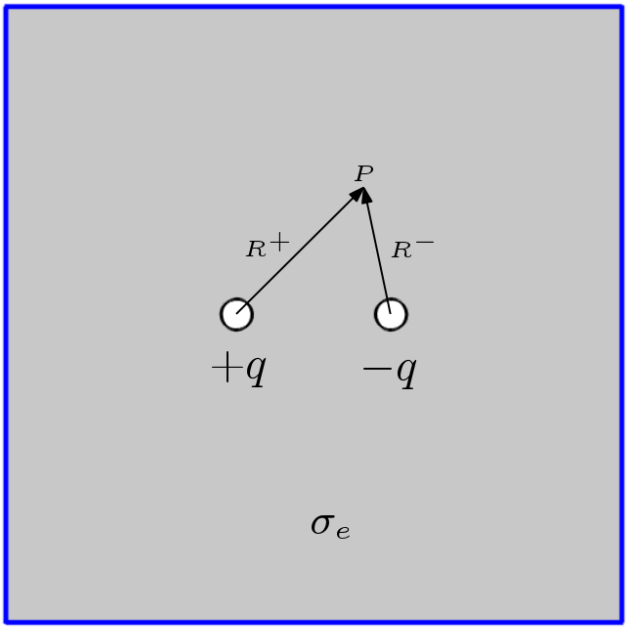

Figure 2.6: A pair of infinite, oppositely charged, parallel cylinders immersed in a medium of conductivity σ_e.

2.6.2.2 Location of exterior boundary

If a traditional Dirichlet or Neumann boundary condition was used to truncate the geometry, the trend shown with increasing accuracy with region of interest size is similar to that shown for the uniform stimulus in Figure 2.4a. However, because these boundaries

are no longer being used to produce the required stimulus (rather they just define the region to mesh) we can use an alternative boundary condition, infinite elements. This avoids the need to include large empty regions in the simulation to avoid the boundary affecting the region of interest. Due to the infinite elements, there was no advantage to including a large area for the external region Figure 2.7. Therefore, for 2D dipole approach trajectories we included approximately and extra 0.5m in each direction additional to the space that the shark's trajectory covered.

2.6.2.3 Mesh density

Similar to the uniform case, for a 2D line dipole, there was little improvement to results from a finer mesh than 'normal' (Figure 2.8). We introduced an additional conducting cylinder into the numerical simulation to approximate the body of the shark. When we examined results for changes in potential, between simulations with different mesh densities, at points along the surface of a cylinder, there was little change in results beyond the 'normal' mesh option (Table 2.4).

Table 2.4: 2D mesh density calibration: Dipole stimulus with a conducting cylinder. Comparison between numerical solutions, with different COMSOL default mesh densities, for the electric potential in the neighbourhood of a pair of infinite, oppositely charged, parallel cylinders and a larger conducting cylinder. Change in electric potential (%) was summed for 100 points between $\theta = 0$ and $\theta = \pi$ (along the cylinder water interface $r = a$)

Mesh density	**Change in potential (%)**
extremely coarse → extra coarse	0.8901
extra coarse → coarser	0.5919
coarser → coarse	0.2905
coarse → normal	0.1337
normal → fine	0.0074
fine → finer	0.0332
finer → extra fine	0.0130
extra fine → extremely fine	0.0033

As long as there were sufficient elements in the region of the source there was little difference in results obtained by modelling the scenario as two equal and opposite cylindrical sources, or two line current sources separated by a finite distance, or an ideal line dipole. To help ensure an accurate representation, we therefore included a circle surrounding our point dipole which resulted in a greater number of elements in that region.

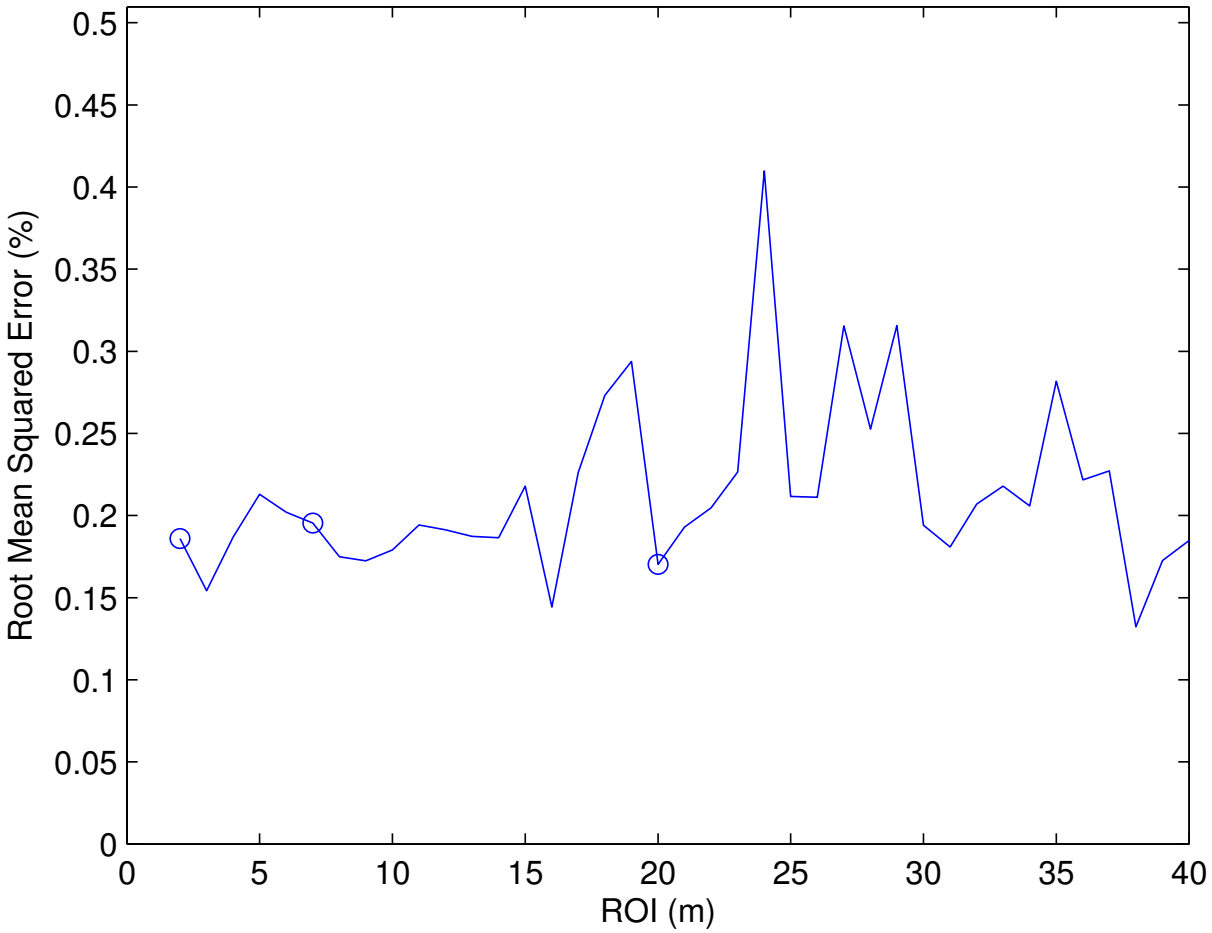

(a) Root Mean Squared error (%) versus Region Of Interest (ROI)

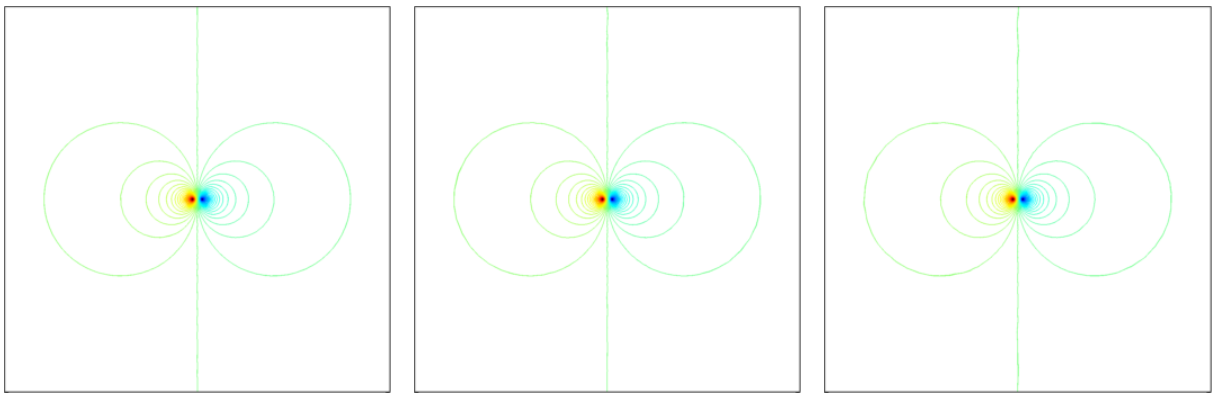

(b) ROI=2m **(c)** ROI=4m **(d)** ROI=20m

Figure 2.7: 2D outer boundary calibration: Dipole stimulus. Comparison between numerical (COMSOL) and analytical solutions for the electric potential in the neighbourhood of a pair of infinite, oppositely charged, parallel cylinders. Figure 2.7a shows the RMS error (in %) for 100 points between r = 0.01 and r = 1.0 m (along $\theta = 0$), with the outer boundary at various locations. Circles in Figure 2.7a mark the ROI's displayed in Figures 2.7b to 2.7d, which show the numerical and analytical solutions overlaid.

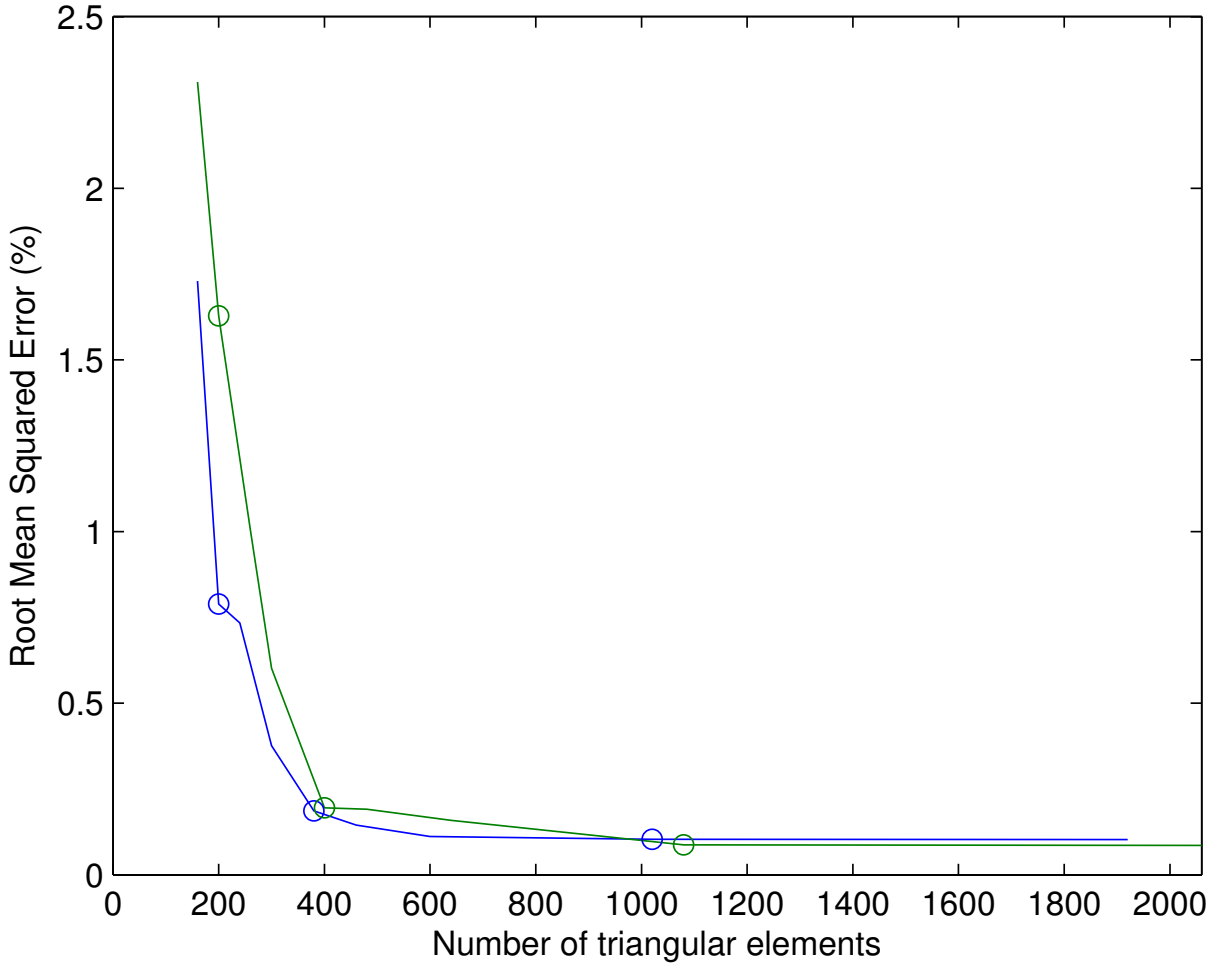

(a) Root Mean Squared error (%) versus number of triangular elements. Blue line shows ROI=2m and green shows ROI=7m.

ROI=2m

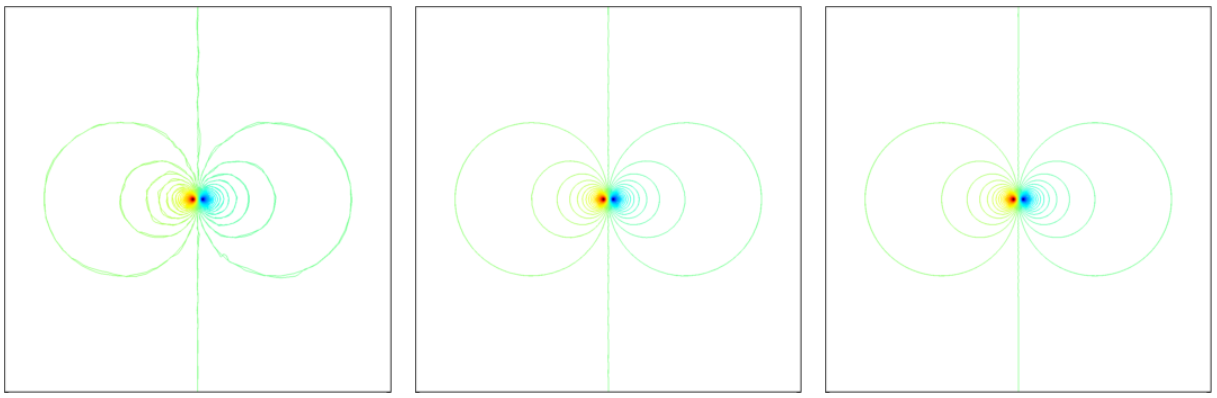

(b) extra coarse (200 tri.) **(c)** normal (380 tri.) **(d)** extra fine (1020 tri.)

Figure 2.8: (Continued on the following page.)

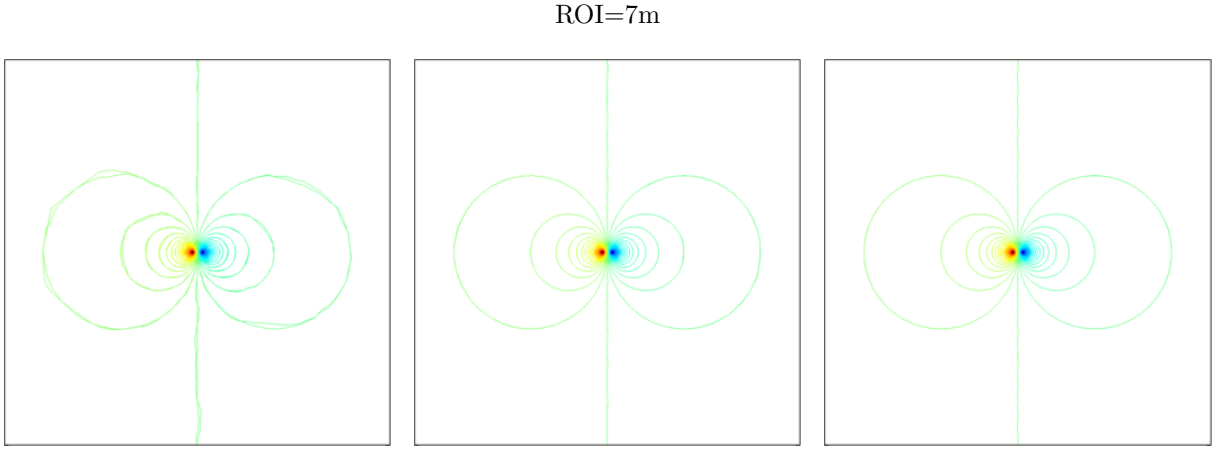

(e) extra coarse (200 tri.) **(f)** normal (400 tri.) **(g)** extra fine (1080 tri.)

Figure 2.8: 2D mesh density calibration: Dipole stimulus. Comparison between numerical (COMSOL) and analytical solutions for the electric potential in the neighbourhood of a pair of infinite, oppositely charged, parallel cylinders. Figure 2.8a shows the RMS error (in %) for 100 points between r = 0.01 and r = 1.0 m (along $\theta = 0$), with different COMSOL default mesh densities. Circles in Figure 2.8a mark the mesh densities displayed in Figures 2.8b to 2.8g, which show the numerical and analytical solutions overlaid.

2.6.3 3D conducting sphere in a uniform electric field

Having already examined meshing, boundary considerations, and overall accuracy of COMSOL extensively in 2D we tried to keep the operations equivalent for our 3D simulations where possible. To ensure this was a reasonable, we compare the numerical results with the analytical results for a 3D conducting sphere in a uniform electric field. With geometry set up as in Figure 2.3, the equations expressing electric potential due do a sphere of radius a in an initially uniform electric field E_0 are [Haus & Melcher, 1989]:

$$\begin{aligned} V(r \leq a, \theta) &= -\frac{3\sigma_e}{\sigma_i + 2\sigma_e} E_0 r cos\theta \\ V(r > a, \theta) &= \left[\left(\frac{\sigma_i - \sigma_e}{\sigma_i + 2\sigma_e} \right) \frac{a^3}{r^3} - 1 \right] E_0 r cos\theta \end{aligned} \tag{2.9}$$

where (r, θ) is the coordinate of interest, σ_i and σ_e are the conductivity of the sphere and external medium respectively.

Figure 2.9a shows a plot of a cutline through the sphere of radius 0.4m, located at the origin in a uniform electric field directed along the y axis. The numerical and analytical results match well, resulting in an approximation error of less than 0.05% within this region (Figure 2.9b).

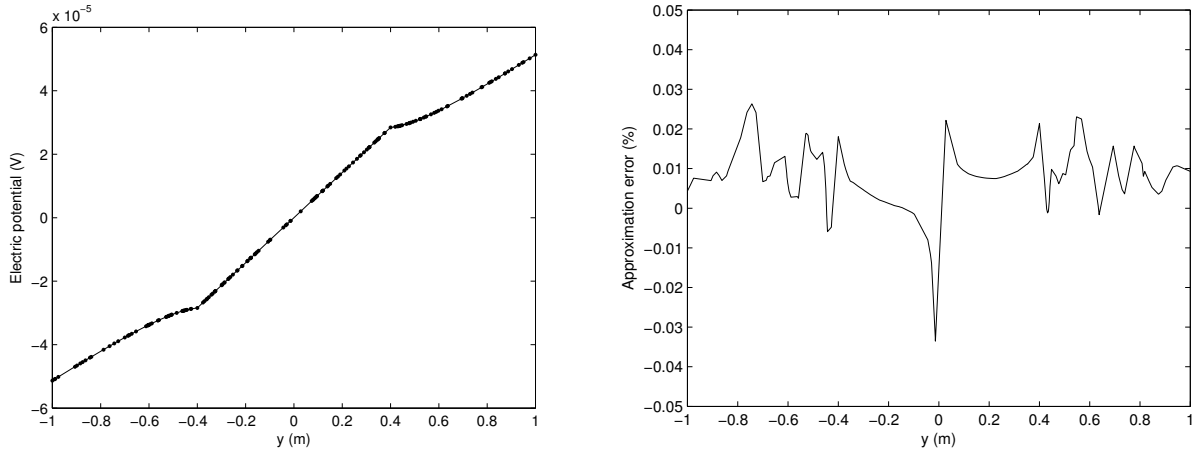

(a) **(b)**

Figure 2.9: 3D mesh and boundary calibration: Uniform stimulus. Figure 2.9a shows a comparison between numerical (COMSOL; circular points) and analytical (solid line) solutions for a conducting sphere in a uniform electric field. The sphere is located at the origin and has radius 0.4 m and is subjected to a uniform electric field of $500\,\mathrm{nV\,cm^{-1}}$ directed along the y axis. Figure 2.9b shows the percent approximation error for the same scenario.

2.6.4 3D point dipole

As above we tried to keep the set up equivalent to our 2D simulations. To examine if this is justified we compare the numerical with the analytical results for a 3D point dipole. The voltage at point distance $\vec{R}$ from the dipole, specified by $\vec{P}$, immersed in a medium of conductivity σ_e is expressed as:

$$V(\vec{R}) = \frac{1}{4\pi\sigma_e}\frac{\left(\vec{P}\cdot\vec{R}\right)}{R^3} \tag{2.10}$$

We implement this source numerically in COMSOL using the built in electric point dipole, specified by dipole moment $\vec{P}$.

Figure 2.10a shows a plot of a cutline aligned with the dipole axis. Due to continuity constraints the numerical solution smoothly transitions between positive and negative, in the analytical solution voltage values tend to infinity at the dipole centre. This means the results are similar at a distance but differ slightly at distances less than a few cm (Figure 2.10b).

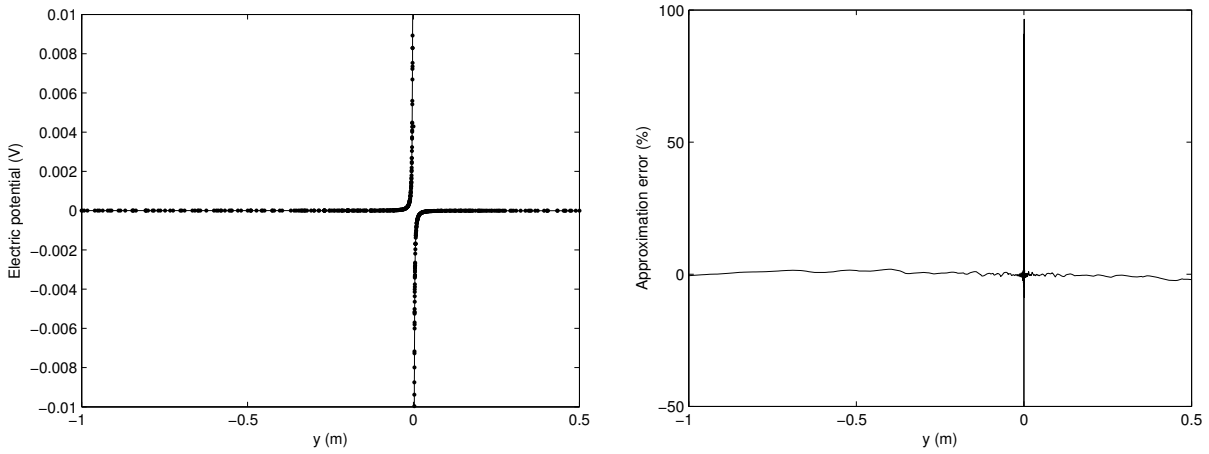

(a) **(b)**

Figure 2.10: 3D mesh and boundary calibration: Dipole stimulus. Figure 2.10a shows a comparison between numerical (COMSOL; circular points) and analytical (solid line) solutions for a three dimensional point dipole. The dipole is located at the origin and directed along the y axis. Figure 2.10b shows the percent approximation error for the same scenario.

While the basic physical laws of electromagnetics are well known, it can be difficult to solve the partial differential equations. Thus, analytical approaches are generally only appropriate for highly simplified models. For more realistic geometrical and biophysical properties numerical approaches are necessary. Furthermore, electroreception is by nature a 3D, time varying problem, and only 3D dynamic studies will adequately capture the relevant electric field information. Because 2D models and quasi-static snapshots are easier to modify and solve much faster, the challenge is to utilize these simplifications to illustrate which morphological and physical properties have the greatest impact on the stimulus received and might merit further investigation. The simulations conducted in this chapter demonstrate that COMSOL provides an accurate representation of two ethologically relevant stimuli: localized prey-like dipole electric sources, and uniform electric fields resembling motion-induced and other fields encountered in the ocean. Existing models of the elasmobranch electroreceptive periphery have all either neglected the presence of body tissues, or approximated the animal as a sphere or cylinder. Chapter 3 examines how the shark's morphology impacts the electric field in the vicinity of the shark. The shark's body may be a sensory accessory structure that acts like an electrical lens. However, the biophysical relations between the shark and environment are rather complex and may be difficult to model, even if many of the details are known.

Chapter 3

Interaction between the electrosensory system and weak electrical stimuli

3.1 Introduction

After years of dispute over the function of the ampullae of Lorenzini, the prediction by Lissmann [1958] that these organs might extract electric information from the environment was eventually confirmed. There is a long history of evidence suggesting this sense plays an important role in prey detection [Kalmijn, 1971]. More recently research that suggests a role in other behaviours such as predator avoidance [Sisneros *et al.*, 1998], communication [Sisneros *et al.*, 1998], detection of mates [Tricas *et al.*, 1995] and navigation [Kalmijn, 1974; Paulin, 1995]. During interactions with other animals the electrosensory array is exposed to small localized fields, whereas if indeed this sense is being used for navigation the stimuli are large uniform fields. Studies have demonstrated that the response of individual ampullae depends not only on the form of the stimulus, but on the relative orientation of the canal [Kalmijn, 1974]. In addition to the spatial organization of the electrosensory array, movements of the animal (and/or its prey) cause temporal variations in the signals canals receive. Thus, the shark must integrate signals over both space and time in order to accumulate information [Kalmijn, 2000]. The optimal way to combine time varying signals from multiple sensors is Bayesian inference [Vilares & Kording, 2011].

Over the past thirty years, different modelling techniques have been used to characterize the spatial and temporal mechanisms responsible for elasmobranch electrosensitivity.

Two and three dimensional analytical models have been developed, each with its specific advantages and disadvantages (see Table 1.1). Models have demonstrated both the morphology of the ampullary array [Berquist, 2003; Brown, 2002; Camperi *et al.*, 2007; Kim, 2007] and the tissues of the animal itself play a role in the effective stimulus received [Adair *et al.*, 1998; Gusev *et al.*, 1986, 1985; Pickard, 1988]. While analytical models have the advantage of being computationally fast and accurate under certain assumptions, they are generally limited to the study of simplified object geometries and make it difficult to examine more complex interactions between fish body geometries and electrical properties. Numerical models generally allow for a more realistic examination of the biophysical and geometrical properties of various tissues in the body shape. However, this comes at the cost of being more computationally demanding. Specifically, when using finite element method (FEM) the geometry has to be discretized into elements, which can be extremely difficult, particularly in three dimensions or when the scale of features of interest differ greatly.

The goal of this chapter was to build on the framework created by Berquist [2003] and use the virtual dogfish to create a morphologically realistic 2D FEM model to examine shark electroreception. In addition to the morphologically realistic model, two geometrical simplifications were also created in order to independently study the effects of different fish body geometries and electrical properties for the first time. Kalmijn [1974] considered the effective stimulus to the ampullary receptors to consist of two main components: (1) the potential drop across the skin surrounding the ampulla pore and (2) the potential drop along the canal due to the tissue it is embedded in. This chapter attempts to characterize the relative influence of these components by investigating the spatial and temporal pattern of voltage drops within canals under differing behaviourally relevant stimuli. Finally, a geometrically simplified 3D FEM shark is presented. These preliminary models illustrate how the morphology of the shark may be shaping electrosensory signals and provides insight into what properties should be considered important for future experimental and modelling efforts.

3.2 Methods

3.2.1 Electrosensory signal modelling

We revisit the virtual dogfish model, described in chapter 4 of the doctoral thesis by Berquist [2003]. This previous approach was an analytical electrostatic model where the static permittivity of seawater, $\epsilon = 7 \times 10^{-10}\,\mathrm{C^2N^{-1}m^{-1}}$, was used for the entire region of

interest and no attempt was made to investigate the role of shark tissues on the effective stimulus to ampullae [Berquist, 2003]. We begin with a numerical electric currents model, where the conductivity of seawater, $\sigma = 4.5\,\mathrm{S\,m^{-1}}$, was initially used for the entire region of interest before specifying relevant conductivities for body tissues. We choose to solve for electric potential using an electric currents model (current conservation via Ohm's law), rather than electrostatics (Gauss' law for electric field), as more data existed in the literature about the conductivity/conductances of various tissues than permittivity.

As mentioned previously the majority of experiments conducted on elasmobranchs focus on two key stimuli:

1. Detection of localized prey-simulating dipole fields. Berquist [2003] chose a dipole of strength $P = 5.6 \times 10^{-16}\,\mathrm{C\,m}$ to simulate prey based on measurements from flatfish, *Pleuronectes platessa*, where electric fields averaged $200\,\mu\mathrm{V\,cm^{-1}}$ at 0.5 cm, $20\,\mu\mathrm{V\,cm^{-1}}$ at 2 cm, $2\,\mu\mathrm{V\,cm^{-1}}$ at 5 cm and $0.2\,\mu\mathrm{V\,cm^{-1}}$ at 10 cm [Kalmijn, 1974]. With the conductivity specified as above, we matched the dipole moment for the equivalent electric currents model as dipole strength $P = 3.6 \times 10^{-6}\,\mathrm{A\,m}$.

2. Orientation in large-scale uniform electric fields. Berquist [2003] chose a constant electric field of magnitude $E = 500\,\mathrm{nV\,cm^{-1}}$ to investigate the large scale uniform field's typical of those induced by water moving in the earth's magnetic field, we will also use this value.

The effective stimulus to ampullary receptor cells is the potential difference between the external pore and the tissues surrounding the ampulla proper (Figure 3.1):

$$\Delta V = V_{pore} - V_{ampulla} \tag{3.1}$$

Whereas previous models have mainly computed these voltage drops analytically, we use a numerical approach to calculate the voltages at the pore (V_{pore}) and the corresponding ampulla ($V_{ampulla}$). Depending on the polarity of the stimulus, the afferent nerves associated with receptor cells respond by increasing or decreasing spiking relative to spontaneous activity. When the pore is negative relative to the ampulla activity is excitatory, whereas when the pore is positive relative to the ampulla activity is inhibitory [Murray, 1962].

While we examine how certain features of the shark distort the stimulus, we neglect to model a common source of noise in the electrosensory system. Through the same mechanisms as the prey they are attempting to detect, sharks produce their own DC and low frequency potentials [Bodznick *et al.*, 1992]. These common mode signals are largely suppressed in higher order efferents [Bodznick *et al.*, 1992]. In later chapters we

will discuss mechanisms for noise reduction in neural computation, however here we focus on examining the impact of the geometry and electrical properties of shark tissues on the stimulus.

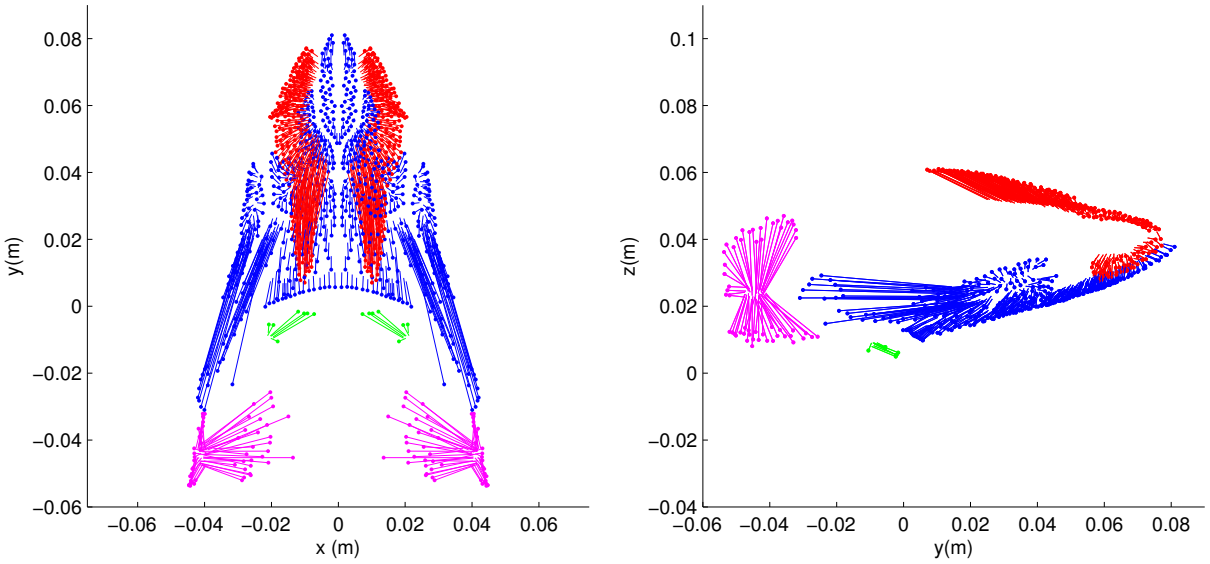

(a) xy plane **(b)** yz plane

Figure 3.1: Peripheral electrosensory system of the spiny dogfish, *Squalus acanthias*. Colour coding indicates ampullarly groupings: blue=buccal, red=superficial ophthalmic (SO), magenta=hyoid, green=mandibular.

3.2.2 2D shark geometries

All geometries were related to the morphologically accurate representation of the peripheral electrosensory system of the spiny dogfish, *Squalus acanthias* (for further details see Berquist [2003]; Figure 3.1). Two dimensional geometries were created by importing .stl files of the various body structures into MATLAB and using the coordinates to generate simplified geometries. Large body structures (shark exterior and brain) the stl was projected into either the xy or yz plane and a contour around the structure was used to create an interpolation curve object for COMSOL via the MATLAB LiveLink (Figures 3.2a and 3.2d). Additionally, two further simplifications were made to the geometry, the fins were removed (Figures 3.2b and 3.2e) and the sharks head was replaced by the estimated minimum volume ellipsoid fit to the coordinates of the ampullary pores (Figures 3.2c and 3.2f).

In two dimensional simulations the ampullae were included as edges in the geometry for the FEM model. This has the benefit of ensuring sufficient resolution of the mesh in the region of interest and makes it easier to use the built in COMSOL post processing

tools. In each plane the 2D coordinates for the base and pore of the ampulla were used to generate geometry (e.g. horizontal plane=xy coordinates, vertical plane=yz coordinates). Neglecting the third dimension resulted in overlapping ampullae (Figure 3.1), therefore we reduced the number of canals for analysis by pairwise testing for intersections of the lines corresponding to the canal coordinates. Canals were removed, starting with the lines with the greatest number of intersections, until no canals intersected each other or the contour representing the brain region.

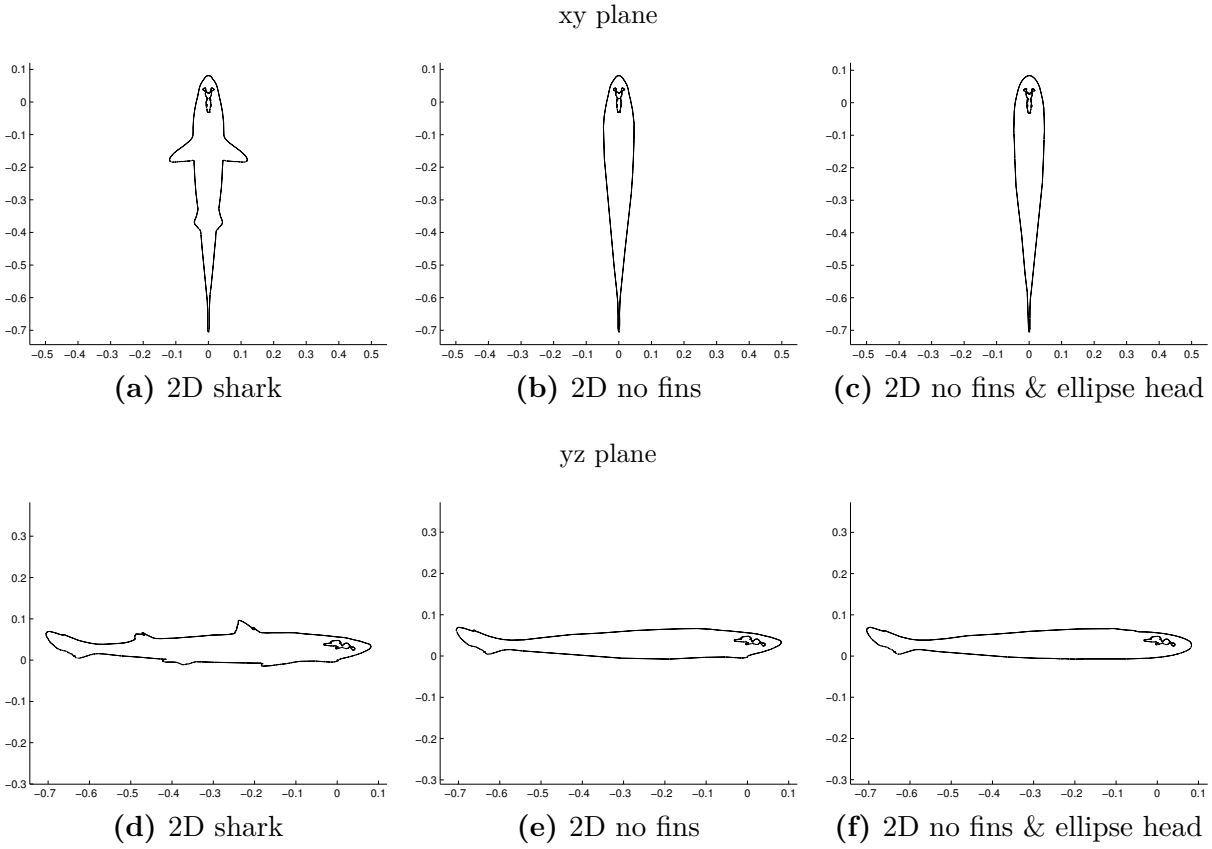

(a) 2D shark **(b)** 2D no fins **(c)** 2D no fins & ellipse head

(d) 2D shark **(e)** 2D no fins **(f)** 2D no fins & ellipse head

Figure 3.2: 2D shark geometries

3.2.3 3D shark geometries

While it was fast and easy to implement and manipulate realistic two dimensional shark geometries in COMSOL, three dimensions proved much more challenging. COMSOL allows for importing of three dimensional geometries from .stl and .vrml files. However, it proved difficult to import the original virtual dogfish as COMSOL requires that a surface geometry be watertight in order to convert it to a solid interior region for meshing. COM-

SOL provides limited tools to automatically repair gaps (and the option of purchasing further import functionality via the CAD Import Module). We found the easiest way to import pre-existing geometries was to use external software, such as Simpleware, to manipulate .stl models prior to importing. Ultimately, even though we did eventually import and mesh the dogfish skin, mesh quality was low and simulations were time consuming, therefore it was later abandoned in favour of a simplified ellipsoid and cone version of a shark (Figure 3.3).

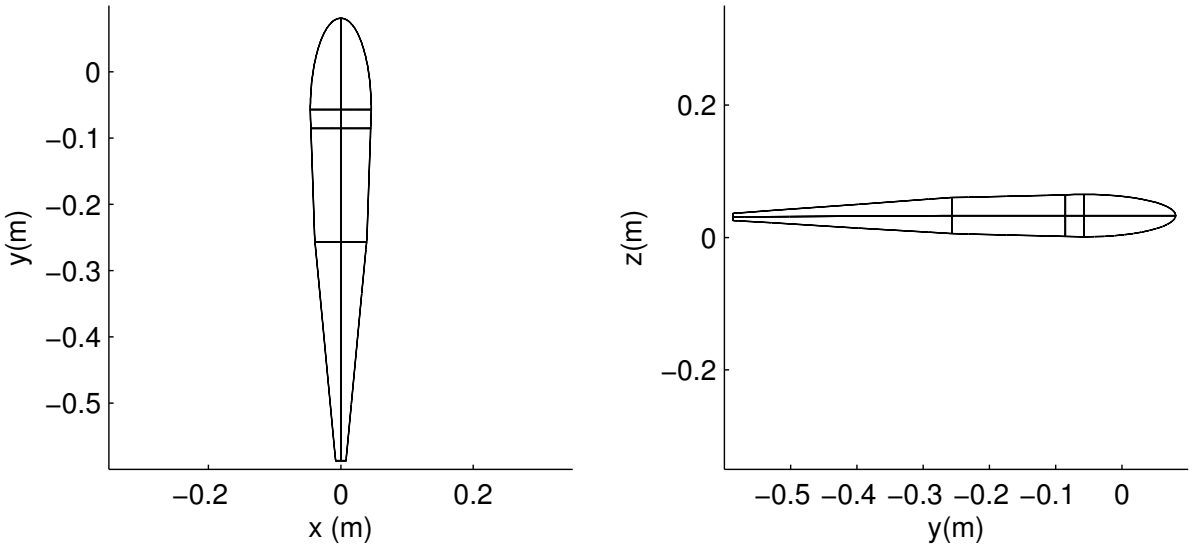

(a) xy plane **(b)** yz plane

Figure 3.3: Simplified 3D shark geometry: the shark is constructed from an ellipsoid head and cone-like body.

During our two dimensional simulations we discovered that the electric properties had a greater impact on the voltage drops in the ampullary array than the geometrical specifics. Therefore, the following simplifications were made to better examine some of the phenomena observed in our 2D simulations. Firstly, we found the approximately minimum volume ellipsoid that contained all ampulla and pore coordinates. Secondly, we projected the pore coordinates onto the closest point on the ellipsoid surface. This resulted in some small alterations to ampulla length and orientation, but meant all pores coordinates were on the surface of the head and all ampulla proper coordinates were located on the interior of the ellipsoid. A cone-like body was created by visually matching geometry primitives to the original shark stl, these features are less important but based on the 2D simulations likely still impact the electric field. Additionally, we originally attempted to include the ampullae as edges in the geometry, which meshed for certain configurations but failed to be robust. Therefore, instead of using the COMSOL post processing tools available for

edges, we exported the values for electric potential interpolated at the locations of the canal pore and ampulla. We also opted to use the 'extra fine' resolution to mesh the dogfish body for the dipole approach and 'extremely fine' for the uniform electric field. This was necessary to ensure a sufficient number of elements were in the vicinity of the shark, as no longer including the ampullae as edges resulted in significantly less elements being included in the shark body under the default 'normal' mesh option.

In this chapter, we build on the previous virtual dogfish electrosensory model to calculate canal voltage drops within large-scale uniform electric fields and local dipole electric fields. We use both 2D and 3D models to examine the effective stimulus to ampullary receptors, in terms of the geometry and electrical properties of the animal.

3.3 Results

3.3.1 Comparison between 2D numerical model and previous 3D analytical model

Previous versions of the virtual dogfish model have examined the spatio-temporal dynamics of canal voltage drops resulting from three dimensional prey-simulating dipoles. The signals were dependent on canal length, angular orientation, and relative distance from the source [Berquist, 2003]. We wish to examine how the electrical properties of shark tissue distort the electric fields sensed by these animals. However, this problem is currently intractable in three dimensions. Thus, firstly we examine the similarities and differences between our two dimensional numerical solutions and the three dimensional analytical solutions presented by Berquist [2003]. Due to the simplifying assumptions mentioned in section 3.2.2, we focus here on the pattern of canal voltage drops rather than the absolute magnitude of individual canals. Secondly, we examine a geometrically simplified three dimensional FEM model of the virtual dogfish. Digital copies of all figures from this chapter are available in Appendix A for higher resolution viewing.

3.3.1.1 Dipole stimulus: Horizontal plane trajectories

For a detailed description of the relevant methods and results obtained by Berquist [2003] see chapter 4 of her thesis. Briefly, we attempted to match our two dimensional numerical models to the approach trajectories she described. As the virtual dogfish moves along its approach trajectory, it encounters and then passes by a dipole located at the origin, with the dipole axis aligned with the negative y-axis. The dogfish begins its trajectory approximately 1 m from the dipole, with its mouth located at approximately x = 0.45 m and y = -0.9 m (Figure 3.4). In the 'unchanged' scenario (green), the dogfish swims past the dipole with a closest approach distance of 0.45 m, in a direction parallel to the orientation of the dipole. In the 'direct' scenario (black), the dogfish is oriented so the it swims directly over the dipole. Finally, in the 'fieldline' scenario (red), the dogfish aligns its body axis such that the average electric field it receives is constant [Kalmijn, 1997]. In all cases of our implementation of the fieldline approach trajectory we pre-calculate the electric field, neglecting any tissue properties, and fix the shark orientation to that (rather than looking at the electric field averaged over the ampullary array and any potential tissue effects). Canal voltage drops, for six locations along each of the described approach trajectories, are displayed in Figures 3.5 to 3.7. Note the changing voltage scales (in keeping with Berquist [2003] we allow the scale for each colourmap to differ between subfigures, as magnitudes of voltage drops differ greatly between locations).

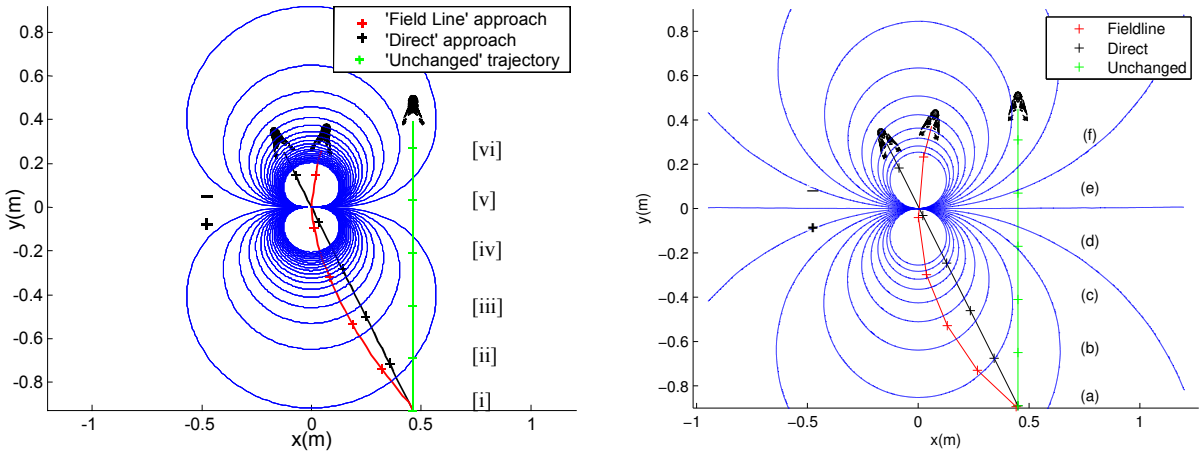

(a) 3D [Berquist, 2003] **(b)** 2D

Figure 3.4: XY approach trajectories in the dipole horizontal plane and locations where canal voltage drops were mapped. Figure 3.4a shows the three dimensional analytical model. Reprinted from Berquist [2003], with permission from Dr. Rachel Berquist. Figure 3.4b shows the numerical solutions for the approximately matched 2D scenarios. In both cases the source is located at the origin. Note: the equipotential contours have been plotted to illustrate the differences between dimensions and may not correspond to matched contour levels.

Figure 3.5 compares the 'unchanged' trajectory computed analytically in three dimensions to the numerical 2D numerical solution. In the dogfish's starting position (Figure 3.5a, i), Berquist [2003] found shorter canals exhibited voltage drops of less than ± 1 nV, with longer canals aligned with the electric field developing the largest voltage drops ranging from -4 to 2 nV. Our 2D models showed similar results with the largest voltage drops ranging from -4 to 3 nV in the canals which were several cm long. The closest the dogfish gets to the dipole under this approach trajectory is 0.45 m (Figure 3.5e, v). Like Berquist [2003] we find the maximum voltage drops in the longest canals never exceed ± 30 nV. The overall general trends from Berquist [2003] were also maintained with all four ampullary groups experiencing both negative and positive voltage drops at any one time.

While the largest voltage drops were still found in longest canals oriented with the electric field, we found strongest negative voltage drops hyoid canals and the strongest positive voltages develop in the buccal canals (whereas Berquist [2003] found strongest negative voltage drops in buccal and strongest positive voltage drops in mandibular and hyoid). Other notable differences in the initial stages of the trajectory (Figures 3.5a to 3.5b, i to ii) the shorter buccal and superficial ophthalmic (SO) groups in the snout exhibit voltage drops of smaller magnitude, likely due to the 2D ampulla being shorter in length (due neglecting the z-dimension and to only using xy coordinates of the pore and ampulla proper). Another difference likely be attributed to flattening the geometry into 2D is the hyoid canals on the left (closest to the source) mainly exhibited negative voltage drops (Figures 3.5a to 3.5b, i to ii), whereas in these early stages Berquist [2003] found the majority of hyoid canals on both sides exhibited positive voltage drops. The hyoid cluster has a fan-like distribution, with distinct dorsal and ventral clumpings and only a small number oriented horizontally [Berquist, 2003]. Thus, it is perhaps not surprising that horizonal (xy) model exhibits differences from three dimensions.

As the dogfish changes location, the source gets closer to the shark's body and the relative angle between the dipole axis and the canals changes causing changes in the polarity and magnitude of the voltage drops. Like Berquist [2003] we find that the long buccal groups on the left, closest to the source, swap polarity (Figure 3.5c, iii). As the shark gets closer (Figure 3.5d, iv), the buccal canals on the right switch to positive and by Figure 3.5e, v the canals on the left and right receive approximately balanced stimulus with the majority of clusters having the same polarity and similar magnitude. Finally, the dogfish passes the dipole (Figure 3.5f, vi) and the long buccal, hyoid and mandibular canals on the left switch polarity again.

Alternative trajectories where dogfish maintains a somewhat constant orientation to

the dipole field ('fieldline' approach; Figure 3.7) or takes a direct path to the dipole source ('direct' approach; Figure 3.6) produce similar distributions of voltage drop magnitudes and polarities. Apart from when the dipole was directly underneath the dogfish, the spatial distribution of voltage drop polarities remains constant and near symmetrical on each side of the head (Figure 3.6; Figure 3.7). The role of different clusters is similar to the 'unchanged' trajectory with strongest negative voltage drops in buccal cluster and strongest positive voltage drops in mandibular and hyoid clusters. However, while the spatial distribution remains somewhat constant, the magnitude of voltage drops along these trajectories increases significantly. In agreement with Berquist [2003], we find short canals initially experience drops of less than 1 nV but develop strong voltage drops of greater than 100 µV as the dogfish passes over the dipole (Figure 3.6e, v; Figure 3.7e, v).

3.3.1.2 Dipole stimulus: Vertical plane trajectories

The vertical plane approach strategies are similar to the horizontal trajectories in section 3.3.1.1. As the virtual dogfish moves along its approach trajectory, it encounters and then passes by a dipole located at the origin, with the dipole axis aligned with the negative y-axis. With the vertical trajectories the dogfish begins its trajectory approximately 0.95 m from the dipole, with its mouth located at approximately z = 0.3 m and y = -0.9 m (Figure 3.8). Figure 3.9 compares the 'unchanged' trajectory computed analytically in three dimensions to the numerical 2D numerical solution. In the dogfish's starting position (Figure 3.9a, i), similar to the horizontal plane the largest voltage drops range from -5 to 3 nV in the canals which were several cm long. The closest the dogfish gets to the dipole under this approach trajectory is 0.3 m (Figure 3.9e, v). The maximum voltage drops in the longest canals never exceed ± 55 nV. However, unlike the horizontal plane trajectories where all four ampullary groups experienced both negative and positive voltage drops at any one time, the mandibular cluster only experiences negative voltage drops at the final phase of the unchanged trajectory (Figure 3.9f).

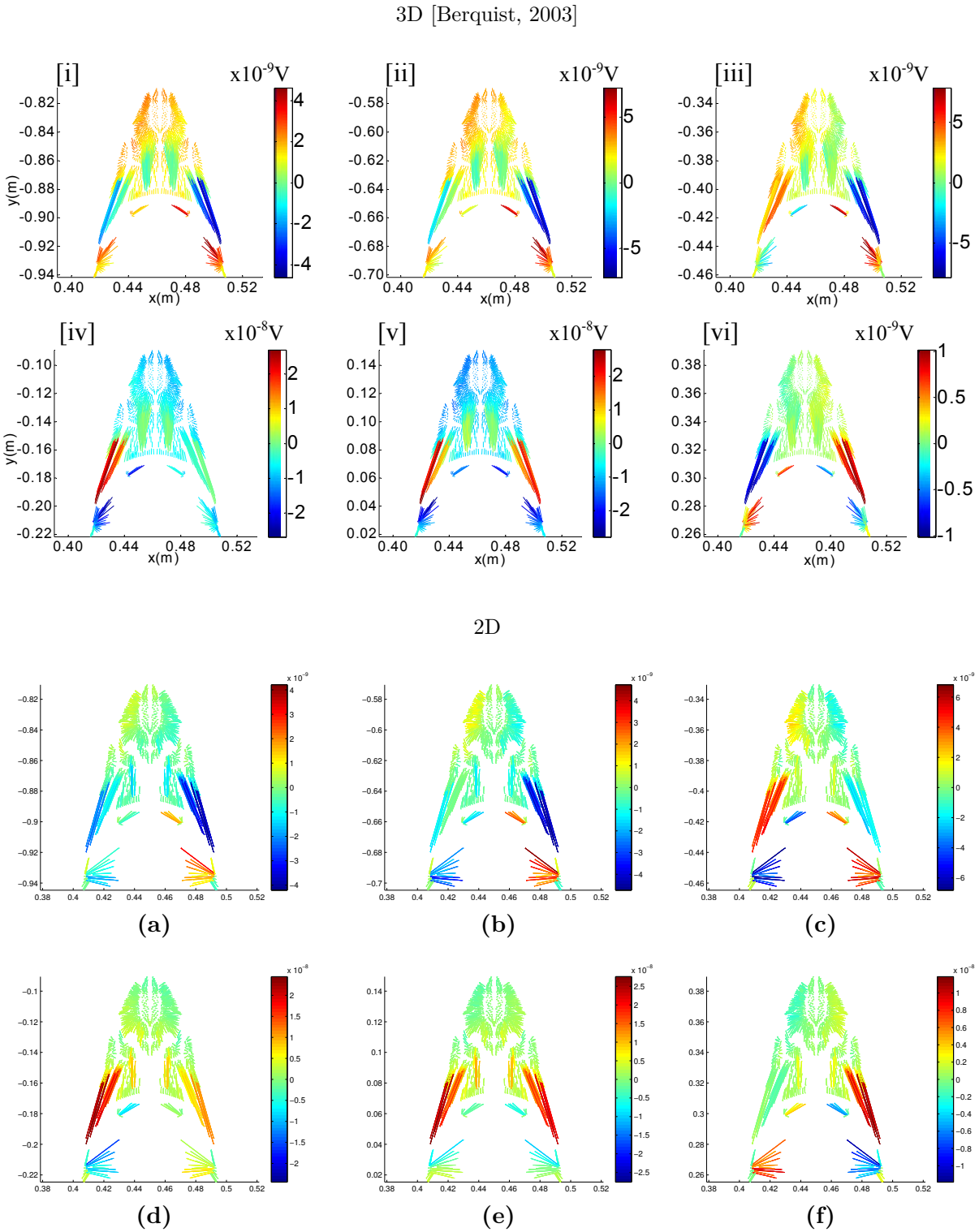

Figure 3.5: Canal voltage drops at each of six locations along an unchanged approach trajectory in the dipole horizontal plane (see Figure 3.4). Figure 3.5i to vi show the 3D analytical solutions, dipole strength $P = 5.6 \times 10^{-16}\,\mathrm{C\,m}$, water permittivity $\epsilon = 7 \times 10^{-10}\,\mathrm{C^2N^{-1}m^{-1}}$. Reprinted from Berquist [2003], with permission from Dr. Rachel Berquist. Figures 3.5a to 3.5f show the numerical solutions for the approximately matched 2D scenarios, dipole strength $P = 3.6 \times 10^{-6}\,\mathrm{A\,m}$, water conductivity $\sigma = 4.5\,\mathrm{S\,m^{-1}}$. Axes show distance from the dipole origin (m). Note the scale for each colourmap to differs between subfigures, as magnitudes of voltage drops differ greatly between locations.

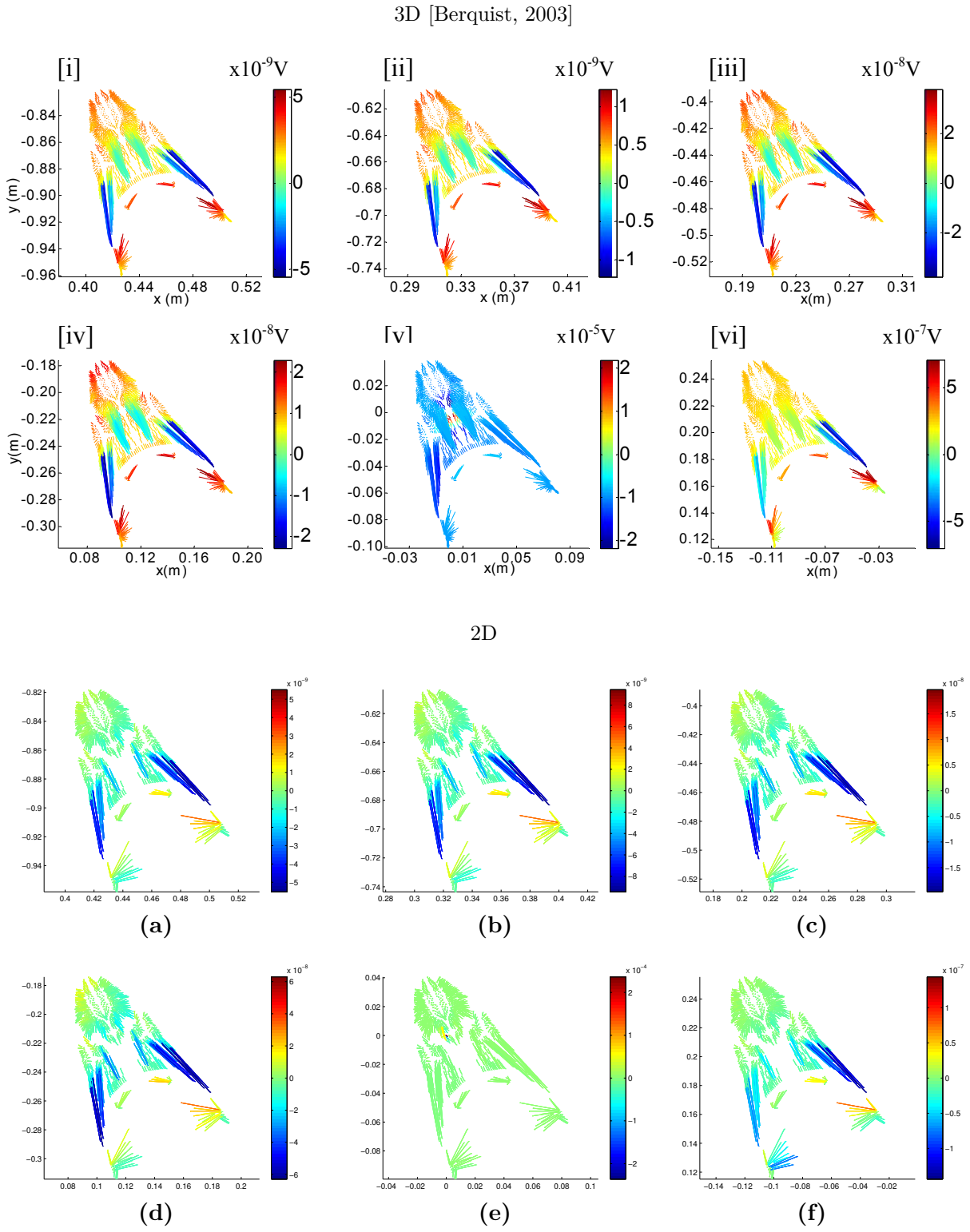

Figure 3.6: Canal voltage drops at each of six locations along a direct approach trajectory in the dipole horizontal plane (see Figure 3.4). Figure 3.6i to vi show the 3D analytical solutions, dipole strength $P = 5.6 \times 10^{-16}\,\mathrm{C\,m}$, water permittivity $\epsilon = 7 \times 10^{-10}\,\mathrm{C^2N^{-1}m^{-1}}$. Reprinted from Berquist [2003], with permission from Dr. Rachel Berquist. Figures 3.6a to 3.6f show the numerical solutions for the approximately matched 2D scenarios, dipole strength $P = 3.6 \times 10^{-6}\,\mathrm{A\,m}$, water conductivity $\sigma = 4.5\,\mathrm{S\,m^{-1}}$. Axes show distance from the dipole origin (m). Note the scale for each colourmap to differs between subfigures, as magnitudes of voltage drops differ greatly between locations.

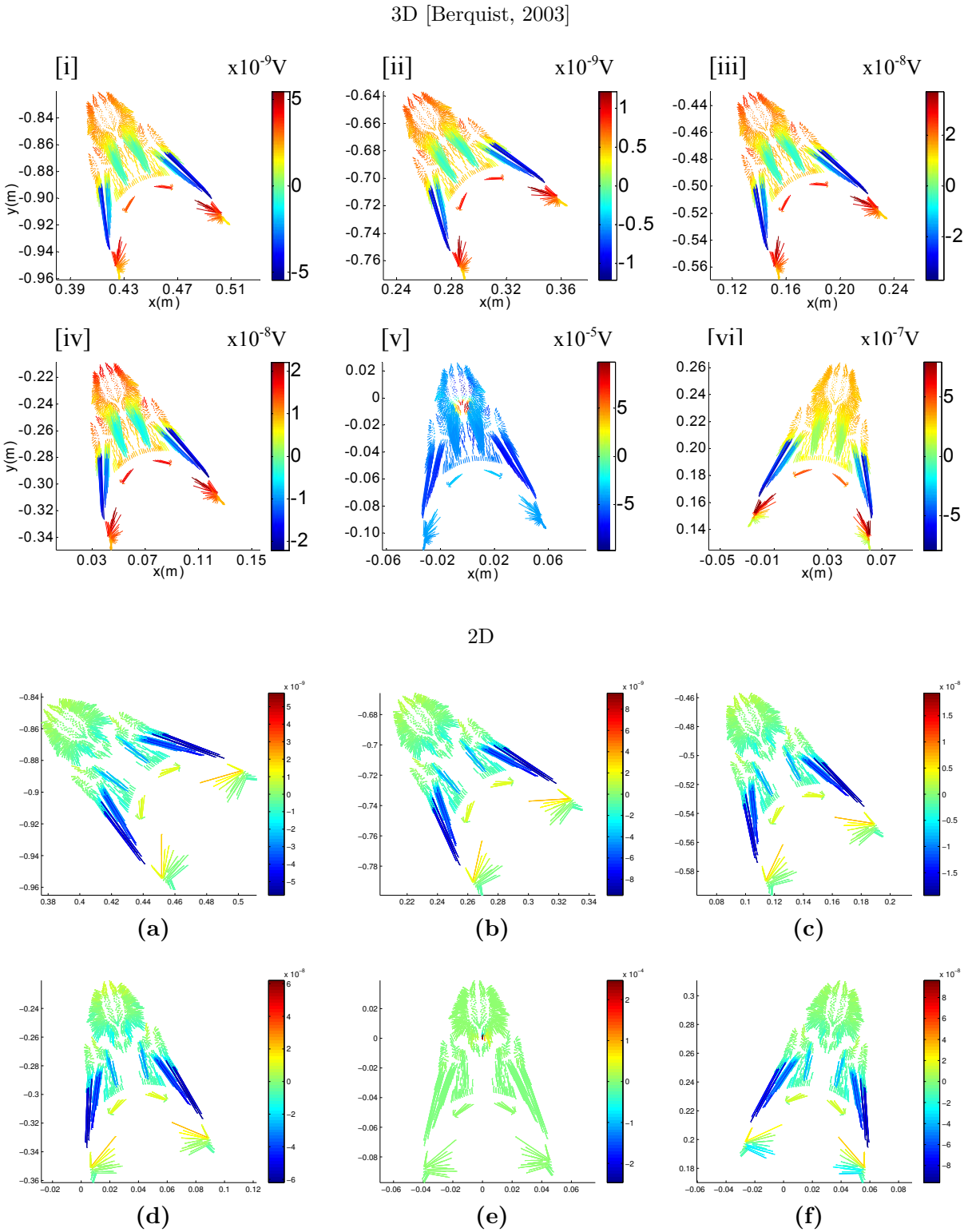

Figure 3.7: Canal voltage drops at each of six locations along a fieldline approach trajectory in the dipole horizontal plane (see Figure 3.4). Figure 3.7i to vi show the 3D analytical solutions, dipole strength $P = 5.6 \times 10^{-16}\,\mathrm{C\,m}$, water permittivity $\epsilon = 7 \times 10^{-10}\,\mathrm{C^2N^{-1}m^{-1}}$. Reprinted from Berquist [2003], with permission from Dr. Rachel Berquist. Figures 3.7a to 3.7f show the numerical solutions for the approximately matched 2D scenarios, dipole strength $P = 3.6 \times 10^{-6}\,\mathrm{A\,m}$, water conductivity $\sigma = 4.5\,\mathrm{S\,m^{-1}}$. Axes show distance from the dipole origin (m). Note the scale for each colourmap to differs between subfigures, as magnitudes of voltage drops differ greatly between locations.

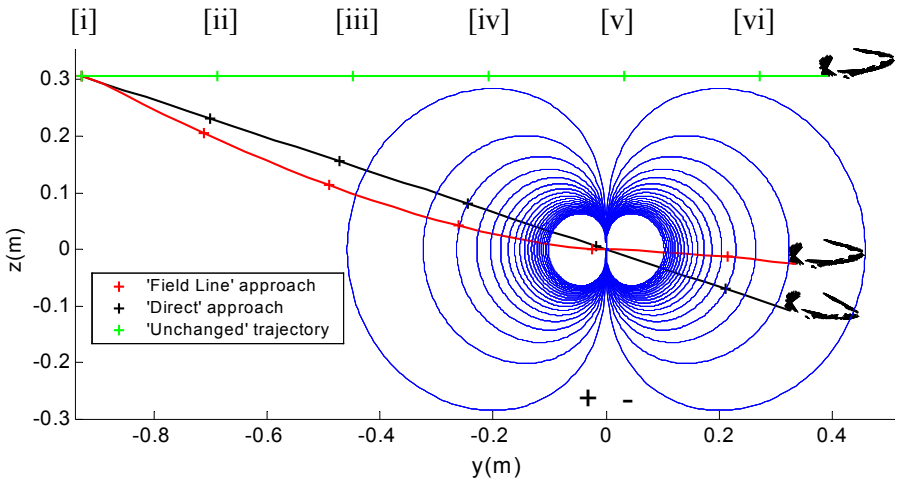

(a) 3D [Berquist, 2003]

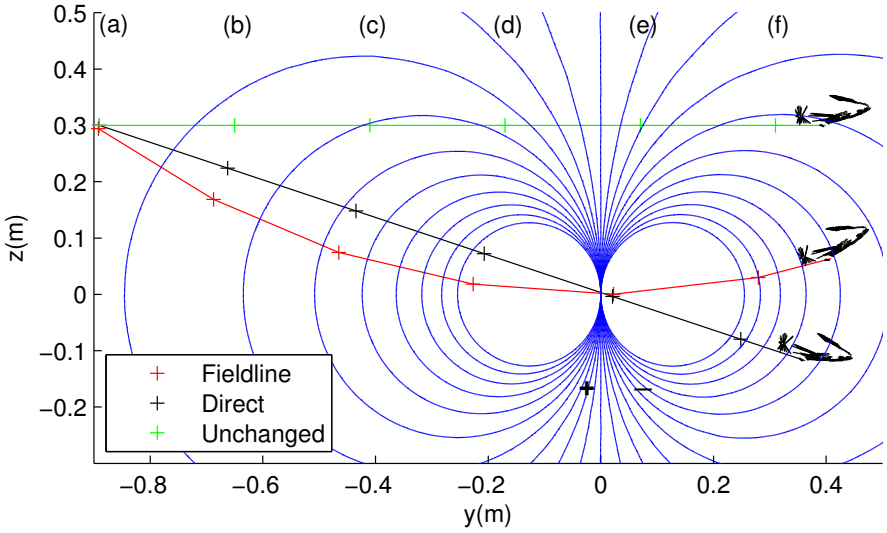

(b) 2D

Figure 3.8: YZ approach trajectories in the dipole vertical plane and locations where canal voltage drops were mapped. Figure 3.8a shows the three dimensional analytical model. Reprinted from Berquist [2003], with permission from Dr. Rachel Berquist. Figure 3.8b shows the approximately equivalent two dimensional numerical model. In both cases the source is located at the origin. Note: the equipotential contours have been plotted to illustrate the differences between dimensions and may not correspond to matched contour levels.

The spatial distribution of canal voltage drops remains similar in the first three locations of the 'unchanged' trajectory. Like Berquist [2003] we found strongest negative voltage drops in the long buccal canals and the strongest positive voltages develop in the hyoid canals (Figures 3.9a to 3.9c, i to iii). Similarly we also find as the dogfish progresses along its trajectory the orientation of the electric field rotates, becoming well aligned with the hyoid canals, resulting in strong positive or negative voltage drops depending on the

canal orientation. Additionally, this rotation of the field causes the polarity of voltage drops in these hyoid and mandibular canals to switch (Figures 3.9d to 3.9f, iv to vi). Again, we find minor differences from Berquist [2003] in our two dimensional simulation, particularly in the relative magnitudes of voltage drops in the shorter buccal and SO canals. However, trends in the spatial distribution of the strongest voltage drops appear to be largely maintained, likely due to strong voltage drops occurring in canals which are well aligned with the source electric field.

Like Berquist [2003], we find the alternative vertical trajectories, where the dogfish approaches and passes by the dipole source ('direct' approach; Figure 3.10; 'fieldline' approach, Figure 3.11), produce similar results to the corresponding horizontal plane trajectories (Figure 3.6; Figure 3.7). As with the 'unchanged' trajectory, the strongest voltage drops were in the long buccal and hyoid canals. The short canals initially experience drops of less than 1 nV, but develop strong voltage drops of greater than 1 µV in the mandibular canals as the dogfish passes over the dipole (Figure 3.10e, v; Figure 3.11e, v).

The overall generalizations of Berquist [2003] hold, despite our two dimensional simulations only considering a smaller subset of ampullae, only one angular orientation at a time and reducing the length of canals that were not well aligned with the horizontal or vertical planes (as we only used either the xy or yz coordinates of pore and ampulla locations and removed overlapping ampullae). At a distance, the long horizontally aligned canals appear responsible for initial detection of prey-like stimuli. As the dogfish approaches and passes over the dipole, shorter more vertically aligned canals around the snout and mouth develop strongest voltage drops. We use these simulations as our baseline model and later will examine the effects of electrical and geometrical properties of shark tissues on the stimulus that ampullae receive.

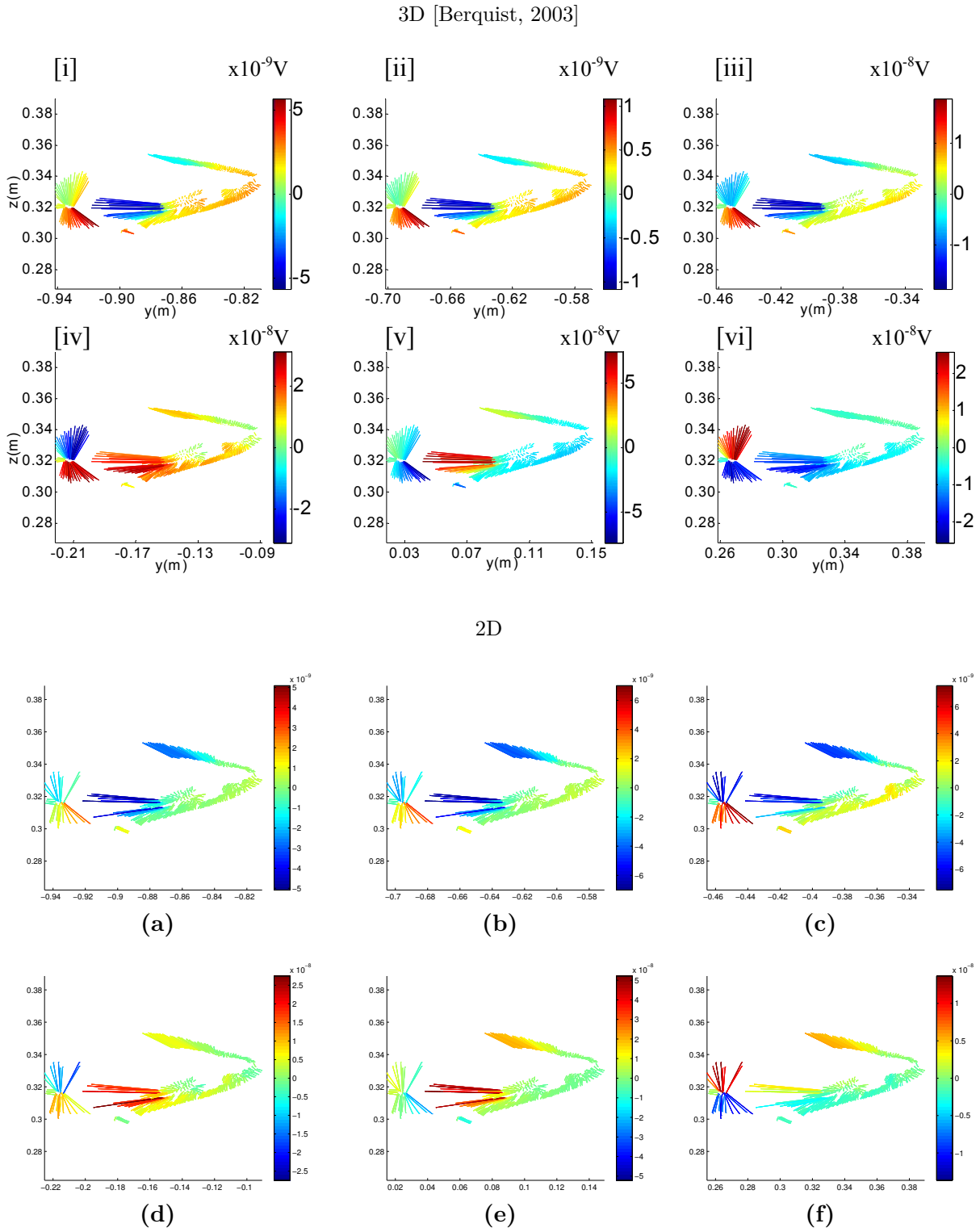

Figure 3.9: Canal voltage drops at each of six locations along an unchanged approach trajectory in the dipole vertical plane (see Figure 3.8). Figure 3.9i to vi show the 3D analytical solutions, dipole strength $P = 5.6 \times 10^{-16}\,\mathrm{C\,m}$, water permittivity $\epsilon = 7 \times 10^{-10}\,\mathrm{C^2N^{-1}m^{-1}}$. Reprinted from Berquist [2003], with permission from Dr. Rachel Berquist. Figures 3.9a to 3.9f show the numerical solutions for the approximately matched 2D scenarios, dipole strength $P = 3.6 \times 10^{-6}\,\mathrm{A\,m}$, water conductivity $\sigma = 4.5\,\mathrm{S\,m^{-1}}$. Axes show distance from the dipole origin (m). Note the scale for each colourmap to differs between subfigures, as magnitudes of voltage drops differ greatly between locations.

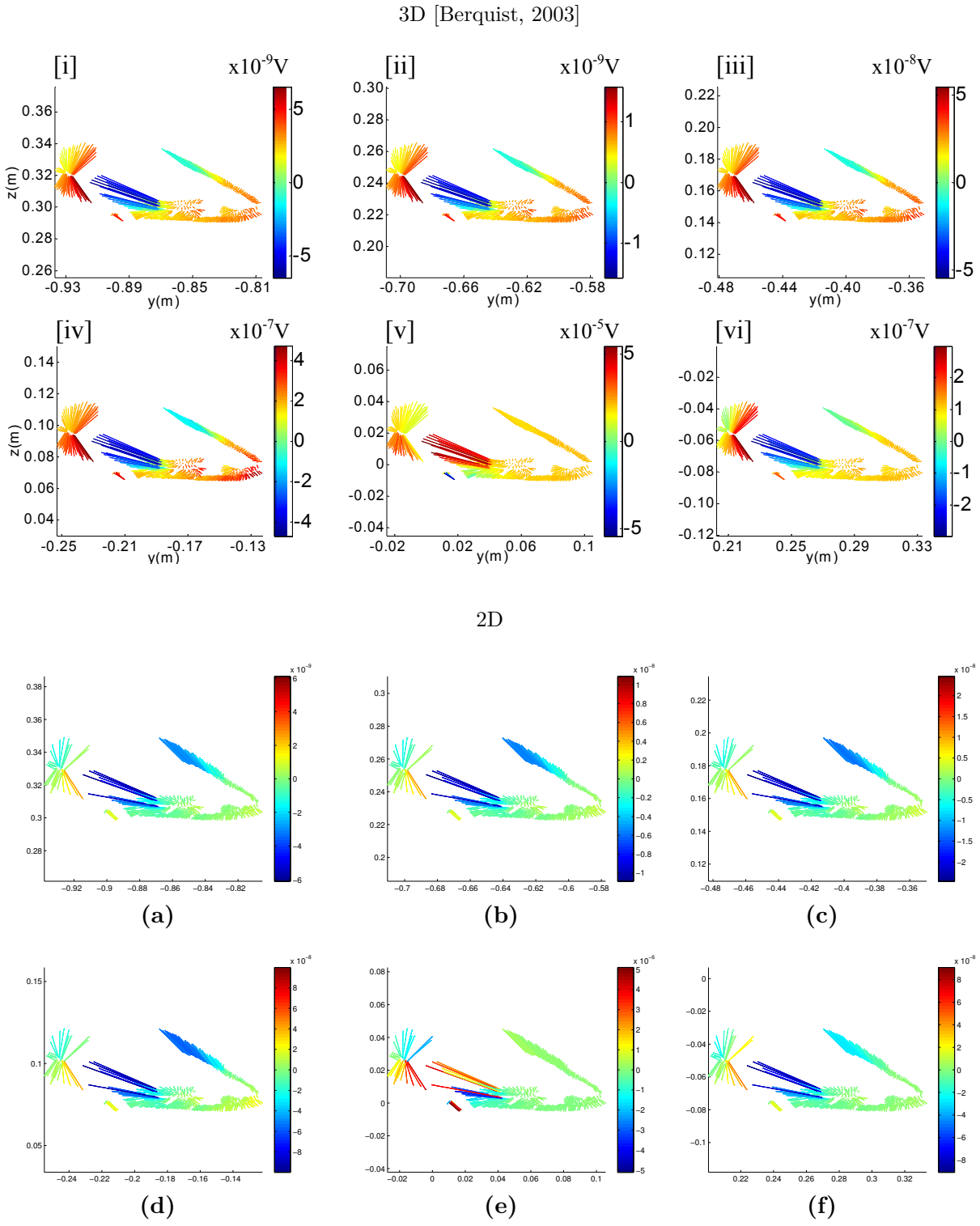

Figure 3.10: Canal voltage drops at each of six locations along a direct approach trajectory in the dipole vertical plane (see Figure 3.8). Figure 3.10i to vi show the 3D analytical solutions, dipole strength $P = 5.6 \times 10^{-16}\,\mathrm{C\,m}$, water permittivity $\epsilon = 7 \times 10^{-10}\,\mathrm{C^2N^{-1}m^{-1}}$. Reprinted from Berquist [2003], with permission from Dr. Rachel Berquist. Figures 3.10a to 3.10f show the numerical solutions for the approximately matched 2D scenarios, dipole strength $P = 3.6 \times 10^{-6}\,\mathrm{A\,m}$, water conductivity $\sigma = 4.5\,\mathrm{S\,m^{-1}}$. Axes show distance from the dipole origin (m). Note the scale for each colourmap to differs between subfigures, as magnitudes of voltage drops differ greatly between locations.

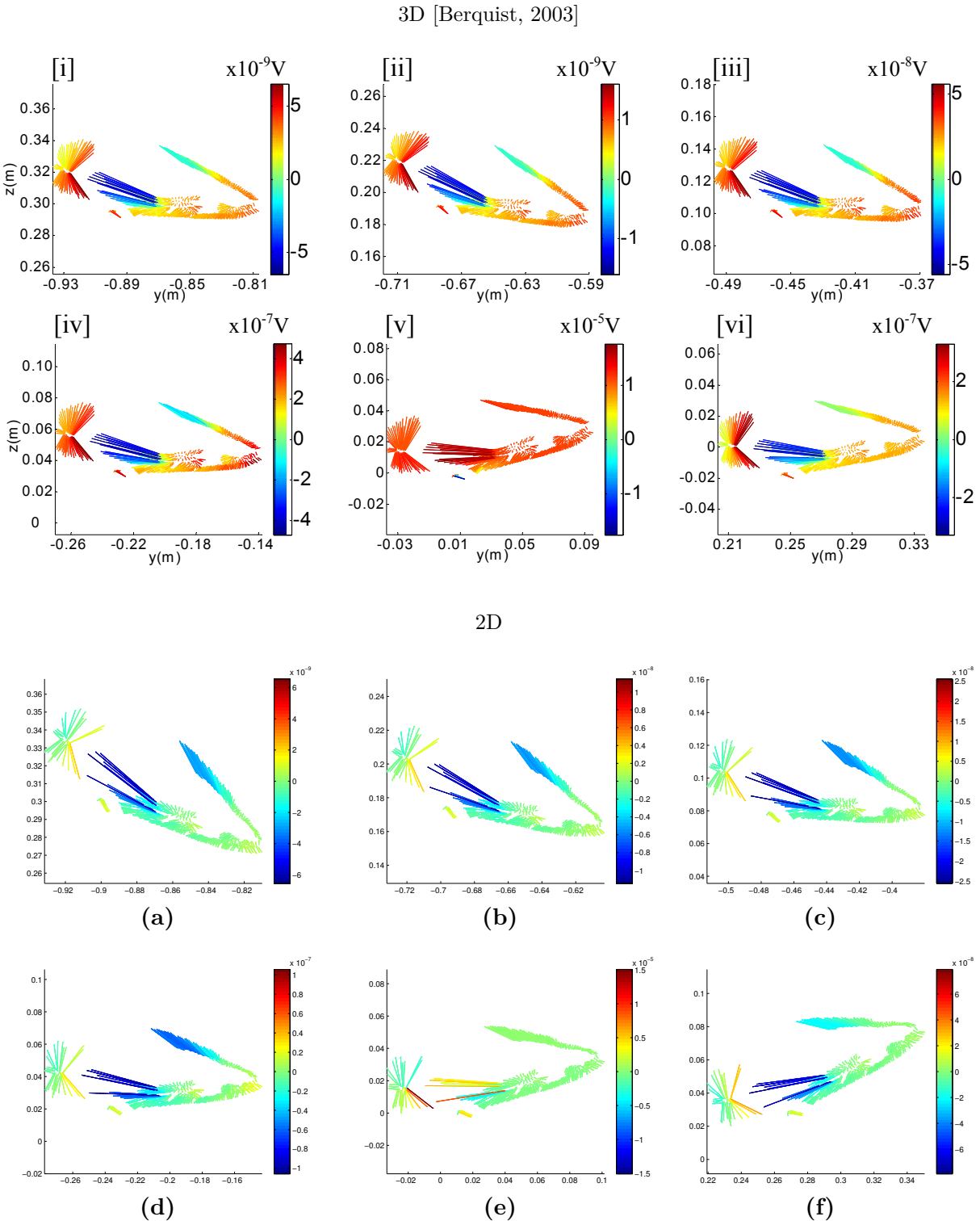

Figure 3.11: Canal voltage drops at each of six locations along a fieldline approach trajectory in the dipole vertical plane (see Figure 3.8). Figure 3.11i to vi show the 3D analytical solutions, dipole strength $P = 5.6 \times 10^{-16}\,\mathrm{C\,m}$, water permittivity $\epsilon = 7 \times 10^{-10}\,\mathrm{C^2N^{-1}m^{-1}}$. Reprinted from Berquist [2003], with permission from Dr. Rachel Berquist. Figures 3.11a to 3.11f show the numerical solutions for the approximately matched 2D scenarios, dipole strength $P = 3.6 \times 10^{-6}\,\mathrm{A\,m}$, water conductivity $\sigma = 4.5\,\mathrm{S\,m^{-1}}$. Axes show distance from the dipole origin (m). Note the scale for each colourmap to differs between subfigures, as magnitudes of voltage drops differ greatly between locations.

3.3.1.3 Uniform electric field stimulus

As with the dipole approach trajectories we attempted to match a 2D numerical solution for canal voltage drops along a sinusoidal trajectory through a constant uniform electric field to the three dimensional analytical solutions described by Berquist [2003]. While we were able to approximately match the corresponding trajectories (Figure 3.12), there were some discrepancies. In the text description of the simulation the oscillation frequency of the head during swimming was described as 0.6 Hz and this is what Figure 3.12a appears to show, but the figure caption says the frequency is 0.66 Hz. Visually we matched the angular head oscillation amplitude to be 0.1 m (Figure 3.12a). The angle of the dogfish head differs to our simulations, suggesting a different oscillation amplitude may have been used. In spite of this, similar trends in the spatial distributions of voltage drops are observed if we examine the absolute values of canal voltage drops (Figures 3.13a to 3.13c), which is what Berquist [2003] appears to have plotted (Figure 3.13 i to iii).

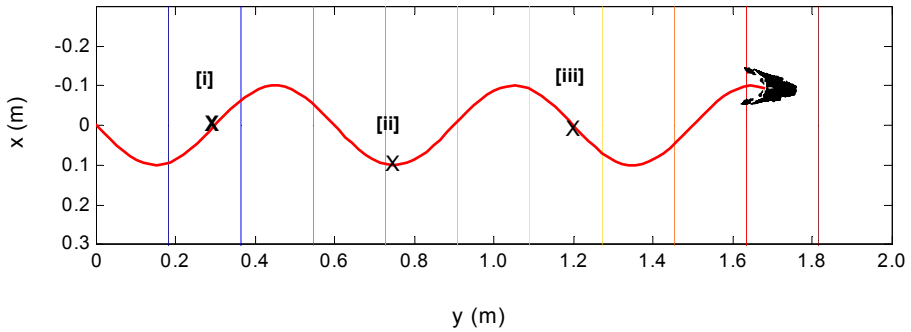

(a) 3D [Berquist, 2003]

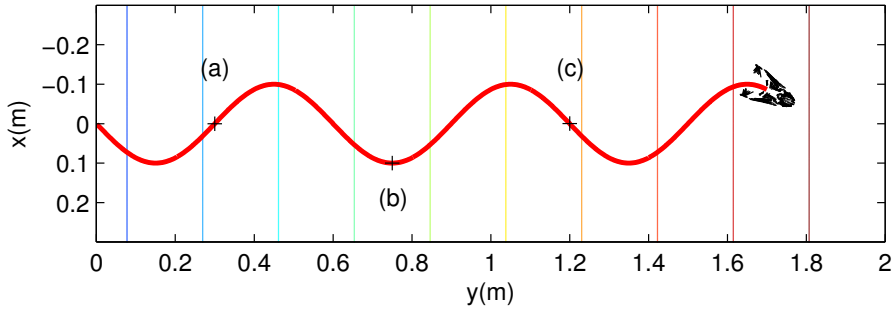

(b) 2D

Figure 3.12: Sinusoidal swimming trajectory (0.6 Hz) of the dogfish moving in a horizontal plane through the constant uniform electric field of magnitude, $\Delta V = 500\,\mathrm{nV\,cm^{-1}}$. The dogfish's mean heading is parallel to the positive voltage gradient. Figure 3.12a shows the three dimensional analytical model. Reprinted from Berquist [2003], with permission from Dr. Rachel Berquist. Figure 3.12b shows the approximately equivalent two dimensional numerical model. Note: the equipotential contours may not correspond to matched contour levels between the two models.

Due to uniformity of the electric field, all changes in the voltage drops experienced by canals are as a direct result of the dogfish's rotational movements. When the dogfish is aligned with the electric field direction the voltage drops on the right and left ampullae are symmetrical (Figure 3.13ii; Figure 3.13b). As the dogfish rotates, canals on one side of the body are in better alignment with the electric field and the distribution between sides becomes increasingly asymmetric (Figure 3.13; Berquist [2003]). The spatial distribution of voltage drops is similar to that of the weak fields experienced in the dipole approach trajectories when the stimulus was far away. It is the long buccal canals that develop the largest voltage drops, due to their alignment with the dogfish body axis. This remains the case even as the shark rotates, as shorter canals even when well aligned with the electric field do not span much difference in voltage amplitude.

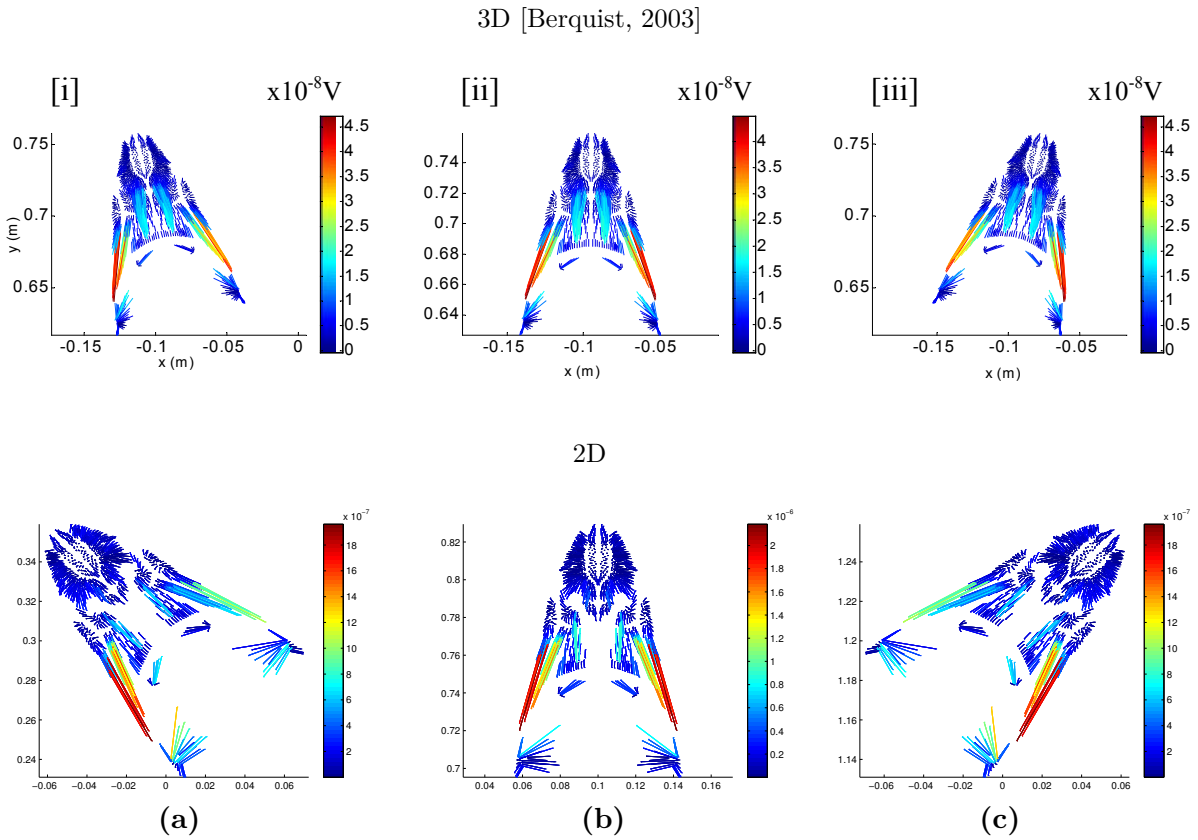

Figure 3.13: Canal voltage drops at each of three locations along a sinusoidal trajectory in a horizontal plane through the constant uniform electric field of magnitude 500 nV cm^{-1} (see Figure 3.12). Figure 3.13i to iii show the 3D analytical solutions. Reprinted from Berquist [2003], with permission from Dr. Rachel Berquist. Figures 3.13a to 3.13c show the absolute values of the numerical solutions for the approximately matched 2D scenarios. Note the scale for each colourmap to differs between subfigures, as magnitudes of voltage drops differ greatly between locations.

3.3.2 How electrical properties of shark tissue distort the stimulus

Simulations of dipole electric sources and uniform electric fields (section 3.3.1) were repeated using tissues of differing electrical properties, based on the values specified in Table 2.3.

3.3.2.1 Uniform electric field stimulus

We first examine the uniform electric field scenario as it is simpler, due to all changes in the voltage drops experienced by canals are as a direct result of the dogfish's rotational movements. When the shark's body axis is aligned with the electric field (Figure 3.14a) there is little difference between the simulations with different electrical properties of shark tissue. This figure does however illustrate some general properties previously mentioned for the simulations where the body of the shark was neglected (all tissue conductivity = σ_{water}; histogram subplots and blue lines). Firstly, the magnitude of the voltage drops scales linearly with canal length. Secondly, there is a non-linear relationship between canal orientation and the normalized voltage drop (voltage drop/canal length). Canals with the pore anterior to the ampulla (270°) experienced the largest positive drops and canals with the pore posterior to the ampulla experienced the largest negative drops (90°), with voltage drops being symmetrical between left (180°) and right (0/360°).

In the default case (all tissue conductivity = σ_{water}; histogram subplots and blue lines) when the shark rotates (Figure 3.14b), the linear relationship remains for canal length. The non-linear relationship with canal orientation becomes skewed, as the voltage drops become increasingly asymmetrical due to certain canals becoming better aligned with the electric field. In contrast to the body parallel simulation, internal voltage gradients do play a more significant role. The shark's body tissues are more resistive than seawater, causing equipotential surfaces to bend towards the shark resulting in all simulations where tissues were included experiencing voltage drops of greater magnitude. Specifying the brain as higher conductivity (red, teal) rather than equal to the conductivity of muscle (green, magenta) does not seem to effect the non-linear relationship with orientation. It does however appear to again increase voltage drops in longer canals, which are more likely to span the tissue and come into proximity of the brain. Conversely adding surface resistance boundary condition for the skin (teal, magenta) decreases the magnitude of voltage drops. The significance of skin resistance is potentially overestimated due to the geometry of the two dimensional simulations resulting in pores located in the shark tissue, rather than pores all providing direct contact with seawater. In summary, for uniform

electric fields both voltage drop across skin and body tissues contribute to the effective stimulus in long canals.

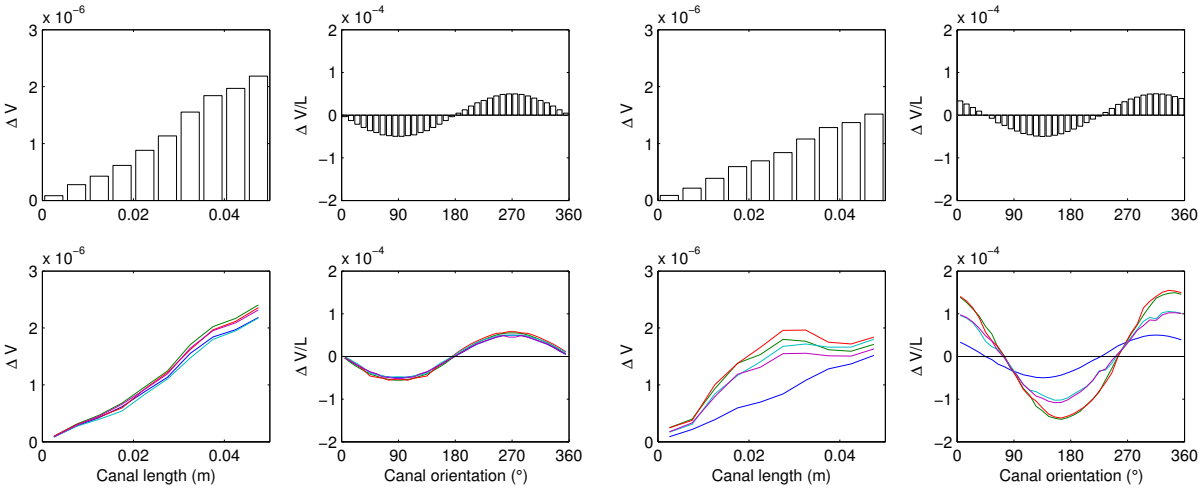

(a) Parallel **(b)** Rotated

Figure 3.14: Canal voltage drops in a uniform electric field, with tissues of differing electrical properties. Figure 3.14b shows the drops from the location (b) in fig. 3.12b. Figure 3.14a shows the drops from location (a) in fig. 3.12b. The upper two figures in each subplot show the relationship between voltage drop and canal length (left) and the relationship between normalized voltage drop and canal orientation (right) under the model: all tissues have the conductivity of seawater. The lower two figures in each subplot show the same histograms when tissues are given different electrical properties. Blue: All $\sigma_{water} = 4.5$; Green: $\sigma_{brain} = \sigma_{body} = 0.5$; Red: $\sigma_{body} = 0.5$, $\sigma_{brain} = 2.1$; Magenta: $\sigma_{brain} = \sigma_{body} = 0.5$, skin surface impedance $= 0.037\,\Omega\mathrm{m}^2$; Teal: $\sigma_{body} = 0.5$, $\sigma_{brain} = 2.1$, skin surface impedance $= 0.037\,\Omega\mathrm{m}^2$.

3.3.2.2 Dipole stimulus: Horizontal plane trajectories

At large distances the local dipole fields appear spatially uniform, thus the dipole approaches showed some similarities to the uniform electric field simulations above. For the unchanged trajectory of a shark passing by a dipole in the horizontal plane (Figure 3.4), the closest the dogfish gets is 0.45 m. At the closest phase (Figure 3.15c) the results look similar to Figure 3.14a suggesting the dogfish body is nearly parallel to the electric field. Like the uniform parallel case the voltage drops do not differ much from the default case (all tissue conductivity $= \sigma_{water}$; histogram subplots and blue lines). Simulations where tissues were given different conductivities did result in voltage drops of greater magnitude (red, green), but the effect of this was largely negated when skin resistance was considered (magenta, teal). For the remainder of the trajectory (Figures 3.15a, 3.15b and 3.15d), the results look similar to Figure 3.14b only the magnitude of drops differs based on distance from the dipole and the asymmetry of canal orientation subplots depends on the relative orientation of canals to the local electric field. Once the shark has passed by the dipole,

body tissue and skin in the tail appears to be shaping the effective stimulus, particularly in the mid to long canals (Figure 3.15d).

For the direct and fieldline trajectories in the horizontal plane (Figure 3.4) the results at a distance again showed similarities to the uniform electric field simulations (due to the similarity between direct and fieldline trajectories, we will henceforth only display fieldline results). In these cases the body of the shark was well aligned with the electric field (Figures 3.16a and 3.16b), so the results look similar to Figure 3.14a.

When the shark is near the dipole and the field is no longer uniform, the shorter canals experience voltage drops of larger magnitude. Unlike the unchanged trajectory where the shark is always at a distance from the dipole in these approach trajectories, due to the reduction in dimensions from 3D to 2D, the dipole is actually located in the shark tissue rather than seawater during phase Figure 3.4 (e) and (f). We further examine what happens in the proximity of the dipole by conducting two further simulations, firstly when the dipole is <1cm away from the dogfish snout (Figure 3.16c) and secondly when the dogfish has passed by the dipole and the body tissues of the shark no longer obscure the source (Figure 3.16d). The short canals become more important at close range (Figure 3.16c) and skin plays a more important role in both short and long canals. This is illustrated by the inclusion of body tissues actually reducing the effective stimulus (red, green), however the addition of skin resistance (magenta, teal) yields results that are similar to the water only simulation. However, when results are normalized for canal length and plotted against canal orientation, the peak magnitude is smaller with the inclusion of skin. Again this may be partially attributed to the reduction in dimensions meaning pores terminate in the shark tissue, beneath the skin, rather than providing direct contact to the external seawater.

Once the dogfish has passed by the dipole (Figure 3.16d) we find that whereas the water only simulation (histograms; blue) showed similar results to the shark parallel to the uniform electric field (Figure 3.14a), when body tissues are included the distribution of voltage drops becomes skewed similar to the shark rotated in the uniform electric field (Figure 3.14b). This suggests that the body of the fish, likely the trunk and tail, are shaping the effective stimulus received by the ampullae. We further investigate the effect of shark geometry on stimulus received in the following section.

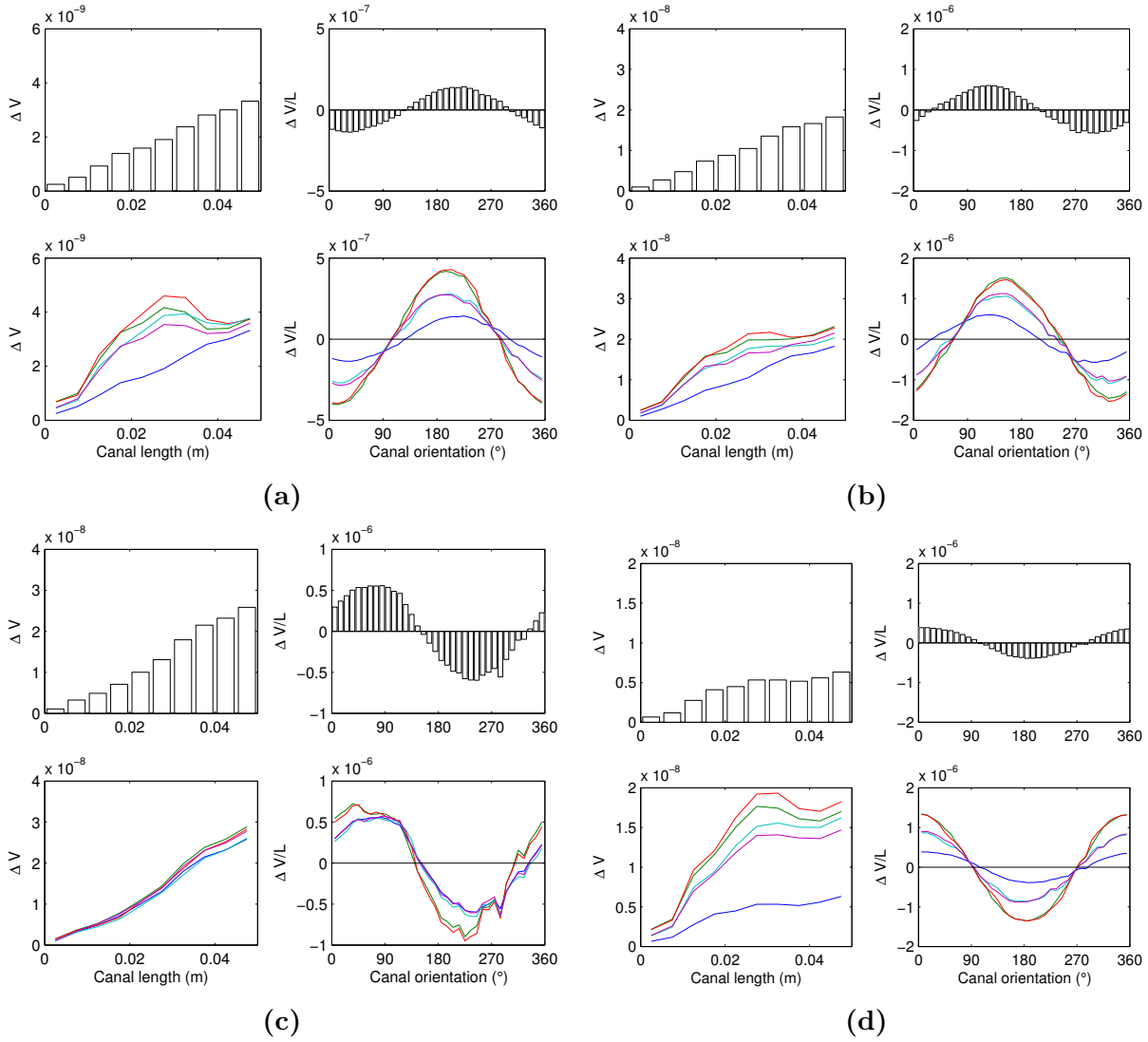

Figure 3.15: Canal voltage drops in the horizontal plane from a 2D dipole, with tissues of differing electrical properties. Figures show the voltage drops from the unchanged trajectory in fig. 3.4b. Figure 3.15a shows the drops from the location (a). Figure 3.15b shows the drops from location (d). Figure 3.15c shows the drops from the location (e). Figure 3.15d shows the drops from location (f). The upper two figures in each subplot show the relationship between voltage drop and canal length (left) and the relationship between normalized voltage drop and canal orientation (right) under the model: all tissues have the conductivity of seawater. The lower two figures in each subplot show the same histograms when tissues are given different electrical properties. Blue: All $\sigma_{water} = 4.5$; Green: $\sigma_{brain} = \sigma_{body} = 0.5$; Red: $\sigma_{body} = 0.5$, $\sigma_{brain} = 2.1$; Magenta: $\sigma_{brain} = \sigma_{body} = 0.5$, skin surface impedance $= 0.037\,\Omega\mathrm{m}^2$; Teal: $\sigma_{body} = 0.5$, $\sigma_{brain} = 2.1$, skin surface impedance $= 0.037\,\Omega\mathrm{m}^2$.

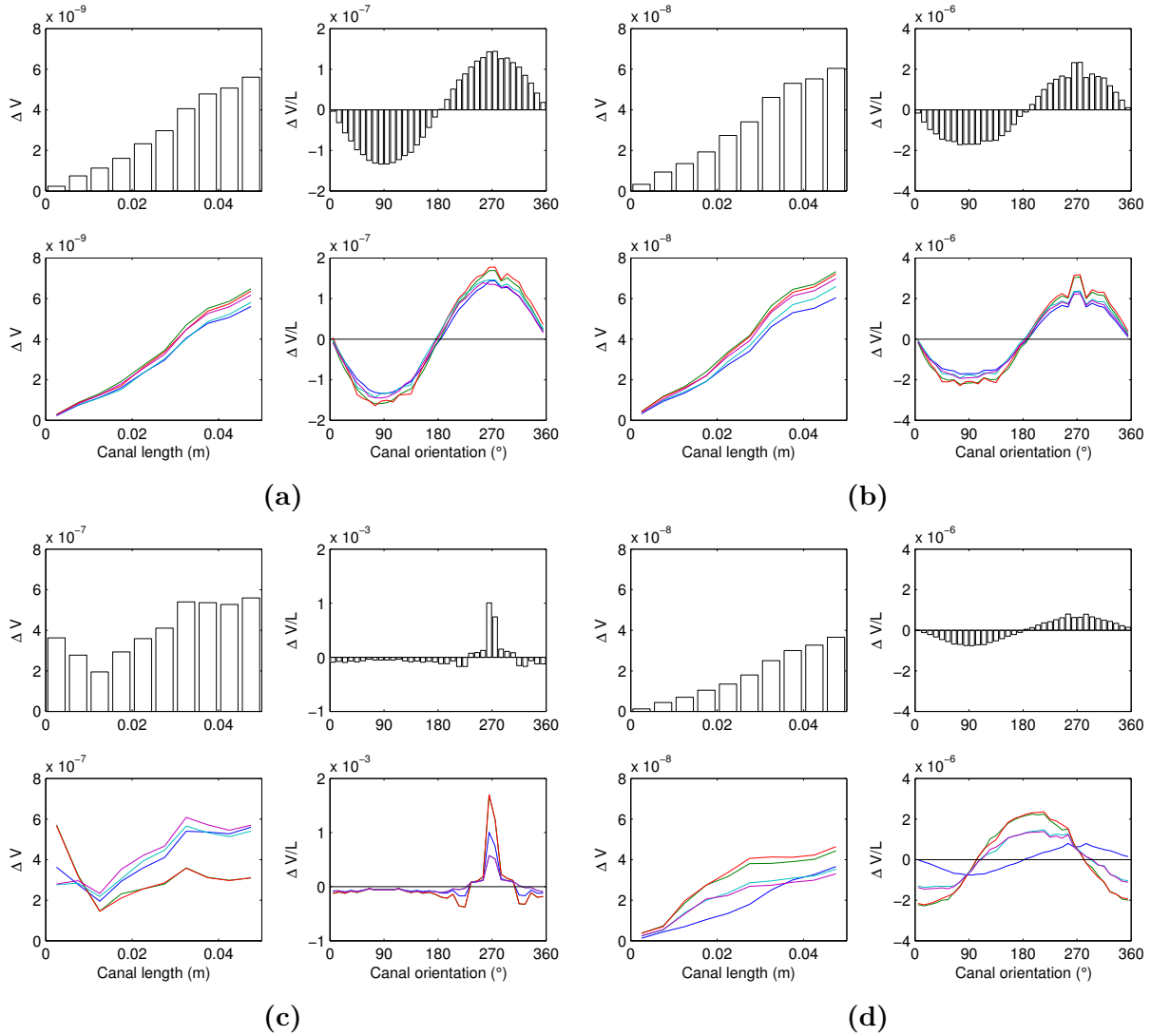

Figure 3.16: Canal voltage drops in the horizontal plane from a 2D dipole, with tissues of differing electrical properties. Figures show the voltage drops from the fieldline trajectory in fig. 3.4b. Figure 3.16a shows the drops from the location (a). Figure 3.16b shows the drops from location (d). Figure 3.16c shows the drops when dipole is <1cm away from the dogfish snout. Figure 3.16d shows the drops when the dogfish has passed by the dipole and the body tissues of the shark no longer obscure the source. The upper two figures in each subplot show the relationship between voltage drop and canal length (left) and the relationship between normalized voltage drop and canal orientation (right) under the model: all tissues have the conductivity of seawater. The lower two figures in each subplot show the same histograms when tissues are given different electrical properties. Blue: All $\sigma_{water} = 4.5$; Green: $\sigma_{brain} = \sigma_{body} = 0.5$; Red: $\sigma_{body} = 0.5$, $\sigma_{brain} = 2.1$; Magenta: $\sigma_{brain} = \sigma_{body} = 0.5$, skin surface impedance $= 0.037\,\Omega\mathrm{m}^2$; Teal: $\sigma_{body} = 0.5$, $\sigma_{brain} = 2.1$, skin surface impedance $= 0.037\,\Omega\mathrm{m}^2$.

3.3.2.3 Dipole stimulus: Vertical plane trajectories

As with the horizontal plane trajectories, in the vertical plane at large distances the local dipole fields appear spatially uniform. For the unchanged trajectory of a shark passing by a dipole in the horizontal plane (Figure 3.8), the closest the dogfish gets is 0.3 m. At the closest phase (Figure 3.17c), the dogfish body is nearly parallel to the electric field and exhibits similarities to Figure 3.14a in spite of the different plane of analysis. Like the uniform parallel case (and instances of the horizontal plane trajectory where the dogfish body axis was aligned with the electric field) simulations where tissues were given different conductivities did result in voltage drops of greater magnitude (red, green), but the effect of this was largely negated except in longer canals when skin resistance was considered (magenta, teal). Conversely, at Figure 3.17d, the dogfish body is nearly perpendicular to the electric field. In this case voltage drops and their interactions with tissue properties are independent of canal length and depend more on the relative orientations of the canals to the local field.

The direct and fieldline trajectories in the vertical plane were similar to their horizontal counterparts. The body of the shark was well aligned with the electric field (Figures 3.18a and 3.18b) so the results look similar to Figure 3.14a. When the shark is near the dipole and the field is no longer uniform, so there is no longer a linear relationship between canal length and magnitude of voltage drop.

As with the horizontal trajectories, the dipole is actually located in the shark tissue rather than seawater during the two phases closest to the dipole. We further examine what happens in the proximity of the dipole by conducting two further simulations, firstly when the dipole is ~5cm away from the dogfish mouth (Figure 3.18c) and secondly when the dogfish has passed by the dipole and the body tissues of the shark no longer obscure the source (Figure 3.18d). In the horizontal plane, at close proximity to the dipole (Figure 3.16c), the inclusion of body tissues reduced the effective stimulus and the addition of skin resistance largely restored voltage drops to similar magnitudes to the water only simulation. This is not the case in the vertical plane trajectory (Figure 3.18c) where both the inclusion of body tissues and skin resistance resulted in smaller magnitude drops. Whereas reduction of dimensions into the frontal plane (XY) still maintained some pores near the surface of the dogfish skin, reduction of the sagittal plane (YZ) resulted in most pores being at least few mm away from the surface, which exacerbates the problem that pores are not directly interfacing with the external seawater.

Once the dogfish has passed by the dipole (Figure 3.18d) in shorter canals the presence of shark tissues and skin increases the effective stimulus, whereas in longer canals the

effective stimulus decreases. This is likely due in part to the orientation of canals, with there being little difference in canals orientated near 90°, increases in magnitude of voltage drops in canals orientated near 180° (positive) and 0° (negative).

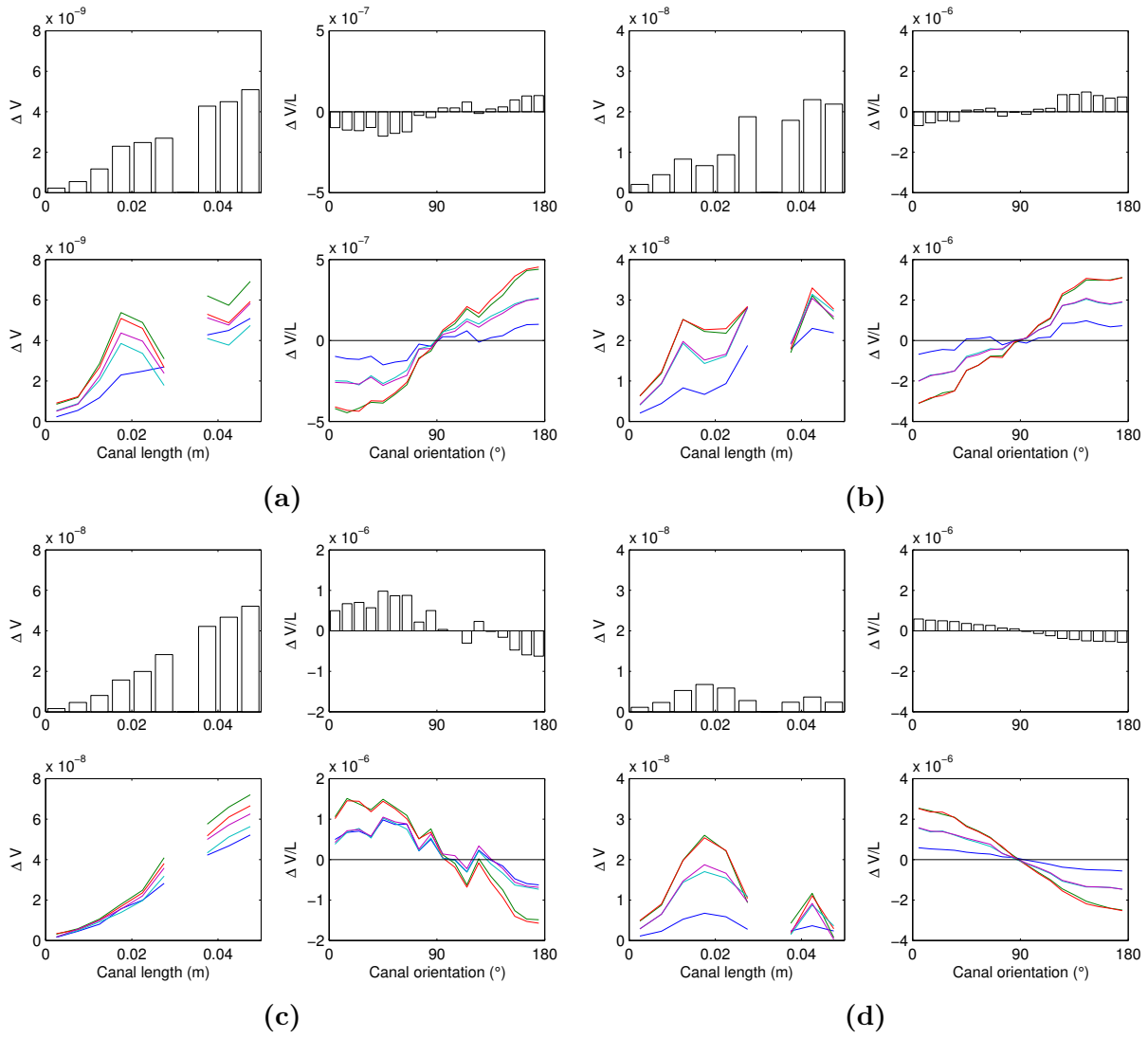

Figure 3.17: Canal voltage drops in the vertical plane from a 2D dipole, with tissues of differing electrical properties. Figures show the voltage drops from the unchanged trajectory in fig. 3.8b. Figure 3.17a shows the drops from the location (a). Figure 3.17b shows the drops from location (d). Figure 3.17c shows the drops from the location (e). Figure 3.17d shows the drops from location (f). The upper two figures in each subplot show the relationship between voltage drop and canal length (left) and the relationship between normalized voltage drop and canal orientation (right) under the model: all tissues have the conductivity of seawater. The lower two figures in each subplot show the same histograms when tissues are given different electrical properties. Blue: All $\sigma_{water} = 4.5$; Green: $\sigma_{brain} = \sigma_{body} = 0.5$; Red: $\sigma_{body} = 0.5$, $\sigma_{brain} = 2.1$; Magenta: $\sigma_{brain} = \sigma_{body} = 0.5$, skin surface impedance $= 0.037\,\Omega\mathrm{m}^2$; Teal: $\sigma_{body} = 0.5$, $\sigma_{brain} = 2.1$, skin surface impedance $= 0.037\,\Omega\mathrm{m}^2$.

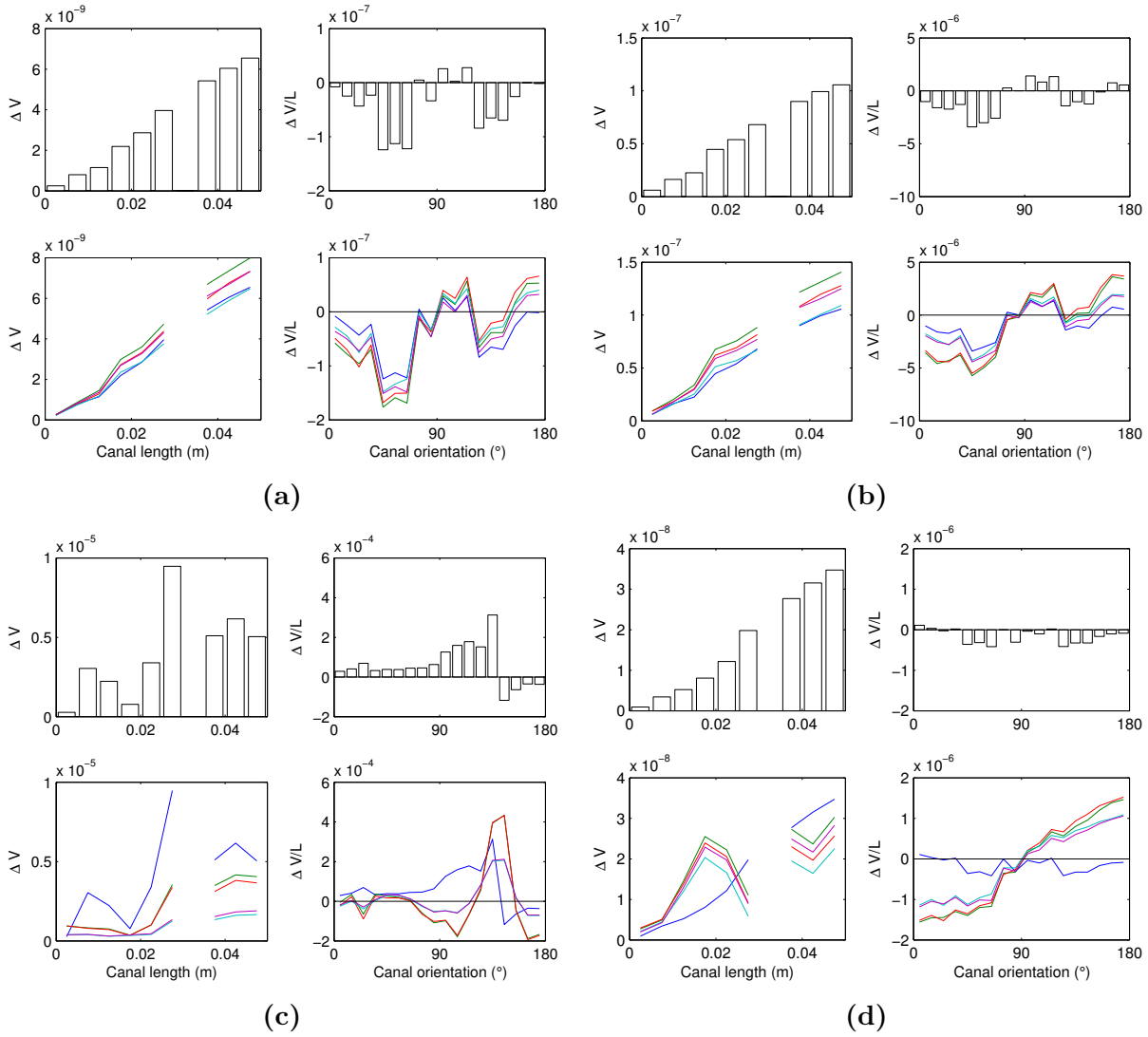

Figure 3.18: Canal voltage drops in the vertical plane from a 2D dipole, with tissues of differing electrical properties. Figures show the voltage drops from the fieldline trajectory in fig. 3.8b. Figure 3.18a shows the drops from the location (a). Figure 3.18b shows the drops from location (d). Figure 3.16c shows the drops when dipole is ~5cm the dogfish mouth. Figure 3.16d shows the drops when the dogfish has passed by the dipole and the body tissues of the shark no longer obscure the source. The upper two figures in each subplot show the relationship between voltage drop and canal length (left) and the relationship between normalized voltage drop and canal orientation (right) under the model: all tissues have the conductivity of seawater. The lower two figures in each subplot show the same histograms when tissues are given different electrical properties. Blue: All $\sigma_{water} = 4.5$; Green: $\sigma_{brain} = \sigma_{body} = 0.5$; Red: $\sigma_{body} = 0.5$, $\sigma_{brain} = 2.1$; Magenta: $\sigma_{brain} = \sigma_{body} = 0.5$, skin surface impedance $= 0.037\,\Omega\mathrm{m}^2$; Teal: $\sigma_{body} = 0.5$, $\sigma_{brain} = 2.1$, skin surface impedance $= 0.037\,\Omega\mathrm{m}^2$.

3.3.3 How geometrical properties of shark tissue distort the stimulus

The effect of shark geometry on the effective stimulus received by ampullae is now examined. Simulations of dipole electric sources and uniform electric fields (section 3.3.1) were repeated under two geometrical simplifications: 1) removal of fins and 2) removal of fins and head replaced by an ellipse. In each case, tissue properties were specified as $\sigma_{body} = 0.5$, $\sigma_{brain} = 2.1$, skin surface impedance $= 0.037\,\Omega\mathrm{m}^2$ and compared to the default water only model ($\sigma_{all} = 4.5$).

3.3.3.1 Uniform electric field stimulus

When the dogfish's body axis was not aligned with the electric field, there was little difference in the voltage drops between the different geometries (Figure 3.19a). The geometry with fins removed (black dashed) was very similar to the 2D shark projection (black solid). However, when both fins were removed and the head was replaced by an ellipse (black dotted) the magnitude of the effective stimulus was slightly larger in the longer canals. Differences based on geometry are smaller in magnitude than the differences between including body tissues (black solid) and the default water only model (grey solid). Conversely, when the dogfish's body axis was aligned with the electric field (Figure 3.19b) both simplifications increase the magnitude of voltage drops, particularly in longer canals, suggesting that tissue in the fins is modifying the electric field.

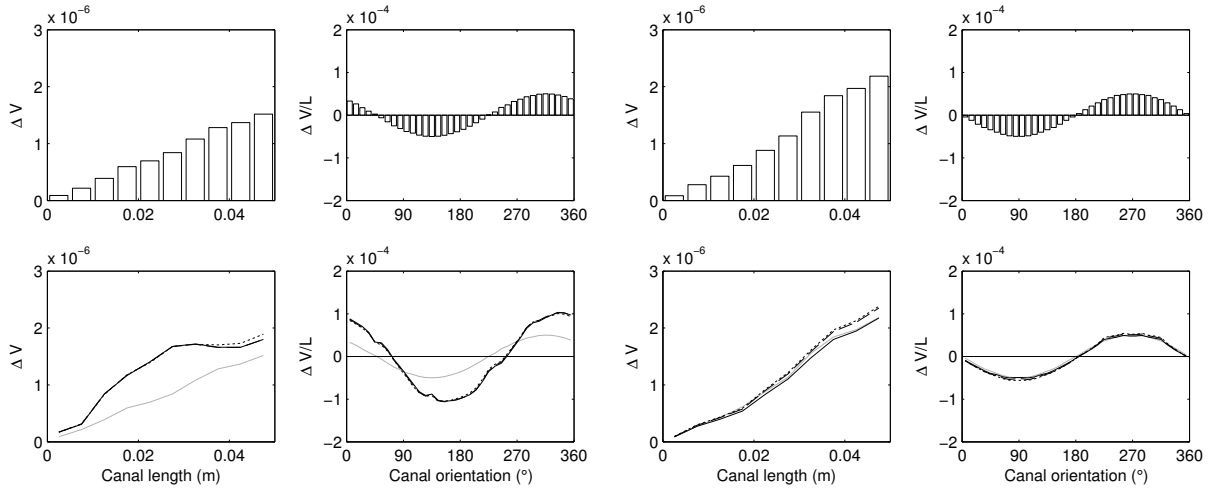

(a) Rotated **(b)** Parallel

Figure 3.19: Canal voltage drops in a uniform electric field, with differing dogfish geometries. Figure 3.19a shows the drops from the location (a) in fig. 3.12b. Figure 3.19b shows the drops from location (b) in fig. 3.12b. The upper two figures in each subplot show the relationship between voltage drop and canal length (left) and the relationship between normalized voltage drop and canal orientation (right) under the model: all tissues have the conductivity of seawater. The lower two figures in each subplot show the same histograms, with differing dogfish geometries. Grey: No body/all $\sigma_{water} = 4.5$; Black solid: 2D shark projection; Black dashed: fins removed; Black dotted: fins removed and head replaced with ellipse.

3.3.3.2 Dipole stimulus: Horizontal plane trajectories

As with the examination of the effect of how the electrical properties of tissues distort the field, there are similarities to the uniform field simulations. At the closest phase (Figure 3.20c) the results look similar to Figure 3.19b. Like the uniform parallel case both geometrical simplifications result in greater magnitude voltage drops, particularly in longer canals. Figures 3.20a and 3.20d show the opposite trend with the magnitude of voltage drops being reduced, particularly in longer canals, again suggesting fins impact the stimulus received by ampullae. However in longest canals, this reduction was smaller in the simplification where the original head geometry was replaced by an ellipse (black dotted). This suggests maybe it is the overall volume of tissue that is important, rather than specific geometry, as the ellipse head is slightly larger than the head based on realistic shark geometry. Finally, in Figure 3.20b there is little difference between any of the shark geometries, much like the uniform rotated simulation (Figure 3.19a).

For the direct and fieldline trajectories in the horizontal plane, the results at a distance were similar, with both geometrical simplifications increasing the magnitude of voltage drops, particularly in longer canals (Figures 3.21a, 3.21b and 3.21d). When the shark

was near the dipole (Figure 3.21c), removal of the fins had little effect (black dashed) but head replacement (black dotted) increased the magnitude of voltage drops likely due to an increase in pores not being located on the shark surface. The relationship normalized voltage drops, and canal orientation did not differ much between the shark geometries.

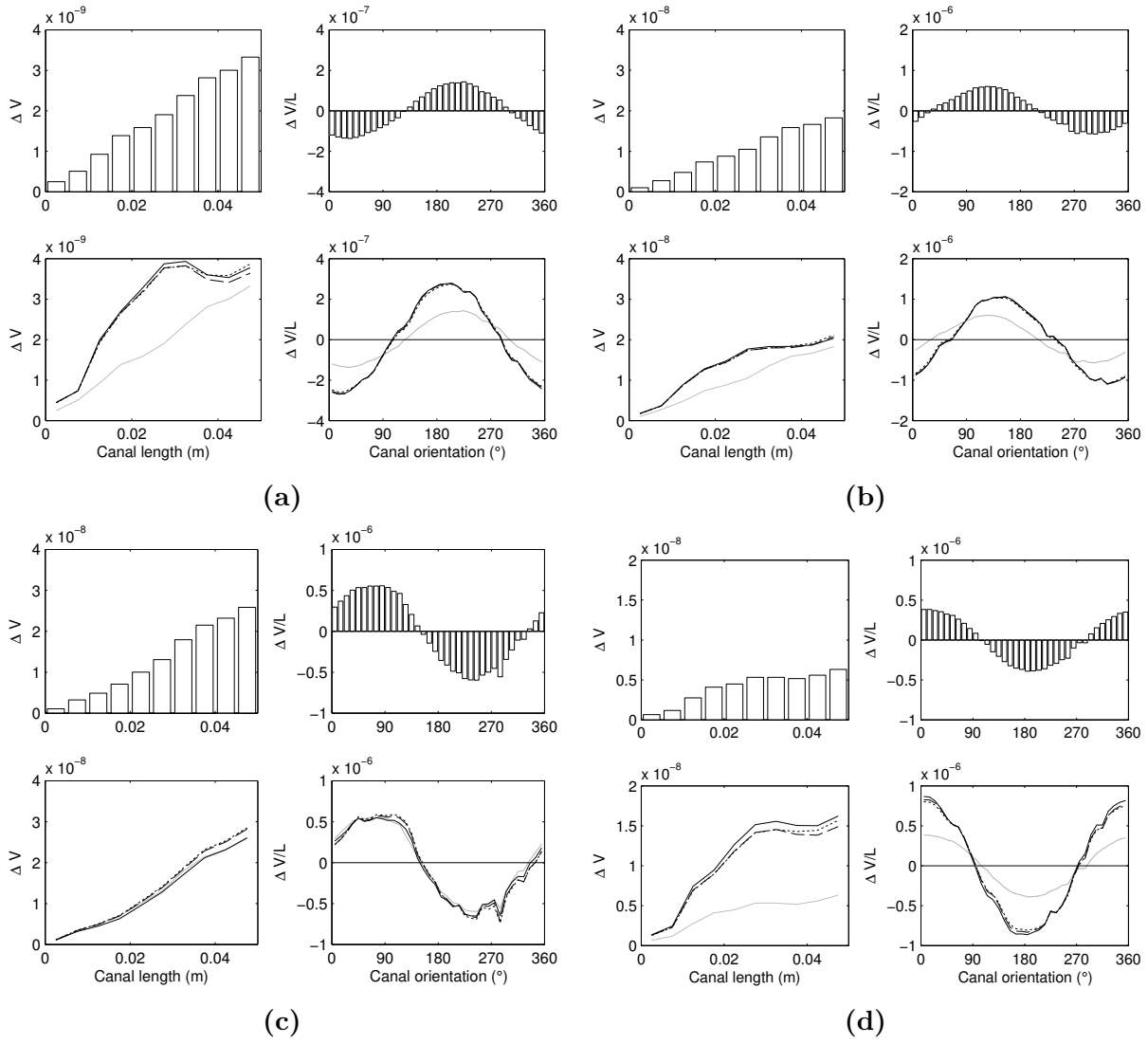

Figure 3.20: Canal voltage drops in the horizontal plane from a 2D dipole, with differing dogfish geometries. Figures show the voltage drops from the unchanged trajectory in fig. 3.4b. Figure 3.20a shows the drops from the location (a). Figure 3.20b shows the drops from location (d). Figure 3.15c shows the drops from the location (e). Figure 3.20d shows the drops from location (f). The upper two figures in each subplot show the relationship between voltage drop and canal length (left) and the relationship between normalized voltage drop and canal orientation (right) under the no body model: all tissues have the conductivity of seawater. The lower two figures in each subplot show the same histograms, with differing dogfish geometries. Grey: No body/all $\sigma_{water} = 4.5$; Black solid: 2D shark projection; Black dashed: fins removed; Black dotted: fins removed and head replaced with ellipse.

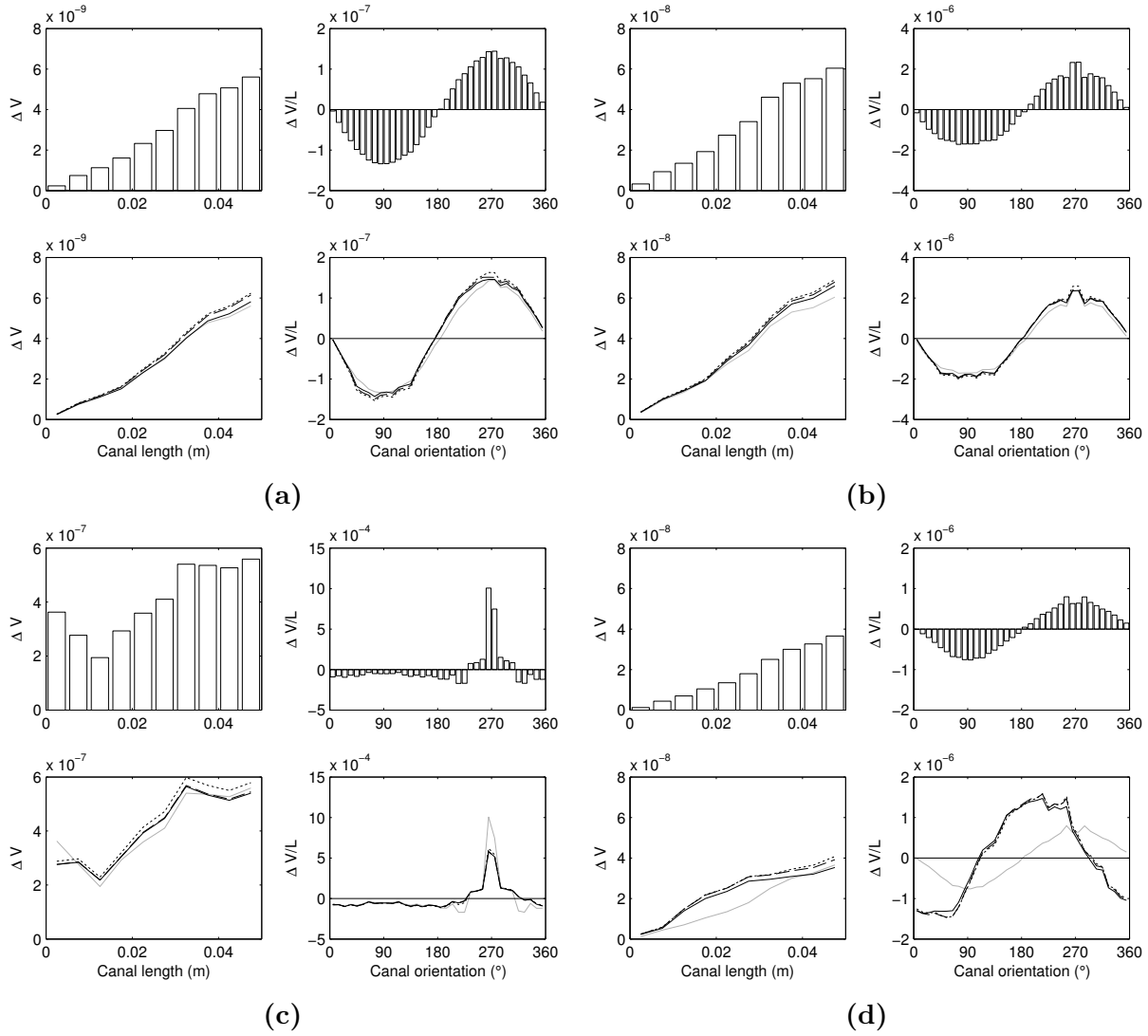

Figure 3.21: Canal voltage drops in the horizontal plane from a 2D dipole, with differing dogfish geometries. Figures show the voltage drops from the fieldline trajectory in fig. 3.4b. Figure 3.21a shows the drops from the location (a). Figure 3.21b shows the drops from location (d). Figure 3.21c shows the drops when dipole is <1cm away from the dogfish snout. Figure 3.21d shows the drops when the dogfish has passed by the dipole and the body tissues of the shark no longer obscure the source. The upper two figures in each subplot show the relationship between voltage drop and canal length (left) and the relationship between normalized voltage drop and canal orientation (right) under the model: all tissues have the conductivity of seawater. The lower two figures in each subplot show the same histograms, with differing dogfish geometries. Grey: No body/all $\sigma_{water} = 4.5$; Black solid: 2D shark projection; Black dashed: fins removed; Black dotted: fins removed and head replaced with ellipse.

3.3.3.3 Dipole stimulus: Vertical plane trajectories

In the vertical plane removal of fins (black dashed) appeared to have very little effect for all phases of the unchanged trajectory (Figure 3.22). Again, replacing the head with an ellipse (black dotted) caused greater changes in magnitude of voltage drops in longer canals and there was little difference between geometries for the relationship between normalized voltage drops and canal orientation (Figure 3.22).

Under the direct and fieldline approaches there was little difference in the relationship between magnitude of voltage drops and canal length as the shark approached the dipole (Figures 3.23a to 3.23c). Examining the relationship between normalized voltage drops and canal orientation revealed some slight alterations in magnitudes of voltage drops but trends exhibited in the realistic geometry were largely maintained. However, once the shark had passed the dipole (Figure 3.23a) there were differences in both magnitude of voltage drops versus length and normalized voltages drops versus canal orientation, again suggesting the fins (or volume of shark tissue) likely impact the stimulus received by ampullae.

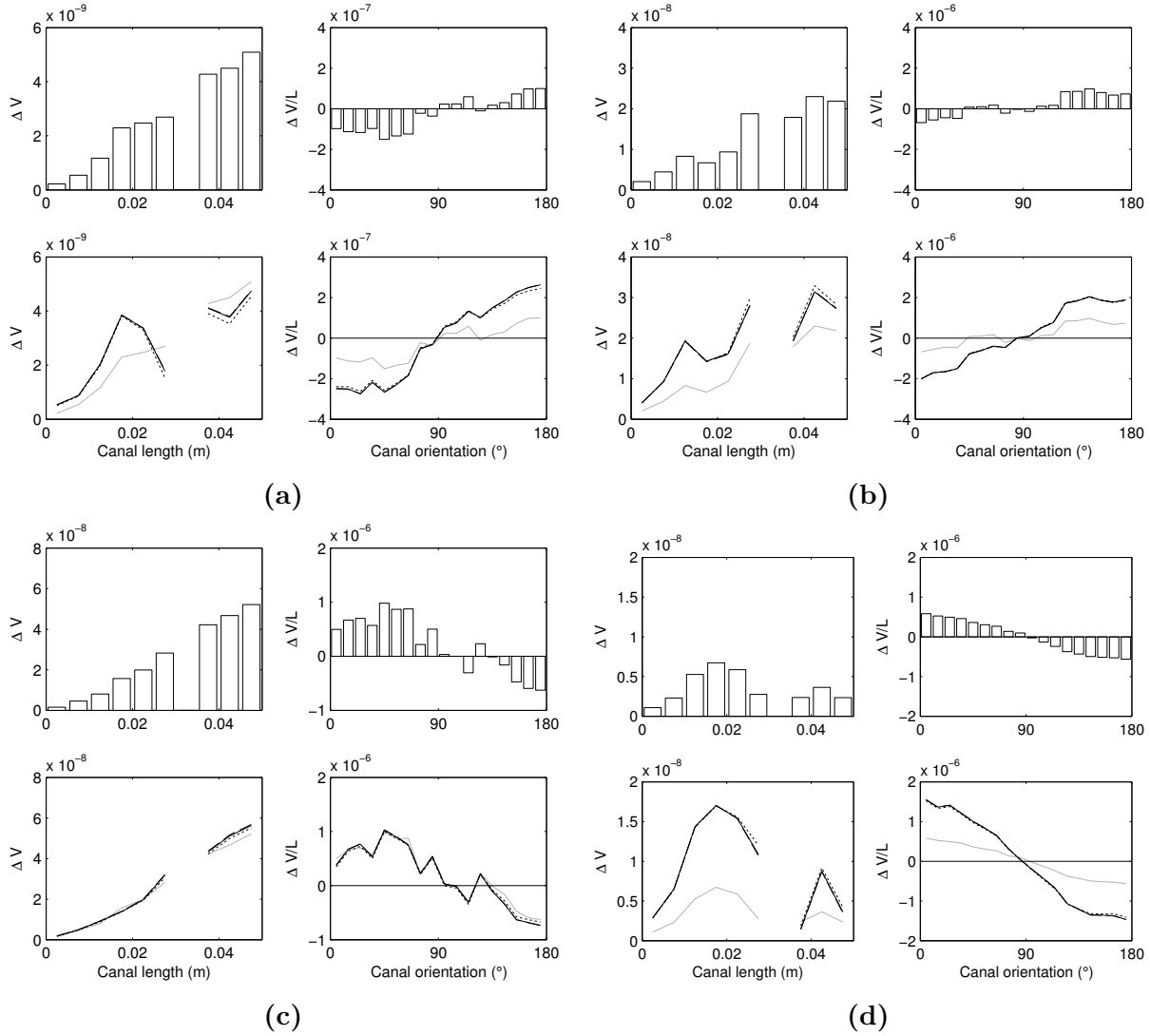

Figure 3.22: Canal voltage drops in the vertical plane from a 2D dipole, with differing dogfish geometries. Figures show the voltage drops from the unchanged trajectory in fig. 3.8b. Figure 3.22a shows the drops from the location (a). Figure 3.22b shows the drops from location (d). Figure 3.22c shows the drops from the location (e). Figure 3.22d shows the drops from location (f). The upper two figures in each subplot show the relationship between voltage drop and canal length (left) and the relationship between normalized voltage drop and canal orientation (right) under the model: all tissues have the conductivity of seawater. The lower two figures in each subplot show the same histograms, with differing dogfish geometries. Grey: No body/all $\sigma_{water} = 4.5$; Black solid: 2D shark projection; Black dashed: fins removed; Black dotted: fins removed and head replaced with ellipse.

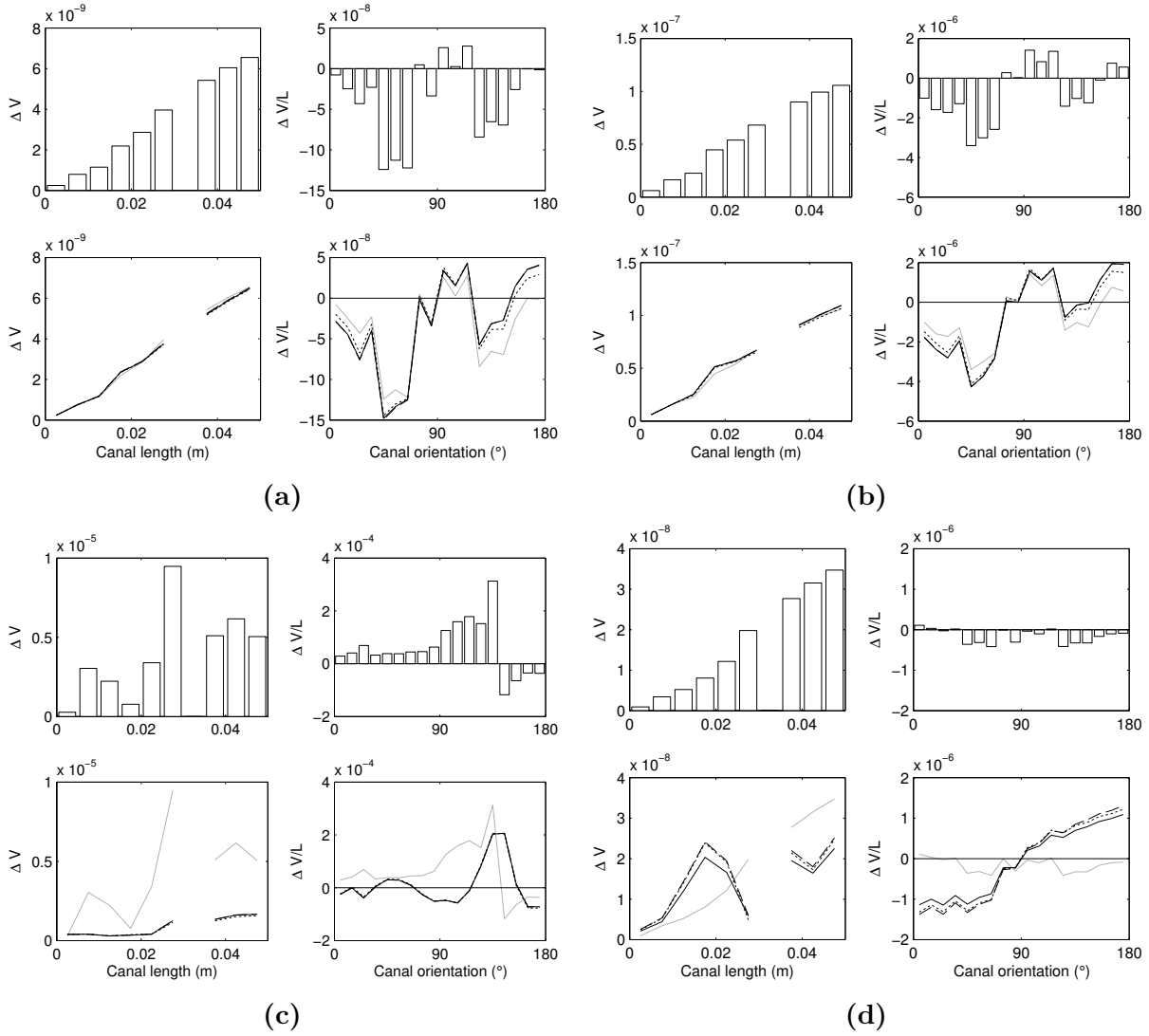

Figure 3.23: Canal voltage drops in the vertical plane from a 2D dipole, with differing dogfish geometries. Figures show the voltage drops from the fieldline trajectory in fig. 3.8b. Figure 3.23a shows the drops from the location (a). Figure 3.23b shows the drops from location (d). Figure 3.23c shows the drops when dipole is ~5cm the dogfish mouth. Figure 3.23d shows the drops when the dogfish has passed by the dipole and the body tissues of the shark no longer obscure the source. The upper two figures in each subplot show the relationship between voltage drop and canal length (left) and the relationship between normalized voltage drop and canal orientation (right) under the model: all tissues have the conductivity of seawater. The lower two figures in each subplot show the same histograms, with differing dogfish geometries. Grey: No body/all $\sigma_{water} = 4.5$; Black solid: 2D shark projection; Black dashed: fins removed; Black dotted: fins removed and head replaced with ellipse

3.3.4 Simplified 3D shark geometry

Our 2D simulations revealed that the effect of adding electrical properties to tissues was of greater magnitude than the differences from geometrical simplifications. Additionally, some of the differences in voltage drops between both electrical properties of tissues and shark geometries can be attributed to the reduction in dimensions (e.g. pores not in contact with animal surface, being unable to examine results when shark geometry overlaps dipole etc). Brain tissue made a small difference in 2D, but mainly only in long canals which came into close proximity of the brain. Long canals often run near parallel to the skin, hence the proximity to the brain was mainly an artefact of flattening 3D geometry into 2D. Therefore, for ease of geometry manipulation and meshing we exclude this from our 3D model and focus solely on body tissues and skin. We now proceed with a simplified shark geometry in three dimensions. In this case the shark has an ellipsoid and cone like geometry (Figure 3.3), but all pore coordinates were mapped to the ellipsoid surface and all simulations were conducted so that the shark geometry did not overlap the dipole (e.g. mouth was just above dipole in both horizontal and vertical approach trajectories).

3.3.4.1 Uniform electric field stimulus

We compare the canal voltage drops in our simplified 3D shark where no tissue properties were specified (Figures 3.24a to 3.24c) with the voltage drops where we have specified body conductivity and skin surface impedance (Figures 3.24d to 3.24f). When the dogfish's body axis was aligned with the electric field (Figures 3.24b and 3.24e) adding tissue properties has little effect in the magnitude of the largest voltage drops in the long buccal canals. However, some shorter canals now experience drops of greater magnitude. This effect appears to be greatest in canals that both aligned with the direction of the electric field and are perpendicular to the skin surface (Figures 3.24d to 3.24f). When the dogfish body axis is rotated relative to the field direction (Figures 3.24a, 3.24c, 3.24d and 3.24f), shark tissues appear to slightly increase the magnitude of voltage drops across much of the ampullary array. Again, long buccal canals experience the largest drops, but the shorter buccal and SO canals aligned with the field now receive greater stimulus (Figures 3.24d and 3.24f).

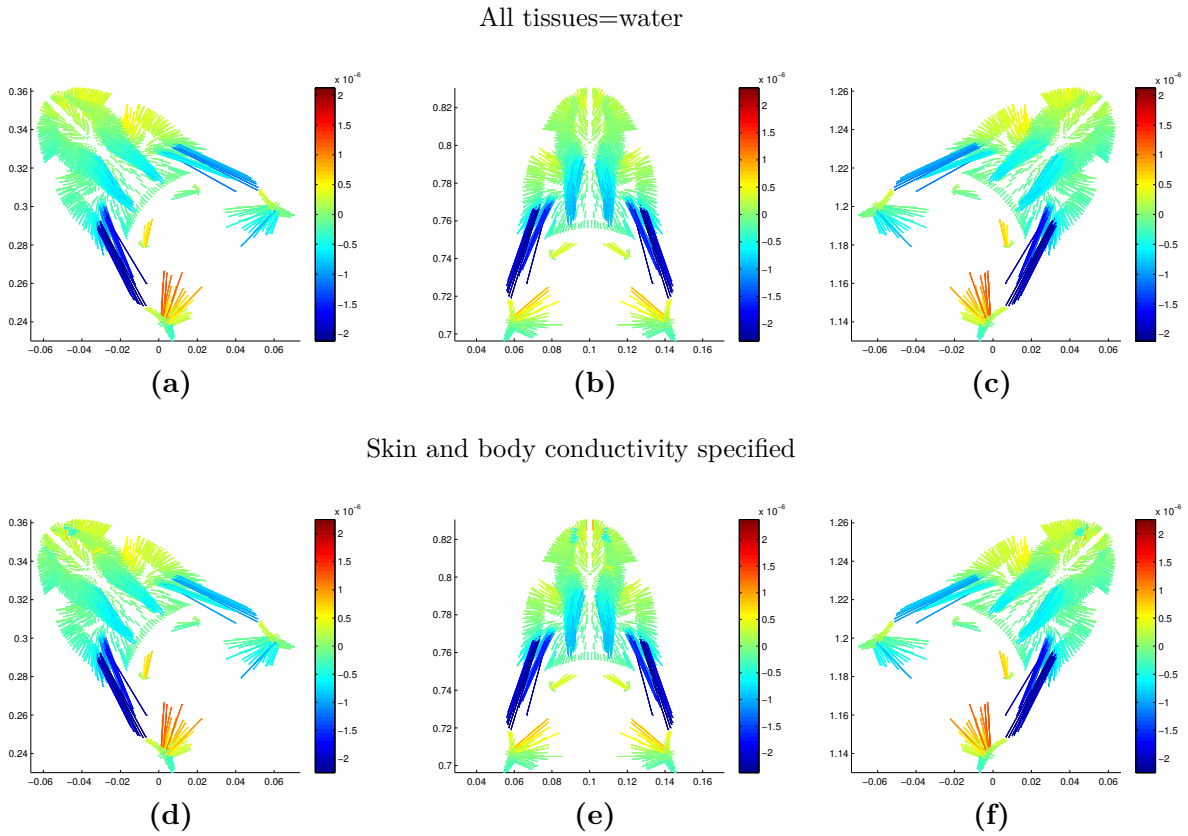

Figure 3.24: Canal voltage drops at each of three locations along a sinusoidal trajectory in a horizontal plane through the constant uniform electric field of magnitude $500\,\mathrm{nV\,cm^{-1}}$ (see Figure 3.12). Figures 3.24a to 3.24c show the numerical solutions for all tissues = water conductivity $\sigma = 4.5\,\mathrm{S\,m^{-1}}$. Figures 3.24d to 3.24f show the numerical solutions when body tissues are specified as $\sigma_{body} = 0.5\,\mathrm{S\,m^{-1}}$, skin surface impedance = $0.037\,\Omega\mathrm{m}^2$. Note the scale for each colourmap to differs between subfigures, as magnitudes of voltage drops differ greatly between locations.

3.3.4.2 Dipole stimulus: Horizontal plane trajectories

At large distances the local dipole fields appear spatially uniform, thus the dipole approaches showed some similarities to the uniform electric field simulations above. At the closest phase (Figures 3.25e and 3.25k) the results look near symmetrical similar to Figures 3.24b and 3.24e suggesting the dogfish body is nearly parallel to the electric field. Whereas in the uniform case there was little difference in the magnitudes of the effective stimulus, in this case there was a slight reduction in the mid to long canals when tissues were included. Likewise for most phases in the unchanged trajectory the voltage drops the magnitudes of peak voltage drops for tissue included simulations (Figures 3.25g, 3.25h, 3.25k and 3.25l) are either similar or slightly reduced relative to the default model (Figures 3.25a, 3.25b, 3.25e and 3.25f). Whereas the inclusion of tissues increases the magnitude of peak voltage drops in (Figures 3.25i and 3.25j) relative to the default model (Figures 3.25c and 3.25d). In particular, some of the shorter buccal and SO canals in the snout experience larger voltage drops, as do many of the longer hyoid (Figure 3.25i) and buccal canals (Figure 3.25j).

When the dogfish is approaching the dipole, the direct and fieldline trajectories are similar to when the dogfish's body axis was aligned with the uniform electric field (Figures 3.24b and 3.24e). The largest voltage drops are still in the long buccal canals, adding tissues (Figures 3.26g to 3.26j) slightly increases the magnitude of these drops (Figures 3.26a to 3.26d). However, now even at a distance some of the shorter buccal and SO canals in the snout experience much larger voltage drops, which increase until they are approximately the same magnitude as those in the much longer canals (Figure 3.26j). As predicted, the local dipole fields do not penetrate the skin well, resulting in voltage drops being smaller in magnitude (Figure 3.26k) than the default case (Figure 3.26e) when the dogfish is in close proximity to the dipole. Once the dogfish has passed over the dipole, the long buccal canals resume being the group exhibiting the strongest stimulation (Figures 3.26f and 3.26l). However, now instead of the shorter snout canals experiencing larger magnitude voltage drops, it is now the hyoid canals at the rear of the head (Figure 3.26l).

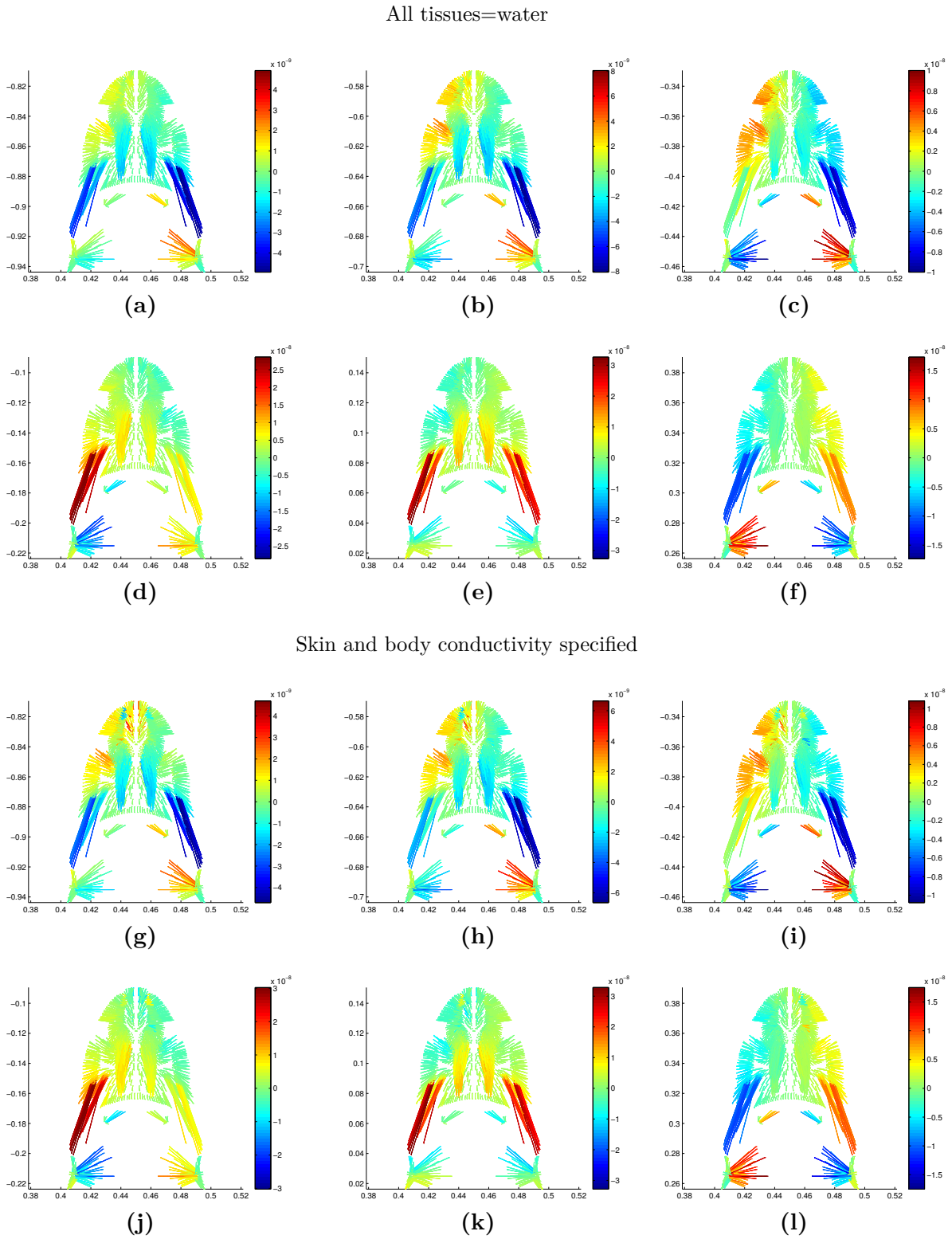

Figure 3.25: Canal voltage drops at each of six locations along an unchanged approach trajectory in the dipole horizontal plane (similar to the 2D trajectories in Figure 3.4, z=0). Figures 3.25a to 3.25f show the numerical solutions for dipole strength $P = 3.6 \times 10^{-6}\,\mathrm{A\,m}$, all tissues = water conductivity $\sigma = 4.5\,\mathrm{S\,m^{-1}}$. Figures 3.25g to 3.25l show the numerical solutions when body tissues are specified as $\sigma_{body} = 0.5\,\mathrm{S\,m^{-1}}$, skin surface impedance = $0.037\,\Omega\mathrm{m}^2$. Axes show distance from the dipole origin (m). Note the scale for each colourmap to differs between subfigures, as magnitudes of voltage drops differ greatly between locations.

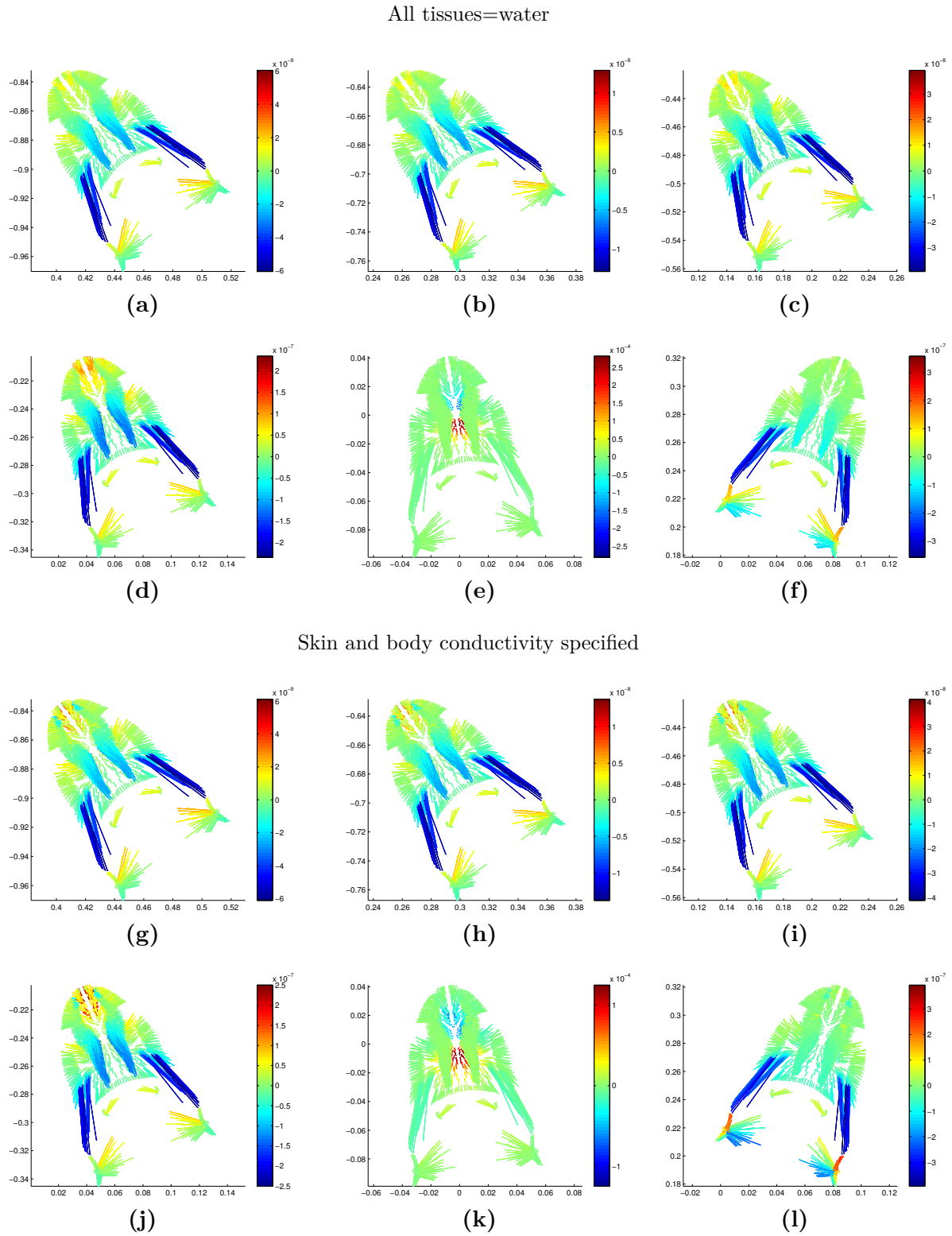

Figure 3.26: Canal voltage drops at each of six locations along an fieldline approach trajectory in the dipole horizontal plane (similar to the 2D trajectories in Figure 3.4, z=0). Figures 3.26a to 3.26f show the numerical solutions for dipole strength $P = 3.6 \times 10^{-6}\,\mathrm{A\,m}$, all tissues = water conductivity $\sigma = 4.5\,\mathrm{S\,m^{-1}}$. Figures 3.26g to 3.26l show the numerical solutions when body tissues are specified as $\sigma_{body} = 0.5\,\mathrm{S\,m^{-1}}$, skin surface impedance $= 0.037\,\Omega\mathrm{m}^2$. Axes show distance from the dipole origin (m). Note the scale for each colourmap to differs between subfigures, as magnitudes of voltage drops differ greatly between locations.

3.3.4.3 Dipole stimulus: Vertical plane trajectories

Similar to section 3.3.4.2, in the vertical plane the inclusion of tissues resulted in magnitudes of peak voltage drops (Figures 3.27g, 3.27h, 3.27k and 3.27l) that are reasonably similar to the default model (Figures 3.27a, 3.27b, 3.27e and 3.27f) for most snapshots of the unchanged trajectory. Whereas the inclusion of tissues increases the magnitude of peak voltage drops in (Figures 3.27i and 3.27j) relative to the default model (Figures 3.27c and 3.27d). The spatial distribution of voltage drops remained similar to Figures 3.27a to 3.27f. Again, several of the shorter buccal and SO canals now experience drops of greater magnitude.

The vertical direct and fieldline approach trajectories showed similarities to the horizontal plane. Again the largest voltage drops are mainly in the long buccal canals, adding tissues (Figures 3.28g to 3.28j) has little effect on the magnitude of these drops (Figures 3.28a to 3.28d). Likewise, at a distance the shorter buccal canals in the snout experience much larger voltage drops, which increase until some are of larger magnitude than those in the much longer canals (Figure 3.28j). Unlike the horizontal plane, when the dogfish is in close proximity to the dipole the voltage drops are of similar magnitude when differing electrical properties are included (Figure 3.28e versus Figure 3.28k). As with the horizontal plane once the dogfish has passed over the dipole, the long buccal canals resume being the group exhibiting the strongest stimulation (Figures 3.28f and 3.28l), along with larger magnitude voltage drops in the hyoid canals at the rear of the head (Figure 3.28l).

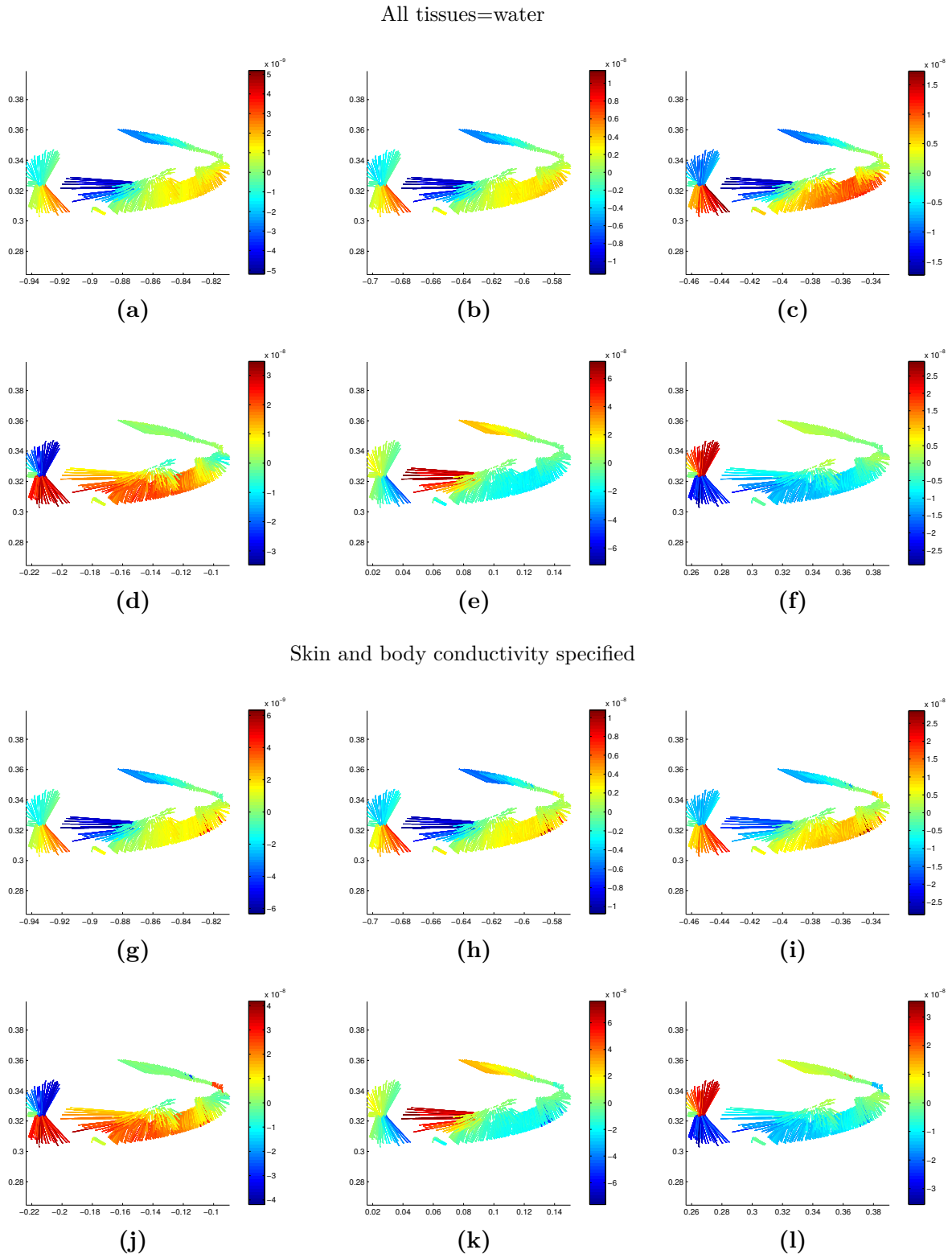

Figure 3.27: Canal voltage drops at each of six locations along an unchanged approach trajectory in the dipole vertical plane (similar to the 2D trajectories in Figure 3.8, x=0). Figures 3.27a to 3.27f show the numerical solutions for dipole strength $P = 3.6 \times 10^{-6}\,\mathrm{A\,m}$, all tissues = water conductivity $\sigma = 4.5\,\mathrm{S\,m^{-1}}$. Figures 3.27g to 3.27l show the numerical solutions when body tissues are specified as $\sigma_{body} = 0.5\,\mathrm{S\,m^{-1}}$, skin surface impedance = $0.037\,\Omega\mathrm{m}^2$. Axes show distance from the dipole origin (m). Note the scale for each colourmap to differs between subfigures, as magnitudes of voltage drops differ greatly between locations.

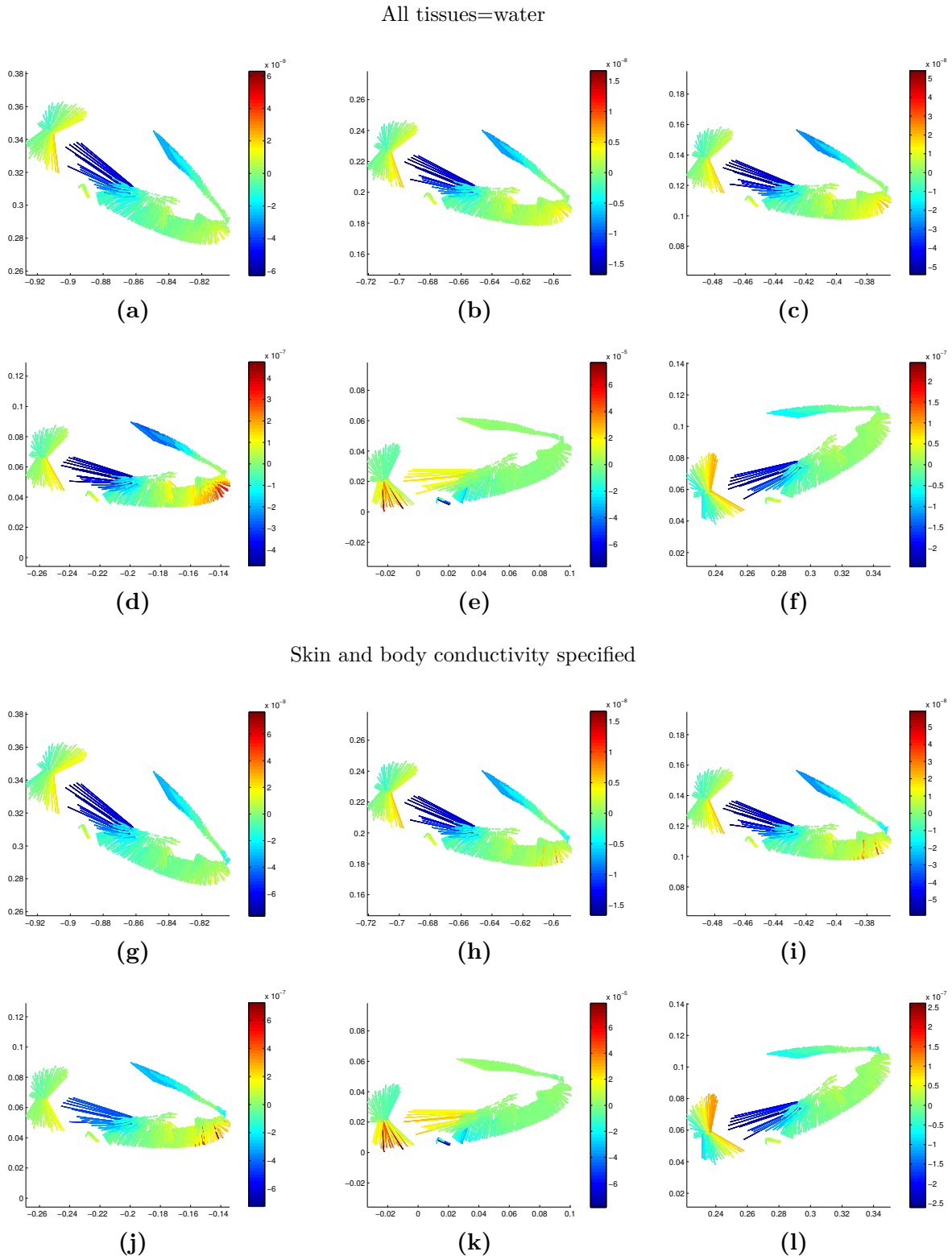

Figure 3.28: Canal voltage drops at each of six locations along an fieldline approach trajectory in the dipole vertical plane (similar to the 2D trajectories in Figure 3.8, x=0). Figures 3.28a to 3.28f show the numerical solutions for dipole strength $P = 3.6 \times 10^{-6}\,\mathrm{A\,m}$, all tissues = water conductivity $\sigma = 4.5\,\mathrm{S\,m^{-1}}$. Figures 3.28g to 3.28l show the numerical solutions when body tissues are specified as $\sigma_{body} = 0.5\,\mathrm{S\,m^{-1}}$, skin surface impedance = $0.037\,\Omega\mathrm{m}^2$. Axes show distance from the dipole origin (m). Note the scale for each colourmap to differs between subfigures, as magnitudes of voltage drops differ greatly between locations.

3.4 Discussion

In this chapter, we have constructed a series of finite element models in order to study the spatial and temporal dynamics of electrosensory signal development in the electrosensory periphery of the spiny dogfish (*S. acanthias*). Although the models rely on simplifying assumptions, the most notable being reduction of dimensions and body geometry, the methods applied here provide the first steps in examining how pre-receptor mechanisms and interactions shape the effective stimulus received by elasmobranch electrosensory systems. Tissue and skin conductivities have long been hypothesised to contribute to the electrical stimulus individual ampullary receptors measure [Kalmijn, 1974].

3.4.1 Passive electrosensory signal modelling using FEM

Despite our two dimensional simulations considering a smaller subset of ampullae, only one angular orientation at a time, reduced length of canals that were not well aligned with the 2D plane and apparent slight differences in the position and orientation of the shark in some simulations, our baseline model (all σ_{water}) was able to reproduce many of the overall generalizations of Berquist [2003] in examining the role of different ampullary groups under different stimuli and trajectories. For the dipole stimulus at a distance, the long horizontally aligned canals appear responsible for initial detection of prey-like stimuli. As the dogfish approaches and passes over the dipole, shorter more vertically aligned canals around the snout and mouth develop the strongest voltage drops. For the uniform stimulus, it is again the long buccal canals that develop the largest voltage drops, due to their alignment with the dogfish body axis. This remains the case even as the shark rotates, as shorter canals even when well aligned with the electric field do not span much difference in voltage amplitude.

The effects of internal tissues (body and brain) and skin conductivity were studied in these 2D simulations. Additionally, we compared the morphologically accurate shark geometry with two geometrical simplifications (fins removed, fins removed and head replaced with ellipsoid), with the aim of building a simplified version of a 3D shark. The 2D geometries were easy to manipulate and each model was simple to implement, using the finite element software COMSOL Multiphysics 4.4 Livelink with MATLAB. For each configuration, the 2D FEM model solved in approximately 1 minute or less (on a Windows 7 Professional 64-bit Intel i7 processor @ 3.20GHz with 16.0 GB RAM).

Additional shortcomings relating to the two dimensional model are when the electrical properties of body tissues have been specified, there are phases of the prey approach

trajectory where the dipole ends up being in the dogfish's internal tissues, rather than in the external environment. We therefore had to limit our analysis to phases of the trajectories where no part of the body intersected with the dipole location. Furthermore, due to the geometry of the two dimensional simulations many pores were located in the shark tissue, rather than all pores providing direct contact with external seawater.

To address these problems we developed a simplified three dimensional model where the shark's body was represented by an ellipsoid and cone geometry. Pore coordinates were mapped to the surface of the estimated minimum volume ellipsoid containing all pore and ampulla coordinates, while ampulla proper coordinates were retained. This resulted in slight modifications to the length and orientation of canals, but ensured that all pores were on the surface, while all ampulla proper were on the interior of the shark. The 3D geometries were more difficult to manipulate and mesh, which resulted in the decision to no longer treating the ampullae as edges in the geometry, but rather interpolating the electric potential at the coordinates of the pore and ampulla in post-processing. Due to this simplification, for the dipole stimulus the 3D FEM model actually solved faster, in approximately 15 seconds or less for each configuration. Whereas due to the large area of mesh required for the external environment, the uniform stimulus was slower in 3D, with each configuration solved in approximately 1 minute 45 seconds.

3.4.2 Large scale uniform fields

Marine elasmobranchs have relatively low skin resistance compared with tissue resistances, therefore Murray [1967] hypothesised that the potential gradient in body tissues will be similar to the uniform external gradient in seawater. He further predicted that the effective stimulus in this case is the gradient through the animals tissues multiplied by the length of the canal aligned with the electric field [Murray, 1967]. This theory was supported by measurements on a marine ray *Platyrhinoidis triseriata*, potential gradients inside the animal significant compared with the external uniform electric field parallel to the body axis [Szabo *et al.*, 1972]. However, these measurements did show some sub-epidermal decrease relative to the voltage gradients exterior to the animal [Kalmijn, 1974]. Kalmijn [1974] presented a qualitative diagram based on these measurements showing the equipotential surfaces bending towards the fish (since animals are more resistive than seawater) and voltage gradients in the body tissues being not much weaker than the external stimulus. He concluded in a large scale uniform field both the voltage drop across the skin and the gradients in the tissues contribute to the effective stimulus [Kalmijn, 1974].

Pickard [1988] built on the qualitative concepts presented above and developed an analytical model of a spherical shark in a uniform electric field. Due to the predominance of long canals, it was concluded that the appropriate expression for electroreceptors is the skin to deep-interior potential, which under the assumptions specified, was independent of skin conductance. The outcome of this model was confirmation that sensory cells in long canals will experience a large fraction of the stimulus that would have over the length of the fish, in the absence of the fish, whereas short canals will experience smaller stimuli [Pickard, 1988].

We attempted to quantify these effects over the entire electrosensory array. Overall, our series of 2D and 3D models suggest the following about how electrical properties of tissues shape the stimulus in a uniform electric field:

- When the body is parallel with the electric field, the inclusion of skin and tissues has little effect on the stimulus received by shorter canals. Whereas, in longer canals the inclusion of body tissues increases the effective stimulus, but this is partially cancelled out by the inclusion of skin.

- When the body is rotated relative to the electric field, the inclusion of body tissues increases the effective stimulus across all length canals, but again this is partially cancelled out by the inclusion of skin.

- Tissues shape the effective stimulus to a greater extent when the body axis is rotated in the electric field, but voltage drops have greater absolute magnitudes when the body axis is aligned with the field direction.

- In absolute terms it is the longest canals aligned with the electric field which experience the greatest advantage by spanning body tissues. However in relative terms when examining the ratio of the canal voltage drops in seawater to the drops when tissues are included, changes of the greatest magnitudes appear in the canals running near perpendicular to the electric field. This is because under the default condition canals would have received near zero voltage drops, whereas due to the distortion caused by the body the electric field has been modified so it is no longer zero.

- However, when we examine the ratio of the canal voltage drops in seawater to the drops when tissues and skin are both included, it is more difficult to interpret trends, the drops now result from an interaction between both the distorting effects of the tissue and skin.

3.4.3 Localized dipole fields

Conversely, Kalmijn [1974] found that when a local dipole field was applied to the same marine rays, *P. triseriata*, the electric fields did not penetrate the body tissues. Thus suggesting for small localized fields, the effective stimulus in both long and short canals is almost entirely the voltage drop across the skin [Kalmijn, 1974].

Gusev *et al.* [1986, 1985] investigated these qualitative concepts via a model of a disk shaped ray in a dipole electric field. This model specified the conductivity of water and skin, under the simplifying assumption that the conductivity of body tissues is approximately equal to that of water, in order to derive a numeric solution. The results of this model suggested that if the dipole axis was aligned with the plane of the disk, then skin caused negligible distortions to the effective stimulus. Whereas when the dipole was perpendicular to the disk plane, the hypothesis of [Kalmijn, 1974] was supported, with voltage gradients inside body tissues being negligibly weak compared to those in surrounding seawater [Gusev *et al.*, 1986]. These conclusions were largely independent of specific conductivities, as long as the conductivity of water was greater than the conductivity of skin. It was concluded that the body acts as an accessory structure, which reduces the effective stimulus of dipoles not belonging to the animals body plane [Gusev *et al.*, 1986].

We attempted to quantify these effects over the entire electrosensory array, with more realistic geometries, under different dipole approach trajectories. Overall, our series of 2D and 3D models suggest the following about how electrical properties of tissues shape the stimulus in a dipole electric field:

- At a distance from the dipole the fields are locally uniform in nature, so results are similar to the uniform electric field simulations.

- As predicted by [Kalmijn, 1974] when the dipole is nearby there is a large voltage drop relative to the dipole stimulus in seawater caused by the resistance of skin. Thus shorter canals are now better suited to sensing the potential distribution directly over skin surface.

- Whereas the modelling of Gusev *et al.* [1986] concluded it sufficient to specify the conductivity of water and skin (as long as $\sigma_{water} > \sigma_{skin}$). In our models, where skin was a surface impedance boundary condition which specified the resistance, we found that the inclusion of tissues with a lower conductivity than the surrounding water impacted results, significantly increasing the voltage drops experienced relative to the skin only simulations.

- Gusev *et al.* [1986] suggested the body acts as an accessory structure, which results in negligible voltage drops for dipoles not belonging to the animals body plane. Results from our unchanged trajectories in the vertical and horizontal planes suggest that this may not be the case. During the initial phases of the trajectory there was some reduction in the stimulus relative to a dipole in seawater. However, despite the shark never getting closer than 0.45m in the horizontal plane (or 0.3m for vertical approach) the voltage drops in the mid to late stages of the trajectory were of the same magnitude or slightly greater than those in seawater alone.

3.4.4 How the animal impacts the stimulus it receives

Here we focussed on the voltage drops over entire electrosensory array and how the body scale pre-receptor mechanisms impact the stimulus received by electrosensors. The morphological and electrical properties of the canal itself and the receptor cells therein also likely effect the stimulus received by individual ampullae. The most comprehensive analysis of electrical properties and morphological structure of the ampullae of Lorenzini was conducted by Waltman [1966] on species of skate from the Rajidae family. He noted that the canal walls had uniquely high resistance, much higher than elasmobranch skin, and two to three orders of magnitude higher than any previously reported values for epithelial resistance. This in combination with the relatively low resistance of the gel filling the canal suggests that, for dc and low frequency signals, the ampullae acts as an ideal submarine cable [Waltman, 1966]. Therefore, the majority of the effective stimulus is signalled by the voltage drop across the sensory epithelium. Additionally, each receptor cell bears a cilium which interfaces with the lumen of the ampulla proper [Waltman, 1966]. While a role in electroreception has yet to be demonstrated, it has been retained from ancestral hair cells in spite of being mechanically isolated at the bottom of the canal. Analogous to a lightning rod, the cilium should draw electrical isopotential lines towards its tip, increasing the voltage gradient and amplifying currents passing through the receptor cell membrane at that point. The specific location of transduction channels in electroreceptor cells is unknown, but transduction channels in mechanosensory hair cells are located at the tips of cilia [Hudspeth, 1982]. The fact that cilia have been retained in electroreceptors, immobilised in electrically conductive gel, suggests that voltage-sensitive transduction channels are at the tips of the cilia in electroreceptors.

Our analysis consisted of a series of snapshots of shark behaviour rotating in a uniform electric field and approach trajectories in the horizontal and vertical plane of a dipole. However shark behaviour is much more complex than our simplified analysis. Kim [2007]

demonstrated that head swaying movements of elasmobranchs would be required to estimate electric field direction in order to follow the fieldline approach trajectory [Kalmijn, 1997]. It would be of interest to model the effect of body parts under more realistic behaviour, including head swaying and tail bending, or match numerical models to video recordings of shark behaviour. It has been suggested electroreceptors are limited to the head region of sharks to avoid the regions of the body which undergo greater bending movements during swimming [Murray, 1974]. However, some motion is necessary for the detection of electric fields that are dc in origin. Dipole approaches depend on both linear and angular movements, and uniform electric fields (similarly the electric field induced by swimming in the earth's magnetic field) require angular movements [Peters *et al.*, 2007]. Conversely, the animal's own movements also act as one of the main sources of noise in the electrosensory system.

In particular, ventilatory movements have been shown to modulate firing rates of electrosensory afferents [Montgomery, 1984a; New, 1990]. Animals are faced with the problem of distinguishing electrosensory information about their external environment (exafference) from electrosensory information that results from their own state/motor activity (reafference). Ventilatory noise is largely removed in the secondary ascending efferent neurons (AENs), suggesting sensory processing suppresses reafference [New, 1990]. Kalmijn [1974] suggested that one advantage of the long ampullary canals arranged in groups is it allows for the sampling of a large area of skin at the pores, while maintaining the ampullae proper nearly isopotential. Thus, providing a common mode signal which may be used to suppress various form of noise via common mode rejection. Indeed the suppression of common mode signals has been well documented in the elasmobranch electrosensory system [Bodznick *et al.*, 1992, 1999; Conley & Bodznick, 1994; Hjelmstad *et al.*, 1996; Montgomery & Bodznick, 1993]. How hindbrain circuitry, specifically the dorsal octavolateralis nucleus (DON), achieves this initial processing is an ongoing area of research, with several models studying the mechanisms behind this phenomenon [Bratby *et al.*, 2014; Montgomery & Bodznick, 1994; Nelson & Paulin, 1995].

The adaptive filter model of reafference suppression supposes that self movement (or self state) affects the measured field by perturbing the self field [Bratby *et al.*, 2014; Montgomery & Bodznick, 1994; Nelson & Paulin, 1995]. That is true. However, this chapter has demonstrated that the self state also affects the external field. The dynamic state-to-sensory transformation is a non-linear distortion of the field, not an additive difference. Specifically, the adaptive filter considers:

$$\vec{E} = \vec{E}(self) + \vec{E}(ext) \tag{3.2}$$

but the reality is:

$$\vec{E} = \vec{E}(self, ext) \tag{3.3}$$

which is a complex interaction that can only be computed numerically.

For any given self and external stimuli, it is possible to predict the electrosensory consequences of the animal's own behaviour, $\vec{E}(self, ext)$, and subtract that expectation from what animal actually sees. But that only works for the particular scenario - it does not generalize (it is unlikely that the animal's brain has the time or resources to consider all possible realities). Under experimental conditions, where an animal is repeatedly presented $\vec{E}(self, ext)$, with identical self and external stimuli every time, subtracting away the predictable component of that signal may work.

However, the fact that animals' are able to subtract away the predictable component from the raw sensory input, $\vec{E} = \vec{E}(self) + \vec{E}(ext)$, to provide an estimate of the sensory signal generated by objects in the external world, $\vec{E}(ext)$, does not necessarily imply adaptive subtraction. The animal finds a solution equivalent to subtracting its own field, $\vec{E}(self)$, because under experimental conditions this is the problem that it is faced with. In the real world the animal faces a non-linear problem which cannot be solved by prediction and subtraction. It can only (or best) be solved by Bayesian inference. The remainder of the thesis is about exploring if and how elasmobranchs might perform Bayesian inference.

Part II

Electrosensory perception as causal inference

Chapter 4

Spontaneous activity of electrosensory afferents: Analyses of interspike interval distributions

4.1 Introduction

Elasmobranchs use their ampullary electroreceptors to detect and locate weak electric fields associated with prey organisms [Kalmijn, 1971]. Stimuli in the order of nanovolts are sufficient to elicit a behavioural response [Kalmijn, 1982; Peters *et al.*, 2007]. In the frequency range of the elasmobranchs' electrosensory system, this signal across the sensory epithelium is comparable to thermal noise [Kalmijn, 1984, 2003]. Bioelectric fields allow sharks to "see" prey even though it may be buried under sand [Kalmijn, 1971] and the weak neuronal signal is buried in thermal noise [Kalmijn, 1984, 2003]. While the sensory signal may be all but invisible in the noise, stochastic afferent spike trains carry information to the brain about state variables of the prey, including for example its location relative to the predator. Sharks' ability to precisely locate the prey and correctly orient its jaws suggests that sharks' brains are able to infer these parameters. How they do this remains to be established, but even in spiking neuron models of elasmobranch electroreception the statistical structure of spike trains has been ignored [Adair *et al.*, 1998; Berquist, 2003; Bratby *et al.*, 2014; Camperi *et al.*, 2007; Montgomery & Bodznick, 1999, 1994; Nelson & Paulin, 1995; Pickard, 1988]. Sharks would do this at their peril. Natural selection favours more effective predators and more evasive prey. The statistical structure of spike trains contains valuable information about the processes generating spikes (e.g. distance to prey). Structure is generally not fully characterised by the first two moments

of the distribution [Kuhn *et al.*, 2003]. Due to the uncertainty in sensory information, the optimal strategy involves computing the conditional probability distribution of world states given what has been observed - the Bayesian *posterior* [Knill & Pouget, 2004]. A Bayes' optimal agent maintains a representation of this distribution, allowing for the efficient integration of information over space and time and multisensory cue combination [Knill & Pouget, 2004].

It is not clear that sharks are Bayesians, but theoretical arguments suggest that many of the computations performed by nervous systems are instances of probabilistic inference [Pouget *et al.*, 2013; Sengupta *et al.*, 2013]. As Levy & Morel [2006] noted, other things being equal Bayesian inference is an optimization that nervous systems should have discovered. Behavioural and psychophysical evidence from a number of species, including humans, suggest that is indeed the case [De Ridder *et al.*, 2014; Friston *et al.*, 2012; Kording, 2014; Lochmann & Deneve, 2011; Loeb & Fishel, 2014; Orban de Xivry *et al.*, 2013; Pouget *et al.*, 2013]. But other things are not necessarily equal. Bayesian methods can be relatively difficult to implement, slow, computationally expensive and at least in some situations can be mimicked by simple rules that make no reference to probability distributions [Domurat *et al.*, 2015]. Energetic costs appear to have shaped the evolution of nervous systems and this may favour sub-optimal mechanisms [Laughlin *et al.*, 1998]. Perhaps it is not even possible to implement Bayesian methods using neurons. Recent research suggest brains are poorly adapted to calculating probabilities, but rather act as a Bayesian sampler [Sanborn & Chater, 2016]. Infinite samples are required for a Bayesian sampler to conform to the laws of probability and finite samples can systematically introduce probabilistic errors [Sanborn & Chater, 2016]. Thus when big fish meets little fish, a simple mechanism such as a linear adaptive array filter [Bratby *et al.*, 2014; Montgomery & Bodznick, 1999, 1994; Nelson & Paulin, 1995] might isolate signals emanating from the prey and allow the predator to out-compete Bayesians in the real world.

The elasmobranch electric sense has special characteristics that make it particularly suitable for examining if and how brains implement Bayesian computation. Many elasmobranchs execute well-aimed strikes in response to both real and simulated prey electric fields [Bedore *et al.*, 2014; Haine *et al.*, 2001; Jordan *et al.*, 2009; Kajiura, 2003; Kajiura & Fitzgerald, 2009; Kajiura & Holland, 2002; Kalmijn, 1971; McGowan & Kajiura, 2009]. While the bioelectric fields surrounding animals in aquatic environments can be considered the sum of multipole sources, at the distance at which sharks initiate their strikes the dipole term is sufficient [Kalmijn, 1988]. This dipole field varies slowly, propagates instantaneously and can be fully characterised using only a handful of parameters. It is therefore relatively easy to analyse the stimulus intensity received by each ampullary

organ expressed as a function of parameters of the signal source. Since the evolutionary origin of vertebrate nervous systems more than half a billion years ago [Monk, 2014; Monk & Paulin, 2014], small electric dipole sources in the ocean would have reliably indicated the live animals. It is only in more modern times that sharks have encountered potentially confusing anthropogenic electric field sources during foraging. Thus the question of *what* causes such fields is literally a no-brainer for a shark: it's food. A shark's brain only has to figure out where it is. Indeed sharks appear either unable to discriminate between, or show no preference for similar magnitude, natural and artificial D.C. electric fields [Kimber *et al.*, 2011]. Whereas hair cells in the vestibular, lateral line and auditory systems all receive feedback from the brain, electroreceptors lack any sign of such efferents [Bodznick, 1989]. Given the lack of efferents, measurements from sense organs are not contaminated by existing brain states, or *prior* beliefs in a Bayesian framework. This simplifies models of how brain states may be updated by measurements.

To a Bayesian, making an inference about the state of the world (here, prey dipole parameters) requires a *likelihood* function of how measurements are generated. In electroreception, a sensory spike train is a sample form a stochastic point process parametrised by prey state variables, which include its dipole strength, location, orientation relative to the predator. The *posterior* density summarizes everything we know about the relevant state variables after the measurement is taken into account. This is computed by continuously modifying a *prior* distribution, as the predator approaches the prey and new measurements become available [Dall *et al.*, 2005; McNamara & Houston, 1980]. Accurate, realistic generative models of electrosensory afferent firing patterns a key pre-requisite for discovering if an how elasmobranchs' brains compute Bayesian posterior probability distributions from electrosensory neuron data. The aim of chapter 4 is to develop such models.

4.2 Methods

4.2.1 Animals and electrophysiological recordings

Spike train recordings were obtained from Professor David Bodznick, Wesleyan University. He has provided the following brief description of the experimental protocol used.

Adult little skates, *L. erinacea*, are captured by otter trawl in Vineyard Sound, held in chilled seawater (ca. 12 °C) and maintained on a diet of squid and fish until used in experiments.

For electrophysiological studies, an animal is anesthetized by immersion in Benzocaine

(Ethyl-p-aminobenzoate, 0.05% in seawater) and then placed on ice during surgery to open the cranial roof exposing the anterior lateral line nerve near its entry into the medulla. While still anesthetized the skate is decerebrated by transecting the caudal forebrain, injected with a muscle relaxant (Pancuronium bromide, ca. $0.5\,\mathrm{mg\,kg^{-1}}$, IV), and positioned in an experimental aquarium of fresh, aerated seawater at 12 °C. The fish's head is held with the cranial opening just above the water surface using a Plexiglas head holder fitted with mouth tubes which supply a steady flow of cold, aerated seawater across the skate's gills. The decerebrate but unanesthetized skates remain healthy and responsive to sensory stimuli for several days under these conditions. All procedures for the care and use of the skates were approved by the Animal Care and Use Committees of both the Marine Biological Laboratory, Woods Hole and Wesleyan University.

Extracellular recordings of spontaneous activity from primary electrosensory afferents in the anterior lateral line nerve are made with sharp glass microelectrodes (20 to 30 MΩ; 4 mol NaCl), conventional electronics, and Cambridge Electronic Design computer interface and Spike2 software. Spike train data, with a 0.2 ms sampling resolution, was exported to MATLAB for analysis.

4.2.2 Analysis of spike trains

Motivated by the automatic spike train analysis described in Pouzat & Chaffiol [2009a], we created MATLAB code to perform basic data analysis and fitting of probability distributions to the spontaneous recordings and output a brief summary using MATLAB's *publish* function. We briefly discuss the individual components below before examining the fitted ISI distributions in more detail.

4.2.3 Tests of stationarity

A spike train is considered non-stationarity if the rate of discharge increases or decreases within a recording. Most quantitative analyses assume stationary neuronal discharges. However, nonstationarities can introduce themselves particularly when working with anaesthetised animals [Spanne *et al.*, 2014]. We first visually inspect the data both as a raster plot and as the cumulative number of spikes as a function of occurrence time. Two statistical tests were also applied to the data. Firstly, regression analysis of the ISIs against their serial number, with a non-zero slope suggesting a trend in the data. Secondly, we performed a Wald-Wolfowitz test based on the number of runs, of consecutive values, above or below the median value (MATLAB function: *runstest*). Trends in activity are indicated by significantly large negative values of the test statistic [Duchamp-Viret

et al., 2005]. The spike train was considered nonstationary if either of the statistical tests were significant at the 0.05 level.

If the spike train failed the tests for stationarity we attempted to prune the record to a segment where spontaneous activity could be considered stationary. We performed regression of cumulative sum of ISIs as a function of their order in the sequence. Pruning began by discarding the ISIs from the first to that at which the cumulative function first intersected the straight-line fit. Stationarity tests were then repeated. If necessary, pruning continued but this time discarding ISIs from the last to that at which the cumulative function last intersected the straight-line fit. This process was repeated iteratively, alternating between discarding segments from the start and end until the period passed stationarity tests or the number of ISI in the sequence was less than 100 (in which case the recording was excluded from analysis due to insufficient samples for accurate fitting, see section 4.2.10).

4.2.4 Periodicity

To discover possible periodicities in the spike trains we again employed both visual inspection and statistical tests. The power spectra was calculated as the magnitude-squared of the Fourier transform via the MATLAB code provided in [Storey *et al.*, 2015] and plotted. We expect large peaks corresponding to the mean firing rate and its harmonics, while other peaks illustrate rhythmic components of neuron discharge. The Wald-Wolfowitz test, used for testing the stationarity, also indicates the presence of periodicities. In this case it is significantly large positive values of the test statistic that suggest periodicity in ISIs [Duchamp-Viret *et al.*, 2005].

4.2.5 Tests of independence between successive intervals

Serial independence is an important criterion for characterising the activity of a neuron as a renewal process. However, many neurons exhibit "memory" in their spiking activity, where the length of the current ISI is influenced by past spiking activity. This memory is commonly quantified in terms of serial correlation (MATLAB function: *autocorr*). Coefficients measure the dependence of pairs of ISIs separated by a number of intervals (lags). Positive coefficients indicate that long ISI tend to be followed by long ones and short followed by short. Negative coefficients indicate that long ISI will tend to be followed by short ones and vice versa.

We also construct the graphical test suggested in Pouzat & Chaffiol [2009a]. ISI are sorted in increasing order. O_j is the "rank" of interval ISI_j, which describes the

arrangement of elements of the original unsorted sequence into the new sorted one. When order (O_{j+k}) is plotted at different lags (k), if the ISI are independent points on the scatter diagram will be uniformly distributed, whereas dependencies will result in an above average number of points localized in some areas. We test this by subdividing the surface of the plots into cells, with subdivisions chosen such that the expected number of points per cell is at least 25. Plots were generated for O_k vs O_{k+1} and O_k vs O_{k+2}. Additionally χ^2 tests were performed on the number of points in each cell with respect to the expected number of points for lags up to $lag = 10 \log_{10}(length(ISI))$.

4.2.6 Central tendency and regularity of stationarity activity

The central tendency and regularity of stationary activity was characterised by the following measures: mean ($\bar{x}$), standard deviation (SD), the coefficient of variation ($SD/\bar{x}$), skewness (g_1; an indicator of distribution symmetry) and kurtosis (g_2; an indicator of peak shape). Additionally, the following non-parametric equivalents were calculated: median (x_M), interquartile range (IQR) and CV_M (IQR/x_M).

The mean and standard deviation above are related to the first and second order moments of the ISI distribution and are easily estimated from experimental data. Skewness and kurtosis represent the third and fourth moments. These higher order moments although less frequently used, help quantify some features which are evident in histograms of ISI distributions. Alternatively if certain assumptions are met, ISI probability density functions (PDF) provide complete information about the statistical structure of the spike train, but require more difficult quantitative methods [Kostal *et al.*, 2011].

4.2.7 Point processes

Motivated by the observation "data of interest are not precise voltage measurements, but rather precise measurements of times of occurrence of events", Perkel *et al.* [1967] introduced a framework where statistical techniques applied to spike train data should be related to the underlying theory of stochastic point processes. A point process describes a series of events in time, separated by random intervals, with outcomes evolving according to a stochastic process. For spike train data the process may be specified in terms of spike times, ISI, or spike counts [Kass *et al.*, 2014]. The simplest point process is the Poisson process.

4.2.7.1 Homogeneous Poisson processes

A homogeneous Poisson process can be described as a stochastic process which is fully characterised by a single constant parameter, τ. This model results in the ISI being independent and identically distributed according to the exponential distribution:

$$f(x|\tau) = \frac{1}{\tau} \exp\left(\frac{-x}{\tau}\right) \tag{4.1}$$

Both the mean and standard deviation of the distribution are equal to τ resulting in $CV = 1$.

While the Poisson process is simple and has appealing distributional properties, real neurons often demonstrate non-Poissonian behaviour. In particular, neurons exhibit a refractory period where the probability of spiking depends on the time since the last spike. Whereas the homogeneous Poisson process assumes the point process is both stationary and independent of past event history, a homogeneous renewal process loosens this assumption so that the probability of an event depends only on the immediately preceding event.

4.2.7.2 Renewal processes

A renewal process specifies the distribution of inter-event waiting times (in this case ISI). The waiting times are mutually independent and in the homogeneous case all come from the same distribution [Kass *et al.*, 2014]. The Poisson process is itself a renewal process, but we can now modify it by adding a "offset" or "dead time" parameter to incorporate refractoriness (see Equation (4.2)).

Theoretically a renewal process can be defined using any PDF that takes on positive values. A number of distributions have been repeatedly used, either due to a direct connection with the physiology of neurons, or because their distributional properties allow a simple, flexible, model of the shape of ISI distributions [Kass *et al.*, 2014]. We fit the empirical ISI distribution with the 6 common two-parameter duration distributions described in Pouzat & Chaffiol [2009a], along with the Normal and Birnbaum Saunders distributions. Their probability density functions are:

- Refractory Exponential:

$$f(x|\tau, d) = \begin{cases} 0 & x < d \\ \frac{1}{\tau} \exp\left(\frac{-(x-d)}{\tau}\right) & x \geq d \end{cases} \tag{4.2}$$

- Normal:

$$f(x|\mu,\sigma) = \frac{1}{\sigma\sqrt{2\pi}} \exp\left(\frac{-(x-\mu)^2}{2\sigma^2}\right) \tag{4.3}$$

- Lognormal:

$$f(x|\mu,\sigma) = \frac{1}{x\sigma\sqrt{2\pi}} \exp\left(\frac{-(\ln x-\mu)^2}{2\sigma^2}\right) \tag{4.4}$$

- Loglogistic:

$$f(x|\mu,\sigma) = \frac{1}{\sigma}\frac{1}{x}\frac{\exp\left((\log(x)-\mu)/\sigma\right)}{\left(1+\exp\left((\log(x)-\mu)/\sigma\right)\right)^2} \tag{4.5}$$

- Weibull:

$$f(x|a,b) = \frac{b}{a}\left(\frac{x}{a}\right)^{b-1} \exp\left(-\left(\frac{x}{a}\right)^b\right) \tag{4.6}$$

- Inverse Gaussian (also known as Wald):

$$f(x|\mu,\lambda) = \sqrt{\frac{\lambda}{2\pi x^3}} \exp\left(\frac{-\lambda}{2\mu^2 x}(x-\mu)^2\right) \tag{4.7}$$

  The Inverse Gaussian describes the distribution of the time a Brownian Motion, with positive drift, takes to reach a fixed positive level. This is distributed according to $f\left(x|\mu=\frac{a}{m},\lambda=\frac{a^2}{\sigma^2}\right)$

- Gamma (Erlang if restricted to integer k):

$$f(x|k,\mu) = \frac{1}{\Gamma(k)\,\mu^k} x^{k-1} \exp\left(\frac{-x}{\mu}\right) \tag{4.8}$$

where $\Gamma(\cdot)$ is the Gamma function. This distribution can arise through various mechanisms e.g. Gamma ISIs could result from a Poisson process of rate $1/\mu$ where only every kth event triggers firing.

- Birnbaum Saunders:

$$f(x|\beta,\gamma) = \frac{1}{\sqrt{2\pi}} \exp\left(-\frac{\left(\sqrt{x/\beta} - \sqrt{\beta/x}\right)^2}{2\gamma^2}\right)\left(\frac{\left(\sqrt{x/\beta} - \sqrt{\beta/x}\right)}{2\gamma x}\right) \tag{4.9}$$

Additionally, we fit several three-parameter distributions. These have the form of "shifted"/"offset" distributions, with a parameter-dependent lower bound (x in the above pdfs has been replaced with $(x-d)$):

- offset Wald
- offset Lognormal
- offset Loglogistic
- offset Weibull
- offset Erlang
- offset Birnbaum Saunders

or censored Poisson processes (obtained from the convolution of an exponential random variable with another distribution):

- ex-Gaussian [Palmer *et al.*, 2011]:

$$f(x|\mu,\sigma,\tau) = \frac{1}{\tau} \exp\left(\frac{\mu}{\tau} + \frac{\sigma^2}{2\tau^2} - \frac{x}{\tau}\right)\phi\left(\frac{x-\mu-\sigma^2/\tau}{\sigma}\right) \tag{4.10}$$

where $\phi(\cdot)$ is the cumulative density of the standard Gaussian distribution

- ex-Wald [Heathcote, 2004]:

$$f(x|m,a,\tau) = \begin{cases} \frac{1}{\tau}\exp\left(-\left(\frac{x}{\tau} - a(m-k)\right)\right) F_W(x|k,a) & m^2 \geq 2/\tau \\ \frac{1}{\tau}\exp\left(\frac{-(a-m)^2}{2x}\right) Re\left[w\left(k'\sqrt{\frac{x}{2}} + \frac{ia}{\sqrt{2x}}\right)\right] & m^2 < 2/\tau \end{cases} \tag{4.11}$$

where $k = \sqrt{m^2 - \frac{2}{\tau}}$, $k' = \sqrt{\frac{2}{\tau} - m^2}$ and $w(z) = \exp(-z^2)[1 - erf(-iz)]$. See Heathcote [2004] for further detail. We reparametrize the ex-Wald in terms of μ the mean, and λ the shape parameters of the Inverse Gaussian $\left(m = \frac{\sqrt{\lambda}}{\mu}, a = \sqrt{\lambda}\right)$.

- ex-Erlang:

$$f(x|\mu, k, \tau) = \frac{\exp\left(\frac{-x}{\tau}\right) x^k \left(x - (\mu x)/\tau\right)^{-k} \left(\Gamma(k) - \Gamma\left(k, x\left(1/\mu - 1/\tau\right)\right)\right)}{\tau\Gamma(k)} \tag{4.12}$$

The ex-Lognormal, ex-Loglogistic, ex-Weibull and ex-Birnbaum Saunders were also fitted, however these had no closed form analytical solutions (that we know of) so these distributions were calculated numerically by convolving the two distributions.

4.2.8 Information theoretic measures

In information theory, entropy is often employed to measure the deviation of a spike train from the Poisson process. Of all the possible PDF describing a renewal process with fixed mean, the exponential distribution has the maximum entropy. Entropy was introduced by Shannon [1948] as a measure of uncertainty of a probability distribution. For a discrete random variable X, the entropy is defined as:

$$H(X) = -\sum_x f_X(x) \log f_X(x) \tag{4.13}$$

In information theory the base of the logarithm is usually taken to be 2, thus relating it to "bits" of information. Elsewhere a natural logarithm is sometimes used for ease of calculation, we use log_2. In the continuous case, the sum is replaced by an integral:

$$H(X) = -\int_0^\infty f(x) \log f(x)\, dx \tag{4.14}$$

Although the two equations for entropy are analogous, Equation (4.14) cannot be directly used to measure uncertainty as it may negative and is not scale invariant [Kapur & Kesavan, 1992].

An alternative measure which overcomes these difficulties is the Kullback-Leibler divergence (KLD) [Kostal & Lansky, 2005], also known as the relative entropy. KLD provides a measure of the distance or divergence between two probability distributions.

The discrete version is expressed as:

$$D_{KL}(f,g) = \sum_{x} f_X(x) \log \frac{f_X(x)}{g_X(x)} \tag{4.15}$$

and analogous continuous version:

$$D_{KL}(f,g) = \int_0^{\infty} f(x) \log \frac{f(x)}{g(x)} dx \tag{4.16}$$

The KLD is a nonsymmetric measure ($D_{KL}(f,g) \neq D_{KL}(g,f)$).

We use KLD to measure how far away the specified model PDF is from the empirical ISI distribution. We compute the discrete KLD for quantized (finite sample interval) spike data. The KLD is evaluated by computing model probabilities in histogram bins using numerical (rectangle) integration. Bins were equal to the sample period and aligned to ensure that each bin contains exactly one sample point. Compared with maximum likelihood fitting, the KLD approach gave better performances for the model probability distributions and data considered here.

4.2.9 Fitting probability density functions

We perform an iterative search process using the interior-point approach to constrained minimization (MATLAB function: *fmincon*) to minimize the KLD for each model PDF. We constrained any parameters influencing the location of the probability distribution to be greater than zero. These constraints ensured all distributions satisfied the renewal process criteria of taking on only positive values. Additionally, positive values of parameters are more plausible for capturing something biologically relevant about neuronal stochastic processes. Where possible initial parameter guesses were obtained by method of moments. However, in some cases these expressions were not available and parameters were estimated heuristically. The parameter values of the PDF are adjusted until maximum fit to the observed data is achieved to within a given tolerance.

Although the interior-point algorithm has many good characteristics, such as low memory usage, the ability to solve large problems quickly and recovery from NaN or Inf results, the parameter search may fail to converge. This occurs if the solver reaches its limit on the number of iterations, or function evaluations, before the change in the objective function becomes smaller than the termination tolerance or the change in parameter values becomes smaller than the function tolerance. Additionally, even if the solver converges it may be to a local rather than global optimum. To minimize the risk of

this when feasible we use the MATLAB *MultiStart* function, which generates a number of starting points (we choose 100) for the constrained minimisation problem. It then uses a local solver to find the optima in the basins of attraction of the starting points and we take the best local solution to estimate the global optimum. The ex-Birnbaum Saunders, ex-Weibull, ex-LogNormal and ex-LogLogistic required the PDFs be calculated by numerical quadrature which was prohibitively slow for multiple runs.

4.2.10 Monte Carlo evaluation

A Monte Carlo study was performed to evaluate potential biases associated with the parameter estimates when using the present implementation of the fitting process. In particular, we were interested in the minimum number of samples required for convergence of pdf fits. Previous analysis of offset Wald and ex-Wald distributions suggested that for the parameter space involved in response time data, a minimum sample size of at least 100 for the offset Wald and 400 for the ex-Wald should be used [Heathcote, 2004]. We took the parameters of the best fitting Wald, offset Wald, ex-Wald, Erlang, offset Erlang and ex-Erlang for three ISI distributions: one with low CV ($\bar{x} = 0.0555$, $CV = 0.1041$), one with intermediate CV ($\bar{x} = 0.0522$, $CV = 0.2395$) and one with high CV ($\bar{x} = 0.0485$, $CV = 0.3108$) and used these to characterise the "true" parameters (Figure 4.1). For each of the theoretical distributions, the Monte Carlo study was performed for sample sizes N = 100, 200, 400, 800, and 1600. A Monte Carlo estimation of the sampling distribution was obtained for each sample size by sampling the theoretical distribution 500 times and performing the pdf fitting described above for each sample.

4.2.11 Assessing goodness of fit

The KLD is useful in selecting the best model among a set of candidate models but fails to assess how well the best model fits the data. In order to examine this we plot the empirical quantiles versus the model derived quantiles, commonly known as a Q-Q plot. A perfect fit would result in a straight line fit with intercept = 0 and slope = 1. Deviations from this diagonal line show where the model fails to agree with the data.

The Q-Q plot can never prove or disprove the independently distributed assumption behind modelling the spike train as a realisation of a renewal process [Pouzat & Chaffiol, 2009a]. Therefore, in addition to the tests we conducted prior to fitting, we also examine the best candidate model using Ogata's tests. Ogata's goodness of fit tests transform the renewal process onto a homogeneous Poisson process with rate 1 [Ogata, 1988]. For a detailed description of how to apply the battery of tests to spike train data see Pouzat

& Chaffiol [2009b]. Briefly, Ogata's first test or the "uniform test" tests the uniformity of transformed event times given the number of events using a Kolmogorov-Smirnov (KS) test. Ogata's second test or "Berman's test" checks the uniformity of transformed inter event intervals, again using a KS test. Ogata's third test examines dependency by plotting the lag 1 transformed intervals. The final "variance vs. mean test" splits the transformed time axis into non-overlapping windows of increasing length and a graph of the variance as a function of the mean event count is produced. The result should be a straight line fit with intercept = 0 and slope = 1. These goodness of fit tests can be also used for counting processes involving history dependencies, or time varying rates, but this is beyond the scope of this chapter.

4.2.12 Interactions between parameters

Linear models (MATLAB function: *fitlm*) were used to analyse patterns between ex-Wald model parameters and ISI sample statistics across the population. Some relationships were linear, while others appear linear on log-log axes, indicating power-law relationships in untransformed data. No natural distinction exists between predictor and response variables when investigating interactions between ex-Wald parameters, therefore we used Principal Component Analysis (PCA) to fit an orthogonal regression (MATLAB function: *pca*). The statistical significance of interactions is examined using both frequentest and Bayesian measures.

4.3 Results

Spontaneous activity was recorded from a total of 40 primary afferent electrosensory neurons in adult skates, the automatically generated reports are included in the electronic supplementary information (see Appendix A). The mean firing rates ranged from 12.7 to 26.1 spikes s^{-1} (21.3 ± 3.1; $\bar{x} \pm SD$). Primary afferent electrosensory neurons in healthy fish typically exhibit a reasonably regular discharge. However, interspike interval duration was not distributed randomly about the mean.

4.3.1 Trend, periodicity, and serial dependency

The nonsignificant results of both applied tests stationarity were considered as a confirmation that the data are meeting the condition of weak stationarity. The presence of trend was indicated in 37 units, i.e. only 3 units (7.5%) demonstrated no trend over the

entire recording. When the samples with trend were pruned using the procedure described in Section 4.2.3, we were able to obtain a segment in which no trend was observed for a period of at least 100 spikes most recordings (37 units, 92.5 %). The 3 units containing no stationary segments were found to exhibit periodicity, indicated by large positive values of the Wald-Wolfowitz test statistic used for testing stationarity. Finally, serial correlation was found in 7 units (17.5 %) via visual examination of autocorrelation and χ^2 plots.

Table 4.1: Basic statistics for raw and pruned spike train recordings

	Raw	**Pruned**
Number of neurons	40	30
Number of ISIs	3332 (1519 – 7787)	1078 (118 – 2553)
Central values		
$\bar{x}$	0.048 (0.038 – 0.079)	0.049 (0.037 – 0.079)
x_M	0.047 (0.038 – 0.078)	0.048 (0.036 – 0.078)
Variabilities		
SD	0.010 (0.005 – 0.021)	0.010 (0.005 – 0.016)
IQR	0.014 (0.006 – 0.024)	0.014 (0.006 – 0.021)
CV	0.215 (0.104 – 0.464)	0.205 (0.100 – 0.311)
CV_M	0.291 (0.135 – 0.508)	0.285 (0.136 – 0.463)
Higher order moments		
g_1	0.681 (−0.302 – 2.838)	0.522 (0.091 – 1.589)
g_2	2.797 (−0.398 – 34.329)	0.716 (−0.608 – 7.668)

Thus 30 units (75.0 %) were retained for further statistical evaluation. This result demonstrates that long-term trends are a common feature of afferent spontaneous activity. On the other hand quasi-stationary segments of activity can be found in the majority of recordings. However, the most common violation of renewal assumptions was non-independence.

4.3.2 Central value and variability of ISIs

Henceforth neurons (or segments of neuronal activity) displaying trend, periodicity or serial dependency are excluded from analysis, as they violate the assumptions of a renewal process. However, their exclusion made little difference to the minimum, maximum and mean values for parametric and non-parametric measures of the central value and variability of ISIs (Table 4.1).

Figure 4.1 shows the recorded interspike interval histograms and spike train plots for three representative afferents, with resting discharge rates near the population mean. There was a positive linear relationship between mean ISI and SD ($SD = 0.185\bar{x} + 0.001$,

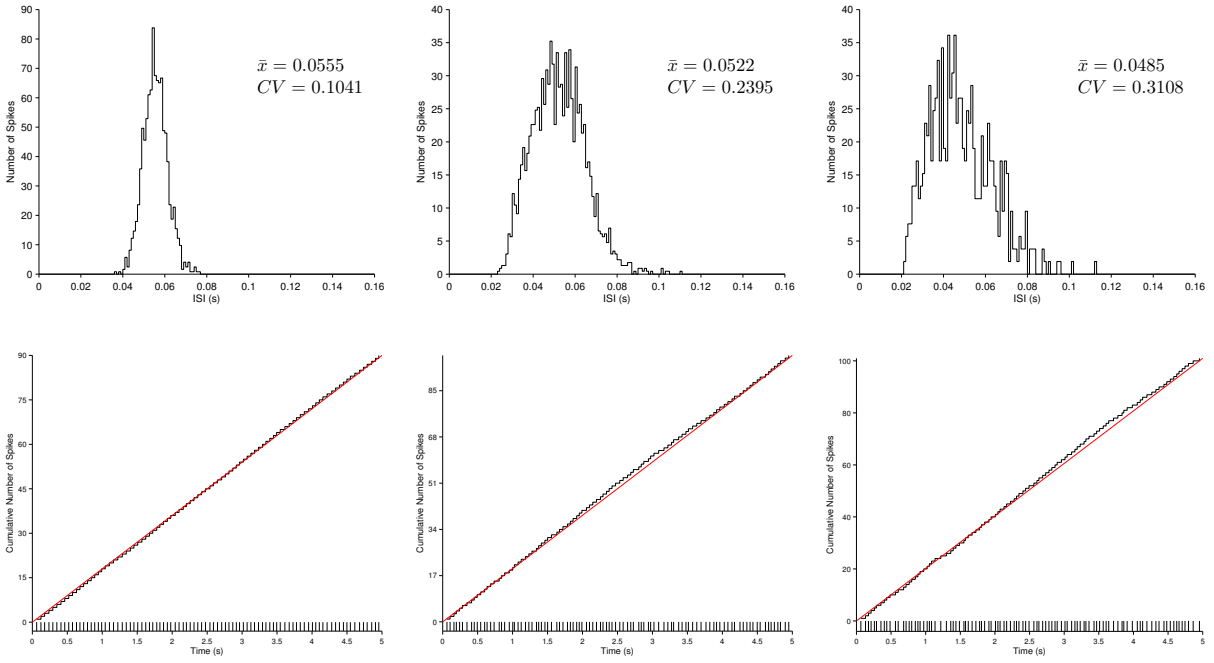

(a) Low **(b)** Intermediate **(c)** High

Figure 4.1: Regularity of spontaneous activity from electrosensory afferents in the little skate, *Leucoraja erinacea*. Units of varying CV were selected with mean ISI near the population mean ($\bar{x} = 0.049$). Upper plots show interspike interval (ISI) histograms binned at 1 ms resolution. Lower plots show the cumulative number of spikes as a function of their occurrence time and a traditional spike raster for the first 5 s of recording.

$r^2 = 0.189$, $p = 0.016$; Figure 4.2a). The variability of neuronal discharge was further examined via the CV, values ranged from 0.100 to 0.311 (0.205 ± 0.069). There was no association between mean ISI and CV (Figure 4.2b). All distributions were skewed to the right, ranging from near normal to near exponential (Figure 4.1). While there was no association between mean ISI and either skewness or excess kurtosis, there was a positive linear relationship between CV and skewness ($g_1 = 2.777CV - 0.047$, $r^2 = 0.372$, $p = 0.0003$; Figure 4.3a). The lack of relationship between mean ISI and CV, skewness and kurtosis suggests that the shape of the ISI distribution is largely independent from the mean interval. The majority of ISI distributions were leptokurtotic (positive excess kurtosis) indicating more ISI concentrated near the mean and tails and fewer ISI in the intermediate regions relative to the normal distribution, however platykurtotic distributions were also found (negative excess kurtosis; Figure 4.3b). The apparent positive trend between CV and excess kurtosis was not statistically significant.

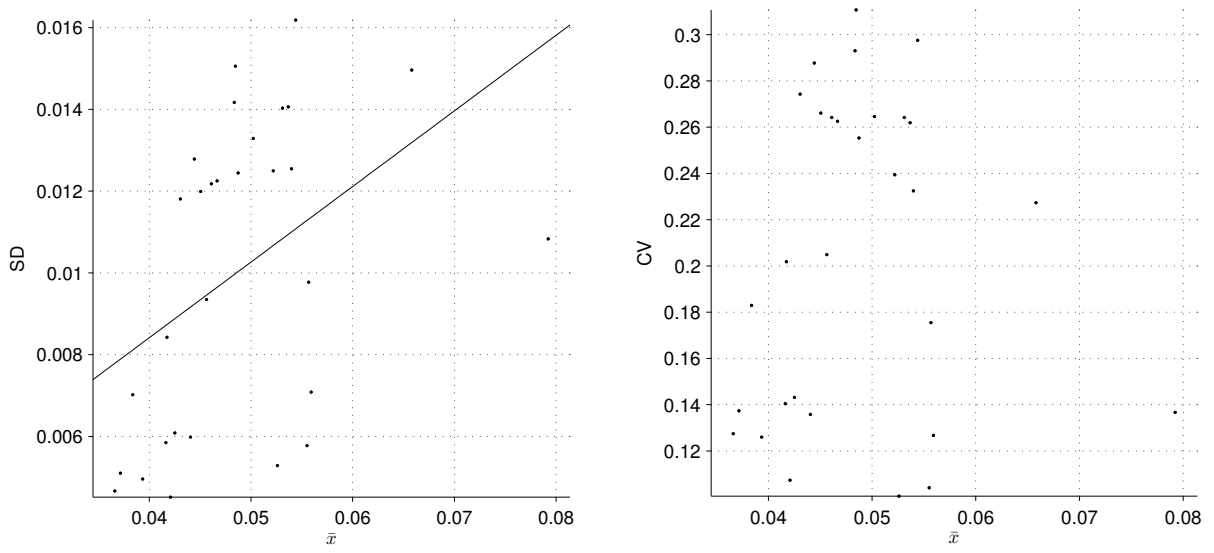

(a) Standard Deviation **(b)** Coefficient of Variation

Figure 4.2: Relationship between mean and variability of ISI for electrosensory primary afferent spontaneous activity in the little skate, *Leucoraja erinacea*. Figure 4.2a shows positive linear relationship between mean ISI and SD ($SD = 0.185\bar{x} + 0.001$, $r^2 = 0.189$, $p = 0.016$). There was no association between mean ISI and CV (Figure 4.2b).

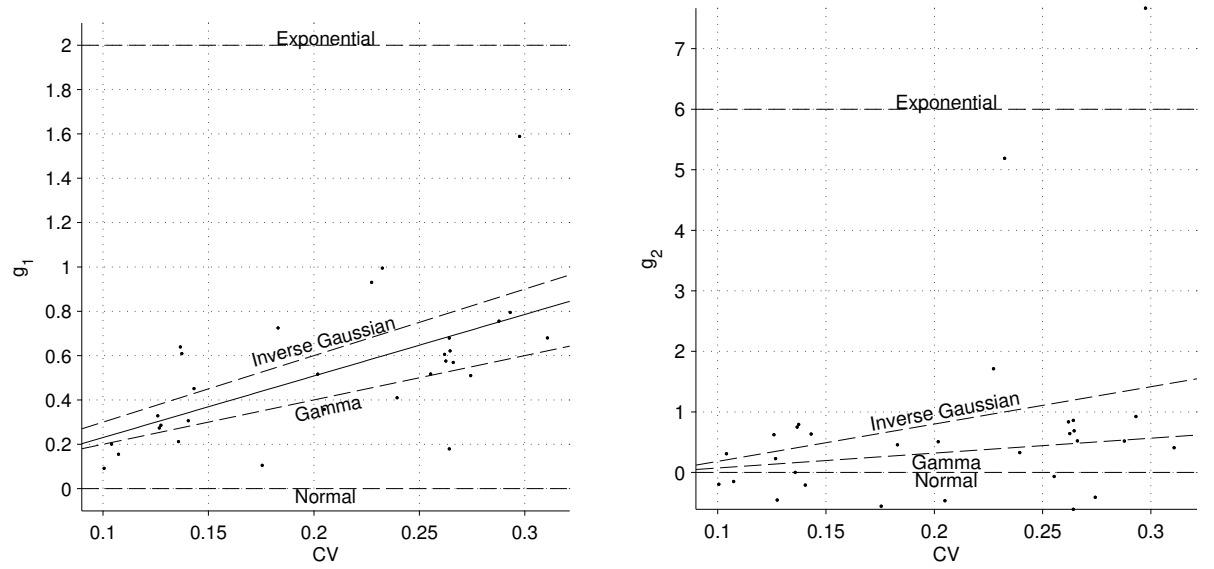

(a) Skewness **(b)** Kurtosis

Figure 4.3: Relationship between regularity (CV) and higher order moments for electrosensory primary afferent spontaneous activity in the little skate, *Leucoraja erinacea*. Figure 4.3a shows a positive linear relationship between CV and skewness (solid line; $g_1 = 2.777CV - 0.047$, $r^2 = 0.372$, $p = 0.0003$). There was no significant association between CV and excess skewness (Figure 4.3b).

4.3.3 Stochastic processes describing spontaneous activity

Until now we have focussed on single parameter estimates (and their interactions) describing the central tendency and variability of afferent ISI. We now attempt to characterise spontaneous activity as a stochastic process with the hope of providing some insight at the neuronal mechanisms responsible for generating spikes.

4.3.3.1 Monte Carlo sampling

Estimation failures. Of the 45,000 fits performed all produced parameter estimates, indicating that the starting point heuristics and fitting procedure are reasonably robust. There were however instances where the estimates were orders of magnitude different from the true parameters (in particular the shape parameters λ and k), we will examine these further below.

Bias, efficiency and consistency. Bias was estimated as the difference between mean of the Monte Carlo parameter estimates and the true value, with positive values indicating overestimation and negative underestimation. Efficiency was estimated by the standard deviation of the parameter estimates. Consistency refers to estimates approaching the true value as the sample size increases. We are mainly interested in the minimum number of spikes required for fitting to generate consistent estimates within the expected parameter range of afferent spike trains.

Tables 4.2 to 4.7 contain the bias and efficiency estimates for the two parameter Gamma and Wald distributions and their respective three parameter offset and exponential convolutions. To compare estimation performance across distributions, it is useful to recognize that the offset parameters (d), the exponential parameters (τ) and the Erlang and Wald parameters (μ) have the same units as the data. Estimation performance can also be judged for all parameters as a proportion of their true values, which are listed in the table captions.

Table 4.2: Absolute bias (Monte Carlo mean - true value) and efficiency (SD) for Erlang parameter estimates. Results are reported for each parameter according to sample size for 3 different distributions ($k_1 = 11$, $\mu_1 = 4.405\text{e-}03$; $k_2 = 17$, $\mu_2 = 3.070\text{e-}03$; $k_3 = 92$, $\mu_3 = 6.033\text{e-}04$) and are based on 500 estimations.

	100	**200**	**400**	**800**	**1600**
k_{Bias}	0.420	0.142	0.104	-0.010	0.030
	0.546	0.292	0.086	0.098	0.046
	3.234	1.420	1.030	0.258	0.224
k_{SD}	1.700	1.189	0.852	0.571	0.449
	2.532	1.779	1.243	0.889	0.655
	13.465	9.238	6.472	4.591	3.442
μ_{Bias}	-7.631e-05	-6.061e-06	-1.287e-05	1.637e-05	-5.119e-06
	-3.290e-05	-2.059e-05	-7.618e-07	-1.125e-05	-4.084e-06
	-8.566e-06	-3.708e-06	-3.528e-06	-2.104e-07	-6.991e-07
μ_{SD}	6.624e-04	4.739e-04	3.464e-04	2.387e-04	1.807e-04
	4.352e-04	3.142e-04	2.251e-04	1.607e-04	1.216e-04
	8.461e-05	5.855e-05	4.200e-05	2.966e-05	2.251e-05

Table 4.3: Absolute bias (Monte Carlo mean - true value) and efficiency (SD) for Wald parameter estimates. Results are reported for each parameter according to sample size for 3 different distributions ($\lambda_1 = 0.482$, $\mu_1 = 4.846\text{e-}02$; $\lambda_2 = 0.850$, $\mu_2 = 5.218\text{e-}02$; $\lambda_3 = 5.055$, $\mu_3 = 5.550\text{e-}02$) and are based on 500 estimations.

	100	**200**	**400**	**800**	**1600**
λ_{Bias}	0.014	0.008	0.005	0.002	0.002
	0.033	0.010	0.008	0.003	0.002
	0.160	0.091	0.040	-0.004	0.010
λ_{SD}	0.072	0.052	0.036	0.025	0.018
	0.128	0.094	0.063	0.042	0.029
	0.748	0.514	0.362	0.261	0.172
μ_{Bias}	-9.069e-05	-2.194e-05	-2.434e-05	5.815e-05	7.180e-06
	-2.138e-05	-8.166e-05	-5.034e-06	-1.729e-05	1.190e-06
	3.342e-05	-1.395e-05	-9.924e-06	-1.079e-05	2.421e-07
μ_{SD}	1.467e-03	1.137e-03	7.554e-04	5.404e-04	3.709e-04
	1.220e-03	8.771e-04	6.408e-04	4.797e-04	2.979e-04
	5.884e-04	4.267e-04	2.915e-04	2.070e-04	1.417e-04

Table 4.4: Absolute bias (Monte Carlo mean - true value) and efficiency (SD) for offset Erlang parameter estimates. Results are reported for each parameter according to sample size for 3 different distributions ($k_1 = 5$, $\mu_1 = 6.820\text{e-}03$, $d_1 = 1.436\text{e-}02$; $k_2 = 17$, $\mu_2 = 3.045\text{e-}03$, $d_2 = 4.121\text{e-}04$; $k_3 = 92$, $\mu_3 = 6.029\text{e-}04$, $d_3 = 3.867\text{e-}05$) and are based on 500 estimations.

	100	**200**	**400**	**800**	**1600**
k_{Bias}	0.510	0.192	0.030	0.078	0.050
	-3.714	-3.070	-2.506	-1.654	-1.182
	-21.320	-18.694	-17.536	-16.554	-13.976
k_{SD}	2.683	1.922	1.137	0.803	0.566
	5.139	4.510	3.303	2.513	1.884
	33.842	28.541	25.596	21.843	18.648
μ_{Bias}	3.012e-04	1.685e-04	1.362e-04	4.360e-06	8.184e-06
	7.434e-04	5.162e-04	3.494e-04	2.102e-04	1.345e-04
	2.411e-04	1.594e-04	1.212e-04	9.545e-05	7.146e-05
μ_{SD}	2.073e-03	1.421e-03	9.645e-04	6.952e-04	5.097e-04
	1.210e-03	8.483e-04	5.300e-04	3.583e-04	2.422e-04
	4.652e-04	3.022e-04	2.194e-04	1.494e-04	1.086e-04
d_{Bias}	-2.418e-04	1.703e-04	1.675e-04	-5.446e-05	-8.334e-05
	7.030e-03	5.710e-03	4.252e-03	2.684e-03	1.903e-03
	9.741e-03	7.538e-03	6.762e-03	5.897e-03	4.815e-03
d_{SD}	6.466e-03	4.703e-03	2.899e-03	2.174e-03	1.486e-03
	8.640e-03	7.084e-03	5.245e-03	3.815e-03	2.788e-03
	1.274e-02	1.056e-02	9.310e-03	7.637e-03	6.493e-03

Table 4.5: Absolute bias (Monte Carlo mean - true value) and efficiency (SD) for offset Wald parameter estimates. Results are reported for each parameter according to sample size for 3 different distributions ($\lambda_1 = 0.482$, $\mu_1 = 4.845\text{e-}02$, $d_1 = 9.574\text{e-}06$; $\lambda_2 = 0.850$, $\mu_2 = 5.218\text{e-}02$, $d_2 = 4.235\text{e-}22$; $\lambda_3 = 5.055$, $\mu_3 = 5.550\text{e-}02$, $d_3 = 2.142\text{e-}20$) and are based on 500 estimations.

	100	**200**	**400**	**800**	**1600**
λ_{Bias}	-0.061	-0.037	-0.017	-0.007	-0.004
	-0.089	-0.064	-0.043	-0.022	-0.013
	-1.526	-1.371	-1.138	-0.963	-0.707
λ_{SD}	0.139	0.108	0.076	0.051	0.030
	0.268	0.208	0.151	0.096	0.065
	2.069	1.828	1.537	1.273	1.071
μ_{Bias}	-0.003	-0.002	-0.001	-0.000	-0.000
	-0.003	-0.002	-0.001	-0.001	-0.000
	-0.010	-0.008	-0.006	-0.005	-0.003
μ_{SD}	0.005	0.004	0.002	0.002	0.001
	0.006	0.005	0.003	0.002	0.001
	0.012	0.010	0.008	0.006	0.005
d_{Bias}	0.003	0.002	0.001	0.000	0.000
	0.003	0.002	0.001	0.001	0.000
	0.010	0.008	0.006	0.005	0.003
d_{SD}	0.005	0.004	0.002	0.001	0.001
	0.006	0.005	0.003	0.002	0.001
	0.012	0.010	0.008	0.006	0.005

Table 4.6: Absolute bias (Monte Carlo mean - true value) and efficiency (SD) for ex-Erlang parameter estimates. Results are reported for each parameter according to sample size for 3 different distributions ($k_1 = 11$, $\mu_1 = 3.557\text{e-}03$, $\tau_1 = 9.325\text{e-}03$; $k_2 = 17$, $\mu_2 = 2.973\text{e-}03$, $\tau_2 = 1.647\text{e-}03$; $k_3 = 92$, $\mu_3 = 5.993\text{e-}04$, $\tau_3 = 3.671\text{e-}04$) and are based on 500 estimations.

	100	**200**	**400**	**800**	**1600**
k_{Bias}	9.040	3.724	1.892	0.804	0.324
	9.410	5.966	2.424	1.502	0.922
	-6.038	-3.160	-0.694	-1.114	-0.676
k_{SD}	18.043	9.324	3.928	2.359	1.630
	16.756	11.794	4.246	2.820	1.690
	12.686	10.171	8.249	7.202	5.517
μ_{Bias}	-4.854e-04	-1.642e-04	-9.065e-05	7.469e-05	1.471e-04
	-6.546e-04	-5.514e-04	-3.773e-04	-2.905e-04	-2.353e-04
	4.203e-05	1.737e-05	-1.861e-06	3.309e-06	2.294e-06
μ_{SD}	1.594e-03	1.308e-03	1.056e-03	8.407e-04	6.991e-04
	9.952e-04	8.349e-04	5.797e-04	4.661e-04	3.250e-04
	1.149e-04	8.794e-05	6.312e-05	5.296e-05	3.753e-05
τ_{Bias}	-2.769e-03	-2.238e-03	-1.917e-03	-2.002e-03	-1.794e-03
	2.605e-03	2.926e-03	2.349e-03	2.134e-03	2.015e-03
	1.476e-03	1.235e-03	1.069e-03	7.352e-04	3.863e-04
τ_{SD}	5.410e-03	5.152e-03	4.552e-03	4.105e-03	3.665e-03
	4.294e-03	4.031e-03	3.432e-03	3.028e-03	2.706e-03
	1.092e-03	1.117e-03	1.081e-03	8.940e-04	5.744e-04

Table 4.7: Absolute bias (Monte Carlo mean - true value) and efficiency (SD) for ex-Wald parameter estimates. Results are reported for each parameter according to sample size for 3 different distributions ($\lambda_1 = 0.400$, $\mu_1 = 3.985\text{e-}02$, $\tau_1 = 8.603\text{e-}03$; $\lambda_2 = 0.761$, $\mu_2 = 4.610\text{e-}02$, $\tau_2 = 6.089\text{e-}03$; $\lambda_3 = 4.934$, $\mu_3 = 5.450\text{e-}02$, $\tau_3 = 1.006\text{e-}03$) and are based on 500 estimations.

	100	**200**	**400**	**800**	**1600**
λ_{Bias}	1150091.291	63001.352	0.092	0.055	0.032
	314817.146	2138.751	0.169	0.092	0.072
	28834.181	1.353	0.735	0.493	0.365
λ_{SD}	11532323.990	482247.622	0.187	0.094	0.057
	2238566.958	47815.411	0.271	0.137	0.101
	345884.086	2.014	1.180	0.774	0.505
μ_{Bias}	-2.143e-03	-1.894e-03	-9.837e-04	-8.539e-04	-8.739e-04
	-2.324e-03	-1.698e-03	-1.703e-03	-1.370e-03	-1.385e-03
	-1.521e-03	-1.435e-03	-1.465e-03	-1.449e-03	-1.341e-03
μ_{SD}	5.794e-03	4.473e-03	3.058e-03	2.440e-03	2.078e-03
	4.604e-03	3.145e-03	2.357e-03	1.652e-03	1.292e-03
	1.999e-03	1.592e-03	1.268e-03	1.095e-03	1.106e-03
τ_{Bias}	2.097e-03	1.869e-03	9.841e-04	8.208e-04	9.336e-04
	2.337e-03	1.731e-03	1.701e-03	1.372e-03	1.333e-03
	1.548e-03	1.418e-03	1.475e-03	1.471e-03	1.365e-03
τ_{SD}	5.495e-03	4.386e-03	2.847e-03	2.407e-03	2.058e-03
	4.267e-03	2.934e-03	2.293e-03	1.504e-03	1.247e-03
	1.678e-03	1.404e-03	1.185e-03	1.073e-03	1.114e-03

As mentioned previously the parameter fits show some biases particularly for smaller sample sizes. We examine these further by plotting the 2.5th, 50th (median), and 97.5th percentiles of the Monte Carlo parameter estimates. In the case of the two parameter distributions, for the specific parameter values used in this Monte Carlo study, the parameter fits to the sampling distributions do not appear strongly biased for sample sizes of 100 or more (Figures 4.4 and 4.5). The median values quickly converge to near the true parameters and the inter-percentile range is relatively symmetric decreasing with increasing sample size.

With the exception of the most skewed offset gamma distribution (which also had the largest d parameter), the offset d for both Erlang and Wald distributions was generally over estimated probably due to true d values being very small and fits constrained to $d > 0$ (Figures 4.6 and 4.7).

The shape parameters k and λ were generally underestimated. The scale parameter μ showed bias in opposite directions for the two distributions, for the offset Erlang μ was overestimated whereas the offset Wald μ was underestimated. The magnitude of these biases was relatively small and the efficiency of estimates increased with sample size (Tables 4.4 and 4.5).

The most noticeable feature of the Monte Carlo simulations was the exponentially convolved distributions sometimes exhibited spuriously large values for the shape parameters k and λ (Figures 4.8 and 4.9; This was so extreme for λ with the smaller sample sizes that we chose not to show the entire 97.5th percentile bar so that we could visualise the trends for larger sample sizes). However, even when the shape parameter estimates were orders of magnitude too large, this did not seem to significantly bias the estimation of the other two parameters (Tables 4.6 and 4.7). Samples of 400 or more ISI did not exhibit these extreme values.

The Monte Carlo study suggests that our fitting algorithm may generate large shape parameters if fits are based on a small number of ISI, but generally provides good parameter estimations for the ISI distributions, at least for the test values that were used.

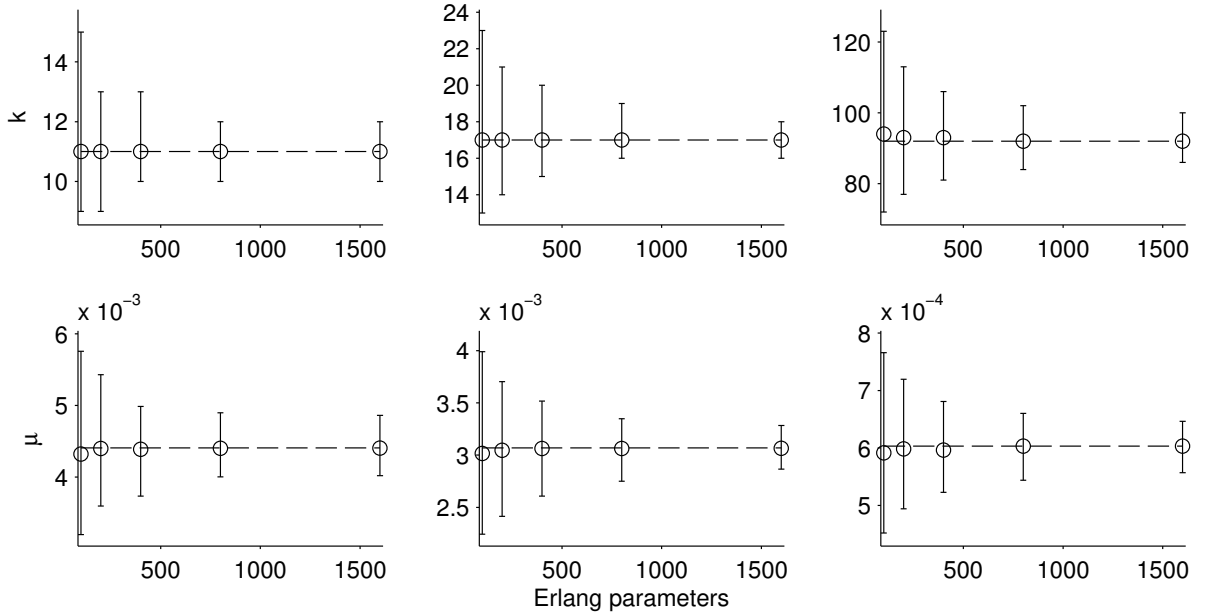

Figure 4.4: Sample size versus Erlang parameter estimates. Median (circle) along with the 2.5th and 97.5th percentiles (error bars) of parameter estimates from Monte Carlo samples. Results are reported for each parameter according to sample size for 3 different distributions ($k_1 = 11$, $\mu_1 = 4.405\text{e-}03$; $k_2 = 17$, $\mu_2 = 3.070\text{e-}03$; $k_3 = 92$, $\mu_3 = 6.033\text{e-}04$) and are based on 500 estimations. The dashed line is the true parameter value.

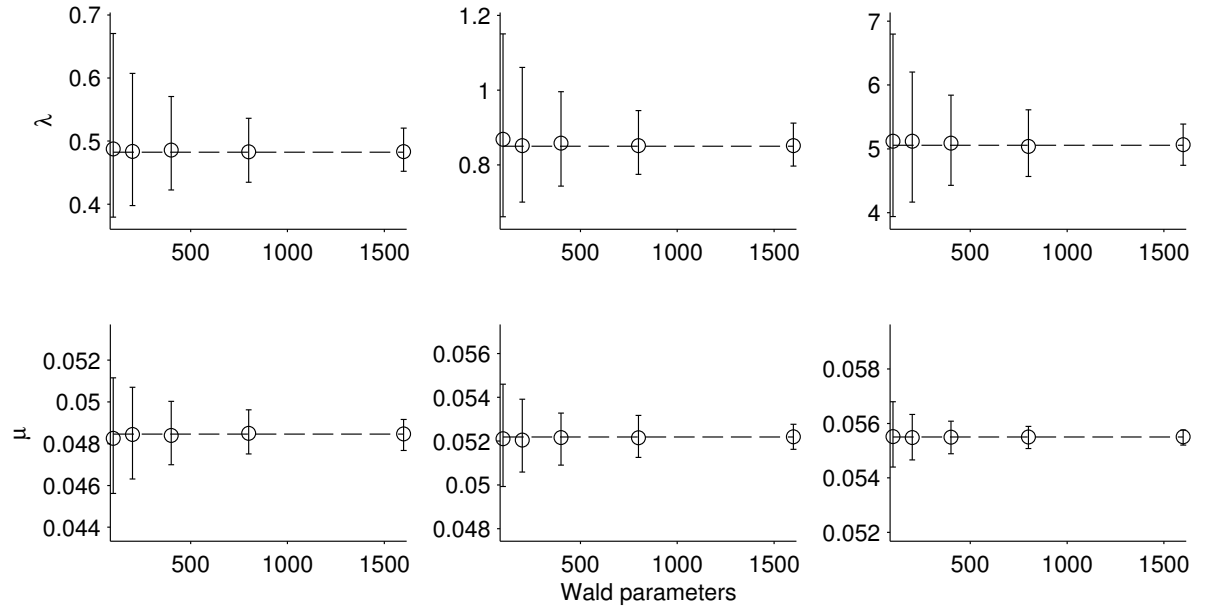

Figure 4.5: Sample size versus Wald parameter estimates. Median (circle) along with the 2.5th and 97.5th percentiles (error bars) of parameter estimates from Monte Carlo samples. Results are reported for each parameter according to sample size for 3 different distributions ($\lambda_1 = 0.482$, $\mu_1 = 4.846\text{e-}02$; $\lambda_2 = 0.850$, $\mu_2 = 5.218\text{e-}02$; $\lambda_3 = 5.055$, $\mu_3 = 5.550\text{e-}02$) and are based on 500 estimations. The dashed line is the true parameter value.

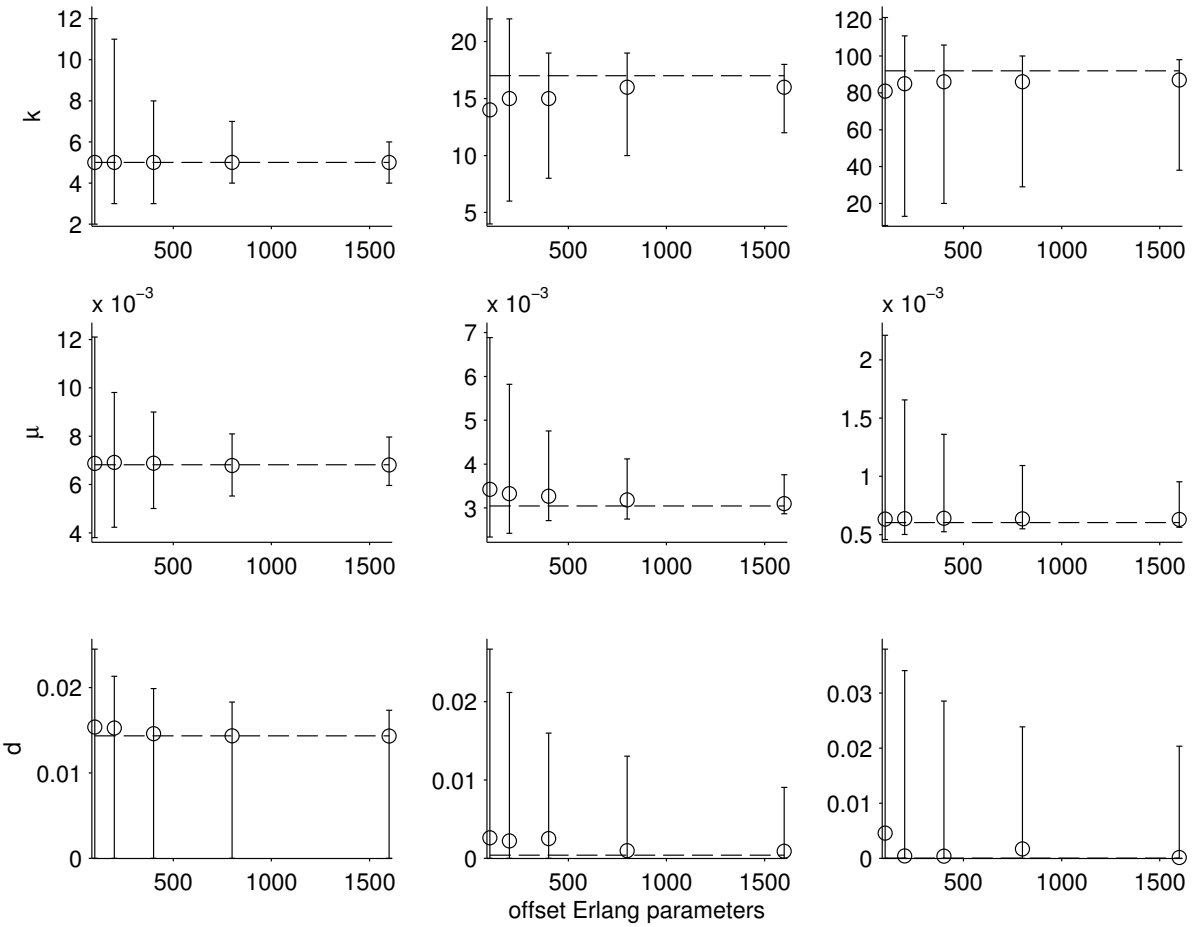

Figure 4.6: Sample size versus offset Erlang parameter estimates. Median (circle) along with the 2.5th and 97.5th percentiles (error bars) of parameter estimates from Monte Carlo samples. Results are reported for each parameter according to sample size for 3 different distributions ($k_1 = 5$, $\mu_1 = 6.820\text{e-}03$, $d_1 = 1.436\text{e-}02$; $k_2 = 17$, $\mu_2 = 3.045\text{e-}03$, $d_2 = 4.121\text{e-}04$; $k_3 = 92$, $\mu_3 = 6.029\text{e-}04$, $d_3 = 3.867\text{e-}05$) and are based on 500 estimations. The dashed line is the true parameter value.

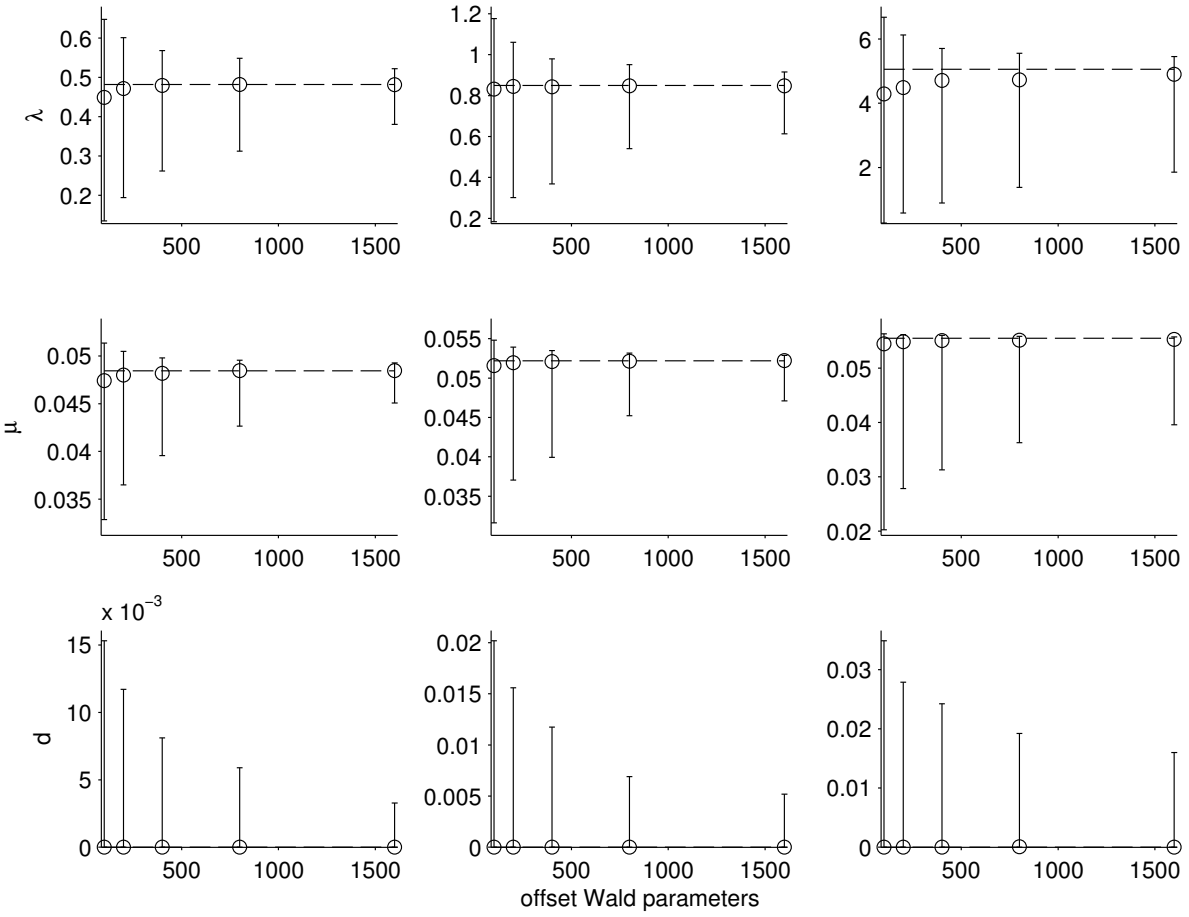

Figure 4.7: Sample size versus offset Wald parameter estimates. Median (circle) along with the 2.5th and 97.5th percentiles (error bars) of parameter estimates from Monte Carlo samples. Results are reported for each parameter according to sample size for 3 different distributions ($\lambda_1 = 0.482$, $\mu_1 =$ 4.845e-02, $d_1 =$ 9.574e-06; $\lambda_2 = 0.850$, $\mu_2 =$ 5.218e-02, $d_2 =$ 4.235e-22; $\lambda_3 = 5.055$, $\mu_3 =$ 5.550e-02, d_3 = 2.142e-20) and are based on 500 estimations. The dashed line is the true parameter value.

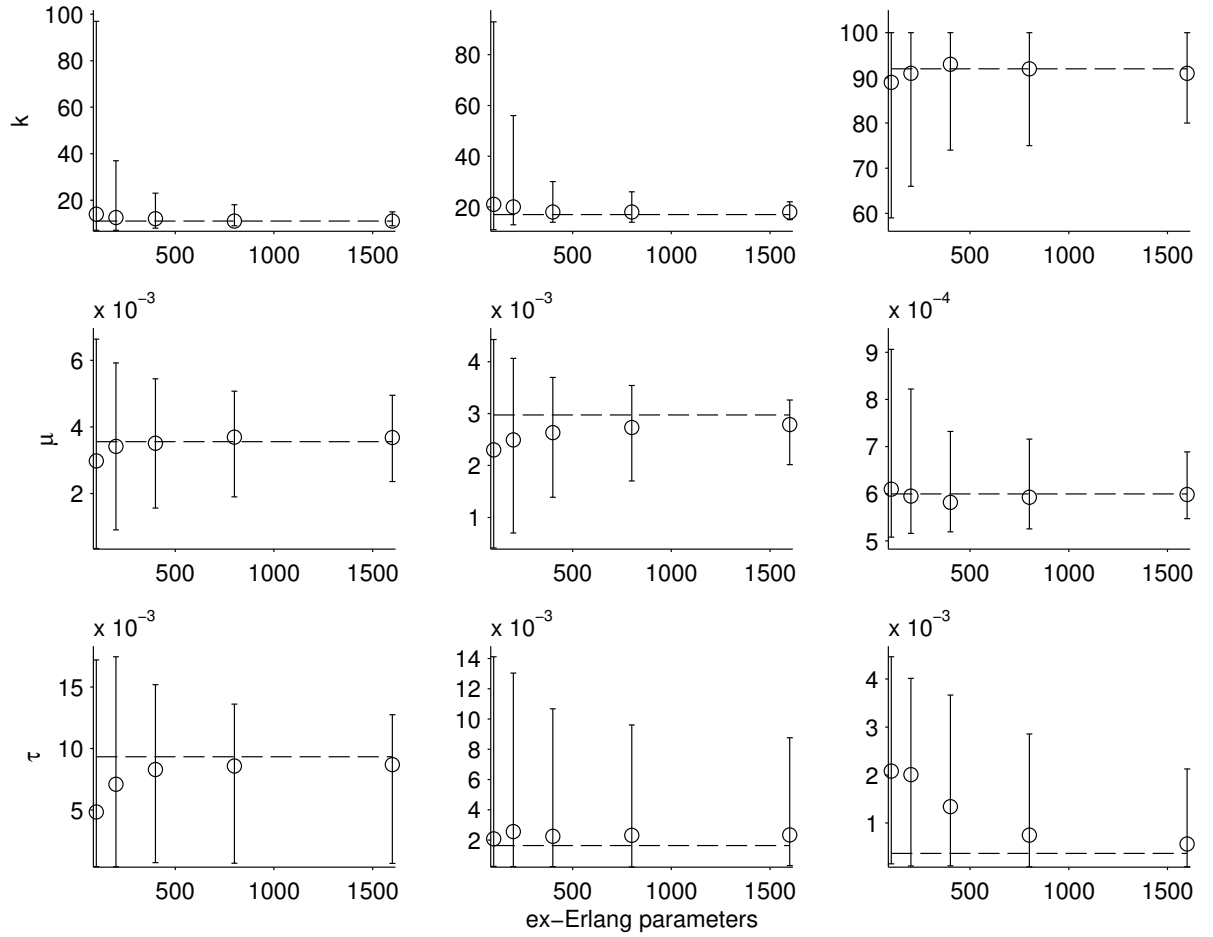

Figure 4.8: Sample size versus ex-Erlang parameter estimates. Median (circle) along with the 2.5th and 97.5th percentiles (error bars) of parameter estimates from Monte Carlo samples. Results are reported for each parameter according to sample size for 3 different distributions ($k_1 = 11$, $\mu_1 = 3.557\text{e-}03$, $\tau_1 = 9.325\text{e-}03$; $k_2 = 17$, $\mu_2 = 2.973\text{e-}03$, $\tau_2 = 1.647\text{e-}03$; $k_3 = 92$, $\mu_3 = 5.993\text{e-}04$, $\tau_3 = 3.671\text{e-}04$) and are based on 500 estimations. The dashed line is the true parameter value.

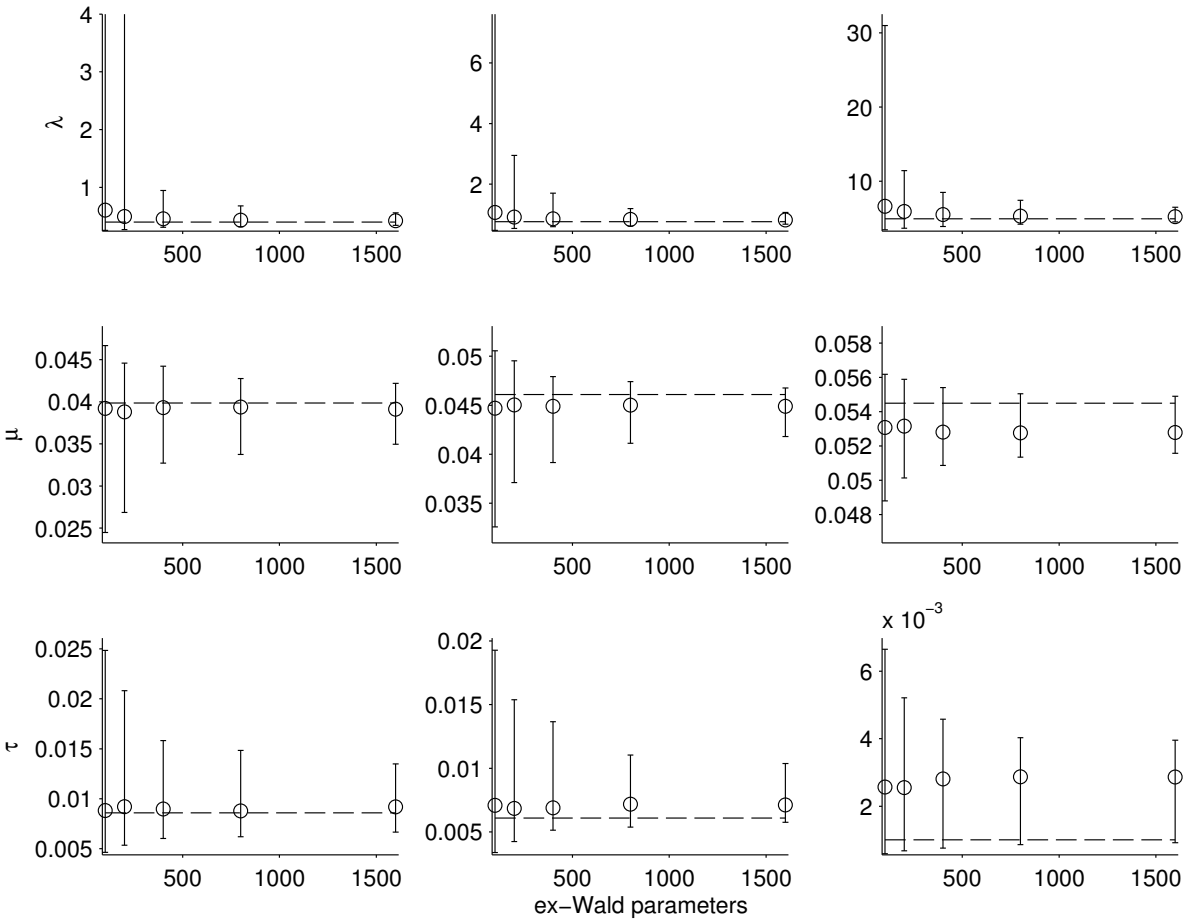

Figure 4.9: Sample size versus ex-Wald parameter estimates. Median (circle) along with the 2.5th and 97.5th percentiles (error bars) of parameter estimates from Monte Carlo samples. Results are reported for each parameter according to sample size for 3 different distributions (λ_1 = 0.400, μ_1 = 3.985e-02, τ_1 = 8.603e-03; λ_2 = 0.761, μ_2 = 4.610e-02, τ_2 = 6.089e-03; λ_3 = 4.934, μ_3 = 5.450e-02, τ_3 = 1.006e-03) and are based on 500 estimations. The dashed line is the true parameter value. Note the y axis limits for λ_1 and λ_2 have been cropped at $10 \times \lambda_{true}$ so that intervals for the larger sample sizes are visible.

4.3.3.2 Probability distribution fits

Based on the mean KLD, ex-Wald is the best fitting probability distribution (Table 4.8). However, there is not much difference between several distributions, with normalised pairwise comparisons to the ex-Wald KLD indicating that the majority of distributions will, at times, fit as well or better (Table 4.8).

Table 4.8: Mean Kullback-Leibler divergence (KLD) and normalized pairwise differences between ex-Wald KLD and other theoretical distributions ($\bar{x}(min, max)$).

	Raw	**Pairwise**
Refractory Exponential	-13.6483	0.0432 (0.0216, 0.0715)
Normal	-14.2308	0.0028 (-0.0007, 0.0087)
Birnbaum Saunders	-14.2666	0.0003 (0.0000, 0.0009)
Erlang	-14.2648	0.0004 (-0.0011, 0.0016)
Loglogistic	-14.2475	0.0017 (-0.0008, 0.0040)
Lognormal	-14.2661	0.0003 (-0.0000, 0.0009)
Weibull	-14.1730	0.0069 (-0.0004, 0.0123)
Wald	-14.2665	0.0003 (0.0000, 0.0009)
offset Birnbaum Saunders	-14.2673	0.0003 (-0.0001, 0.0009)
offset Erlang	-14.2700	0.0001 (-0.0011, 0.0008)
offset Loglogistic	-14.2484	0.0016 (-0.0008, 0.0037)
offset Lognormal	-14.2668	0.0003 (-0.0000, 0.0009)
offset Weibull	-14.2658	0.0003 (-0.0028, 0.0034)
offset Wald	-14.2670	0.0003 (-0.0001, 0.0009)
ex-Gaussian	-14.2624	0.0006 (-0.0008, 0.0027)
ex-Birnbaum Saunders	-14.2678	0.0002 (-0.0011, 0.0013)
ex-Erlang	-14.2677	0.0002 (-0.0001, 0.0009)
ex-Loglogistic	-14.2558	0.0011 (-0.0008, 0.0026)
ex-Lognormal	-14.2673	0.0003 (-0.0000, 0.0009)
ex-Weibull	-14.2515	0.0014 (-0.0012, 0.0043)
ex-Wald	-14.2709	-

We further investigated a subset of best fitting models Birnbaum Saunders (BS), Erlang (Er), Lognormal (LN), Wald (W) and their offset and exponentially convolved counterparts. Table 4.9 reinforces there is very little difference in how well this subset of distributions fits electrosensory afferent data. The majority of analysed spike train segments passed the KS test for uniformity of transformed event times for the entire subset of best fitting distributions. Likewise, although the proportion of segments passing the KS test for uniformity of transformed inter event intervals (Berman's test) was lower, there was little difference between the distributions.

Table 4.9: Kolmogorov-Smirnov (KS) tests for fittings of observed ISIs to theoretical distributions

	Uniform	**Berman**
Birnbaum Saunders	28 (93%)	22 (73%)
Erlang	26 (87%)	26 (87%)
Lognormal	28 (93%)	22 (73%)
Wald	28 (93%)	22 (73%)
offset Birnbaum Saunders	28 (93%)	22 (73%)
offset Erlang	27 (90%)	24 (80%)
offset Lognormal	28 (93%)	22 (73%)
offset Wald	28 (93%)	22 (73%)
ex-Birnbaum Saunders	28 (93%)	22 (73%)
ex-Erlang	28 (93%)	23 (77%)
ex-Lognormal	28 (93%)	22 (73%)
ex-Wald	27 (90%)	22 (73%)

The BS, Er, LN and W distributions can all approximate a Gaussian or slightly skewed Gaussian, but in all cases fits were improved slightly by adding in an offset (Figure 4.10). With the exception of offset Erlang (the second best fit), the exponential convolutions outperformed the corresponding distributions with an arbitrary delay. Figure 4.11 suggests that the subset of distributions is equivalent for more normal-like distributions (low CV) and the slight differences between distributions become more apparent as variability is increased (high CV).

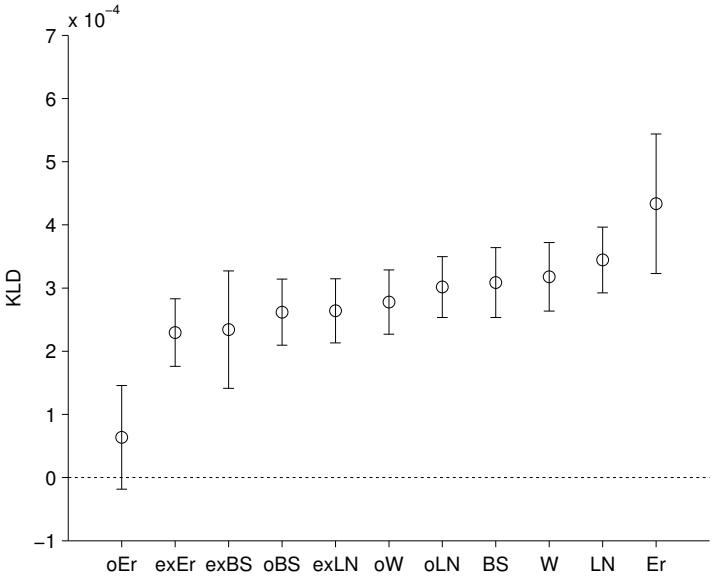

Figure 4.10: Normalized pairwise differences between ex-Wald Kullback-Leibler divergence (KLD) and other theoretical distributions, $\bar{x} \pm SE$. Birnbaum Saunders (BS), Erlang (Er), Lognormal (LN), Wald (W), offset Birnbaum Saunders (oBS), offset Erlang (oEr), offset Lognormal (oLN), offset Wald (oW), ex-Birnbaum Saunders (exBS), ex-Erlang (exEr), ex-Lognormal (exLN).

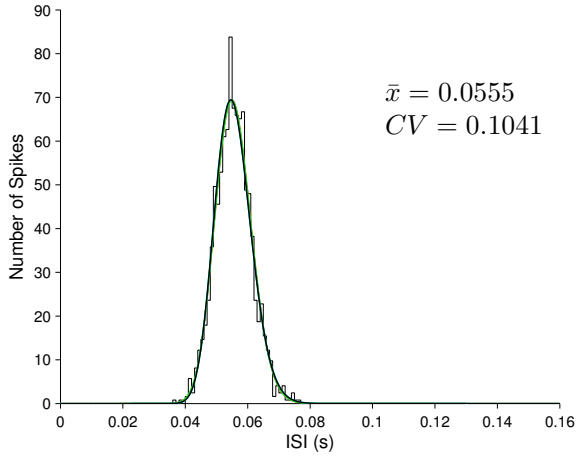

(a)

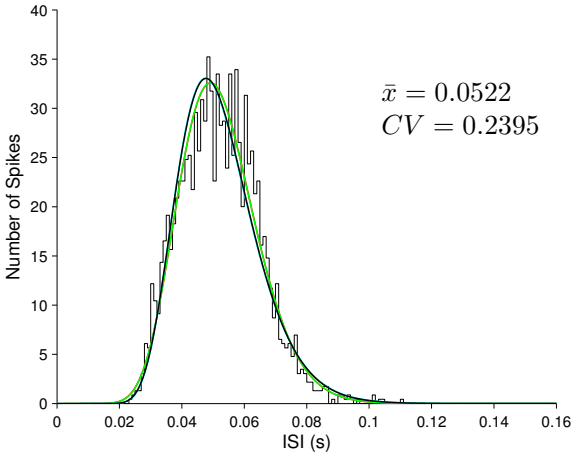

(b)

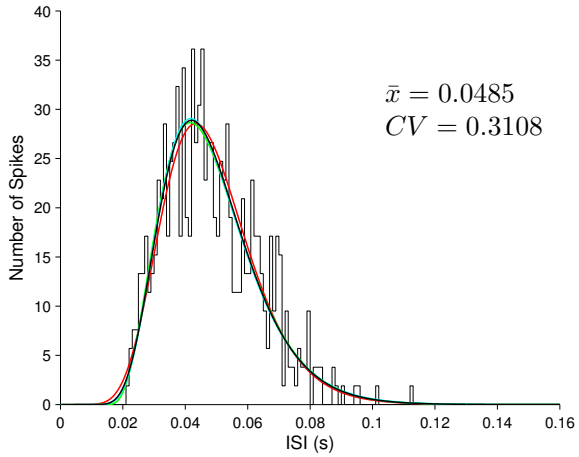

(c)

Figure 4.11: Interspike interval (ISI) histograms binned at 1 ms resolution, with fits overlaid. Offset Erlang (green), offset Wald (cyan), ex-Erlang (red), ex-Wald (black).

We looked at the relationship between normalized pairwise differences between ex-Wald KLD and CV for several probability distributions (Figure 4.12). For the couple of spike trains with lowest CV, oEr and exBS provided slightly better fits than exW, whereas differences between exW and the oBS, oW and exEr distributions were essentially non-existent. For the majority of the midrange CVs (~0.125 to 0.224) exW provided the best fit. However, there was a negative linear relationship between the normalized pairwise differences for oBS, oEr, oW, exEr and CV, implying that the goodness of fit of the alternative distributions approached that of exW for spike trains with the highest CV (Figure 4.12). In the case of oEr (the second best candidate model) this trend suggests oEr may provide as good, or better fit than exW for CVs in the mid to upper range (~0.225 to 0.311).

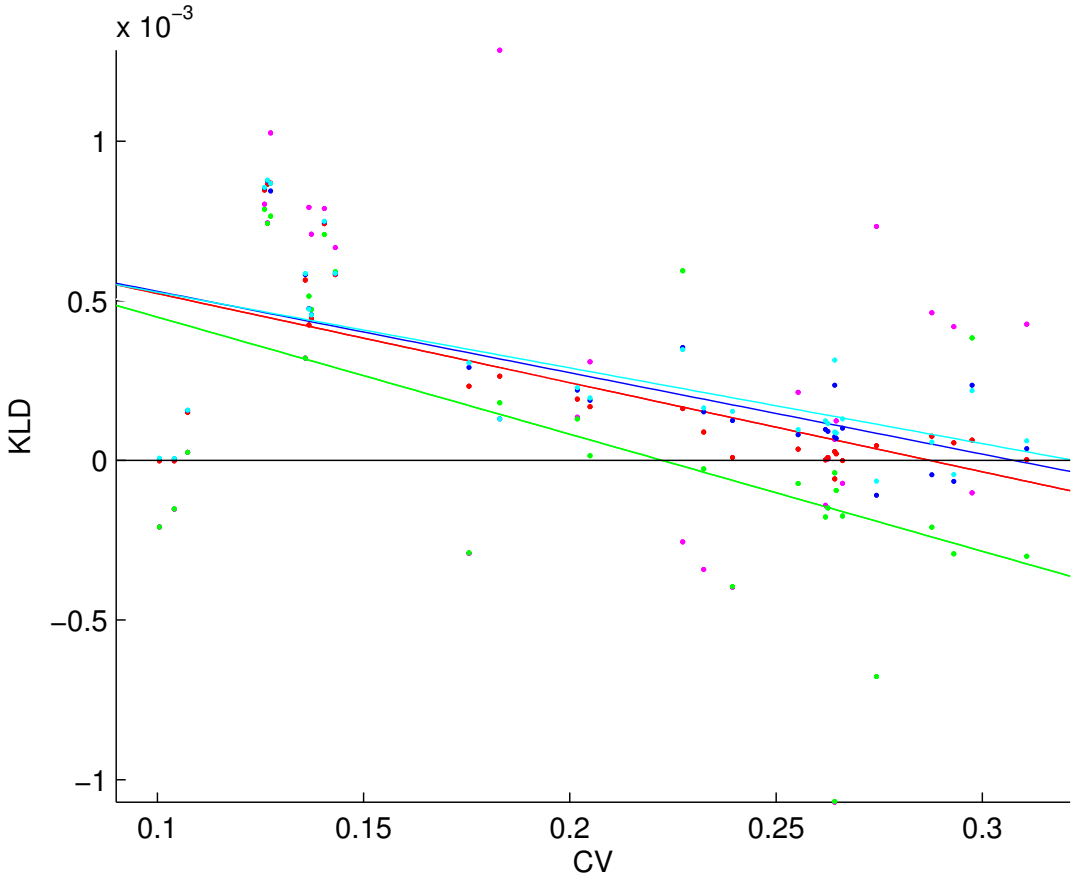

Figure 4.12: Normalized pairwise differences between ex-Wald Kullback-Leibler divergence (KLD) and other theoretical distributions as a function of Coefficient of Variation (CV). Positive values indicate worse fitting relative to ex-Wald, negative values indicate better. Offset Birnbaum Saunders (blue; $KLD = 0.000785 - 0.00255CV$, $r^2 = 0.375$, $p = 0.00032$), offset Erlang (green; $KLD = 0.00826 - 0.00367CV$, $r^2 = 0.316$, $p = 0.00123$), offset-Wald (cyan; $KLD = 0.000764 - 0.00237CV$, $r^2 = 0.375$, $p = 0.000666$), ex-Birnbaum Saunders (magenta; no significant linear relationship p=0.0859), ex-Erlang (red; $KLD = 0.000802 - 0.00279CV$, $r^2 = 0.429$, $p = 8.49e - 05$).

Fitted offset Erlang models have a mean offset of 0.0105 ± 0.0087 s ($\bar{x} \pm SD$), fitted offset Wald models have a mean offset of 0.0019 ± 0.0051 s, and fitted offset Birnbaum-Saunders models have a mean offset of 0.0023 ± 0.0052 s. These offsets are symptomatic of a discrepancy between the two-parameter duration distributions and the data. For any given neuron, the offset required to place a model with the best-fitting shape in the best-fitting location along the time axis is a fixed time period, which can be large relative to the neuron's inter-spike intervals. Realistic interpretation of such a model implies that each neuron has a precise internal clock, allowing it to wait for a specified time after a spike before initiating a process that will trigger the following spike. It seems implausible that neuronal inter-spike interval distributions would be generated by a combination of a timer with clock-like regularity followed by a stochastic process with high variability.

Based on this analysis we conclude that while other distributions may provide better fits for specific spike train segments, looking at the entire data set ex-Wald is the best fit out of the candidate models we tested. Ex-Wald provides a model capable of capturing the variability observed in spontaneous activity of electrosensory primary afferents (Figure 4.13).

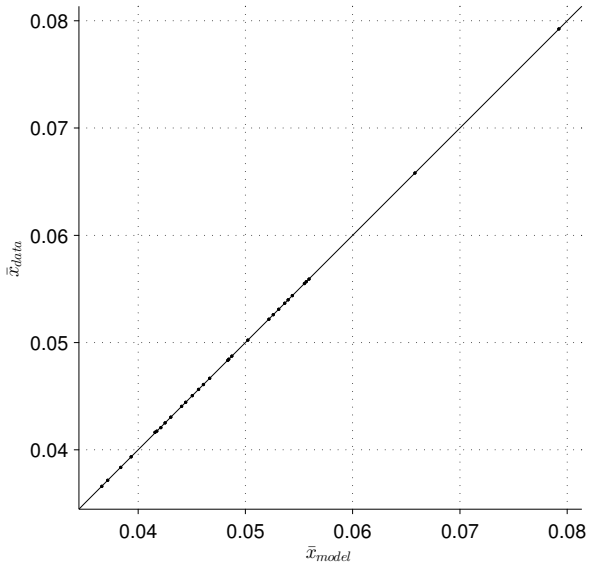

(a)

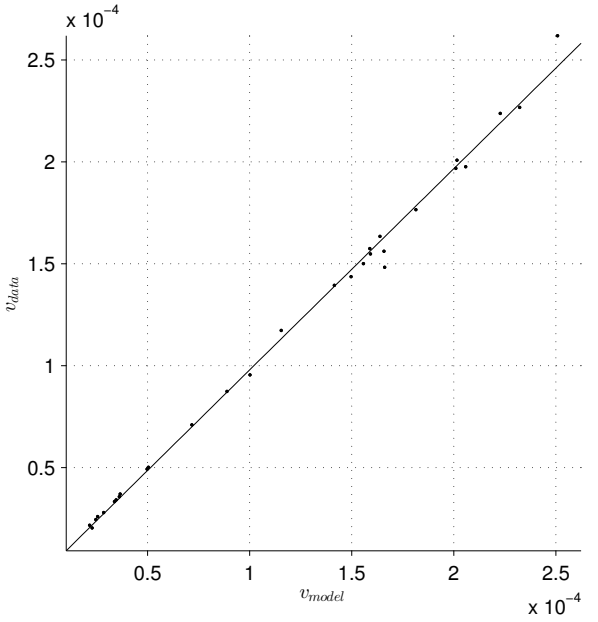

(b)

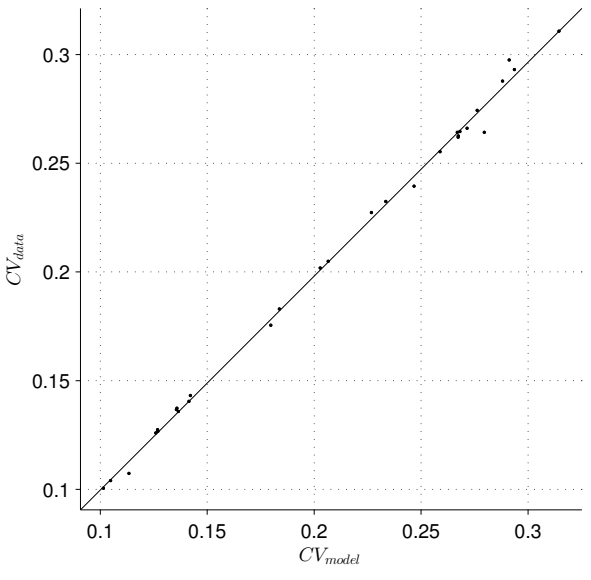

(c)

Figure 4.13: Relationship between Ex-Wald theoretical and observed data moments. Figure 4.13a shows a positive linear relationship between the model mean and data mean ($\bar{x}_{data} = 1.000\bar{x}_{model} + 4.565e-06$, $r^2 = 1.000$, $p = 1.41e-79$). Figure 4.13b shows a positive linear relationship between the model variance and data variance ($v_{data} = 0.987v_{model} - 6.997e-07$, $r^2 = 0.996$, $p = 2.47e-35$). Figure 4.13c shows a positive linear relationship between the model coefficient of variation (CV) and data CV ($CV_{data} = 0.984CV_{model} + 0.001$, $r^2 = 0.997$, $p = 1.25e-37$).

4.3.3.3 Relationships between parameters

Having identified ex-Wald as the best fitting candidate model, we now consider the implications of this distribution in the context of sensory processing models. All three parameters in the ex-Wald distribution have dimensions of time. No natural distinction exists between predictor and response variables when investigating interactions between ex-Wald parameters, so we used Principal Component Analysis (PCA) to fit a linear regression. In the case of electrosensory afferents, the combination of PC1+PC2 mainly describes the relationship between λ and τ which explains 98.81% of the variance (Figure 4.14). PC3, the error term in the regression, mainly consists of μ and accounts for the remaining 1.19% of variance (Figure 4.14).

This analysis implies that μ (the mean censoring time) is largely independent of the other two parameters. The fitting of power laws using linear regression on log-transformed data further supports μ being relatively constant ($\mu = 0.044 \pm 0.008$; $\bar{x} \pm SD$). μ is independent of τ (Figure 4.14a) and shows no to weak correlation with λ (Figure 4.14b). μ is less variable relative to λ ($\lambda = 1.681 \pm 1.444$) and τ ($\tau = 0.005 \pm 0.003$). Mean λ scales with $1/\tau^{0.889}$ (Figure 4.14c).

Censoring mean, μ, has a strong linear relationship with the ISI mean (Figure 4.15b), suggesting that the relatively constant μ may be due to spontaneous activity having a reasonably constant firing rate. While τ also shows a positive linear relationship with ISI mean, the relationship is much weaker due to the high variability in τ for a given firing rate (Figure 4.15a). The interaction between τ and λ is reinforced when examining the relationships of these parameters with data CV. Figure 4.15c shows that CV scales proportional to $\tau^{0.464}$, but has a slightly stronger relationship with λ in the opposite direction (CV$\sim\lambda^{-0.438}$; Figure 4.15d). τ appears to be mainly influencing the variability of the ISI distribution, with a strong positive linear relationship between τ and variance (Figure 4.15e).

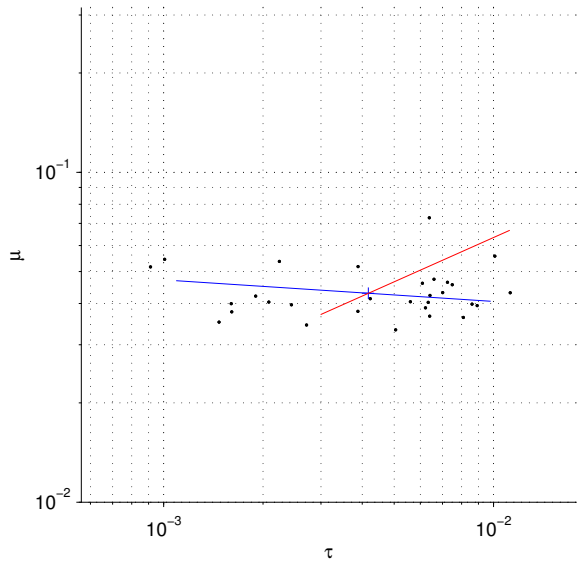

(a)

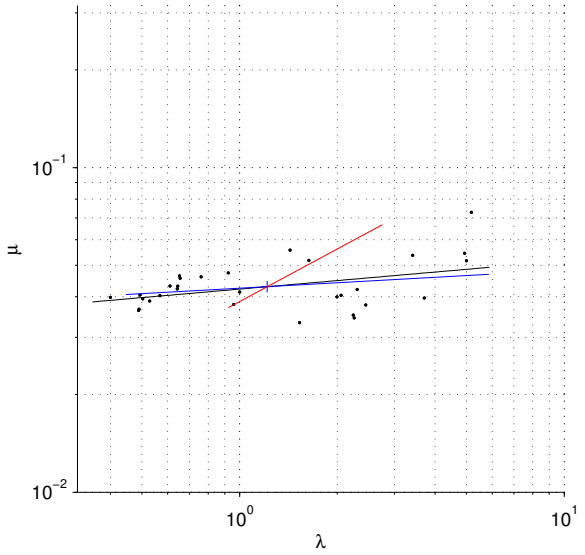

(b)

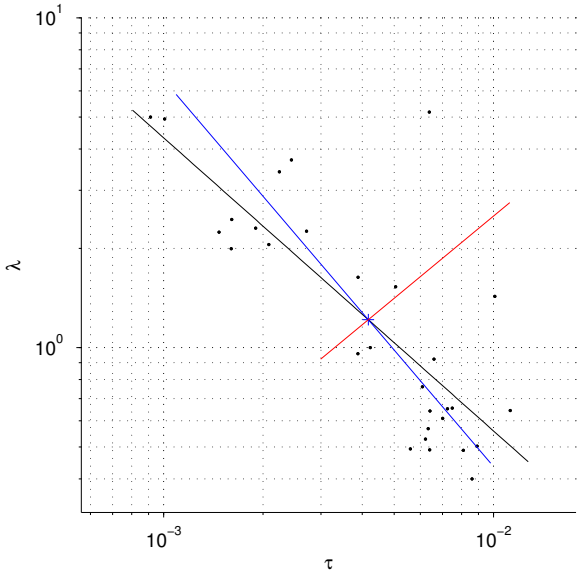

(c)

Figure 4.14: Ex-Wald parameter correlations investigated via power law regression and orthogonal regression using Principal Components Analysis (PCA). Black line=power law fit, Blue line=PC1, Red line=PC2. PC1 accounts for 87.48% of variance, PC2 accounts for 11.33%, leaving 1.19% to be explained by PC3. Figure 4.14a shows no significant relationship between τ and μ (power law fit p=0.991; posterior probability ratio $\mu(\tau)$=1.027). Figure 4.14b shows a weak to non-significant positive relationship between λ and μ (power law fit: $\mu = 0.042\lambda^{0.087}$, $r^2 = 0.172$, p=0.023; posterior probability ratio $\mu(\lambda)$=0.061). Figure 4.14c a significant negative relationship between τ and λ (power law fit: $\lambda = 0.009\tau^{-0.889}$, $r^2 = 0.618$, p=2.637e-07; posterior probability ratio $\lambda(\tau)$=9.931e-07).

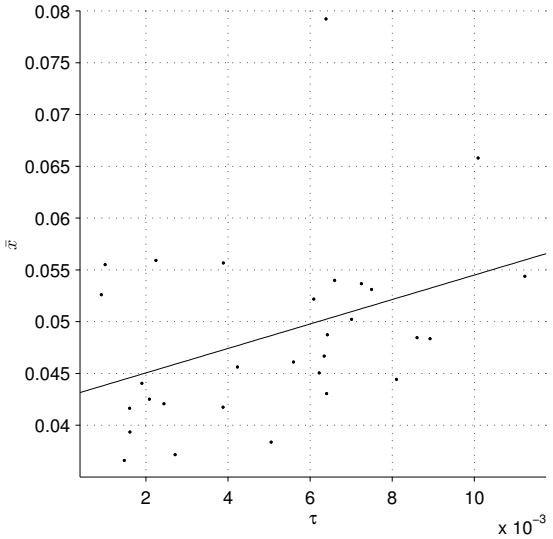

(a)

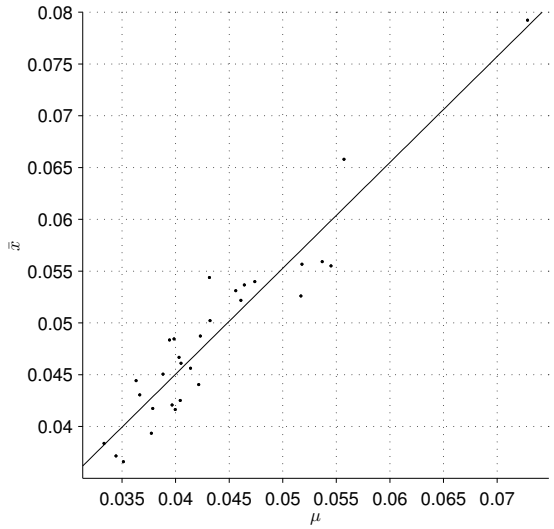

(b)

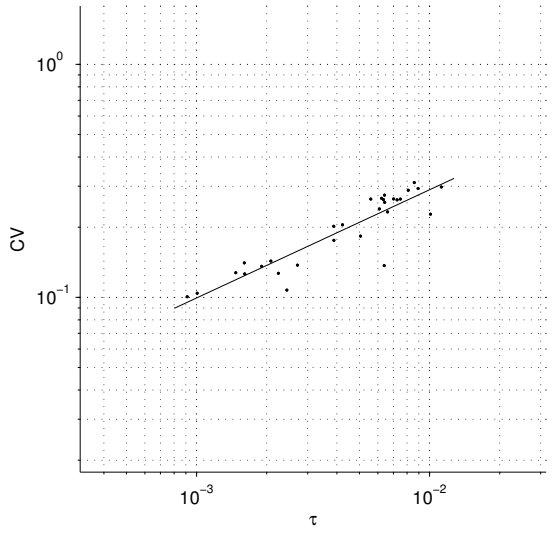

(c)

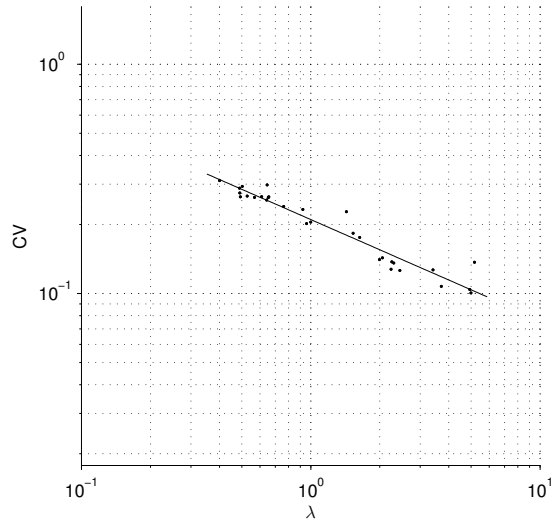

(d)

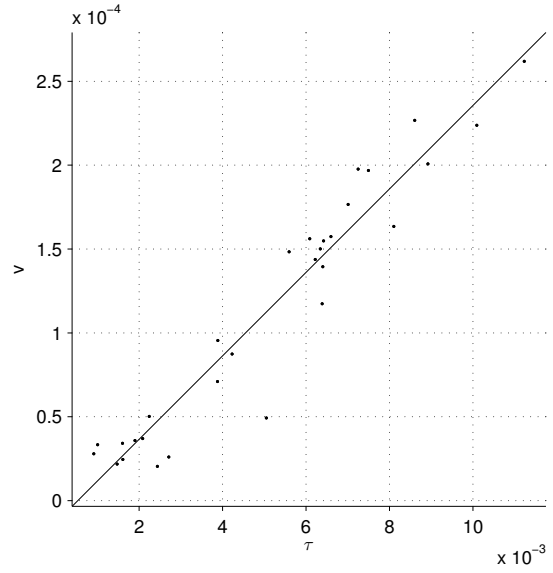

(e)

Figure 4.15: Relationship between Ex-Wald parameters and data moments. Figure 4.15a shows a positive linear relationship between τ and the data mean ($\bar{x} = 1.181\tau + 0.043$, $r^2 = 0.148$, $p = 0.036$). Figure 4.15b shows a positive linear relationship between μ and the data mean ($\bar{x} = 1.022\mu + 0.004$, $r^2 = 0.895$, $p = 3.24e-15$). Figure 4.15c shows a positive power law relationship between τ and the data CV ($CV = 2.457\tau^{0.464}$, $r^2 = 0.820$, $p = 6.37e-12$). Figure 4.15d shows a negative power law relationship between λ and the data CV ($CV = 0.210\lambda^{-0.438}$, $r^2 = 0.932$, $p = 6.62e-18$). Figure 4.15e shows a positive linear relationship between τ and the data variance ($v = 0.025\tau - 1.32e-05$, $r^2 = 0.926$, $p = 2.36e-17$).

4.4 Discussion

Previous studies in elasmobranchs have noted that spontaneous activity of primary afferents is reasonably regular, but not normally distributed. However, these studies have generally focussed on the mean, variance, and in rare cases the higher order moments, to assess the normality of the ISI distribution. In the present study we use these metrics to investigate the firing rate and its variability and compare our results to the existing literature. Additionally, we fit several two-parameter probability distributions commonly used in neuroscience literature, as well their offset counter parts and the lesser known convolutions of the two-parameter distributions with an exponential random variable. We compare the goodness of fit of these distributions to probability models from other afferents and interpret the potential implications for sensory processing. Our results show that spontaneous activity in electrosensory afferent neurons can be accurately modelled as inverse Gaussian-censored Poisson processes.

4.4.1 Spontaneous firing rate and its variability

Primary afferent neurons in a variety of sensory systems exhibit spontaneous activity in the absence of any stimulus. This discharge plays an important role in the sensitivity and response properties of electrosensory afferents [Tricas & New, 1998].

The average discharge rate from our study on adult little skates, *L. erinacea*, was 21.3 spikes s^{-1} at 12 °C. Spike rate was greater than the previously reported values from the same species of 1.67 spikes s^{-1} [Conley & Bodznick, 1994] and 8.6 spikes s^{-1} [New, 1990], likely due in part to the higher experimental temperature. Despite being at a lower temperature, the discharge rate was higher than that of *P. triseriata*, which averaged 15 to 18 spikes s^{-1} at 16 to 18 °C [Montgomery, 1984a,b]. Conversely, the discharge rate was lower than that of *U. halleri* at 34.2 spikes s^{-1} [Tricas & New, 1998], *R. eglanteria* at 44.9 spikes s^{-1} [Sisneros *et al.*, 1998] and *D. sabina* at 52.1 spikes s^{-1} [Sisneros & Tricas, 2002b].

While there are reasonably large differences in values reported for spontaneous firing rate, variability as reflected in CV values appears to be relatively conserved across species and different conditions. The CV of afferent units in our study on *L. erinacea* ranged from 0.104 to 0.464 (0.215 ± 0.076; $\bar{x} \pm SD$) in raw spike trains. This range was reduced slightly (0.100 to 0.311; 0.205 ± 0.069) when only segments of spikes trains that passed the renewal process tests were retained. These values are very similar to those reported for adult *R. eglanteria* [0.20 ± 0.03; Sisneros *et al.*, 1998], *D. sabina* [0.163 ± 0.057; Sisneros & Tricas,

2002b] and *U. halleri* where CV ranged from 0.13 to 0.34 [0.22±0.04; Tricas & New, 1998]. The majority of research has been conducted on skates and rays, however steady state discharge of the dogfish, *S. canicula*, has also been examined under different temperatures and static electric currents. While the mean ISI was dependent on temperature and on current strength, the CV under all conditions investigated was near constant, between 0.20 and 0.30 [Bromm *et al.*, 1975]. We found no significant trend between mean ISI and CV, whereas Tricas & New [1998] found slower units exhibited greater regularity. However the authors questioned the biological significance of the relationship due to the high variability in CV among units with a given mean.

Afferents from adult skates and rays exhibit reasonably regular discharge. However, both ontogenetic and seasonal variation in activity has been demonstrated. Male Atlantic stingrays, *D. sabina*, show a decrease in CV (increase in regularity) corresponding to onset of the reproductive season, while there was no difference in discharge rates [Sisneros & Tricas, 2000]. This seasonal change in afferent activity is mirrored by the ontogenetic changes. Discharge rate remains constant, but variability decreases from the neonate to juvenile stages [Sisneros & Tricas, 2002b]. Similarly, variability decreases from the embryonic to juvenile stages in clearnose skates, *R. eglanteria*, which is coupled with an increase in discharge rate [Sisneros *et al.*, 1998]. These differences in afferent properties have been hypothesized to represent adaptive plasticity in the electrosensory system, enhancing an individuals fitness by allowing young animals to detect potential predators and adult animals to detect potential mates [Sisneros & Tricas, 2002a]. Regular afferents encode information about steady state or slowly varying stimuli, whereas irregular afferents are more suited to encoding higher frequency.

Afferent discharge of other octavolateralis senses also display greater diversity in variability. Whereas elasmobranch electrosensory afferents are mainly classed as regular, mechanosensory lateral line afferents in *D. sabina* exhibit regular ($CV < 0.40$), irregular ($CV > 0.40$, $g_1 > 0$) and silent (only respond when stimulated) discharge patterns. The variability of spontaneous discharge appears to be linked to neuromast position as well as morphology, with ventral non-pored canals having a greater proportion of silent units than pored canals (either ventral or dorsal) and dorsal canals showing more irregular units than ventral canals [Maruska & Tricas, 2004]. The greater diversity in afferent responses may be due to differences in stimulus characteristics. Water movement is complex, consisting of both high and low frequency components. Therefore, diversity in responses of neuromasts at different locations may allow individuals to sample the spectrum of frequencies available to the lateral line system [Maruska & Tricas, 2004].

In addition to rate and variability, higher order moments (skewness g_1 and kurtosis g_2)

have been used to assess the normality of electrosensory afferent discharge [Tricas & New, 1998]. It was found ISI distributions in *U. halleri* ranged from bilaterally symmetrical ($g_1 \approx 0.08$) at low CV values, to slightly right skewed ($g_1 \approx 0.71$) in intermediate to highest CV units. We found for the pruned spike trains in *L. erinacea* skewness increased linearly in relation to CV with minimum value near normal (0.091). The maximum value (1.589) never reached the skewness of an exponential distribution ($g_1 = 2$). Regardless of CV, Tricas & New [1998] found most units were found to be leptokurtotic ($g_2 > 0$). However, while this was also the case for the majority of our ISI distributions, we also found some platykurtotic distributions (10/30 units had $g_2 < 0$). Tricas & New [1998] suggested that leptokurtotic distributions indicated more ISI concentrated near the mean than expected from a normal distribution, implying a high degree of regularity. While this is likely the case, leptokurtotic distributions can also indicate more items in the tails, whereas platykurtotic distributions have fewer items near the mean and in the tails and more items in the intermediate regions [Sokal & Rohlf, 1981]. We attempted to avoid some of the ambiguity in examining distribution moments by fitting probability density functions to the ISI distribution.

4.4.2 Spontaneous activity as a stochastic process

Regarding spontaneous activity from the dogfish, *S. canicula*, Bromm & Tagmat [1977] state "The interspike interval distributions of steady state discharges in the Lorenzinian ampulla followed a Gamma probability density function with small disturbances, thus usually a Gaussian description was sufficient [Bromm *et al.*, 1975]". However, in our examination of Bromm *et al.* [1975], there was no description of ISI distributions beyond mean, standard deviation, CV and ISI histograms. Thus, it is likely the description of distributions as Gamma to Gaussian -like was made solely based on visual inspection. Beyond this description, to our knowledge elasmobranch electrosensory afferent responses have not been examined as a stochastic process. However, electroreception has independently evolved multiple times in many taxa of fishes and amphibians [Baker *et al.*, 2013]. Additionally, the electric sense belongs to the octavolateralis senses, hence it is related to the other specialised hair cell-based systems (lateral line, auditory and vestibular), as they share evolutionary and developmental origins [Gillis *et al.*, 2012]. We now compare our findings on spontaneous activity as a stochastic process firstly to electroreception in other vertebrates and finally to the other octavolateralis senses.

Ampullary electroreceptors, hypothesized to be homologous to the ampullae of Lorenzini, are found in wide variety of non-teleost fish, spanning several different taxonomic

groups [Baker *et al.*, 2013]. In contrast to elasmobranchs which rely solely on ampullary electroreceptors, weakly electric fish possess two classes of receptor, ampullary and tuberous. Tuberous receptors are specialized for active electrolocation and communication, thus are tuned to high frequencies within the range of the species own electric organ discharge [Hagiwara *et al.*, 1965]. Ampullary organs are similar to elasmobranch electroreceptors in that they are sensitive to the low frequency environmental electric fields [Suga, 1967]. Research conducted on the ampullary organs of two species of Catfish, *Claris guriepinus* and *Ictahrus nebulosus*, illustrated spontaneous activity can be well fitted by a Gamma distribution [Teunis *et al.*, 1990, 1991a]. In both species it was suggested that spontaneous spiking results from a limited number of membrane events, whereby Stein's model was proposed as a description of the possible firing mechanism responsible for stochastic fluctuations [Teunis *et al.*, 1990, 1991a]. The Gamma shape parameter corresponds to the firing threshold of the spike generator and Gamma scale parameter corresponds to the input rate of synaptic quanta [Teunis *et al.*, 1991b]. Experimental manipulation of the mean firing rate revealed differing trends in the Gamma parameters, depending on the stimulus strength [Teunis *et al.*, 1991b].

Whereas electroreception involves physiological responses of the same form as the stimuli, other octavolateralis senses convert various mechanical stimuli into physiological responses through mechanoelectrical transduction. Lateral line afferents in Zebrafish, *Danio rerio*, exhibit spontaneous spiking which has been shown to result from hair cell neurotransmission [Trapani & Nicolson, 2011]. These neurons show Poisson-like behaviour, with no bursting or rhythmic spiking and ISI histograms being fit by either a single-phase or two-phase exponential decay equation [Trapani & Nicolson, 2011, note these equations were fit to the peak of the histogram, so the single phase exponential would be equivalent to our refractory exponential (eq. (4.2))]. Further research suggests that fits achieved with a two-phase exponential were no better than with a single exponential decay [Levi *et al.*, 2015]. Similar to the stingray lateral line mechanoreceptors, auditory afferents in the midshipman fish, *Porichthys notatus*, exhibit heterogeneity with regular, irregular and silent ISI distributions. Sisneros & Bass [2003] classified any units with ISIs that were normally distributed as regular. However, the remaining spontaneously active neurons were classified as irregular, with no further description of the ISI distribution.

4.4.3 Spontaneous activity as a censored Poisson process

Our results show that spontaneous activity in electrosensory afferent neurons can be accurately modelled as inverse Gaussian-censored Poisson processes. This family of probability distributions was derived to model response time distributions in human decision-making, and called the ex-Wald (convolution of an exponential and Wald) distribution [Schwarz, 2001, 2002]. The same result has been found in mammalian vestibular semicircular canal afferent neurons, which exhibit greater heterogeneity in ISI distributions than skate electrosensory afferents [Hoffman & Paulin [2015]; Paulin *et al.* [2016]; Appendix B].

By using KLD as a fitting metric we selected the model that best describes how uncertainty about when the next spike will occur is distributed over time since the last spike. This distribution is required in order to infer causal parameters of the interval distribution, including state variables of stimulus sources, from observed spike times. Ex-Wald is the best among the candidate models that we considered. The two next-best biologically plausible candidates are ex-Erlang and ex-Birnbaum-Saunders models. These are also censored Poisson processes. Both the Erlang and Wald distributions are members of the Generalized Inverse Gaussian (GIG) family of probability distributions [Leiva *et al.*, 2015]. The GIG family are time-to-barrier distributions for drift-diffusion processes, which are common models for neuronal spiking with a straightforward biophysical interpretation [Xing *et al.*, 2015]. The Birnbaum-Saunders distribution is not a member of the GIG family, but rather the cumulative damage family [Leiva *et al.*, 2015]. However, it has been argued that as the Birnbaum-Saunders distribution models a Wiener process of accumulated fatigue in time (with positive drift) it can be viewed as an approximation to the inverse Gaussian, under certain parameterizations [Bhattacharyya & Fries, 1982]. The parameters of both the Birnbaum-Saunders and inverse Gaussian distributions may be linked to values with biological interpretations via the integrate-and-fire model of neuron spiking [Leiva *et al.*, 2015].

The cluster of censored Poisson models at the top of our ranking suggests that, even if the ex-Wald model is not exact, spiking in electrosensory afferent neurons involves a Poisson process censored by a drift-diffusion process. The model implies that there is an underlying Poisson process with a high mean rate, ranging from about 100Hz to about 1KHz in different afferents, and a drift-diffusion process that suppresses events in the Poisson process, or at least prevents them from appearing at the output, until it reaches a threshold point.

The range of frequencies represented by the Poisson component (0.1 - 1KHz) matches the low pass filtering bandwidth of ampullary sense organs in rays [Waltman, 1966].

This is the expected output bandwidth of ampullary organs given thermal noise inputs, suggesting that the Poisson component of spontaneous afferent spike trains is, ultimately, a response to thermal noise in sensory coupling and transduction [Basano & Ottonello, 1975]. The fluctuation-dissipation theorem then implies that the Poisson component carries information about the response of afferents to small stimuli [Kubo, 1966; Marconi *et al.*, 2008]. The mean interval, τ, is a sufficient statistic for a Poisson process, which means that the posterior density of this single parameter captures all of the information that a spike train sample contains about causal parameters of the process that generated it [Zacks, 2014].

Individual electrosensory afferent spike trains are not samples from a Poisson processes, rather they appear to be random sub-samples of this process. The censoring distribution (Wald, or other) in effect pulls out a random sub-sample of spikes in the Poisson process, so it is transmitted to the brain in random pieces. We hypothesise that censoring occurs because rapid spiking (as required by extremely short intervals being most likely in a Poisson process) is energetically inefficient. Breaking up information between a group of neurons, transmitting in parallel, allows individual neurons to spike at a near optimal rate [Balasubramanian, 2015]. Therefore a group of sensory afferent neurons converging to a secondary neuron can be thought of as a "super-afferent" that delivers a Poisson sample to the brain. The "super-afferent" delivers information more efficiently than a single afferent could, in a form that would allow neurons there to perform Bayesian inference in a simple, natural way.

This abstract model may provide a useful framework for investigating not only central mechanisms of inference in electroreception (see Chapter 5), but also peripheral mechanisms of sensory transduction and spike coding. The fact that one model has been found to fit octavolateralis neuron firing patterns on two distinct branches of the vertebrate phylogenetic tree, elasmobranch electroreception (here) and mammalian vestibular system [Hoffman & Paulin [2015]; Paulin *et al.* [2016]; Appendix B], suggests that the model may extend to all vertebrate octavolateralis senses, including in particular the mammalian auditory system, whose sensitivity to acoustic energy rivals the elasmobranchs' sensitivity to electrical energy [Bialek, 1987; Chen *et al.*, 2011].

Chapter 5

Bayesian inference in the elasmobranch electrosensory system

5.1 Introduction

The brain receives a continual stream of data from a variety of sensory modalities. Understanding the basis of sensory systems and information processing in the brain is a central part to modern neuroscience research. However, how the brain organizes this incoming in information from sense organs and controls muscles to produce a properly coordinated responses remains unclear [Kayser & Shams, 2015]. In interacting with the world the brain faces two key challenges. Firstly, perception usually relies on the integration of cues from multiple different sensory systems, each providing a noisy and potentially biased estimate about the state of the world [Kayser & Shams, 2015]. Secondly, the brain must perform causal inference, that is decide which sensory inputs likely had the same source of origin [Kayser & Shams, 2015]. In this chapter, causes are world states, including body states, and the effect is a sensory spike train.

The elasmobranch electrosensory system provides a simple model to examine the mechanisms underlying causal inference in the vertebrate brain. The electric sense belongs to the octavolateral system and hence shows similarities to the vestibular, lateral line and auditory systems [Bodznick & Montgomery, 2005]. Transduction in elasmobranch electroreceptors is mediated by sensory hair cells, thus comparative analysis may provide insight into hair cell mechanisms elsewhere. Electroreception allow us to examine the flow of information from peripheral sensory structures, to the destination brain centres [Bullock, 1993]. Whereas hair cells in the vestibular, lateral line and auditory systems all receive feedback from the brain, electroreceptors lack any sign of such efferents [Bul-

lock, 1993]. In ampullary electroreception measurements are passive, with the stimulus strength falling off predictably as a function of distance. Given the lack of efferents, sensors encode the measurement process undistorted by feedback from the brain.

In early electrosensors, the scenario is further simplified as the only other sources of electric fields would have been other slowly moving living things. The electrosensory signal would therefore reliably indicate the distance and direction of other animals. Early sensory neurons likely evolved as simple threshold detectors, therefore we can begin with a simple one dimensional model in which state variable of interest is distance to source. Such a sensor would provide late pre-Cambrian animals with a means to detect proximity to other animals and therefore react in ethologically meaningful ways, such as striking or fleeing [Monk & Paulin, 2014]. Indeed, the onset of carnivory has been hypothesised to be the driving force behind the evolution of neurons [Monk, 2014]. Therefore understanding how the modern day elasmobranch brain infers predator/prey location may provide us with insights into general principles of brain evolution and brain function.

5.2 Perception as causal inference

In the introduction we mentioned several key concepts for this chapter including *measurement process*, *causal inference* and *state estimation*. Here we elaborate on these and demonstrate how causal inference must underly perception (or maybe even be perception).

Imagine you obtained some data from a particular collection of things. It could be the length of a piece of string, or the distance to another animal and so on. Such measurements are called samples and like the analysis of spike trains in the previous chapter you can use the obtained data in two ways. The most straightforward approach give a detailed description of the sample. For example, you can calculate a point estimate of how long the string is, such as the mean or median, and some measure of the measurement spread, such as standard deviation, variance.

However, if you wanted to generalize the properties from sample to a population this requires inferential statistics. In inferential statistics the data is represented by a probability distribution. Under a frequentist approach probability is the limit of a samples relative frequency in a large number of trials. Under a Bayesian approach you can use probabilities to represent the uncertainty in the sample. Bayes' theorem (Equation (5.1)) provides the optimal strategy for modifying beliefs based on uncertainty in the data.

$$f(x|z) = \frac{f(z|x)f(x)}{p(z)} \tag{5.1}$$

Let the state of the world, or in this specific example string length, be represented by x and the measurements by z. $f(z|x)$ is the *likelihood* of the measurements (z) given string length (x), $f(x)$ is our *prior* knowledge of string length, $p(z)$ is the *evidence* which in practice amounts to a normalization term. The *likelihood* $f(z|x)$ represents the generative relationship between string length (x) and measurement (z). Calculation of the *posterior* $f(x|z)$ allows optimal decisions i.e decisions that maximize or minimise some performance criterion, by integrating expected state-dependent costs over the posterior density of states. For example if you cut a length of string that is a little too short you have to find a new piece (big cost), but if it's a little longer than necessary that's no big deal (little cost). Analogously in predator-prey interactions it may cost energy if an animal decides to strike/flee too soon, but it's potentially fatal to act too slowly (life-lunch principle).

Therefore it would appear that if nervous systems could evaluate the posterior density of relevant state variables given sense data, then they should. Evidence supporting this idea of neuronal computation of Bayesian posteriors has accumulated over the past two decades [Bobrowski *et al.*, 2008; Fischer & Pena, 2011; Ganguli & Simoncelli, 2014; Hoyer & Hyvarinen, 2003; Karmali & Merfeld, 2012; Lochmann & Deneve, 2008, 2011; MacNeilage *et al.*, 2008; Paulin, 2005, 2015; Rich *et al.*, 2015], although controversy in this field should be acknowledged [Bowers & Davis, 2012a,b; Jones & Love, 2011]. One such argument by Bowers & Davis [2012a] is given the computational cost of implementing Bayesian inference why would we expect the brain to be Bayesian? Nervous systems would be better served by using simple, cheap tricks to make adequate decisions without computing posterior probabilities along the way. In this chapter we will demonstrate that there is a cheap trick for performing Bayesian inference using spiking neurons and it predicts cerebellar-like architecture in the electrosensory brainstem.

5.3 Inference from Poisson samples

We revisit the distribution of ISI in a homogeneous Poisson process (Equation (4.1)). The mean interval, τ, is a sufficient statistic for a Poisson process, which means that the posterior density of this single parameter captures all of the information that a spike train sample contains about causal parameters of the process that generated it.

$$f(x|\tau) = \frac{1}{\tau} \exp\left(\frac{-x}{\tau}\right) \tag{5.2}$$

As mentioned previously the homogeneous Poisson is the simplest stochastic process, the probability of firing a spike in a small time interval is independent of the firing activity at all other times. Due to their tractability and simplicity, Poisson processes are often appealing as a practical start point for computation involving point processes (similarly to Normal distributions commonly being applied to continuous random variables), even though individual spike trains are rarely Poisson [Kass *et al.*, 2014].

Suppose that one spike was observed at time $t_0 < t$ and no further spikes have been observed. The likelihood function for this process is expressed by:

$$f(\tau|\text{no spike in}\,(t_0,t]) = \frac{1}{\tau}\exp\left(\frac{-(t-t_0)}{\tau}\right) \tag{5.3}$$

If the posterior density of the Poisson parameter τ at time t_0 was $f_0(\tau)$, then substituting these expressions into Bayes rule (Equation (5.1)) the inference problem takes the form:

$$f(\text{no spike in}\,(t_0,t]\,|\tau) = \frac{f(\tau|\text{no spike in}\,(t_0,t])f_0(\tau)}{A} \tag{5.4}$$

Where the normalizing denominator $A = A(\tau,t)$ ensures that $f(\tau)$ is a probability density, i.e. it integrates to 1 over the range of τ. Equation (5.4) shows that the posterior density of τ changes smoothly during inter-spike intervals, decaying exponentially as a function of the last spike time, adjusted by the normalizing denominator.

5.4 Neurons as computers for inference from Poisson samples

It has been demonstrated that a network of Poisson neurons can perform Bayesian inference similar to Monte Carlo methods such as particle filtering [Huang & Rao, 2014, 2016], and that individual spikes are likely the operands of neural computation [Monk, 2014]. Paulin [2015] suggests that "neurons are natural computers for inference from Poisson samples". Consider the leaky integrate and fire neuron. Its sub-threshold membrane potential v evolves over time according to the following differential equation [Gabbiani & Koch, 1998]:

$$C\frac{dv}{dt} = I(t) - \frac{v}{R} \tag{5.5}$$

where C represents the membrane capacity, $I(t)$ is the input current and R is the membrane resistance.

In the case of constant input current I, during interspike intervals the leaky integrate

and fire model decays exponentially towards the steady-state voltage $v = IR$:

$$v(\tau, t) = IR\left(1 - \exp\left(\frac{-t}{\tau}\right)\right) \tag{5.6}$$

with time constant $\tau = RC$ [Gabbiani & Koch, 1998].

Here mean ISI is proportional to the voltage threshold (v_{th}). Accordingly, Poisson spike trains can be obtained from integrate and fire neurons by resetting the threshold after each spike to a new random value according to the distribution, $p(v) = \frac{1}{v_{th}} \exp\left(\frac{-v}{v_{th}}\right)$ [Gabbiani & Koch, 1998]. Based on these assumptions, a leaky integrator could easily track the numerator in Equation (5.4) for this inference problem.

If we have secondary neurons firing randomly with mean intensity proportional to membrane potential v, inference requires some mechanism to continuously normalize membrane potentials across the population. Accumulating evidence suggests that normalization of neuronal populations plays a role in a variety of sensory modalities, brain regions and species [Carandini & Heeger, 2012]. We implement normalization in our neural particle filter by adding a tertiary layer of neurons that sum the activity of secondary neurons, with a short time constant, and feedback this signal onto secondary population to achieve the required normalization [Paulin, 2015].

Hence the problem for modelling mechanisms of inference in the electrosensory system is not to determine whether it is possible for neurons to evaluate expressions like Equation (5.1), but to determine if and how central electrosensory neurons in the dorsal octavolateralis nucleus (DON) actually do it. The equivalence between exponential likelihoods and the leaky integrator dynamics of neuronal membranes evident in Equations (5.4) and (5.6) indicates that there may be a simple and efficient strategy that a population of afferent neurons converging onto central secondary neurons (AEN) could compute Bayesian posterior densities of variables that parameterize sensory spike trains, if those spike trains are samples from Poisson processes.

5.5 Inference in the electrosensory system

We demonstrated in the previous chapter electrosensory afferent spike trains are not samples from Poisson processes. However, it is not the individual afferents that require Poisson statistics, rather the targets in the brain should receive Poisson input. Electrosensory afferents converge onto secondary neurons (AEN), therefore a group of afferents can be thought of as a "super-afferent" that delivers samples to the brain. Our model implies that the Poisson component τ carries information about small stimuli.

5.5.1 Are "super-afferents" samples from Poisson processes?

Despite the importance of electroreception in the behaviour of elasmobranchs, the anatomical information concerning the convergence of the electroreceptive periphery onto the central nervous system is sparse. Generally, it has been concluded that convergence and divergence in this pathway is very low [Rotem *et al.*, 2014]. Each ampulla appears to be the origin of 5-16 afferent nerve fibres [Kempster *et al.*, 2013]. Recordings from whole animal preparations suggest afferent receptive fields can typically be isolated to a single ampullary pore, whereas AEN receptive fields may be receiving input from 2-7 pores [New, 1990]. Recordings from isolated brain stem preparations suggest that each AEN is innervated by 2-5 fibres [Rotem *et al.*, 2014].

Convergence of afferent neurons onto AEN means that events arriving at the DON could have Poisson statistics (and therefore exponential ISI) even though individual sensory afferents do not. The Poisson limit theorem states that sums of stochastic independent point processes converge to Poisson processes, even if those point processes are non-Poissonian themselves [Arratia *et al.*, 1990; Streit, 2010]. Using the values above as a guide, we simulated 20s duration spike trains that were either ex-Wald or Gaussian. In this case we used the mean fitted values from the ex-Wald fits in chapter 4, that is $\mu = 0.0436$, $\lambda = 1.6808$, $\tau = 0.0051$, to parameterize the ex-Wald distribution and the matched mean $(\mu + \tau)$ and standard deviation $(\sqrt{\frac{\mu^3}{\lambda} + \tau^2})$ to parameterize the Gaussian. For both distributions, the summed response with 2 neurons is obviously not Poisson (Figures 5.1a and 5.1b). However, as the number of neurons increases the distributions become more Poisson-like (Figure 5.1). We tested the fits using the time-transformation tests from the previous chapter, in these simulations by 10 neurons the summed ex-Wald passed Berman's test at the 95% level whereas the summed Gaussian did not. Additionally, we used the KS test to test how well the exponential distribution fits the simulated data. The exponential distribution (with parameter $\tau^* = (\mu + \tau)/N$) provided a statistically significant fit to the ex-Wald data at 10 summed spike trains (KS statistic=0.0179, p=0.1396). However, these numbers were simulation dependent, for both models the summed distributions visually appeared Poisson-like by 5 neurons and statistically were not significantly different from the exponential distribution by 10-20 summed trains.

Similar results were obtained when spike train parameters were bootstrap sampled, from the chapter 4 ex-Wald fits, for each spike train (Figure 5.2). Simulations by 10 neurons the summed ex-Wald passed Berman's test at the 95% level whereas the summed Gaussian did not. Likewise, the exponential distribution provided a statistically significant fit to the ex-Wald data at 10 summed spike trains (KS statistic=0.0127, p=0.5650).

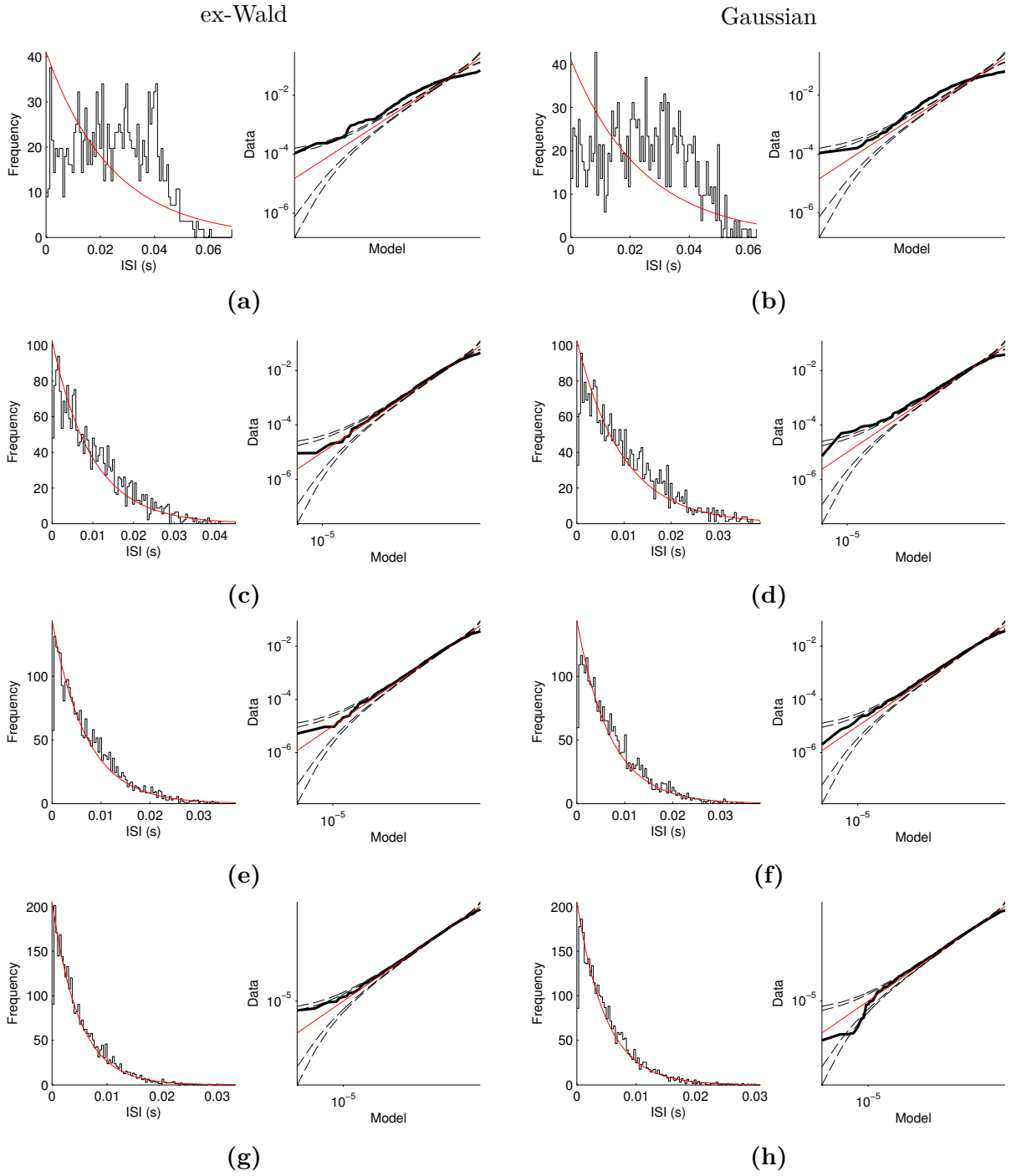

Figure 5.1: Histograms and QQ plots with 90 and 95% confidence bands. Figures 5.1a and 5.1b show the simulated "super afferent" responses of 2 summed ex-Wald and Gaussian neurons respectively, Figures 5.1c and 5.1d: 5 neurons, Figures 5.1e and 5.1f: 7 neurons and Figures 5.1g and 5.1h: 10 neurons. Each ex-Wald spike train was sampled from the distribution with the following parameters $\mu = 0.0436$, $\lambda = 1.6808$, $\tau = 0.0051$. Each Gaussian spike train was sampled from the distribution with matched mean and standard deviation.

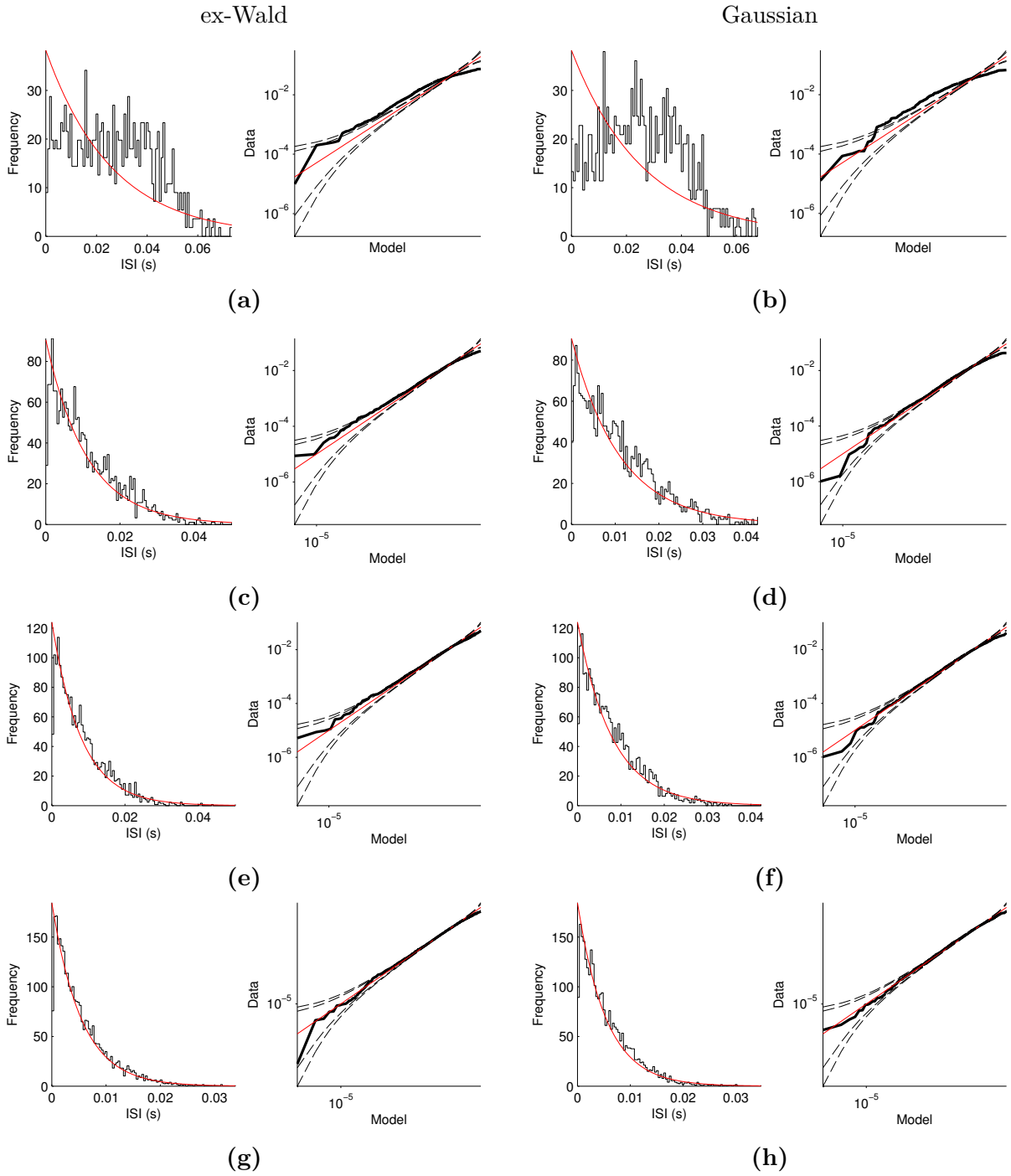

Figure 5.2: Histograms and QQ plots with 90 and 95% confidence bands. Figures 5.2a and 5.2b show the simulated "super afferent" responses of 2 summed ex-Wald and Gaussian neurons respectively, Figures 5.2c and 5.2d: 5 neurons, Figures 5.2e and 5.2f: 7 neurons and Figures 5.2g and 5.2h: 10 neurons. Each ex-Wald spike train was based on a bootstrap sample of files containing ex-Wald fits to electrosensory afferent spontaneous activity. Each Gaussian spike train was sampled from the distribution with matched mean and standard deviation.

5.5.2 Example and performance evaluation

Figures 5.3 and 5.4 show a simulation of a neural particle filter described in Paulin [2015], written in MATLAB, with parameters based on the values from the literature and our spike train analysis.

There is a signal source at a fixed distance causing the "super afferent" to spike with ISI sampled from either: 1) the sum of 5 independent ex-Wald afferent spike trains (each with distribution parametrized by $\mu = 0.0436$, $\lambda = 1.6808$, $\tau = 0.0051$; Figure 5.4, sample mean ISI=0.0095) or 2) the mean matched Poisson distribution (τ^*=0.0097; Figure 5.3, sample mean ISI=0.0096). No averaging is done by the "super afferent", its mean ISI is therefore 5 times shorter than that of the independent ex-Wald afferents. The filter has 2025 secondary neurons (the DON consists of in the order of 2000 AEN; Paul & Roberts [1977]; Rotem *et al.* [2014]), each described by Equation (5.6), with membrane time constants spaced uniformly between 0 and 25ms ($\sim 2.5 \times \tau^*$). The simulation updates at time step length 1.0ms or at the occurrence of primary neuron spikes. Each secondary neuron fires randomly in each time step, with probability proportional to its membrane potential. All secondary neuron membrane potentials are divided in proportion to the total number of spikes in the secondary population on the previous time step. This division is performed by an additional population of 10,000 tertiary neurons (AEN receive input from tens of thousands of parallel fibres and inter neurons; Bodznick *et al.* [1999]; Paul & Roberts [1977]), scaled so that the expected number of spikes in the secondary population is 135, 1/15 of the population size (this selection was largely arbitrary).

In each of the figures, (a) shows the sample spike train, lasting 1s (chosen as a sufficiently short period to view effect of individual spikes), with ISI distribution as described above (Figures 5.3a and 5.4a). This provides the input to AEN, which respond according to Equation (5.6).

The solid red line in the next trace (b) shows the median of the posterior density of τ^* given the spike train, computed numerically from Bayes rule (Equation (5.4)), with initial prior, $f_0(\tau)$, exponential on $1/\tau^*$ at t = 0 (corresponding to expecting prey to appear at a distance, therefore longer ISI more probable). This shows the true posterior median, within numerical error. The posterior median jumps to lower values of τ^* at spike times and drifts towards higher values of τ^* during interspike intervals. Open circles in (b) represent the median of the posterior estimated by the lattice of AENs. For both versions of the sensory spike train there is good agreement between the exact posterior median and the neural particle filter at all times (Figures 5.3b and 5.4b).

The three graphs in (c) are spatial histograms of spike locations in the AEN popula-

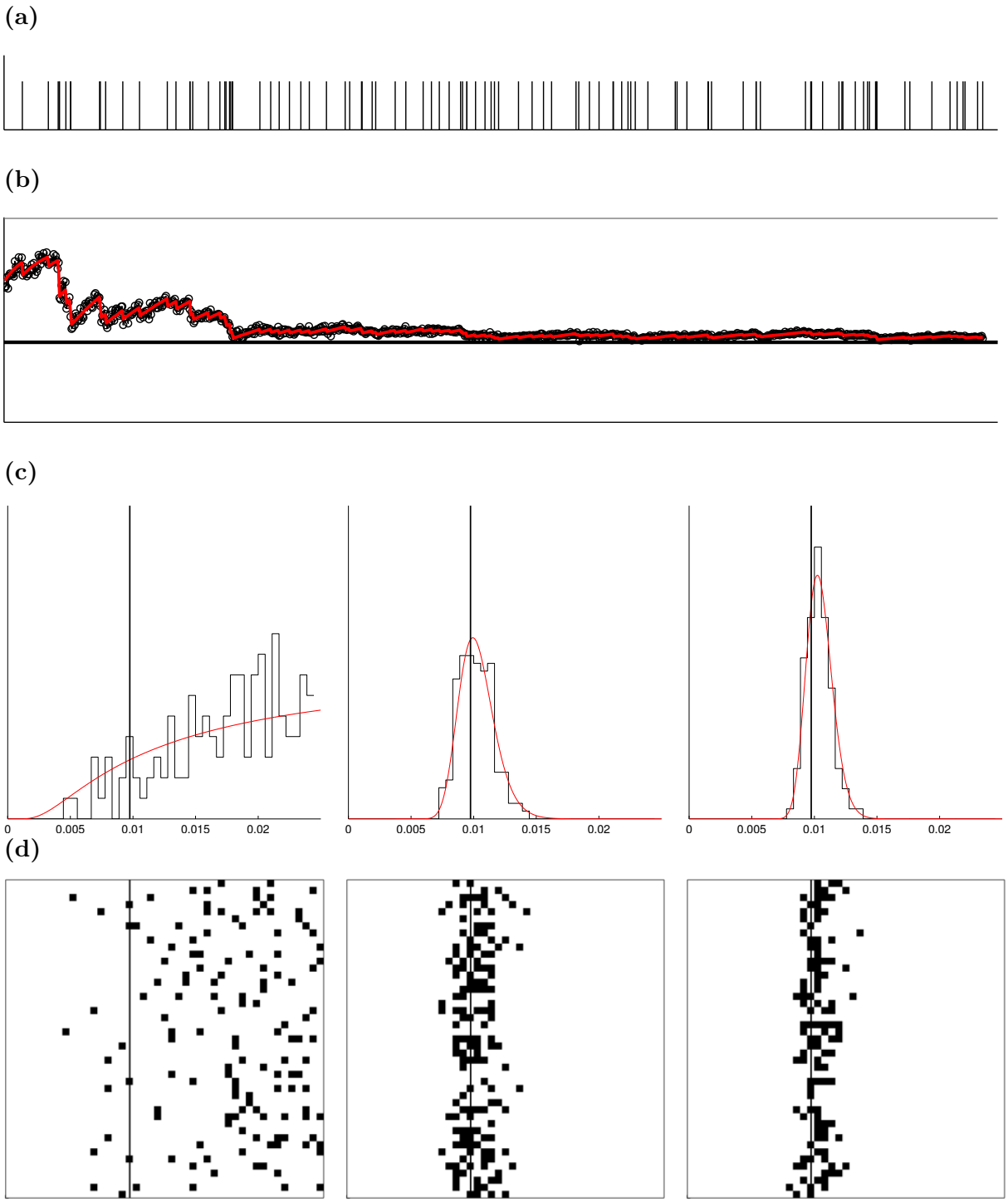

Figure 5.3: Simulation of neural Bayesian particle filter. (a) Sample sensory Poisson spike train τ^*=0.0097, sample mean ISI=0.0096. (b) Exact Bayesian posterior median (red) and neural Bayesian posterior median (circles) at sample times. (c) Spatial histograms of spike locations in three snapshots, mapped in τ^*-space, overlaid by the numerically computed posterior density of τ^* at the corresponding times. (d) 2-D spatial maps of spiking activity at the snapshot times. Columns in the 2D map align with bins in the spatial histograms.

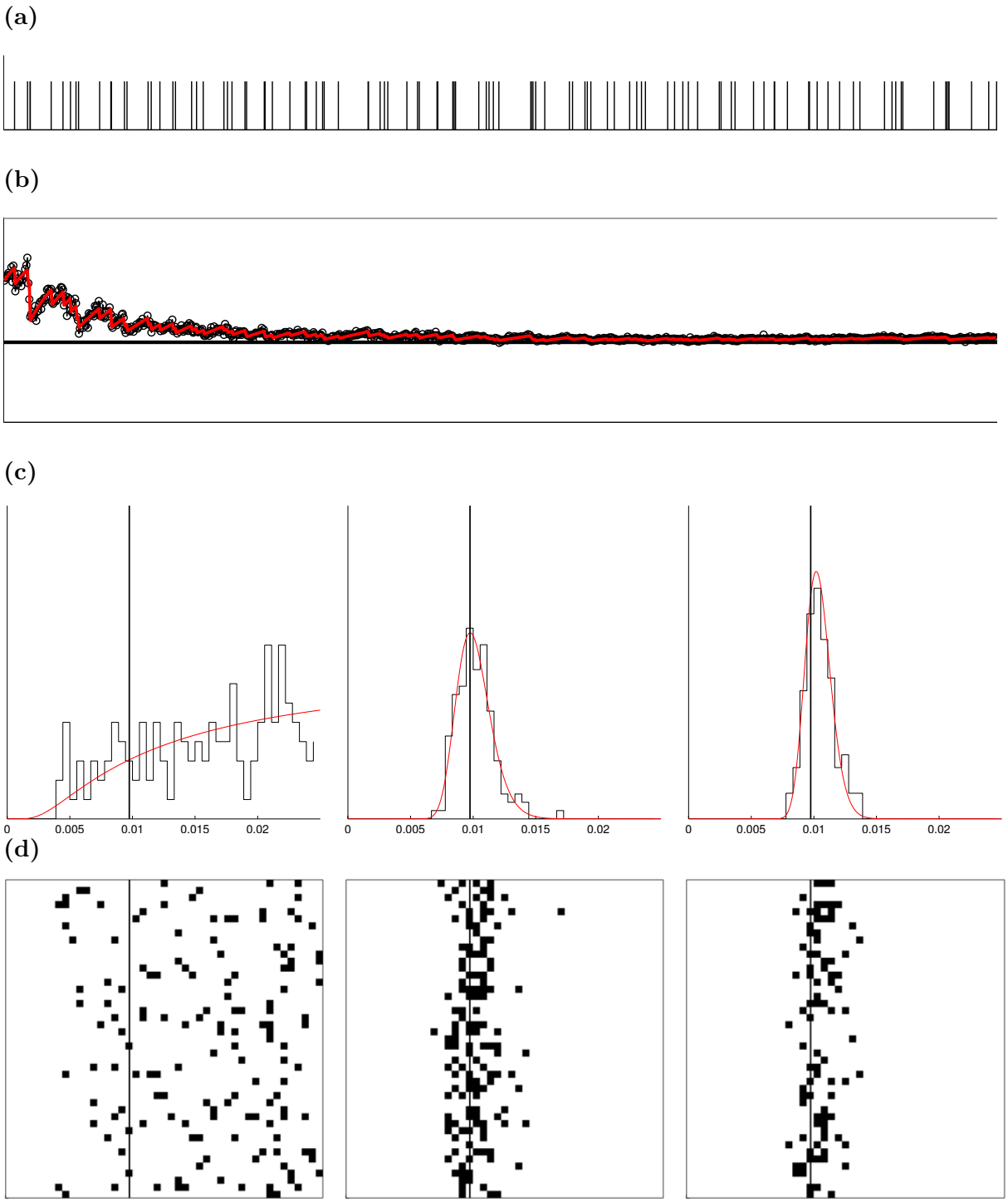

Figure 5.4: Simulation of neural Bayesian particle filter. (a) Sample "super afferent" sensory spike train. 5 summed ex-Walds with $\mu = 0.0436$, $\lambda = 1.6808$, $\tau = 0.0051$, sample mean ISI=0.0095. (b) Exact Bayesian posterior median (red) and neural Bayesian posterior median (circles) at sample times. (c) Spatial histograms of spike locations in three snapshots, mapped in τ^*-space, overlaid by the numerically computed posterior density of τ^* at the corresponding times. (d) 2-D spatial maps of spiking activity at the snapshot times. Columns in the 2D map align with bins in the spatial histograms.

tion, with τ^* divided into 45 bins of equal width, with 'snapshots' of activity taken at t = 0, t = 0.5s and at t = 1s. The true parameter value, τ^*=0.0097, is shown in each plot by a vertical line. The initial spike histogram is a random sample from the exponential initial prior density on $1/\tau^*$, however convergence is largely unaffected by choice of prior. As spikes arrive the true posterior density becomes increasingly Gaussian and narrower and the neural particle filter infers it accurately (Figures 5.3c and 5.4c).

The three graphs in Figures 5.3d and 5.4d, again show 'snapshots' at the time points to above. In this case, plots represent the activity of the secondary neuron lattice, where the 2025 proposal points corresponding to AEN time constants have been laid out in a 45x45 array. Here we presented the parameter characterising the posterior as τ^*, corresponding to secondary neuron time constants. However, with an appropriate coordinate rescaling they can equivalently be interpreted as maps of Poisson intensities $1/\tau^*$, or the more interesting real world maps of distance to the prey item (Paulin [2015]; for a dipole prey there is an inverse cubic transformation between distance and Poisson intensity).

The circuitry of the neural particle filter presented here was derived by Paulin [2015] under the assumption of a homogeneous Poisson process (i.e τ^* is fixed/the prey item and predator are stationary). Under these conditions, with sufficiently large numbers of neurons, the neural particle filter asymptotically approaches exactly Bayes rule [Paulin, 2015]. Figure 5.3 shows the results based on samples from a homogeneous Poisson process, whereas Figure 5.4 shows samples from a Poisson-like "super afferent" based on the sum of 5 simulated primary afferents. Examining the two plots there is very little difference between the two, particularly considering spikes in all neurons (primary, secondary and tertiary) is stochastic in nature. If the input to AEN is indeed Poisson, then sharks can make Bayes optimal decisions, however even non-Poisson input can perform sub-optimal inferences due to convergence of repeated measurements.

5.6 Discussion

The spiking neural particle filter model described in Paulin [2015], applied here to neural circuitry of the shark electrosensory system, can infer the fixed parameter of a Poisson process, or an underlying real world state such as distance to a signal source. This scenario may be too simplistic for modern agile animals, however fossil evidence suggests that primitive nervous systems evolved around the onset of carnivory [Monk & Paulin, 2014]. Initially sensory neurons could have been simple threshold detectors, equipping late pre-Cambrian animals with a means to detect proximity to other animals and therefore

react in ethologically meaningful ways, such as striking or fleeing [Monk & Paulin, 2014]. Indeed modern electroreceptors have been implicated not only in prey detection but also predation reduction strategies with shark, skate and ray embryos exhibiting a "freeze" response to predator-mimicking electric fields [Ball *et al.*, 2016; Kempster *et al.*, 2013; Sisneros *et al.*, 1998].

All animals emit a variety of signals in their vicinity. In early electrosensors, a simple threshold trigger would suffice, as the only other sources of electric fields would have been other slowly moving living things. The electrosensory signal would therefore reliably indicate the distance and direction of other animals, with a threshold indicating when there is an animal within some critical distance. Bioelectric fields are proportional to the cube of distance, suggesting that when animals were very slow moving threshold triggering would have occurred at a very short range, where field strength is strong [Paulin, 2015]. However, as animals became more agile natural selection would have favoured sensors that maximize the signal received, driving the selection of the threshold sensor to the physical limit of sensitivity imposed by thermal noise [Paulin, 2015].

Evolution appears to have developed a solution for maximizing sensory system sensitivity in the presence of noise. Although the thermal noise is inevitable for living cells, the weak electrosensory signals can still be encoded by an array of electrosensors measuring deviations from this noise process. Electroreception by elasmobranchs is therefore inherently a statistical inference problem, in which properties of signal sources must be determined from observations of a noise process that they parameterize.

Once animals had sensory neurons that produced spikes conditional on critical states of the world, it became possible for them to perform inference about the world based on these spikes [Monk, 2014]. An animal capable of successfully implementing Bayes rule, extracts the maximum information about the world states from sensory spikes [Monk & Paulin, 2014]. If computations are done on the time scale of incoming spikes, this would allow for rapid decisions about the dynamic state of the world, thus providing vital information to the animal when decisions can involve fatal interactions [Monk & Paulin, 2014]. We showed that this computation is possible, in principle, using a simple network of spiking neurons can construct and represent the Bayesian posterior density of a fixed Poisson parameter, or equivalently a signal source at fixed distance.

The model suggests that thermal noise is a consequence of maximizing sensitivity of sensors. Therefore, it is unsurprising that electrosensory afferents also show sensitivity to thermal stimuli [Akoev *et al.*, 1980; Braun *et al.*, 1994; Bromm *et al.*, 1975, 1976; Hensel, 1974; Hensel & Nier, 1971; Murray, 1959, 1960; Nier *et al.*, 1976; Sand, 1938]. Brown [2003] suggested the gel in ampullary organs acts as thermoelectric semiconductor in a

novel mode of "sensing temperature without ion channels". This sensitivity may be an emergent property from natural selection driving the ability to sense electric fields down to the limit imposed by thermodynamics.

The model predicts that sensory input to secondary neurons should be modelled as observations from a Poisson process parametrized by relevant state variables. Here we argue that convergence of afferent neurons onto AEN means that events arriving at the DON could have Poisson statistics even though individual sensory afferents do not. We demonstrated the summed distributions visually appeared Poisson-like by 5 neurons and statistically were not distinguishable from the exponential distribution by 10-20 summed trains. Given that the literature suggests each AEN is innervated by 2-5 fibres [Rotem *et al.*, 2014] and our bootstrap sampled ex-Walds did appear to potentially converge to a Poisson distribution with fewer afferents than summed mean parameter ex-Walds, a more thorough examination is warranted. While we focussed on the stationary case, which was equivalent to estimating the Poisson parameter τ^* in summed spontaneous afferent spike trains, we assume in the dynamic case there is some predictable change in τ^* which has yet to be confirmed.

The model predicts that arrays of secondary neurons represent the posterior density of world states via the time constants of secondary neurons in the AEN. Our lattice points spanned membrane time constants spaced uniformly between 0 and 25ms ($\sim 2.5 \times \tau^*$), which is seemed plausible given the electrophysiological values of membrane time constant across neuron types from literature range from tenths of ms to hundreds ms [Tripathy *et al.*, 2014]. However, Rotem *et al.* [2007] found that response of activated neurons within the DON (assumed to be the AEN) decayed with 70ms, suggesting this to be their membrane time constant. Additionally, there should be a systematic relationship between membrane time constants, synaptic input weights and the state-space receptive fields of secondary neurons [Paulin, 2015]. In our stationary, one dimensional model, this was not testable, should this circuitry be extended to the more realistic dynamic case relationships could be examined [Paulin, 2015].

The model predicts that secondary neurons have some mechanism to continuously normalize membrane potentials across the population. This requires that as sensory inputs fluctuate, the activity of some secondary neurons is stimulated while others is suppressed, such that the firing in a random sample of the population remains constant [Paulin, 2015]. Recent intracellular recordings in the DON suggest that stimulating the afferent nerve activates a mixture of excitatory and inhibitory feed-forward synapses [Rotem *et al.*, 2014]. This could potentially provide the internal circuitry required for normalization. The cerebellar-like circuits of the DON have been hypothesised to act as an 'adaptive

filter', responsible for the removal of self generated noise [Bodznick *et al.*, 1999; Bratby *et al.*, 2016; Montgomery & Bodznick, 1994]. These models suggest the DON subtracts away the predictable common mode signals via a summing of the input of parallel fibres with afferent input, whereas the neural particle filter predicts that parallel fibres act via a tertiary layer of neurons that adjusts the AENs responses to afferent inputs [Paulin, 2005; Rotem *et al.*, 2007]. The data of Rotem *et al.* [2014] suggest this adjustment of AEN response is mediated by an inhibitory interneuron that is activated by the afferent nerve.

While here we focussed on the electrosensory system, ampullary electroreceptors are octavolateralis senses. Thus, they share developmental and anatomical similarities with the other senses derived from hair cells such as vestibular, lateral line and auditory systems [Bodznick & Montgomery, 2005]. These similarities extend to the central projections and central processing of information in cerebellar-like circuitry [Bodznick & Montgomery, 2005]. Ancestral electroreceptors could have bootstrapped from simple threshold trigged devices performing quasi-stationary, one-dimensional inferences, however this is a special case that is not relevant to other senses, or electroreception in extant animals [Paulin, 2015]. The evolution of agility means that bioelectric fields vary both spatially and temporally, depending on the configuration of both predator and prey. Bayesian inference provides a means of both updating belief about world states based on dynamics and allowing for the integration of multiple sensory systems. Due to similarities between cerebellar-like structures and the cerebellum accumulating evidence suggests that the cerebellum also plays a role in dynamic state estimation [Baumann *et al.*, 2014; Bell *et al.*, 2008; Paulin, 2005].

We hypothesize that the statistical organization of spiking activity in the electrosensory periphery and anatomy of the CNS may reflect an efficient solution for maximizing sensory system sensitivity in the presence of noise, via Bayesian neural computation. This strategy may be common to other octavolateralis senses.

Chapter 6

General Discussion

In this thesis we developed a theory of how the functional design of the electrosensory system in sharks reflects the inevitability of noise in high-precision measurements, and how the CNS may have developed an efficient solution to this problem via Bayesian neural computation (Figure 6.1).

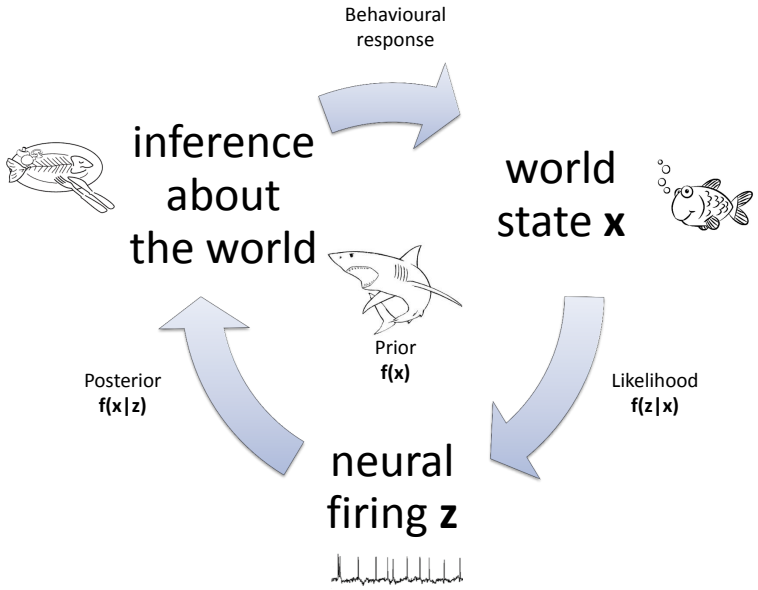

Figure 6.1: Schematic of Bayesian inference in the elasmobranch electrosensory system. A generative model (*likelihood*) maps the state of the world **x** to sensory spikes **z**, the brain combines this with existing beliefs (*priors*) to compute the *posterior*. The *posterior* is continuously updated as new observations become available, allowing the shark to make inferences about the state of the world.

We investigated the physics governing the interaction between the electrosensory system and weak electrical stimuli in the aquatic environment (Figure 6.1: world state). Using geometrically accurate 2D and simplified 3D FEM models of the dogfish, we examined the role of electrical properties and geometry in shaping the effective stimulus

received by electroreceptors. We demonstrated that self movement (or self state) not only affects the measured field, by perturbing the self field, but also affects the external field.

Next, we considered the spontaneous activity of electrosensory afferents, which is related to how these neurons fire in response to small stimuli (Figure 6.1: neural firing). We demonstrated elasmobranch electrosensory afferent spike trains and inter-spike interval distributions typically have fairly regular spontaneous inter-spike intervals with skewed Gaussian-like variability and can be accurately modelled as inverse Gaussian-censored Poisson processes.

Finally, we implemented a spiking neural particle filter which takes simulated electorsensory spike trains and can successfully infer the fixed Poisson parameter, or the equivalent real world state, distance to a source (Figure 6.1: inference about the world).

We now discuss the significance of these results in a general context, and hypotheses that emerge from these results. We finish with a short discussion of limitations of the current research and future directions based on the work presented here.

6.1 Alternative framework for electroreception

Animals are faced with the problem of distinguishing electrosensory information about their external environment (exafference) from electrsensory information that results from their own state/motor activity (reafference). Classical models have suggested that the DON acts as an adaptive filter to suppress this reafference [Bratby *et al.*, 2014; Montgomery & Bodznick, 1994; Nelson & Paulin, 1995]. In chapter 3 we demonstrated that self movement (or self state) not only affects the measured field, by perturbing the self field, but also affects the external field. The dynamic state-to-sensory transformation is a nonlinear distortion of the field, not an additive difference. The shark faces a nonlinear problem which cannot be solved by prediction and subtraction. It can only (or best) be solved by Bayesian inference.

Bayesian inference and Bayes optimality provides an alternative framework for looking at electroreception. In this framework we can make and test predictions about neural computation, and think about technology (measuring devices) that exploit simple properties of materials to observe nature at the limits determined by statistical physics.

6.2 "Super afferent" spike trains

Poisson spiking neurons can perform Bayesian inference [Huang & Rao, 2014, 2016; Paulin, 2015]. In chapter 4, we discovered individual electrosensory afferent spike trains are not samples from a Poisson processes, rather they appear to be random sub-samples of this process. However, because electrosensory afferent neurons converge onto secondary neurons, we consider the convergent input a "super afferent" with the pulse train received by a target neuron approaching a Poisson process with shorter mean intervals as the number of independent convergent spike trains increases. The distributions of spikes may represent a trade off, with evolution driving the selection of energy efficient inverse Gaussian interval distributions at the sensory periphery [Xing *et al.*, 2015], whereas input to secondary neurons from convergent afferent should have a Poisson distribution to allow for a simple and efficient strategy of how central secondary neurons could compute Bayesian posterior [Paulin, 2015].

This abstract model may provide a useful framework for investigating not only central mechanisms of inference in electroreception, but also peripheral mechanisms of sensory transduction and spike coding. The fact that one model has been found to fit octavolateralis neuron firing patterns on two distinct branches of the vertebrate phylogenetic tree, elasmobranch electroreception (here) and mammalian vestibular system [Hoffman & Paulin [2015]; Paulin *et al.* [2016]; Appendix B], suggests that the model may extend to all vertebrate octavolateralis senses.

6.3 Inference in the electrosensory system

We demonstrated a spiking neural particle filter which takes simulated electrosensory "super afferent" spike trains and can successfully infer the fixed Poisson parameter, or the equivalent real world state, distance to a source (chapter 5). The circuit obtained by converting the mathematical model to a network structure bears a striking resemblance to the cerebellar-like hindbrain circuits of the dorsal octavolateral nucleus. Electroreceptors share developmental and anatomical similarities with the other senses derived from hair cells such as vestibular, lateral line and auditory systems [Bodznick & Montgomery, 2005]. These similarities extend to the central projections and central processing of information in cerebellar-like circuitry [Bodznick & Montgomery, 2005].

The elasmobranchs' ability to sense electric fields down to a limit imposed by thermodynamics seems extraordinary. However we predict that the theories presented here

generalize to other sensory systems, particularly the other octavolateralis senses which share cerebellar-like circuitry, suggesting that the cerebellum itself also plays a role in dynamic state estimation.

6.4 Limitations of models

Some aspects of our modelling are obviously oversimplified when put in the specific context of the elasmobranch electroreception.

First, the main shortcoming of our FEM modelling approach is that simulations were conducted using either two dimensions or a geometrically simplified shark model. These models still advance knowledge of how the morphology and electrical properties of shark tissues alter the stimulus received by electrosensors, as previous models either neglect the presence of the body or have even less realistic geometries. Our analysis consisted of a series of snapshots of shark behaviour rotating in a uniform electric field and approach trajectories in the horizontal and vertical plane of a dipole. The model could simply be extended to analyse trajectories at a finer temporal resolution. However, shark behaviour is much more complex than our simplified analysis. It would be of interest to model the effect of body parts under more realistic behaviour, including head swaying and tail bending, or match numerical models to video recordings of shark behaviour. It has been suggested electroreceptors are limited to the head region of sharks to avoid the regions of the body which undergo greater bending movements during swimming [Murray, 1974].

Second, our examination of afferent spike trains focussed on spontaneous activity, under the assumption that this represents the limit of the dynamic case i.e. how afferents respond to small signals. Theoretically, the approaches used for basic data analysis and fitting of probability distributions can be extended to deal with counting processes involving history dependencies, or time varying rates [Pouzat & Chaffiol, 2009b], which would be required for examining dynamic recordings.

Finally, we showed the neural circuitry associated with the electrosensory system is capable of performing quasi-stationary, one-dimensional inferences, however this is a special case that is not relevant to other senses, or electroreception in extant animals [Paulin, 2015]. The evolution of agility means that bioelectric fields vary both spatially and temporally, depending on the configuration of both predator and prey. Extending this to the more realistic dynamic case would allow for the examination of several predictions, relating to the systematic relationship between neural circuitry components [Paulin, 2015].

This research highlighted that the interactions between the shark, environment and

brain are rather complex and can be difficult to model, even if many of the details are known. Which perhaps makes the hyperacuity of the elasmobranchs' electric sense even more remarkable, given that dogfish appear capable of performing inferences in brains weighing <4 g [Northcutt, 1977] and drawing only microwatts of power.

6.5 Future directions

Several interesting lines of research stem from our current models.

- Provide a better approximation of voltage drop distortions that result from the shark's presence in an electric field. This area could benefit from additional experimental data. Ideally, simultaneous video recording of sharks' trajectories in 3D and measurements of the electric field in the water surrounding the shark would allow a better analysis of the accuracy of 2D and geometrically simplified 3D FEM models.
- Additionally, video recordings would provide a framework to model the effect of body parts under more realistic behaviour, including head swaying and tail bending. This would be relatively simple to implement in 2D models but 3D geometries were more difficult to manipulate and mesh in COMSOL.
- The inclusion of voltage sources such as the sharks' own bioelectric field, as well as other sources of self-noise, would allow more detailed comparison of the adaptive filter vs Bayesian inference frameworks.
- Here we focussed on the voltage drops over entire electrosensory array and how the body scale pre-receptor mechanisms impact the stimulus received by electrosensors. The morphological and electrical properties of the canal itself and the receptor cells therein also likely effect the stimulus received by individual ampullae. It would be interesting to implement individual ampullae FEM models to examine this effect. In particular, can we identify the function of the receptor cell cilium which interfaces with the lumen of the ampulla proper?
- Examination of stimulus-response data from afferent neurons presented with weak electrical stimuli to determine if the censored Poisson distributions are indeed capable of fitting afferent spike train dynamics.
- Examination of ascending efferent neuron responses to determine if central convergence of afferents does result in a "super afferent" delivering a Poisson sample to the brain.

- Extending the quasi-stationary, one-dimensional spiking neural particle filter to the more realistic dynamic case.

- Investigation of other sensory systems using the Bayesian framework presented here, particularly the other octavolateralis senses which share cerebellar-like circuitry, to determine if the theories presented here generalize to other sensory systems.

The elasmobranchs' ability to sense electric fields down to a limit imposed by thermodynamics seems extraordinary. Operating at this limit, the efficiency of the elasmobranch electrosense exceeds electronic sensing/computing technology by many orders of magnitude. We predict that the theories presented here generalize to other sensory systems, particularly the other octavolateralis senses which share cerebellar-like circuitry. Cerebellar-like-circuitry is an evolutionary precursor of cerebellum, but much more tractable. Thus, the elasmobranch electrosense provides a viable approach to understanding the cerebellum and its role in dynamic state estimation.

References

Adair, R.K., Astumian, R.D. & Weaver, J.C. (1998). Detection of weak electric fields by sharks, rays, and skates. *Chaos: An Interdisciplinary Journal of Nonlinear Science*, **8**, 576–587.

Ahn, S. & Kim, D. (2012). A Finite Element Method of electric image in weakly electric fish. In T. Ziemke, C. Balkenius & J. Hallam, eds., *From Animals to Animats 12*, no. 7426 in Lecture Notes in Computer Science, 127–135, Springer Berlin Heidelberg.

Akoev, G., Volpe, N. & Zhadan, G. (1980). Analysis of effects of chemical and thermal stimuli on the ampullae of Lorenzini of the skates. *Comparative Biochemistry and Physiology Part A: Physiology*, **65**, 193 – 201.

Antipin, N.P., Krylov, B.V. & Cherepnov, V.L. (1984). Topography of the ampullary system of *Raja clavata* and its role in electroorientation. *Neurophysiology*, **16**, 628–633.

Arratia, R., Goldstein, L. & Gordon, L. (1990). Poisson approximation and the Chen-Stein method. *Statistical Science*, **5**, 403–424.

Atkinson, C.J.L. & Bottaro, M. (2006). Ampullary pore distribution of *Galeus melastomus* and *Etmopterus spinax*: possible relations with predatory lifestyle and habitat. *Journal of the Marine Biological Association of the UK*, **86**, 447–448.

Bacher, M. (1983). A new method for the simulation of electric fields, generated by electric fish, and their distorsions by objects. *Biological Cybernetics*, **47**, 51–58.

Baker, C.V.H., Modrell, M.S. & Gillis, J.A. (2013). The evolution and development of vertebrate lateral line electroreceptors. *The Journal of Experimental Biology*, **216**, 2515–2522.

Balasubramanian, V. (2015). Heterogeneity and efficiency in the brain. *Proceedings of the IEEE*, **103**, 1346–1358.

Ball, R.E., Oliver, M.K. & Gill, A.B. (2016). Early life sensory ability-ventilatory responses of thornback ray embryos (*Raja clavata*) to predator-type electric fields. *Developmental Neurobiology*, **76**, 721–729.

Basano, L. & Ottonello, P. (1975). Thermal noise as a source of Poisson distributions. *American Journal of Physics*, **43**, 452–453.

Bastian, J. (1986). Gain control in the electrosensory system: a role for the descending projections to the electrosensory lateral line lobe. *Journal of Comparative Physiology A: Neuroethology, Sensory, Neural, and Behavioral Physiology*, **158**, 505–515.

Baumann, O., Borra, R.J., Bower, J.M., Cullen, K.E., Habas, C., Ivry, R.B., Leggio, M., Mattingley, J.B., Molinari, M., Moulton, E.A., Paulin, M.G., Pavlova, M.A., Schmahmann, J.D. & Sokolov, A.A. (2014). Consensus paper: The role of the cerebellum in perceptual processes. *The Cerebellum*, **14**, 197–220.

Bedore, C.N. & Kajiura, S.M. (2013). Bioelectric fields of marine organisms: voltage and frequency contributions to detectability by electroreceptive predators. *Physiological and Biochemical Zoology*, **86**, 298–311.

Bedore, C.N., Harris, L.L. & Kajiura, S.M. (2014). Behavioral responses of batoid elasmobranchs to prey-simulating electric fields are correlated to peripheral sensory morphology and ecology. *Zoology*, **117**, 95–103.

Bell, C.C. & Maler, L. (2005). Central neuroanatomy of electrosensory systems in fish. In T.H. Bullock, C.D. Hopkins, A.N. Popper & R.R. Fay, eds., *Electroreception*, 68–111, Springer, New York.

Bell, C.C., Han, V. & Sawtell, N.B. (2008). Cerebellum-like structures and their implications for cerebellar function. *Annual Review of Neuroscience*, **31**, 1–24.

Bennett, M.V.L., Wurzel, M. & Grundfest, H. (1961). The electrophysiology of electric organs of marine electric fishes I. Properties of electroplaques of *Torpedo nobiliana*. *The Journal of General Physiology*, **44**, 757–804.

Berquist, R.M. (2003). *The virtual dogfish: a graphical and computational model of the peripheral electrosensory system of the spiny dogfish, Squalus acanthias*. PhD thesis, University of Otago, Dunedin, New Zealand.

Berquist, R.M. & Paulin, M.G. (2001). The virtual dogfish: An environment for modelling neural computations in cerebellar-like circuitry of the elasmobranch electrosensory system. *Neurocomputing*, **38-40**, 1107–1112.

Bhattacharyya, G.K. & Fries, A. (1982). Fatigue failure models - Birnbaum-Saunders vs. Inverse Gaussian. *IEEE Transactions on Reliability*, **R-31**, 439–441.

Bialek, W. (1987). Physical limits to sensation and perception. *Annual Review of Biophysics and Biophysical Chemistry*, **16**, 455–478.

Blonder, B.I. & Alevizon, W.S. (1988). Prey discrimination and electroreception in the stingray *Dasyatis sabina*. *Copeia*, **1988**, 33–36.

Bobrowski, O., Meir, R. & Eldar, Y.C. (2008). Bayesian filtering in spiking neural networks: Noise, adaptation, and multisensory integration. *Neural Computation*, **21**, 1277–1320.

Bodznick, D. (1989). Comparisons between electrosensory and mechanosensory lateral line systems. In S. Coombs, P. Gorner & H. Munz, eds., *The Mechanosensory Lateral Line*, 653–678, Springer New York.

Bodznick, D. & Boord, R. (1986). Electroreception in Chondrichthyes. In T.H. Bullock & W. Heiligenberg, eds., *Electroreception*, 225–256, John Wiley and Sons, New York.

Bodznick, D. & Montgomery, J.C. (2005). The physiology of low-frequency electrosensory systems. In T.H. Bullock, C.D. Hopkins, A.N. Popper & R.R. Fay, eds., *Electroreception*, vol. 21 of *Springer Handbook of Auditory Research*, 132–153, Springer, New York.

Bodznick, D. & Northcutt, R.G. (1984). An electrosensory area in the telencephalon of the little skate, *Raja erinacea*. *Brain Research*, **298**, 117–124.

Bodznick, D., Montgomery, J.C. & Bradley, D.J. (1992). Suppression of common mode signals within the electrosensory system of the Little Skate *Raja erinacea*. *The Journal of Experimental Biology*, **171**, 107–125.

Bodznick, D., Montgomery, J.C. & Carey, M. (1999). Adaptive mechanisms in the elasmobranch hindbrain. *The Journal of Experimental Biology*, **202**, 1357–1364.

Bodznick, D., Montgomery, J. & Tricas, T.C. (2003). Electroreception: Extracting behaviorally important signals from noise. In S.P. Collin & N.J. Marshall, eds., *Sensory Processing in Aquatic Environments*, 389–403, Springer New York.

Bowers, J.S. & Davis, C.J. (2012a). Bayesian just-so stories in psychology and neuroscience. *Psychological Bulletin*, **138**, 389–414.

Bowers, J.S. & Davis, C.J. (2012b). Is that what Bayesians believe? Reply to Griffiths, Chater, Norris, and Pouget (2012). *Psychological Bulletin*, **138**, 423–426.

Bratby, P., Montgomery, J. & Sneyd, J. (2014). A biophysical model of adaptive noise filtering in the shark brain. *Bulletin of Mathematical Biology*, **76**, 455–475.

Bratby, P., Sneyd, J. & Montgomery, J. (2016). Computational architecture of the granular layer of cerebellum-like structures. *The Cerebellum*, 1–11.

Braun, H.A., Wissing, H., Schafer, K. & Hirsch, M.C. (1994). Oscillation and noise determine signal transduction in shark multimodal sensory cells. *Nature*, **367**, 270–273.

Bromm, B. & Tagmat, A.T. (1977). Regression analysis of non-stationary discharges in neurons; Adaptation in the electrosensory afferent of dogfish. *Biological Cybernetics*, **28**, 41–49.

Bromm, B., Hensel, H. & Nier, K. (1975). Response of the ampullae of Lorenzini to static combined electric and thermal stimuli in *Scyliorhinus canicula*. *Cellular and Molecular Life Sciences*, **31**, 615–618.

Bromm, B., Hensel, H. & Tagmat, A.T. (1976). The electrosensitivity of the isolated ampulla of lorenzini in the dogfish. *Journal of Comparative Physiology A: Neuroethology, Sensory, Neural, and Behavioral Physiology*, **111**, 127–136.

Broun, G.R. & Govardovskii, V.I. (1983). Electroreceptor mechanisms of the ampullae of lorenzini in skates. *Neurophysiology*, **15**, 139–146.

Brown, B. (2010). Temperature response in electrosensors and thermal voltages in electrolytes. *Journal of Biological Physics*, **36**, 121–134.

Brown, B.R. (2002). Modeling an electrosensory landscape: behavioral and morphological optimization in elasmobranch prey capture. *The Journal of Experimental Biology*, **205**, 999–1007.

Brown, B.R. (2003). Neurophysiology: Sensing temperature without ion channels. *Nature*, **421**, 495.

Brown, B.R., Hutchison, J.C., Hughes, M.E., Kellogg, D.R. & Murray, R.W. (2002). Electrical characterization of gel collected from shark electrosensors. *Physical Review E*, **65**, 061903.

Brown, B.R., Hughes, M.E. & Russo, C. (2005). Infrastructure in the electric sense: admittance data from shark hydrogels. *Journal of Comparative Physiology A: Neuroethology, Sensory, Neural, and Behavioral Physiology*, **191**, 115–123.

Brown, H.R. & Ilyinsky, O.B. (1978). The ampullae of Lorenzini in the magnetic field. *Journal of Comparative Physiology A: Neuroethology, Sensory, Neural, and Behavioral Physiology*, **126**, 333–341.

Brown, H.R., Andrianov, G.N. & Ilyinsky, O.B. (1974). Magnetic field perception by electroreceptors in Black Sea skates. *Nature*, **249**, 178–179.

Budelli, R. & Caputi, A.A. (2000). The electric image in weakly electric fish: perception of objects of complex impedance. *The Journal of Experimental Biology*, **203**, 481–492.

Bullock, T., Bodznick, D. & Northcutt, R. (1983). The phylogenetic distribution of electroreception: Evidence for convergent evolution of a primitive vertebrate sense modality. *Brain Research Reviews*, **6**, 25–46.

Bullock, T.H. (1993). Significance of findings on electroreception for general neurobiology. In *How do Brains Work?*, 545–568, Birkhauser Boston.

Camilieri-Asch, V., Kempster, R.M., Collin, S.P., Johnstone, R.W. & Theiss, S.M. (2013). A comparison of the electrosensory morphology of a euryhaline and a marine stingray. *Zoology*, **116**, 270–276.

Camperi, M., Tricas, T.C. & Brown, B.R. (2007). From morphology to neural information: the electric sense of the skate. *PLoS Computational Biology*, **3**, e113.

Caputi, A.A., Budelli, R., Grant, K. & Bell, C.C. (1998). The electric image in weakly electric fish: physical images of resistive objects in *Gnathonemus petersii*. *The Journal of Experimental Biology*, **201**, 2115–2128.

Carandini, M. & Heeger, D.J. (2012). Normalization as a canonical neural computation. *Nature Reviews Neuroscience*, **13**, 51–62.

Chen, F., Zha, D., Fridberger, A., Zheng, J., Choudhury, N., Jacques, S.L., Wang, R.K., Shi, X. & Nuttall, A.L. (2011). A differentially amplified motion in the ear for near-threshold sound detection. *Nature Neuroscience*, **14**, 770–774.

Chen, L., House, J.L., Krahe, R. & Nelson, M.E. (2004). Modeling signal and background components of electrosensory scenes. *Journal of Comparative Physiology A: Neuroethology, Sensory, Neural, and Behavioral Physiology*, **191**, 331–345.

Conley, R.A. & Bodznick, D. (1994). The cerebellar dorsal granular ridge in an elasmobranch has proprioceptive and electroreceptive representations and projects homotopically to the medullary electrosensory nucleus. *Journal of Comparative Physiology A: Neuroethology, Sensory, Neural, and Behavioral Physiology*, **174**, 707–721.

Dall, S.R.X., Giraldeau, L.A., Olsson, O., McNamara, J.M. & Stephens, D.W. (2005). Information and its use by animals in evolutionary ecology. *Trends in Ecology & Evolution*, **20**, 187–193.

De Ridder, D., Vanneste, S. & Freeman, W. (2014). The Bayesian brain: Phantom percepts resolve sensory uncertainty. *Neuroscience & Biobehavioral Reviews*, **44**, 4–15.

Domurat, A., Kowalczuk, O., Idzikowska, K., Borzymowska, Z. & Nowak-Przygodzka, M. (2015). Bayesian probability estimates are not necessary to make choices satisfying Bayes' rule in elementary situations. *Frontiers in Psychology*, **6**, 1194.

Duchamp-Viret, P., Kostal, L., Chaput, M., Lansky, P. & Rospars, J.P. (2005). Patterns of spontaneous activity in single rat olfactory receptor neurons are different in normally breathing and tracheotomized animals. *Journal of Neurobiology*, **65**, 97–114.

Egeberg, C.A., Kempster, R.M., Theiss, S.M., Hart, N.S. & Collin, S.P. (2014). The distribution and abundance of electrosensory pores in two benthic sharks: a comparison of the wobbegong shark, *Orectolobus maculatus*, and the angel shark, *Squatina australis*. *Marine and Freshwater Research*, **65**, 1003–1008.

Fields, R.D. & Ellisman, M.H. (1988). Functionally significant plasticity of synaptic morphology: studies on the ribbon synapse of the ampullae of Lorenzini. *Neuroscience*, **25**, 705–720.

Fields, R.D., Fields, K.D. & Fields, M.C. (2007). Semiconductor gel in shark sense organs? *Neuroscience Letters*, **426**, 166–170.

Fischer, B.J. & Pena, J.L. (2011). Owl's behavior and neural representation predicted by Bayesian inference. *Nature Neuroscience*, **14**, 1061–1066.

Friedman, J., Torres, D., Schmid, T., Dong, J. & Srivastava, M.B. (2010). A biomimetic quasi-static electric field physical channel for underwater ocean networks. In *Proceedings of the Fifth ACM International Workshop on UnderWater Networks*, WUWNet '10, 7:1–7:8, ACM, New York, NY, USA.

Friston, K., Samothrakis, S. & Montague, R. (2012). Active inference and agency: optimal control without cost functions. *Biological Cybernetics*, **106**, 523–541.

Gabbiani, F. & Koch, C. (1998). Principles of spike train analysis. In *Methods in Neuronal Modeling: From Synapses to Networks*, 313–360, MIT Press, Cambridge, MA.

Ganguli, D. & Simoncelli, E.P. (2014). Efficient sensory encoding and Bayesian inference with heterogeneous neural populations. *Neural Computation*, **26**, 2103–2134.

Gillis, J.A., Modrell, M.S., Northcutt, R.G., Catania, K.C., Luer, C.A. & Baker, C.V.H. (2012). Electrosensory ampullary organs are derived from lateral line placodes in cartilaginous fishes. *Development (Cambridge, England)*, **139**, 3142–3146.

Gomez-Sena, L., Pedraja, F., Sanguinetti-Scheck, J.I. & Budelli, R. (2014). Computational modeling of electric imaging in weakly electric fish: Insights for physiology, behavior and evolution. *Journal of Physiology-Paris*, **108**, 112–128.

Griffiths, D.J. (1999). *Introduction to Electrodynamics*. Addison Wesley, Upper Saddle River, N.J, 3rd edn.

Gusev, V., Krylov, B. & Suvorova, T. (1986). An analysis of the spatial mechanisms responsible for electrosensitivity in rays-modelling results. *Biological Cybernetics*, **54**, 263–268.

Gusev, V.M., Krylov, B.V. & Suvorova, T.P. (1985). Role of the body in primary signal processing by the electroreceptor system of the skate. *Neurophysiology*, **17**, 478–482.

Hagiwara, S., Szabo, T. & Enger, P.S. (1965). Electroreceptor mechanisms in a high-frequency weakly electric fish, *Sternarchus albifrons*. *Journal of Neurophysiology*, **28**, 784–799.

Haine, O.S., Ridd, P.V. & Rowe, R.J. (2001). Range of electrosensory detection of prey by *Carcharhinus melanopterus* and *Himantura granulata*. *Marine and Freshwater Research*, **52**, 291–296.

Hallez, H., Vanrumste, B., Grech, R., Muscat, J., De Clercq, W., Vergult, A., D'Asseler, Y., Camilleri, K.P., Fabri, S.G., Van Huffel, S. & Lemahieu, I. (2007). Review on solving the forward problem in EEG source analysis. *Journal of NeuroEngineering and Rehabilitation*, **4**, 46.

Haus, H.A. & Melcher, J.R. (1989). *Electromagnetic Fields and Energy*. Prentice Hall.

Heathcote, A. (2004). Fitting Wald and ex-Wald distributions to response time data: An example using functions for the S-PLUS package. *Behavior Research Methods, Instruments, & Computers*, **36**, 678–694.

Heiligenberg, W. (1975). Theoretical and experimental approaches to spatial aspects of electrolocation. *Journal of Comparative Physiology A: Neuroethology, Sensory, Neural, and Behavioral Physiology*, **103**, 247–272.

Hensel, H. (1974). Effect of temporal and spatial temperature gradients on the ampullae of Lorenzini. *Pflugers Archiv European Journal of Physiology*, **347**, 89–100.

Hensel, H. & Nier, K. (1971). Integrated static activity of the ampullae of Lorenzini after long-term exposure to various temperatures. *Pflugers Archiv European Journal of Physiology*, **323**, 279–283.

Hjelmstad, G., Parks, G. & Bodznick, D. (1996). Motor corollary discharge activity and sensory responses related to ventilation in the skate vestibulolateral cerebellum: implications for electrosensory processing. *The Journal of Experimental Biology*, **199**, 673–681.

Hoffman, L. & Paulin, M. (2015). Spontaneous discharge in mammalian vestibular afferents modelled as Gamma-censored Poisson processes. Proceedings of the 38th Annual MidWinter Meeting of the Association for Research in Otolaryngology (abstract), Baltimore, USA.

Hoshimiya, N., Shogen, K., Matsuo, T. & Chichibu, S. (1980). The *Apteronotus* EOD field: Waveform and EOD field simulation. *Journal of Comparative Physiology A: Neuroethology, Sensory, Neural, and Behavioral Physiology*, **135**, 283–290.

Hoyer, P.O. & Hyvarinen, A. (2003). Interpreting neural response variability as Monte Carlo sampling of the posterior. In S. Becker, S. Thrun & K. Obermayer, eds., *Advances in Neural Information Processing Systems 15*, 293–300, MIT Press.

Huang, Y. & Rao, R.P. (2014). Neurons as Monte Carlo samplers: Bayesian inference and learning in spiking networks. In Z. Ghahramani, M. Welling, C. Cortes, N.D. Lawrence & K.Q. Weinberger, eds., *Advances in Neural Information Processing Systems 27*, 1943–1951, Curran Associates, Inc.

Huang, Y. & Rao, R.P.N. (2016). Bayesian inference and online learning in Poisson neuronal networks. *Neural Computation*, **28**, 1503–1526.

Hudspeth, A.J. (1982). Extracellular current flow and the site of transduction by vertebrate hair cells. *Journal of Neuroscience*, **2**, 1–10.

Humphries, S., Jr (2010). *Finite-Element Methods for Electromagnetics*. Electronic edition Field Precision LLC.

Jones, M. & Love, B.C. (2011). Bayesian Fundamentalism or Enlightenment? On the explanatory status and theoretical contributions of Bayesian models of cognition. *The Behavioral and Brain Sciences*, **34**, 169–188; disuccsion 188–231.

Jordan, L.K. (2008). Comparative morphology of stingray lateral line canal and electrosensory systems. *Journal of Morphology*, **269**, 1325–1339.

Jordan, L.K., Kajiura, S.M. & Gordon, M.S. (2009). Functional consequences of structural differences in stingray sensory systems. Part II: electrosensory system. *The Journal of Experimental Biology*, **212**, 3044–3050.

Josberger, E.E., Hassanzadeh, P., Deng, Y., Sohn, J., Rego, M.J., Amemiya, C.T. & Rolandi, M. (2016). Proton conductivity in ampullae of Lorenzini jelly. *Science Advances*, **2**, e1600112.

Kajiura, S. (2003). Electroreception in neonatal bonnethead sharks, *Sphyrna tiburo*. *Marine Biology*, **143**, 603–611.

Kajiura, S.M. (2001). Head morphology and electrosensory pore distribution of carcharhinid and sphyrnid sharks. *Environmental Biology of Fishes*, **61**, 125–133.

Kajiura, S.M. & Fitzgerald, T.P. (2009). Response of juvenile scalloped hammerhead sharks to electric stimuli. *Zoology*, **112**, 241 – 250.

Kajiura, S.M. & Holland, K.N. (2002). Electroreception in juvenile scalloped hammerhead and sandbar sharks. *The Journal of Experimental Biology*, **205**, 3609–3621.

Kajiura, S.M., Cornett, A.D. & Yopak, K.E. (2010). Sensory adaptations to the environment: Electroreceptors as a case study. In J.C. Carrier, J.A. Musick & M.R. Heithaus, eds., *Sharks and Their Relatives II: Biodiversity, Adaptive Physiology, and Conservation*, CRC Press/Taylor & Francis, Boca Raton, FL.

Kalmijn, A. (1984). Theory of electromagnetic orientation: a further analysis. In *Comparative Physiology of Sensory Systems*, 525–560, Cambridge University Press, Cambridge.

Kalmijn, A.J. (1971). The electric sense of sharks and rays. *The Journal of Experimental Biology*, **55**, 371–383.

Kalmijn, A.J. (1972). Bioelectric Fields in Seawater and the Function of the Ampullae of Lorenzini in Elasmobranch Fishes. SIO Reference Contribution No. 72-83, Scripps Institution of Oceanography, UC San Diego.

Kalmijn, A.J. (1974). The detection of electric fields from inanimate and animate sources other than electric organs. In A. Fessard, ed., *Electroreceptors and Other Specialized Receptors in Lower Vertebrates*, vol. 3 of *Handbook of Sensory Physiology*, 147–200, Springer-Verlag, New York.

Kalmijn, A.J. (1982). Electric and magnetic field detection in elasmobranch fishes. *Science*, **218**, 916–918.

Kalmijn, A.J. (1988). Detection of weak electric fields. In J. Atema, R.R. Fay, A.N. Popper & W.N. Tavolga, eds., *Sensory Biology of Aquatic Animals*, 151–186, Springer New York.

Kalmijn, A.J. (1997). Electric and near-field acoustic detection, a comparative study. *Acta physiologica Scandinavica. Supplementum*, **638**, 25–38.

Kalmijn, A.J. (2000). Detection and processing of electromagnetic and near-field acoustic signals in elasmobranch fishes. *Philosophical Transactions: Biological Sciences*, **355**, 1135–1141.

Kalmijn, A.J. (2003). Graded positive feedback in elasmobranch ampullae of Lorenzini. *American Institute of Physics Conference Proceedings*, **665**, 133–141.

Kapur, J.N. & Kesavan, H.K. (1992). Entropy optimization principles and their applications. In V.P. Singh & M. Fiorentino, eds., *Entropy and Energy Dissipation in Water Resources*, no. 9 in Water Science and Technology Library, 3–20, Springer Netherlands.

Karmali, F. & Merfeld, D.M. (2012). A distributed, dynamic, parallel computational model: the role of noise in velocity storage. *Journal of Neurophysiology*, **108**, 390–405.

Kass, R.E., Eden, U.T. & Brown, E.N. (2014). Point processes. In *Analysis of Neural Data*, Springer Series in Statistics, 563–603, Springer New York.

Kayser, C. & Shams, L. (2015). Multisensory causal inference in the brain. *PLoS Biology*, **13**, e1002075.

Kempster, R.M., McCarthy, I.D. & Collin, S.P. (2012). Phylogenetic and ecological factors influencing the number and distribution of electroreceptors in elasmobranchs. *Journal of Fish Biology*, **80**, 2055–2088.

Kempster, R.M., Hart, N.S. & Collin, S.P. (2013). Survival of the stillest: Predator avoidance in shark embryos. *PLoS ONE*, **8**, e52551.

Kim, D. (2007). Prey detection mechanism of elasmobranchs. *Biosystems*, **87**, 322–331.

Kimber, J.A., Sims, D.W., Bellamy, P.H. & Gill, A.B. (2011). The ability of a benthic elasmobranch to discriminate between biological and artificial electric fields. *Marine Biology*, **158**, 1–8.

Klimley, A.P. (1993). Highly directional swimming by scalloped hammerhead sharks, *Sphyrna lewini*, and subsurface irradiance, temperature, bathymetry, and geomagnetic field. *Marine Biology*, **117**, 1–22.

Knill, D.C. & Pouget, A. (2004). The Bayesian brain: the role of uncertainty in neural coding and computation. *Trends in Neurosciences*, **27**, 712–719.

Kording, K.P. (2014). Bayesian statistics: relevant for the brain? *Current Opinion in Neurobiology*, **25**, 130–133.

Kostal, L. & Lansky, P. (2005). Similarity of interspike interval distributions and information gain in a stationary neuronal firing. *Biological Cybernetics*, **94**, 157–167.

Kostal, L., Lansky, P. & Pokora, O. (2011). Variability measures of positive random variables. *PLoS ONE*, **6**, e21998.

Kubo, R. (1966). The fluctuation-dissipation theorem. *Reports on Progress in Physics*, **29**, 255.

Kuhn, A., Aertsen, A. & Rotter, S. (2003). Higher-order statistics of input ensembles and the response of simple model neurons. *Neural Computation*, **15**, 67–101.

Kuvshinov, A., Junge, A. & Utada, H. (2006). 3-D modelling the electric field due to ocean tidal flow and comparison with observations. *Geophysical Research Letters*, **33**, L06314.

Kuvshinov, A.V. (2008). 3-D global induction in the oceans and solid earth: Recent progress in modeling magnetic and electric fields from sources of magnetospheric,ionospheric and oceanic origin. *Surveys in Geophysics*, **29**, 139–186.

Laughlin, S.B., de Ruyter van Steveninck, R.R. & Anderson, J.C. (1998). The metabolic cost of neural information. *Nature Neuroscience*, **1**, 36–41.

Lavoue, S., Miya, M., Arnegard, M.E., Sullivan, J.P., Hopkins, C.D. & Nishida, M. (2012). Comparable ages for the independent origins of electrogenesis in African and South American weakly electric fishes. *PLoS ONE*, **7**.

Lehner, G. (2008). *Electromagnetic Field Theory for Engineers and Physicists*. Springer-Verlag Berlin Heidelberg.

Leiva, V., Tejo, M., Guiraud, P., Schmachtenberg, O., Orio, P. & Marmolejo-Ramos, F. (2015). Modeling neural activity with cumulative damage distributions. *Biological Cybernetics*, **109**, 421–433.

Levi, R., Akanyeti, O., Ballo, A. & Liao, J.C. (2015). Frequency response properties of primary afferent neurons in the posterior lateral line system of larval zebrafish. *Journal of Neurophysiology*, **113**, 657–668.

Levy, W.B. & Morel, D. (2006). A Bayesian constraint on neural computation. In *2006 IEEE International Symposium on Information Theory*, 655–658.

Lissmann, H.W. (1958). On the function and evolution of electric organs in fish. *The Journal of Experimental Biology*, **35**, 156–191.

Lochmann, T. & Deneve, S. (2008). Information transmission with spiking Bayesian neurons. *New Journal of Physics*, **10**, 055019.

Lochmann, T. & Deneve, S. (2011). Neural processing as causal inference. *Current Opinion in Neurobiology*, **21**, 774–781.

Loeb, G.E. & Fishel, J.A. (2014). Bayesian action & perception: Representing the world in the brain. *Frontiers in Neuroscience*, **8**.

Lu, J. & Fishman, H.M. (1994). Interaction of apical and basal membrane ion channels underlies electroreception in ampullary epithelia of skates. *Biophysical Journal*, **67**, 1525–1533.

Lu, J. & Fishman, H.M. (1995). Ion channels and transporters in the electroreceptive ampullary epithelium from skates. *Biophysical Journal*, **69**, 2467–2475.

MacNeilage, P.R., Ganesan, N. & Angelaki, D.E. (2008). Computational approaches to spatial orientation: From transfer functions to dynamic Bayesian inference. *Journal of Neurophysiology*, **100**, 2981–2996.

Marconi, U.M.B., Puglisi, A., Rondoni, L. & Vulpiani, A. (2008). Fluctuation-dissipation: Response theory in statistical physics. *Physics Reports*, **461**, 111–195.

Maruska, K.P. & Tricas, T.C. (2004). Test of the mechanotactile hypothesis: neuromast morphology and response dynamics of mechanosensory lateral line primary afferents in the stingray. *The Journal of Experimental Biology*, **207**, 3463–3476.

McGowan, D.W. & Kajiura, S.M. (2009). Electroreception in the euryhaline stingray, *Dasyatis sabina*. *The Journal of Experimental Biology*, **212**, 1544–1552.

McNamara, J. & Houston, A. (1980). The application of statistical decision theory to animal behaviour. *Journal of Theoretical Biology*, **85**, 673–690.

Mehaffey, W.H., Doiron, B., Maler, L. & Turner, R.W. (2005). Deterministic multiplicative gain control with active dendrites. *The Journal of Neuroscience*, **25**, 9968–9977.

Mello, W. (2009). The electrosensorial pore system of the cephalofoil in the four most common species of hammerhead shark (Elasmobranchii: Sphyrnidae) from the Southwestern Atlantic. *Comptes Rendus Biologies*, **332**, 404–412.

Metcalf, H.E. (1915). The ampullae of Lorenzini in *Acanthias vulgaris*. *Transactions of the American Microscopical Society*, **34**, 131–148.

Meyer, C.G., Holland, K.N. & Papastamatiou, Y.P. (2005). Sharks can detect changes in the geomagnetic field. *Journal of The Royal Society Interface*, **2**, 129–130.

Molteno, T.C.A. & Kennedy, W.L. (2009). Navigation by induction-based magnetoreception in elasmobranch fishes. *Journal of Biophysics*, **2009**, Article ID380976.

Monk, T. (2014). *The Evolutionary Origin of Nervous Systems and Implications for Neural Computation*. PhD thesis, University of Otago.

Monk, T. & Paulin, M.G. (2014). Predation and the origin of neurones. *Brain, Behavior and Evolution*, **84**, 246–261.

Monk, T., Paulin, M.G. & Green, P. (2015). Ecological constraints on the origin of neurones. *Journal of Mathematical Biology*, **71**, 1299–1324.

Montgomery, J. & Bodznick, D. (1999). Signals and noise in the elasmobranch electrosensory system. *The Journal of Experimental Biology*, **202**, 1349–1355.

Montgomery, J.C. (1984a). Frequency response characteristics of primary and secondary neurons in the electrosensory system of the thornback ray. *Comparative Biochemistry and Physiology Part A: Physiology*, **79**, 189–195.

Montgomery, J.C. (1984b). Noise cancellation in the electrosensory system of the thornback ray; common mode rejection of input produced by the animal's own ventilatory movement. *Journal of Comparative Physiology A: Neuroethology, Sensory, Neural, and Behavioral Physiology*, **155**, 103–111.

Montgomery, J.C. & Bodznick, D. (1993). Hindbrain circuitry mediating common mode suppression of ventilatory reafference in the electrosensory system of the little skate *Raja erinacea*. *The Journal of Experimental Biology*, **183**, 203–216.

Montgomery, J.C. & Bodznick, D. (1994). An adaptive filter that cancels self-induced noise in the electrosensory and lateral line mechanosensory systems of fish. *Neuroscience Letters*, **174**, 145–148.

Moore, D.M. & McCarthy, I.D. (2014). Distribution of ampullary pores on three cat-shark species (*Apristurus* spp.) suggest a vertical-ambush predatory behaviour. *Aquatic Biology*, **21**, 261–265.

Murray, R. (1967). The function of the ampullae of Lorenzini of elasmobranchs. In P. Cahn, ed., *Lateral Line Detectors*, 277–293, Indiana University Press, Bloomington.

Murray, R. & Potts, W. (1961). The composition of the endolymph, perilymph and other body fluids of elasmobranchs. *Comparative Biochemistry and Physiology Part A: Physiology*, **2**, 65–75.

Murray, R.W. (1959). The response of the ampullae of Lorenzini to combined stimulation by temperature change and weak direct currents. *The Journal of Physiology*, **145**, 1–13.

Murray, R.W. (1960). The response of the ampullae of Lorenzini of elasmobranchs to mechanical stimulation. *The Journal of Experimental Biology*, **37**, 417–424.

Murray, R.W. (1962). The response of the ampullae of Lorenzini of elasmobranchs to electrical stimulation. *The Journal of Experimental Biology*, **39**, 119–128.

Murray, R.W. (1974). The Ampullae of Lorenzini. In A. Fessard, ed., *Electroreceptors and Other Specialized Receptors in Lower Vertrebrates*, no. 3 / 3 in Handbook of Sensory Physiology, 125–146, Springer Berlin Heidelberg.

Nelson, M.E. (1994). Adaptive filtering in the electrosensory system. In F.H. Eeckman, ed., *Computation in Neurons and Neural Systems*, 209–214, Springer US.

Nelson, M.E. & Paulin, M.G. (1995). Neural simulations of adaptive reafference suppression in the elasmobranch electrosensory system. *Journal of Comparative Physiology A: Neuroethology, Sensory, Neural, and Behavioral Physiology*, **177**, 723–736.

New, J.G. (1990). Medullary electrosensory processing in the little skate. I. Response characteristics of neurons in the dorsal octavolateralis nucleus. *Journal of Comparative Physiology. A, Sensory, Neural, and Behavioral Physiology*, **167**, 285–294.

Nier, K., Hensel, H. & Bromm, B. (1976). Differential thermosensitivity and electric prepolarization of the ampullae of Lorenzini. *Pflugers Archiv European Journal of Physiology*, **363**, 181–185.

Norris, H.W. (1929). The distribution and innervation of the ampullae of lorenzini of the dogfish, *Squalus acanthias*. Some comparisons with conditions in other plagiostomes and corrections of prevalent errors. *The Journal of Comparative Neurology*, **47**, 449–465.

Northcutt, R.G. (1977). Elasmobranch central nervous system organization and its possible evolutionary significance. *American Zoologist*, **17**, 411–429.

Ogata, Y. (1988). Statistical models for earthquake occurrences and residual analysis for point processes. *Journal of the American Statistical Association*, **83**, 9–27.

Orban de Xivry, J.J., Coppe, S., Blohm, G. & Lefevre, P. (2013). Kalman filtering naturally accounts for visually guided and predictive smooth pursuit dynamics. *The Journal of Neuroscience*, **33**, 17301–17313.

Palmer, E.M., Horowitz, T.S., Torralba, A. & Wolfe, J.M. (2011). What are the shapes of response time distributions in visual search? *Journal of Experimental Psychology. Human Perception and Performance*, **37**, 58–71.

Paul, C.R. (2008). *Analysis of Multiconductor Transmission Lines*. John Wiley & Sons.

Paul, D.H. & Roberts, B.L. (1977). Studies on a primitive cerebellar cortex. I. The anatomy of the lateral-line lobes of the dogfish, *Scyliorhinus canicula*. *Proceedings of the Royal Society of London. Series B, Biological Sciences*, **195**, 453–466.

Paulin, M., Pullar, K. & Hoffman, L. (2016). Heterogeneity and randomness in vestibular afferent neuron firing increases efficiency (bits per Joule) without lowering bandwidth (bits per second). NeuroEng 2016: 9th Australasian Workshop on Neuro-Engineering and Computational Neuroscience (abstract), Brisbane, Australia.

Paulin, M.G. (1995). Electroreception and the compass sense of sharks. *Journal of Theoretical Biology*, **174**, 325–339.

Paulin, M.G. (2005). Evolution of the cerebellum as a neuronal machine for Bayesian state estimation. *Journal of Neural Engineering*, **2**, S219–S234.

Paulin, M.G. (2015). The origin of inference: Ediacaran ecology and the evolution of Bayesian brains. *arXiv:1504.02927*.

Peabody, J.E. (1897). The ampullae of Lorenzini of the Selachii. *The Biological Bulletin*, **1**, 163–178.

Perkel, D.H., Gerstein, G.L. & Moore, G.P. (1967). Neuronal spike trains and stochastic point processes. *Biophysical Journal*, **7**, 391–418.

Peters, R.C. & Evers, H.P. (1985). Frequency selectivity in the ampullary system of an elasmobranch fish (*Scyliorhinus canicula*). *The Journal of Experimental Biology*, **118**, 99–109.

Peters, R.C., Eeuwes, L.B.M. & Bretschneider, F. (2007). On the electrodetection threshold of aquatic vertebrates with ampullary or mucous gland electroreceptor organs. *Biological Reviews*, **82**, 361–373.

Pickard, W. (1988). A model for the acute electrosensitivity of cartilaginous fishes. *IEEE Transactions on Biomedical Engineering*, **35**, 243–249.

Pouget, A., Beck, J.M., Ma, W.J. & Latham, P.E. (2013). Probabilistic brains: knowns and unknowns. *Nature Neuroscience*, **16**, 1170–1178.

Pouzat, C. & Chaffiol, A. (2009a). Automatic spike train analysis and report generation. An implementation with R, R2html and STAR. *Journal of Neuroscience Methods*, **181**, 119–144.

Pouzat, C. & Chaffiol, A. (2009b). On goodness of fit tests for models of neuronal spike trains considered as counting processes. *arXiv:0909.2785*.

Pruis, G.W., Gilding, B.H. & Peters, M.J. (1993). A comparison of different numerical methods for solving the forward problem in EEG and MEG. *Physiological Measurement*, **14**, A1.

Raschi, W. (1986). A morphological analysis of the ampullae of Lorenzini in selected skates (Pisces, Rajoidei). *Journal of Morphology*, **189**, 225–247.

Raschi, W. & Adams, W.H. (1988). Depth-related modifications in the electroreceptive system of the eurybathic skate, *Raja radiata* (Chondrichthyes: Rajidae). *Copeia*, **1988**, 116–123.

Rich, D., Cazettes, F., Wang, Y., Pena, J.L. & Fischer, B.J. (2015). Neural representation of probabilities for Bayesian inference. *Journal of Computational Neuroscience*, **38**, 315–323.

Rotem, N., Sestieri, E., Cohen, D., Paulin, M., Meiri, H. & Yarom, Y. (2007). The functional architecture of the shark's dorsal-octavolateral nucleus: an in vitro study. *The Journal of Experimental Biology*, **210**, 2730–2742.

Rotem, N., Sestieri, E., Hounsgaard, J. & Yarom, Y. (2014). Excitatory and inhibitory synaptic mechanisms at the first stage of integration in the electroreception system of the shark. *Frontiers in Cellular Neuroscience*, **8**.

Sanborn, A.N. & Chater, N. (2016). Bayesian brains without probabilities. *Trends in Cognitive Sciences*, **20**, 883–893.

Sand, A. (1938). The function of the ampullae of Lorenzini, with some observations on the effect of temperature on sensory rhythms. *Proceedings of the Royal Society of London. Series B, Biological Sciences*, **125**, 524–553.

Schwarz, W. (2001). The ex-Wald distribution as a descriptive model of response times. *Behavior Research Methods, Instruments, & Computers*, **33**, 457–469.

Schwarz, W. (2002). On the convolution of inverse Gaussian and exponential random variables. *Communications in Statistics - Theory and Methods*, **31**, 2113–2121.

Schweitzer, J. (1986). Functional organization of the electroreceptive midbrain in an elasmobranch (*Platyrhinoidis triseriata*). *Journal of Comparative Physiology A: Neuroethology, Sensory, Neural, and Behavioral Physiology*, **158**, 43–58.

Sengupta, B., Stemmler, M.B. & Friston, K.J. (2013). Information and efficiency in the nervous system-A synthesis. *PLOS Computational Biology*, **9**, e1003157.

Shannon, C.E. (1948). A mathematical theory of communication. *The Bell System Technical Journal*, **27**, 379–423.

Sisneros, J.A. & Bass, A.H. (2003). Seasonal plasticity of peripheral auditory frequency sensitivity. *The Journal of Neuroscience*, **23**, 1049–1058.

Sisneros, J.A. & Tricas, T.C. (2000). Androgen-induced changes in the response dynamics of ampullary electrosensory primary afferent neurons. *The Journal of Neuroscience*, **20**, 8586–8595.

Sisneros, J.A. & Tricas, T.C. (2002a). Neuroethology and life history adaptations of the elasmobranch electric sense. *Journal of Physiology-Paris*, **96**, 379–389.

Sisneros, J.A. & Tricas, T.C. (2002b). Ontogenetic changes in the response properties of the peripheral electrosensory system in the Atlantic stingray (*Dasyatis sabina*). *Brain, Behavior and Evolution*, **59**, 130–140.

Sisneros, J.A., Tricas, T.C. & Luer, C.A. (1998). Response properties and biological function of the skate electrosensory system during ontogeny. *Journal of Comparative Physiology A: Neuroethology, Sensory, Neural, and Behavioral Physiology*, **183**, 87–99.

Sokal, R.R. & Rohlf, F.J. (1981). *Biometry: The Principles and Practice of Statistics in Biological Research*. WH Feeman and Company, New York, 2nd edn.

Spanne, A., Geborek, P., Bengtsson, F. & Jorntell, H. (2014). Spike generation estimated from stationary spike trains in a variety of neurons in vivo. *Frontiers in Cellular Neuroscience*, **8**.

Storey, G.P., Gonzalez-Fernandez, G., Bamford, I.J., Hur, M., McKinley, J.W., Heimbigner, L., Minasyan, A., Walwyn, W.M. & Bamford, N.S. (2015). Nicotine modifies corticostriatal plasticity and amphetamine rewarding behaviors in mice. *eneuro*, ENEURO.0095.

Streit, R.L. (2010). *Poisson point processes: imaging, tracking, and sensing*. Springer Science & Business Media.

Suga, N. (1967). Coding in tuberous and ampullary organs of a gymnotid electric fish. *The Journal of Comparative Neurology*, **131**, 437–451.

Szabo, T., Kalmijn, A.J., Enger, P.S. & Bullock, T.H. (1972). Microampullary organs and a submandibular sense organ in the fresh water ray, *Potamotrygon*. *Journal of Comparative Physiology A: Neuroethology, Sensory, Neural, and Behavioral Physiology*, **79**, 15–27.

Teunis, P.F.M., Bretschneider, F. & Peters, R.C. (1990). Convergence ratio and transduction in catfish electroreceptive organ. *Comparative Biochemistry and Physiology Part A: Physiology*, **97**, 405–410.

Teunis, P.F.M., Bretschneider, F., Bedaux, J.J.M. & Peters, R.C. (1991a). Synaptic noise in spike trains of normal and denervated electroreceptor organs. *Neuroscience*, **41**, 809–816.

Teunis, P.F.M., Bretschneider, F., van Groeningen, C., Peters, R.C. & Bedaux, J.J.M. (1991b). Quantitative aspects of transduction in an electroreceptor organ studied by means of experimental manipulation of the interspike interval. *Neuroscience*, **42**, 283–289.

Theiss, S.M., Collin, S.P. & Hart, N.S. (2011). Morphology and distribution of the ampullary electroreceptors in wobbegong sharks: implications for feeding behaviour. *Marine Biology*, **158**, 723–735.

Trapani, J.G. & Nicolson, T. (2011). Mechanism of spontaneous activity in afferent neurons of the zebrafish lateral-line organ. *The Journal of Neuroscience*, **31**, 1614–1623.

Tricas, T.C. (1982). Bioelectric-mediated predation by swell sharks, *Cephaloscyllium ventriosum*. *Copeia*, **1982**, 948–952.

Tricas, T.C. (2001). The neuroecology of the elasmobranch electrosensory world: Why peripheral morphology shapes behavior. *Environmental Biology of Fishes*, **60**, 77–92.

Tricas, T.C. & New, J.G. (1998). Sensitivity and response dynamics of elasmobranch electrosensory primary afferent neurons to near threshold fields. *Journal of Comparative Physiology A: Neuroethology, Sensory, Neural, and Behavioral Physiology*, **182**, 89–101.

Tricas, T.C., Michael, S.W. & Sisneros, J.A. (1995). Electrosensory optimization to conspecific phasic signals for mating. *Neuroscience Letters*, **202**, 129–132.

Tripathy, S.J., Savitskaya, J., Burton, S.D., Urban, N.N. & Gerkin, R.C. (2014). NeuroElectro: a window to the world's neuron electrophysiology data. *Frontiers in Neuroinformatics*, **8**.

Tyler, R.H., Mysak, L.A. & Oberhuber, J.M. (1997). Electromagnetic fields generated by a three dimensional global ocean circulation. *Journal of Geophysical Research: Oceans*, **102**, 5531–5551.

Vilares, I. & Kording, K. (2011). Bayesian models: the structure of the world, uncertainty, behavior, and the brain. *Annals of the New York Academy of Sciences*, **1224**, 22–39.

Waltman, B. (1966). Electrical properties and fine structure of the ampullary canals of Lorenzini. *Acta Physiologica Scandinavica*, **66**, 3–60.

Whitehead, D.L., Gauthier, A.R., Mu, E.W., Bennett, M.B. & Tibbetts, I.R. (2015). Morphology of the ampullae of Lorenzini in juvenile freshwater *Carcharhinus leucas*. *Journal of Morphology*, **276**, 481–493.

Wueringer, B. & Tibbetts, I. (2008). Comparison of the lateral line and ampullary systems of two species of shovelnose ray. *Reviews in Fish Biology and Fisheries*, **18**, 47–64.

Wueringer, B.E. (2012). Electroreception in Elasmobranchs: Sawfish as a Case Study. *Brain, Behavior and Evolution*, **80**, 97–107.

Xing, J., Berger, T., Sungkar, M. & Levy, W.B. (2015). Energy efficient neurons with generalized inverse Gaussian conditional and marginal hitting times. *IEEE Transactions on Information Theory*, **61**, 4390–4398.

Zacks, S. (2014). *Parametric Statistical Inference: Basic Theory and Modern Approaches*, vol. 4 of *International Series in Nonlinear Mathematics*. Elsevier.

Appendix A

Electronic supplemental information

The following are available electronically on the DVD provided.

A.1 How to create models using the COMSOL GUI

A description and simple example of how to implement models via the COMSOL GUI.

A.2 How to generate .m files in COMSOL for use in MATLAB

A description and simple example of how generate files in COMSOL for use in MATLAB.

A.3 High resolution pictures

Copies of COMSOL/MATLAB generated figures for high resolution viewing. Figures are arranged by chapter and labelled by figure label. For captions see thesis text.

A.4 Spike train summaries

Basic data analysis and fitting of probability distributions to the spontaneous activity of electrosensory primary afferents.

Appendix B

Ex-Wald model of vestibular afferent discharge

Our results show that spontaneous activity in electrosensory afferent neurons can be accurately modelled as inverse Gaussian-censored Poisson processes. The same result has been found in mammalian vestibular semicircular canal afferent neurons, which exhibit greater heterogeneity in ISI distributions than skate electrosensory afferents.

This paper, in preparation, demonstrates that vestibular afferents can also be accurately modelled as inverse Gaussian-censored Poisson processes and discusses the implications of these distributions for models of neural computation.

The fact that one model has been found to fit octavolateralis neuron firing patterns on two distinct branches of the vertebrate phylogenetic tree, elasmobranch electroreception (thesis) and mammalian vestibular system (here), suggests that the model may extend to all vertebrate octavolateralis senses.

Distributed, heterogenous, noisy spiking activity in the vestibular nerve is an efficient way to transmit high-acuity data for Bayesian inference.

Michael Paulin[1], and Kiri Pullar[1], and Larry Hoffman[2]

[1]*Department of Zoology, University of Otago, Dunedin, New Zealand; and*

[2]*Department of Head & Neck Surgery and Brain Research Institute,*

David Geffen School of Medicine at UCLA,

Los Angeles, California 90095-1624

Abstract

Models of neural computation for Bayesian inference require modelling sense data as samples drawn from probability distributions whose parameters are variables of interest to the observer. We recorded spontaneous spiking activity of vestibular semicircular canal afferent neurons in chinchillas. Statistical model identification showed that firing patterns of these neurons can be described by an effectively two-parameter family of censored Poisson processes, whose inter-spike interval distributions are a convolution of an exponential and an inverse Gaussian distribution. Model analysis suggests that the Poisson parameter corresponds to a high bandwidth signal that may contain information about head state, while the inverse Gaussian represents post-spike inhibition that censors the Poisson process and improves energy efficiency. Central neurons receiving such spike trains could continuously compute the posterior density of the Poisson parameter by exploiting a natural correpondence between the dynamics of neuronal membrane potentials and the likelihood function for sequential inference from a Poisson process. We conclude that the seemingly inefficient, noisy, heterogeneous, distributed functional organization of the vestibular nerve is a fast, efficient way to transmit high-acuity, high-bandwidth information in a form that would permit central vestibular neurons to quickly, simply and efficiently compute Bayesian posterior probability distributions of state variables that quantify head orientation and movements.

Introduction

Bayesian inference requires a model of the observed system and the measurement process in the form of a probability distribution parameterised by variables of interest to the observer (Gelman et al., 2013). In Bayesian neural models, sense data are treated as samples drawn from the measurement distribution, and the brain infers the posterior distribution of parameters from the samples (Berniker & Kording, 2011; Doya, 2007; Knill & Pouget, 2004; Kording, 2014). Statistically optimal decisions and control actions require computing Bayesian posterior distributions of variables that affect outcomes of the decisions and actions (J. O. Berger, 1985; Kording & Wolpert, 2004, 2006), implying that evolution should select nervous systems to compute Bayesian posteriors of such variables if there is a way that they could do it (K. Friston, 2010, 2012; Levy, 2006). A growing body of evidence indicates that nervous systems can, and do perform Bayesian inference (Chater, Oaksford, Hahn, & Heit, 2010; Colombo & Series, 2012; De Ridder, Vanneste, & Freeman, 2014; Kording, 2014; O'Reilly, Jbabdi, & Behrens, 2012; Trimmer et al., 2011). Developing appropriate statistical models of sensory inputs to the brain is a prerequisite for testing whether brains compute Bayesian posteriors from sense data, and for determining how they do it.

The vestibular system, which monitors head orientation and movement in vertebrates, provides a convenient, low-dimensional model system. Each semicircular canal of the vestibular apparatus isolates a single degree of freedom of head movement, rotation around the canal axis, and transmits spike trains to the brain on a dedicated branch of the vestibular nerve (J. M. Goldberg et al., 2012). Spiking acitivity on an individual canal branch can be parameterized by a single state variable such as angular velocity. The situation can be further simplified by considering spontaneous activity which occurs while the head is stationary. This special case is very simple yet biologically relevant, because it corresponds to important behavioural and clinical issues of postural stability and perceptual threshold sensitivity in the vestibular system (Karmali, Chaudhuri, Yi, & Merfeld, 2016; Merfeld, 2011; Rey et al., 2016).

Canal branches of the vestibular nerve each contain large populations of neurons with heterogeneous stochastic spiking behaviour (J. M. Goldberg, 2000; J. M. Goldberg & Fernandez, 1971; J. M. Goldberg, Smith, & Fernandez, 1984; Honrubia, Hoffman, Sitko, & Schwartz, 1989; Oleary, Dunn, & Honrubia, 1974; Sadeghi, Chacron, Taylor, & Cullen, 2007). Some neurons fire rapidly and regularly with approximately Gaussian inter-spike interval variability. Others fire slowly and irregularly with approximately Poisson variability.

There is a range of different behaviours between these extremes. Similar functional organization has been found in the vestibular nerve of different species from fish to primates (Boyle & Highstein, 1990; Brontestewart & Lisberger, 1994; Honrubia, Sitko, Kimm, Betts, & Schwartz, 1981; Oleary & Honrubia, 1976), but it remains unclear why the nerve is organized this way. On the face of it, the observed pattern of organization is very inefficient. A signal representing a single degree of freedom of motion, with a bandwidth in the order of tens of Hz (Carriot, Jamali, Chacron, & Cullen, 2014; Cromwell, Newton, & Carlton, 2001; Grossman, Leigh, Abel, Lanska, & Thurston, 1988; Li, Paulin, Smith, Hullar, & Hoffman, 2016), should easily be carried by a single neuron firing a few tens of spikes per second (Kass, Eden, & Brown, 2014). At most a few neurons each firing a few spikes per second should provide sufficient channel capacity to transmit information about head rotation around one axis. But in mammals, each semicircular canal nerve branch contains thousands of afferent neurons, and transmits in the order of a hundred thousand spikes per second, even when the head is not moving (Baird, Desmadryl, Fernandez, & Goldberg, 1988; Hoffman & Honrubia, 2002; Honrubia, Kuruvilla, Eichel, & Mamikunian, 1987). This apparent excess capacity, by a factor of at least three orders of magnitude, is somewhat surprising, given that the high energetic cost of spiking appears to have been a strong constraint on nervous system evolution (Isler, 2013; Monk, Paulin, & Green, 2015; Niven & Laughlin, 2008). The high level of randomness or noise in many vestibular neurons is particularly puzzling. Transmitting noise uses energy but, by definition, does not provide information. We might therefore expect evolution to have selected afferents to be as regular as possible, with small coefficients of variation (CV) and high signal-to-noise ratios (SNR). Such neurons are possible, because they exist in vestibular nerves of all species (J. M. Goldberg et al., 2012). But then why aren't all vestibular afferent neurons as regular as possible? In particular, why do some of them have highly irregular, Poisson-like firing statistics? Poisson variability implies that spike times are as random as possible given the constraint that spiking is parameterized by the stimulus (Landolt & Correia, 1978; Softky, 1995). If such neurons encode stimulus parameters in firing rate then they are not merely inefficient, they are as inefficient as they could possibly be.

Semicircular canal afferent neuron firing activity has previously been modelled using linear transfer functions that map head angular velocity to instantaneous firing rate (Baird et al., 1988; Cullen, 2012; J. M. Goldberg et al., 2012; Oleary & Honrubia, 1976). Using such models the posterior distribution of head angular velocity could be computed by a Kalman filter, which is a Bayesian state estimator for linear dynamical systems (Haykin, 2001; Liu & Chen, 1998; Schiff, 2009). Behavioural and comparative evidence suggests that there is a

neural analog of a Kalman filter in the vestibulo-cerebellar brainstem, the central target of vestibular sensory neurons (Bastian, 2011; Bell, Han, & Sawtell, 2008; Herzfeld & Shadmehr, 2014; Manto et al., 2012; Miall, Christensen, Cain, & Stanley, 2007; Miall & King, 2008; Molinari, Restuccia, & Leggio, 2009; Nixon & Passingham, 2001; Paulin, 1993; Selva & Oman, 2012). This is a particular example of the Bayesian brain hypothesis, which predicts that sense data will be transformed into a representation of the posterior distribution of relevant causal variables at an early stage of sensory processing (Kording, 2014; Kording et al., 2007; Orbán & Wolpert, 2011; Wolpert, 2007). However, it is not plausible that the vestibulo-cerebellum implements the Kalman filter algorithm. It requires algebraic operations not naturally suited to neuronal implementation, and does not generalize to nonlinear dynamical state estimation problems that nervous systems of agile animals would appear to be able to solve with ease.

Proposed algorithms for statistical computation in nervous systems often assume that incoming sensory spike trains have Poisson statistics (J. M. Beck et al., 2008; Brown, Frank, Tang, Quirk, & Wilson, 1998; Deneve, 2008; Huang & Rao, 2016; Lehky, 2010; Ma, 2010; Zemel, Dayan, & Pouget, 1998). This is a general simplifying assumption for inference from point processes (Kass et al., 2014; Landolt & Correia, 1978), which may be particularly germane for Bayesian models of neural computation for dynamical state estimation. The likelihood function for sequential Bayesian inference from a Poisson process is an exponential decay function of time between events (Koyama, Eden, Brown, & Kass, 2010) (See *Methods*). Neuronal membranes, whose electrical potential decays exponentially towards resting potential between synaptic input events (Koch & Segev, 1989), are natural computers for evaluating these likelihoods. The consequent advantages of Poisson data for statistical computation in the central nervous system could explain why peripheral neurons might transmit data in what seems to be a very inefficient form. Central neurons vastly outnumber sensory afferent neurons, and higher efficiency in central computation would greatly outweigh lower efficiency in data acquisition.

Canal afferent spike trains are generally more regular than expected for Poisson processes and most do not have the exponential inter-spike interval distributions that characterise Poisson processes (J. M. Goldberg, 2000; J. M. Goldberg & Holt, 2013; Sadeghi et al., 2007). However, as in other sensory systems, vestibular afferent neurons form parallel channels that converge onto central target neurons (J. M. Goldberg, 2000; Straka & Dieringer, 2000; Straka, Holler, & Goto, 2002). Parallel organization of spiking communication channels has energetic advantages that are optimized when sub-channels

are more regular than Poisson processes (Balasubramanian, 2015; T. Berger & Levy, 2010; Sengupta & Stemmler, 2014). Because sums of stochastic point processes converge to Poisson processes (Arratia, Goldstein, & Gordon, 1990; Chen, 1975), convergence of afferent axons onto central targets means that events arriving at central target neurons could have Poisson statistics, with the requisite exponential inter-spike interval distribution, even if spike trains transmitted by individual sensory afferent axons do not.

We hypothesized that the curious and seemingly inefficient statistical organization of spiking activity in the vestibular nerve may reflect the inevitability of statistical noise in high-precision measurements, coupled to a trade-off between the energetic advantages of regular firing in parallel channels for transmitting spikes to the brain and the advantages of Poisson data for Bayesian neural computation. The aim of this investigation is to model vestibular sense data in a way that allows this hypothesis to be tested, and to provide an empirical foundation for testable models of neural mechanisms for Bayesian inference in the brain.

Methods

All procedures involving animals were approved by the UCLA Chancellor's Animal Research Committee.

Single afferent electrophysiology

- Anesthesia with sodium pentobarbital; heart, respiratory rates, and O2 saturation were monitored; core temperature maintained at 38.5°C;
- superior vestibular nerve exposed medial to ampullae;
- individual afferents recorded for spontaneous and rotation evoked discharge using standard methods.

Spiketrain analyses

- The data used for this investigation came from the database maintained in the laboratory, representing primarily 20 second epochs of spontaneous discharge from afferents projecting from the horizontal and superior semicircular canal cristae.
- Afferents were distinguished by epithelia of origin by response phase relative to turntable kinematics (i.e. recording from the superior vestibular nerve of the right labyrinth).

- Spiketimes were determined using custom Matlab scripts (MGP) and basic interspike interval statistics determined.

- Distributions of interspike intervals (ISI) for each afferent were fitted to two different models the maximum likelihood criterion between model and data, using MATLAB. Intervals that were isolated, either much smaller or much larger than intervals in the main lobe of the distribution, were considered outliers and deleted. After fitting, intervals with very low probability according to the model were considered to be additional outliers and were also deleted. The model was then re-fitted.

- One model is an offset gamma distribution (OSG). A gamma distribution is the waiting time for a certain number of events in a Poisson process. It has a shape parameter, k = number of events, and a scale parameter, theta = Poisson intensity. A gamma is exponential for k = 1, converging towards a Gaussian as k gets larger. Shapes of empirical ISI distributions resemble those of gamma distributions, but it is necessary to include an additional fixed waiting time in each interval in order for the OSG model to fit the observations. This offset is a fixed parameter, not a random variable. Realism would require any mechanism that implemented this model to contain a precise clock.

- The other model is a gamma-censored Poisson (GCP) distribution. In this model the ISI distribution is exponential, the ISI distribution of a Poisson process, that is left-censored using a gamma process. The gamma process acts as a `gate', blocking the production of the next spike in the Poisson process until an event occurs in the gamma process. For example the Poisson events could be generated by a noisy signal crossing a threshold, but the threshold trigger could be de-activated after a spike and require a certain number of random events (e.g. molecules binding to a receptor) before it is re-activated. Thus threshold crossings occur, but do not generate spikes, during a refractory period. The gamma distribution of the refractory period gives a gamma-like shape to the ISI distribution, which is a convolution of a gamma and an exponential.

Results

1. Identifying a model of spiking activity in canal afferents

Inter-spike interval (ISI) histograms of three spike trains illustrating typical ISI distributions in the data are displayed in three sub-plots of figure 1(a). The spike trains had mean intervals 13.1 ms, 16.7ms and 32.5ms, with corresponding mean rates 76.3, 59.9 and 30.8

spikes/second and coefficients of variation (CV) 0.038, 0.28 and 0.52 respectively. CV is a dimensionless measure of regularity, whose expected value is 1 for an irregular Poisson process and 0 for a perfectly regular process with equal intervals. Observed ISI distributions range from narrow, nearly-symmetric and Gaussian-like in units that fire rapidly and regularly, like the unit on the left, to broad, positively skewed and exponential-like in units that fire more slowly and irregularly, like the one on the right. The center sub-plot shows an intermediate form. Axes have been scaled to fit the shape of each ISI distribution. In reality, the distributions vary from tall and thin to short and wide, as indicated by the inset in the left sub-plot, showing the three distributions overlaid on the same scale with a common aspect ratio.

Figure 1(b) is a scatterplot of mean ISI versus CV for all neurons. It shows that fast, regular units are more common than slow, irregular units. This scatterplot closely resembles previously published plots of similar data in a variety of species (refs), indicating that our sample is representative of activity in the nerve and reflects a common statistical pattern that has been observed previously not only in chinchillas but in a range of other species.

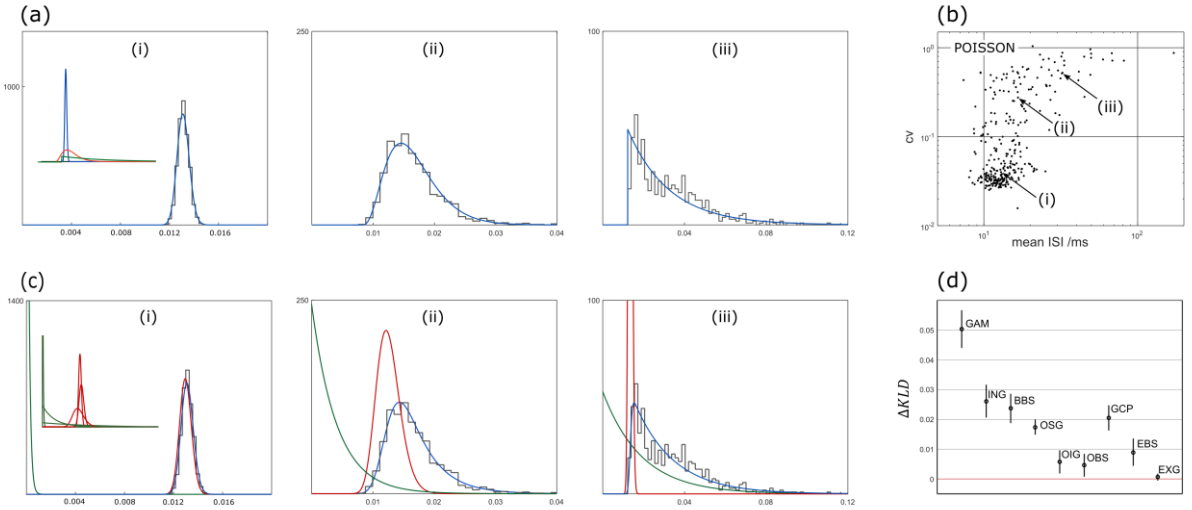

Figure 1: GIG-censored poisson model characterises heterogeneity in afferent firing statistics. **(a)** Spontaneous inter-spike interval (ISI) distributions of three representative units: **i** - regular, **ii** - intermediate and **iii** - irregular. Best fitting gamma censored Poisson models are overlaid on the empirical histograms. Inset in **i** shows models overlaid with common aspect ratio. **(b)** Scatterplot of mean ISI versus coefficient of variation (CV) for all units. Points corresponding to the three representative units are indicated. Note the concentration of very regular units and relatively few units near the line CV = 1 which corresponds to a

Poisson process. **(c)** Same three units with exwald model overlaid. The exwald model decomposes into an exponential and a Wald (inverse Gaussian) distribution. Note that the exponential components of the three units are very different but the Wald components are relatively similar. **(d)** Goodness of fit. ΔKLD measures how much further away the specified model is from the empirical distribution, measured by Kullback-Liebler divergence, relative to the exwald model for all units (mean ± SEM). The models are gamma (GAM), Wald or inverse Gaussian (ING), Birnbaum-Saunders (BBS), offset Gamma (OSG), offset inverse Gaussian (OIG), offset Birnbaum-Saunders (OBS), gamma censored Poisson (GCP), exponential Birnbaum-Saunders (EBS) and exponential Gaussian (EXG). Exwald is the best fitting model overall, corresponding to the line ΔKLD = 0.

During initial exploratory data analysis we considered a number of candidate models to fit the observed ISI distributions. Candidates must be approximately Gaussian in some region of their parameter space and become positively skewed elsewhere. Many probability distributions satisfy the first condition because of the Central Limit Theorem, and many also satisfy the second. Among initial candidates, the Weibull and log-normal distributions turned out to have very large fitting errors relative to other models'. Inspecting plots of fitted models showed that Weibull and log-normal distributions differ qualitatively in shape from the data distributions. Because including these models would cloud the analysis of subtler differences between other candidate models, we do not discuss them further.

Data exploration identified three suitable candidate models: The gamma, inverse Gaussian and Birnbaum-Saunders distributions. These distributions have all been used previously to model neuronal inter-spike interval distributions (Barbieri, Quirk, Frank, Wilson, & Brown, 2001; Heil, Neubauer, Irvine, & Brown, 2007; Iyengar & Liao, 1997; Leiva et al., 2015). They are all members of the Generalized inverse Gaussian (GIG) family (Xing, Berger, Sungkar, & Levy, 2015). The GIG family are time-to-barrier distributions for drift-diffusion processes, or Brownian motion under a driving force. The inverse Gaussian itself is the distribution of times taken for Brownian motion with constant drift to reach a fixed threshold. The gamma and Birnbaum-Saunders distributions have simple special interpretations, as waiting times for a specified number of events in a Poisson process, and time-to-failure when Gaussian-sized defects accumulate, respectively. Not only do these models contain members with shapes resembling the shapes observed in the data, they are each consistent with a generic biophysically realistic neuron model in which spiking results from a stochastic process that drives an internal state variable to a threshold, and is then reset (Xing et al., 2015).

Inspecting plots of fitted models overlaid on empirical ISI distributions indicated that fits for nearly all neurons for all three candidates could be substantially improved by including a time-shift parameter, which de-couples the shape of the fitted distribution from its location along the time axis. This introduces three new models: The offset gamma, offset inverse Gaussian and offset Birnbaum-Saunders distributions.

The offset models all accurately fit not only the shapes but also the locations of empirical distributions. This is illustrated in figure 1(a) where the best fitting offset gamma model has been overlaid on each of the three example data distributions. This model evidently fits each of these example distributions with high accuracy. Quantitative analysis and inspection of plots shows that this holds true for all of the data. However, as will be seen below, the offset gamma turns out to be the poorest of the three offset GIG candidate models.

Fitted offset gamma models have a mean offset of 7.0±4.6 ms (mean ± s.d.), fitted offset inverse Gaussian models have a mean offset of 2.8±6.0 ms, and fitted offset Birnbaum-Saunders models have a mean offset of 3.2±5.8 ms. These offsets are symptomatic of a discrepancy between the GIG models and the data. For any given neuron, the offset required to place a model with the best-fitting shape in the best-fitting location along the time axis is a fixed time period, typically large relative to the neuron's inter-spike intervals. Realistic interpretation of such a model implies that each neuron has a precise internal clock, allowing it to wait for a specified time after a spike before initiating a GIG process that will trigger the following spike. This is not impossible, but it does seem implausible that neuronal inter-spike interval distributions would be generated by a combination of a timer with crystaline precision followed by a stochastic process with high variability. Rather more problematically, a large proportion of fitted latencies are negative. They are predictions, not delays. Negative offset implies that a neuron must initiate the stochastic process that triggers each spike at a precise time *before* the random time at which the preceding spike will occur. This violates causality.

Vestibular neurophysiologists and modellers have established that spiking variability in vestibular afferent neurons is controlled by a post-spike inhibitory stochastic process, and that heterogeneity in spiking statistics, i.e. variations in inter-spike interval distributions across neurons, are controlled by differences in the parameters of that process (Kalluri, Xue, & Eatock, 2010; Smith & Goldberg, 1986). We hypothesized that this post-spike inhibitory process, which dominates the shape of observed ISI distributions, generates refractory periods with a GIG distribution. By censoring another stochastic process, this could account

for discrepancies between GIG models and data. The simplest model consistent with the assumption that the censored process carries information about the stimulus is that it is a Poisson process. Poisson processes arise naturally in simple physical processes (Basano & Ottonello, 1975) and are the generic limiting case when point processes are combined, analogous to the Gaussian limiting case when measurements of continuous variables are combined (Chen, 1975). In the absence of specific information pointing to an alternative model, Poisson processes are the natural maximum entropy prior for point process inference (Jaynes & Bretthorst, 2003). The correspondence between the likelihood function for sequential inference from a Poisson process and the dynamics of neuronal membrane potentials provides specific information *favouring* a Poisson process model of the observations in the case of neural computation. Thus, having established that afferent ISI distributions are not Poisson processes, the argument that on empirical and theoretical grounds they *ought* to be Poisson processes still stands. Our hypothesis is that semicircular canal afferent spiking does indeed contain a Poisson process, but it is hidden to varying degrees in different afferents by another process with a GIG distribution.

The hypothesis that the observed sensory spike trains are Poisson processes censored by GIG processes introduces a further three models: Gamma censored Poisson, inverse Gaussian censored Poisson, and Birnbaum-Saunders censored Poisson distributions. The inverse Gaussian censored Poisson has previously been called the exwald distribution (Schwarz, 2001). We also considered a Gaussian censored Poisson model at this point. Gaussians are members of the GIG family, but were not considered initially because Gaussians are never skewed and the data distributions always are. Gaussian censored Poisson distributions do have the general characteristics of the empirical distributions, forming a continuum of models ranging from Gaussian to Poisson, with a range of positively skewed intermediate forms.

A GIG censored Poisson spike train is a Poisson spike train with random segments removed by blocking spike generation for a random interval after a spike occurs. Because the time to the next event in a Poisson process is independent of time since the last event, the time to the next spike at the end of post-spike inhibition has a Poisson distribution with the same parameter as the uncensored process. Poisson processes have exponentially distributed intervals, and so the distribution of intervals in a GIG censored Poisson process is the distribution of the sum of a GIG distributed and an exponentially distributed random variable. This is a convolution of the GIG and an exponential.

In total we now have ten candidate models: Three GIG models, three offset GIG models and four GIG censored Poisson models, including the Gaussian censored Poisson. Goodness of fit for all candidates is summarized in figure 1(d). The inverse Gaussian censored Poisson or exwald distribution is the best candidate, having the smallest Kullback-Liebler divergence between data and model. The performance of other candidates is displayed in figure 1(d) by plotting the mean pairwise difference in K-L divergence between data and model, relative to the exwald distribution. The exwald model itself scores zero, with no variability, because it performs precisely as well as itself for every neuron, and is not shown on the plot. Because our spike train datasets are large, thousands of spikes in most records, the picture remains essentially unchanged, and the conclusions are not affected, whether we use Kullback-Liebler divergence, mean squared fitting error or the AIC statistic as a performance metric.

Figure 1(d) shows that the offset GIG models all perform better than the corresponding naked GIG models. The gamma censored Poisson and Birnbaum-Saunders censored Poisson models also out-perform their plain GIG counterparts, but they do not perform as well as the offset GIG models. However, GIG censored Poisson models have a technical advantage over the offset models in that they do not require a physical mechanism that violates causality. The exwald model out-performs every other model. In this case, the censored Poisson model does not merely correct latency errors in the inverse Gaussian model, it also more accurately characterizes the observed shapes of ISI distributions. The Gaussian censored Poisson model comes a close second to the exwald model. This indicates that censoring distributions in the exwald model are all approximately Gaussian which, as will be seen below, is true.

Figure 1C shows fitted exwald models for the units displayed in figure 1(a), together with the decomposition into inverse Gaussian and exponential components. The Poisson components vary markedly between these neurons (τ = 140μs, 4.1ms and 19.0ms respectively), but the censoring components are all approximately Gaussian with similar location and shape parameters. The ISI distribution of the most regular unit, on the left, closely resembles the censoring distribution. This is because the Poisson component of this model has very short intervals relative to intervals in the censoring process. A spike is observed almost immediately after each refractory period, and therefore the distribution of intervals between spikes is largely determined by the distribution of refractory periods. At the other extreme, the ISI distribution of the most irregular unit resembles the interval distribution of the uncensored Poisson component, but shifted to the right. This is because the Poisson component for this unit has long and highly variable intervals relative to refractory periods.

Post-spike inhibition in effect adds a small, relatively constant delay, shifting the distribution to the right while adding a small amount of additional variation. Alternatively, the censoring process can be thought of as chopping a small segment from the left edge of the Poisson distribution. Either way the effect is the same, because the right tail of an exponential distribution is the same shape as the full distribution, shifted to the right.

The censoring distributions for the three units in figure 1 are similar. The censoring process blocks spiking for about 13ms after each spike, plus or minus a millisecond or two. The censoring distribution for the intermediate unit (figure 1C, ii) is broader, but also has a mean of about 13ms. As will be seen in the following section, the intermediate example in this figure has an atypically broad censoring distribution. It was chosen as an example because the broader censoring distribution makes it easier to visualize how the exwald distribution decomposes into an exponential and an inverse Gaussian or Wald distribution, and how the exwald model accounts for the location and shape of the data.

In summary, the results presented in this section show that GIG censored Poisson processes are good models of spontaneous firing activity in chinchilla semicircular canal afferent neurons. Given our data the exwald distribution is the best among candidates considered.

2. Exwald model-based analysis of spiking patterns

We parameterized the exwald model with three free parameters: μ, λ and τ. Two of these, μ and λ, are parameters of the inverse Gaussian or censoring component, while the third, τ, is the parameter of the censored Poisson process. The inverse Gaussian is the distribution of times taken for Brownian motion with constant drift to reach a barrier. With our parameterization, μ is the mean time to reach the barrier, λ is the reciprocal of the standard deviation of Brownian increments, and τ is mean interval of the censored Poisson process. These parameters all have dimensions of time, and are reported in milliseconds.

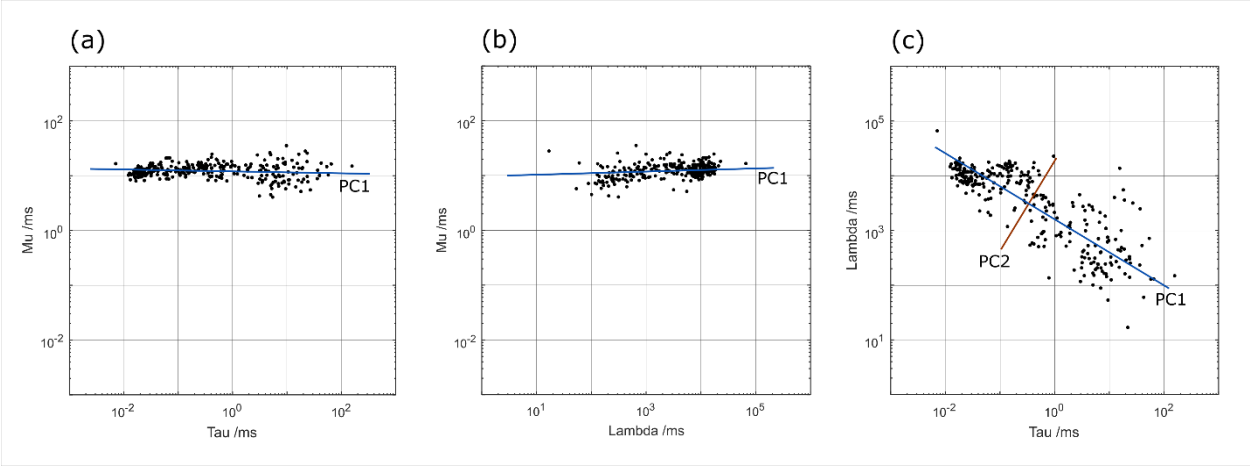

Fig 2. Scatterplots of fitted parameters of the exwald model. All three plots have the same square aspect ratio. Lines are principal component axes. **(a)** The mean μ of censoring distributions is approximately 12ms, independent of the Poisson mean τ. **(b)** μ, which characterises mean drift rate in the censoring process, is also independent of the parameter λ, which characterizes variability in the drift **(c)** log λ varies roughly in proportion to log τ, indicating a power law relationship between these parameters.

Figure 2 shows log-log scatterplots of fitted parameters of the exwald model for all neurons. All axes are the same length and the plots have unit aspect ratio, which helps to visualize the three-dimensional structure of the parameter cloud. It is a flat ellipsoid lying almost parallel to the log τ - log λ plane. Parameters τ and λ co-vary over four orders of magnitude, while μ varies independently over only about 0.1% of that range. Principal component axes are overlaid on the data. Linear relationships on these log-log plots are power laws in μ–λ–τ space.

The first principal component (PC1) explains 91.67% of the variance in logged parameter values. This component is in the direction (-0.015, - 0.516, 0.856) in log μ–λ–τ space. It is almost entirely a combination of log τ and log λ, mostly log τ. The second principal component (PC2) explains 7.60% of the variance. It is in the direction (0.213, 0.835, 0.507). This is also predominantly a combination of log τ and log λ, and is almost perpendicular to PC1 in the log τ - log λ plane. The remaining principal component (PC3) accounts for only 0.74% of variance. It is in the direction (0.977, - 0.190, - 0.098), nearly parallel to the log μ axis.

This principal components analysis confirms the first impression provided by figure 2, that μ is effectively constant across the population, is independent of the other parameters, and has relatively small variance (Figure 2A, B). It can therefore be modelled simply by using its estimated mean (12.19ms) and standard deviation (3.94ms).

Almost all of the variation in firing behaviour among these neurons can be accounted for by τ and λ, which are strongly correlated. Linear regression of log λ as a function of log τ gives a slope estimate of -0.54, meaning that λ varies roughly in proportion to $1/\sqrt{\tau}$. $1/\sqrt{\tau}$. This indicates that noise variance in the censoring process is coupled to the Poisson rate of the censored process.

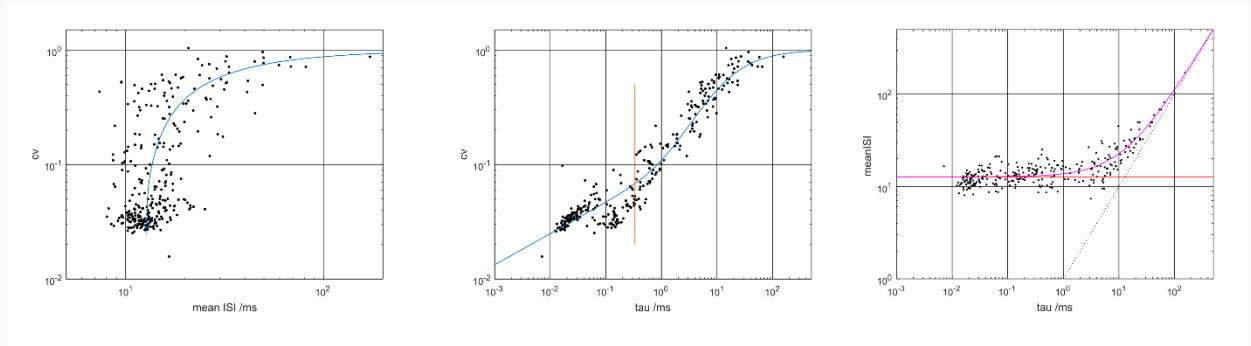

Figure 3: Exwald parameters and descriptive statistics. **(a)** CV as a function of mean interspike interval for all units. Data as in figure 1(b), with curve showing cv for given mean ISI predicted by the exwald model. **(b)** CV as a function of the Poisson parameter of the exwald model for all units. Curve shows the cv for given τ predicted by the exwald model. Vertical bar indicates the data discretization interval at 330μS [remove?]. The plot shows that differences in spiking regularity are largely accounted for by differences in τ. (c) For large τ, greater than the mean censoring interval at about 12ms, the mean ISI approaches τ, as expected for the uncensored Poisson process (dotted line). For small τ the mean ISI is constrained to approximate the mean of the censoring distribution. Plots (b) and (c) show how the pattern seen in the traditional scatterplot (a) can be simplified and explained in terms of 'hidden variables' that are parameters of the exwald model.

Figure 3 shows how the exwald model accounts for simple descriptive statistics - mean inter-spike interval and CV, which have been used in the past to characterize heterogeneity in vestibular afferent spiking behaviour. Figure 3A is a scatterplot of mean ISI versus CV, containing the same data as figure 1(b). The curve drawn on this plot shows the expected CV for a neuron with a given mean ISI, computed from principal components. We computed

model parameters on PC1 corresponding to a specified mean interval, then computed the CV of that model. This figure shows that when we map from exwald model parameter space to the traditional space of descriptive statistics for spike trains, we obtain an elegant and novel characterization of the observed pattern that, unlike earlier characterizations (cf Goldberg fig), explains how the pattern could emerge from an underlying stochastic process model.

The data plotted in figure 3B shows how the CV of a spike train co-varies with the Poisson parameter, τ, of the exwald model fitted to that spike train. The overlaid curve is the relationship predicted by the exwald model, the expected value of CV given a value of τ. There is a very strong relationship between these variables. The figure shows that most of the variation in firing regularity among these neurons can be explained by variation in τ, as anticipated from the principal components analysis. This indicates that τ may be preferable to CV or CV* as a descriptive statistic for quantifying firing regularity of vestibular afferent neurons. CV and CV* describe the behaviour, but τ describes the behaviour while connecting it to an underlying stochastic process model that characterizes how the behaviour is generated.

Figure 3B also shows that some neurons - the fastest and most regular ones - transmit information about astonishingly fast processes, down to about 10 microsecond intervals between events. A Bayesian observer could infer rates of these very fast processes, up to about 100KHz, by estimating τ from afferent spike trains, even though the afferent firing rates are about a thousand times slower than that, at less than 100Hz. It is undeniably possible to estimate τ from such data, because we just did.

The vertical line at about 0.3ms in figure 3B indicates the sampling interval used for digitizing spike time data, corresponding to a sample rate of 3KHz. We had expected this to be fast relative to timescales in the data, and were surprised to find a parameter with the dimensions of time and values as small as about 100 microseconds for some neurons. We carried out simulation studies, drawing samples from exwald distributions and fitting exwald models to the samples, to check whether fitted parameters are close to true parameters when samples come from a known model, and whether quantization during data acquisition might bias fitted model parameters. The answers are yes, and no. In particular, the unexpectedly small values of τ found in some neurons do not appear to be artifacts of data quantization or the fitting procedure.

The relationship between mean interval and CV of intervals in vestibular afferent spike trains can be further unpacked by looking at the mean inter-spike interval as a function of τ, as shown in figure 3C. The dotted line on the right of this plot corresponds to where τ is equal to the mean ISI, which is where the data would lie if the spike trains were Poisson processes. The horizontal line shows the mean censoring interval, and the curve shows the exwald model-predicted mean ISI for a specified τ. On the right, spiking is more Poisson-like as τ becomes large relative to μ, because typical interval lengths in the Poisson process are long relative to censoring intervals, and the censoring has relatively less effect. On the left, τ becomes small relative μ, intervals in the Poisson process become negligible relative to censoring intervals, and the inter-spike interval distribution approaches that of the censoring process.

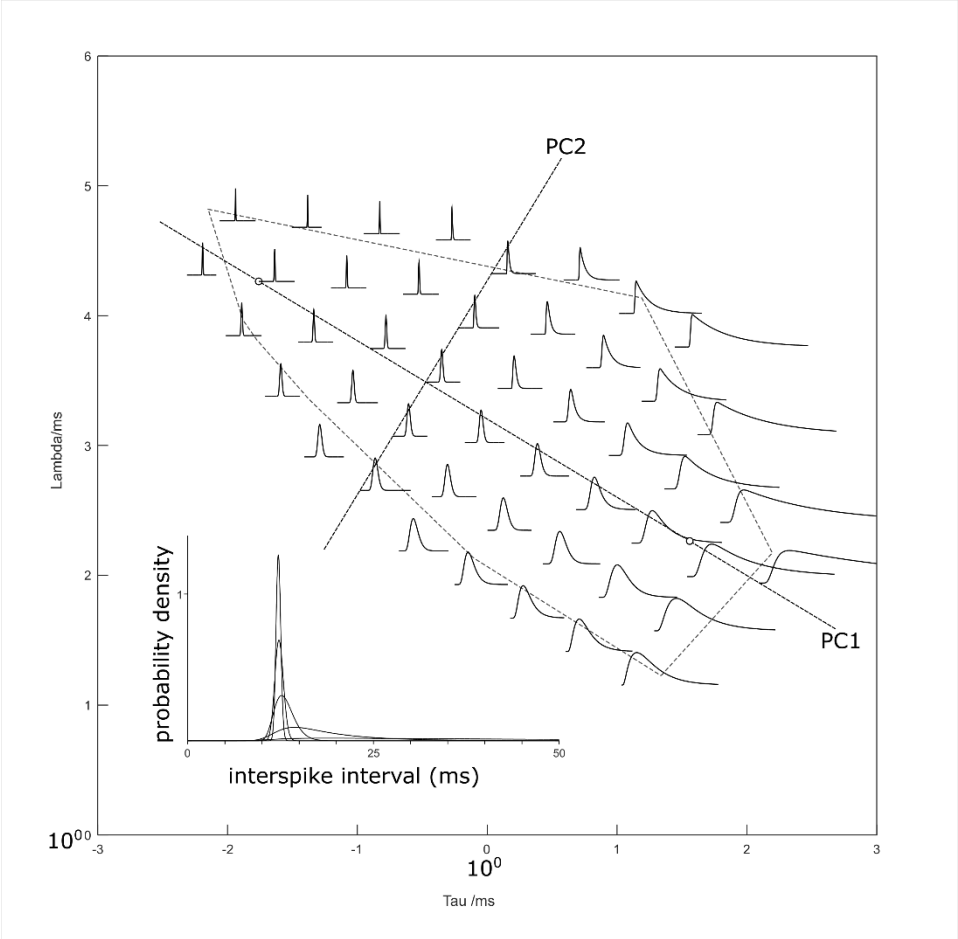

Fig 4: Map of ISI distributions in the τ–μ parameter plane of the exwald model. This plane accounts for more than 99% of between-neuron variability in spontaneous firing patterns. The first principle component alone accounts for more than 90% of the variability. ISI distributions in the map have been scaled to the same height. Inset shows the true change in

shape along the first principle axis, at four points equally spaced between the circles marked on the axis. Dashed polygon is the convex hull enclosing the fitted parameters (τ, μ) for all neurons in our sample (c.f. figure 2(c)).

Figure 4 shows a map of ISI distributions in the log τ–λ plane of exwald parameter space. This plane, which is very nearly parallel to the PC1-PC2 plane, accounts for almost all (99.26%) of the variation in spiking behaviour between neurons. The dashed line shows the convex hull of fitted points, defining the boundary of parameter values found in the sample. Exwald distributions are drawn on a grid aligned with the principal component axes. Each distribution is drawn with a time axis on which t=0 is located at the point in parameter space corresponding to that distribution. Distributions are scaled vertically, so that they are all the same height in the map, for the same reason that the three sub-plots in figure 1A were individually scaled, i.e. differences in real shapes across the map are so extreme that it is very difficult to visualize the shapes as well as differences between shapes on a single plot using the same aspect ratio. The inset (lower left) shows the true range of shape changes along the PC1 axis between the two points marked with open circles, showing that in reality the ISI distributions of the most regular units are so tall and narrow and the distributions of the least regular units are so short and wide that when they are plotted together with the same aspect ratio it is difficult to see the shape of either of them.

The map illustrates that heterogeneity in firing behavior among chinchilla semicircular canal afferent neurons is almost fully accounted for (>99%) by just two parameters, τ and λ. These parameters are strongly corrrelated, such that a single parameter, PC1, which is a linear combination of them, accounts for most of the pattern (>91%). Towards the upper left of the map, where the first principle axis crosses the boundary of the data cloud, distributions are tall, narrow and symmetric. Neurons in this part of the map fire rapidly and regularly with mean rate near $1/\mu$. As we move along the first principal axis, ISI distributions become progressively flatter, wider and more positively skewed, representing neurons that fire slowly and irregularly with increasingly Poisson-like ISI distributions. Shape changes along the second principal axis are less pronounced. The main effect along PC2 is that the leading edge of the ISI distribution becomes sharper, corresponding to less-variable refractory periods.

Comparison of the map in figure 4 with the scatterplot in figure 2C shows that the cloud of parameter points is more concentrated near the first principal axis within the convex hull, so the map over-emphasizes the contribution of the second axis to shape variability. The

pattern is quite well characterized by the first principle axis alone, which defines a continuum from narrow, sharply censored ISI distributions that have small positive skew to broad, less sharply-censored ISI distributions that have large positive skew. It also appears that the density of data points tends to increases in concert with regularity. That is, the more censoring that takes place at a given value of τ, the more neurons transmit a signal with that value of τ.

Discussion

Statistical model identification has shown here that generalized inverse GIG censored Poisson processes are accurate models of spontaneous firing activity of chinchilla semicircular canal afferent neurons. The exwald, or inverse Gaussian censored Poisson distribution (Schwarz, 2001), is the best model among candidates that we considered. GIG distributions have previously been used to model neuronal firing patterns, not only because they resemble inter-spike interval distributions of various kinds of neurons, but also because they emerge as interval statistics when a stochastic dynamic process evolves to a threshold state and is then reset, as occurs in neuronal spiking mechanisms (T. Berger, Levy, & Jie, 2011; Iyengar & Liao, 1997). Our results show that spontaneous inter-spike intervals of chinchilla semicircular canal afferent neurons are approximately GIG-distributed, but they differ systematically from GIG distributions and are more accurately represented by a convolution of an inverse Gaussian distribution with an exponential distribution.

Descriptive statistics and plots indicate that our data is qualitatively and quantitatively similar to previously published data from vestibular neurons, not only from chinchillas but also from other species, indicating that our results are likely to hold for vertebrate vestibular afferent neurons in general. Because a spike train can be fully reconstructed from its inter-spike intervals, a statistical model of intervals between spikes is a complete statistical model of a spike train. We have only considered spontaneous firing activity, so it remains to be seen whether and how the exwald model may generalize to driven or dynamic responses of vestibular afferent neurons. However, spontaneous activity is the low-signal limit of the general dynamical case, and so it follows that the exwald model must be accurate for small signals. There is merely a question about how small is “small”.

The small-signal regime is clinically and behaviourally significant, because postural stability and motor agility, especially in large bipeds with long muscle-activation delays like ourselves, requires measuring small forces and accelerations quickly and accurately. The transduction

mechanism of vestibular hair cells has a very small dynamic range and adapts very rapidly (Eatock & Songer, 2011; Gillespie & Müller, 2009; Howard, Roberts, & Hudspeth, 1988). This means that even during large, fast head movements, these receptor cells are in fact responding to small changes in head acceleration. Because of this, and because a time-varying or inhomogenous Poisson process is itself a Poisson process (Kass et al., 2014), it is plausible that the exwald model may account not only for spontaneous activity but also for driven activity of vestibular neurons. The simplest generalization of our results is to propose that each afferent neuron generates a spike train with an exwald distribution of intervals, whose time-varying parameters are functions of some kinematic state variable(s) of the head. Given that the exwald model is a very accurate description when the head is stationary, continuity requires that any accurate statistical model of afferent firing must approach an exwald distribution for small head movements. Therefore the exwald model provides a foundation for and an empirical constraint on models of vestibular afferent firing during head movements.

Heterogeneity of vestibular afferent spiking activity has previously been characterized using the CV* statistic, which was invented specifically for this purpose (J. M. Goldberg et al., 1984). CV* is a transformation of the coefficient of variation or CV, a dimensionless statistic that quantifies variability of a point process. It was introduced in vestibular spike train analysis in order to compensate for systematic changes in the CV of individual afferent neurons at different mean firing rates, providing a standardized measure of spiking variability that allows neurons with different firing rates to be compared on an equal footing. Data from figure 2A in Goldberg (2000) (appendix?) shows that the standard deviation of inter-spike intervals in semicircular canal afferent neurons scales approximately as a 3/2 power-law function of the mean inter-spike interval. This is a characteristic of inverse Gaussian distributions. CV* effectively transforms this power law structure out of descriptive statistics of vestibular afferent spiking variability. In doing this it simplifies the statistical description of population spiking variability, as intended, but at the expense of concealing a clue to explaining that variability. The 3/2 power law evident in Goldberg's figure 2A indicates that semicircular canal afferent firing activity is approximately inverse Gaussian during stimulation over a wide dynamic range. This is *prima facie* evidence that dynamic models of vestibular afferent responses may require little or no structural modification of the exwald model. In retrospect, the data in Goldberg 1984 table 1 is even more revealing. That data indicates power-law scaling with an exponent near 3/2, characteristic of inverse Gaussian distributions, for units with highest mean firing rates, smoothly changing to an exponent near 1,

characteristic of exponential distributions, for units with the lowest mean firing rates. The exwald model can explain this pattern in a very simple way.

Our results indicate that energy efficiency may be an important determinant of functional anatomy in the vestibular nerve. There is good evidence that energy efficiency is an important constraint on nervous system design (Faisal, White, & Laughlin, 2005; K. J. Friston, 2009; Laughlin, 2001, 2004; Laughlin, van Steveninck, & Anderson, 1998; Levy & Baxter, 1996; Niven & Laughlin, 2008; Xing et al., 2015). Indeed in the context of evolving self-organizing thermodynamic structures, energy efficiency may be a global design criterion that defines attractors in the space of possible organisms (England, 2013, 2015). The consequences of selection for energy efficiency may simply be more obvious in nervous systems than in other organ systems because neurons are much more energetically expensive than other cell types (Balasubramanian, 2015; Niven & Laughlin, 2008; Sengupta, Stemmler, & Friston, 2013). A predicted consequence of evolutionary selection for energy efficiency is that nervous systems should perform Bayesian inference and be Bayes-optimal decision-makers (K. J. Friston, 2009; Levy, 2006; Schwartenbeck, FitzGerald, Dolan, & Friston, 2013).

Neurons have a baseline energetic cost, and a cost per spike which increases faster than the rate of spiking (Alle, Roth, & Geiger, 2009; Balasubramanian, 2015; Laughlin, 2001; Lewis, Gilmour, Moorhead, Perry, & Markham, 2014; Sengupta & Stemmler, 2014). As a consequence of this, individual neurons are most efficient at particular firing rates, and populations are most efficient when high-bandwidth signals are distributed across neurons so that individuals fire at these rates (Balasubramanian, 2015). Analysis of information transmission and power consumption in spiking neuron models indicates that myelinated axons are most energetically efficient when they fire in the order of 100 spikes per second (D. H. Goldberg, Sripati, & Andreou, 2003), with generalized inverse Gaussian distributions of inter-spike intervals (T. Berger & Levy, 2010; Xing et al., 2015). These results imply that the most efficient way to construct a high-capacity communication channel using myelinated axons, maximizing bits per joule while achieving a specified capacity in bits per second, is to employ many neurons each firing on average about 100 spikes per second with a generalized inverse Gaussian distribution of inter-spike intervals. Our data and analysis shows that this is approximately true in semicircular canal branches of the vestibular nerve in chinchillas. However, closer inspection revealed systematic deviations from GIG models, and statistical system identification showed that inter-spike interval distributions are more

accurately described by exwald distributions, which contain inverse Gaussians as a limiting case.

The small but systematic mismatch between the exwald model fitted to data and predictions based on a theoretical model of neuron energetics (T. Berger & Levy, 2010; Xing et al., 2015) suggests that there may be incorrect or missing assumptions in the model. One possibility is that the analysis is correct, but only considers energy efficiency in the nerve and fails to take into account that evolution may select less efficient components if they make the organism more efficient. Neurons themselves illustrate this point, since they are by far the most energetically expensive cell type, and yet evolution evidently deems them worth having at least in some organisms. Neurons in the central nervous system vastly outnumber sensory afferent neurons, and therefore it may be energetically advantageous for sensory neurons to transmit data in a form that the central nervous system can process more efficiently, even if this makes the sensory neurons less efficient than they could be. Other things being equal, Bayesian inference is an efficiency that evolution ought to have discovered (K. J. Friston, 2009; Levy, 2006). There is good evidence from psychophysical and behavioral studies indicating that nervous systems can and do perform Bayesian inference (De Ridder et al., 2014; de Xivry, Coppe, Blohm, & Lefevre, 2013; K. J. Friston, Samothrakis, & Montague, 2012; Kording, 2014; Lochmann & Deneve, 2011; Loeb & Fishel, 2014; Pouget, Beck, Ma, & Latham, 2013).

Sense data are provided in the form of stochastic point processes which on certain theoretical grounds we might expect to be Poisson processes. Poisson processes arise naturally from simple mechanisms and as limiting cases of complex mechanisms, analogously to the way that normal distributions often emerge naturally in samples from continuous processes (Basano & Ottonello, 1975; Chen, 1975). They are the simplest class of stochastic point processes, as measured for example by Jaynes' principle of maximum entropy (Jaynes & Bretthorst, 2003). Their simple structure means that inference from Poisson processes is relatively simple both analytically and computationally (Kass et al., 2014; Koyama et al., 2010). It is surprising, and perhaps surprising that it is not better known, that neurons are natural computers for real-time inference from Poisson processes. Suppose that a spike occured at time $t_0 < t$ and no spikes have occurred since then. If the posterior density of the Poisson parameter τ at time t_0 was $f_0(\tau)$, then Bayes rule for the posterior density at a later time t is:

$$f(\tau \mid no\ spike\ in\ (t_0, t]) = A\, f(\ no\ spike\ in\ (t_0, t] \mid \tau)\, f_0(\tau) \qquad (1)$$

Where $A = A(\tau, t)$ is a normalizing factor which ensures that $f(\tau)$ is a probability density, i.e. it integrates to 1 over the range of τ. If spiking is a Poisson process with mean interval τ then the probability density of another spike following any spike decays exponentially with time constant τ. This defines the likelihood function for continuous inference from the process:

$$f(\,no\ spike\ in\ (t_0, t] \mid \tau) = \frac{1}{\tau} e^{-(t-t_0)/\tau} \qquad (2)$$

Substituting the likelihood function (2) into Bayes rule (1) shows that the posterior density of τ at any point in the parameter space during inter-spike intervals is an exponential decay function of the density at the last data input spike time, adjusted by a normalizing factor. Neurons are natural computers for this operation because neuronal membrane potentials decay exponentially towards resting membrane potential if they receive no inputs. The membrane potential therefore exactly tracks the likelihood.

Normalization simply means that the total activity in a population of neurons performing the computation (1) must be regulated. Activity normalization is so common in populations of real neurons that it has been called a canonical operation in neural computation (J.M. Beck, Latham, & Pouget, 2011; Carandini & Heeger, 2012; Eliasmith & Martens, 2011; Louie, Khaw, & Glimcher, 2013). Various computational models have been proposed and evidence indicates that normalization is implemented by different mechanisms in different parts of nervous systems of different animals (Carandini & Heeger, 2012). In that case the problem for modelling mechanisms of inference in central vestibular pathways is not to determine whether neurons *can* evaluate expressions like (1), but to determine if and how central vestibular neurons actually do it. The exact correspondence between exponential likelihoods and the leaky integator dynamics of neuronal membranes evident in equations (1) and (2) indicates that there may be a strikingly simple way that a population of neurons in the vestibular brainstem could compute Bayesian posterior densities of variables that parameterize sensory spike trains, if those spike trains are samples from Poisson processes.

Semicircular canal afferent spike trains are not samples from Poisson processes. We have shown, however, that they are random sub-samples of samples from Poisson processes. Each afferent spike train can be thought of as being constructed from an underlying Poisson process by extracting a spike then waiting for a random interval before extracting another. If a group of neurons do this independently at random, sub-sampling from independent Poisson processes with a common parameter τ, then they can collectively represent a sample from a Poisson process with that parameter. From equation (1), a neuron receiving

convergent inputs from the group could infer the Bayesian posterior density of τ at a point. A group of sensory afferent neurons converging to a secondary neuron can be thought of as a 'super-afferent' that delivers a Poisson sample to the brain. The super-afferent delivers information more efficiently than a single afferent could, in a form that would allow neurons there to perform Bayesian inference in a simple, natural way. This idea may explain the statistical organization of spiking activity in the vestibular nerve. It makes the strong prediction that the collective activity of afferent neurons that converge onto a particular central target neuron will be a Poisson process, whose mean rate matches the membrane time constant of the target. Target neuron dynamics are likely to be affected by the normalization operation, presumably implemented by diffuse feedforward and/or feedback pathways in the target population, and so testing this prediction may require a neural population model with some biophysical detail to account for this.

The first thing a Bayesian must do with data is to compute the posterior distribution(s) of relevant variables. Since the vestibular nerve transmits information about head orientation and movements to the vestibulo-cerebellum, this would suggest that the vestibulo-cerebellum may be a Bayesian dynamical estimator for kinematic state variables of the head. This suggestion is consistent with various strands of circumstantial evidence indicating that there is a neural analog of a Kalman filter in the vestibulo-cerebellum (Paulin, 1989, 1993; Selva & Oman, 2012; Young, 2011; Young & Oman, 1969). The Kalman filter is an algorithm for real-time Bayesian dynamical state estimation given samples from a linear Gaussian process (Haykin, 2001). It was the most general form of a Bayesian dynamical state estimator known until the modern development of random sample-based or MC inference algorithms (Bolviken, Acklam, Christophersen, & Stordal, 2001; Doucet, De Freitas, & Gordon, 2001; Gordon, Salmond, & Smith, 1993). The idea that vestibulo-cerebellum is a generalized Kalman filter implemented by neurons is consistent with the broader hypothesis that the cerebellum is a general nonlinear dynamical state estimator. The cerebellum is essential for motor agility and various other tasks that require dynamical prediction (Baumann et al., 2015; Paulin, 1993). Agility requires predicting kinematics of the body and objects and agents in the environment as quickly and accurately as possible. Real time Bayesian inference is the gold standard for that task. In animal interactions that involve power and agility it may be energetically favourable to employ bigger Bayesian brains than bigger muscles, despite the fact that gram-for-gram, spiking neurons are more energetically costly than active muscle cells (Balasubramanian, 2015; Rolfe & Brown, 1997). This may explain why most neurons in the human brain are in the cerebellum (Itō, 1984).

In conclusion, the exwald model provides a potential solution to long-standing puzzles about statistical patterns of firing activity in the vestibular nerve. It provides an empirical foundation not only for developing realistic biophysical models of how these patterns arise, but also for developing realistic models of neural computation for Bayesian inference, or whatever it is that all those neurons are doing in the cerebellum (Marr, 2010).

References

Alle, H., Roth, A., & Geiger, J. R. P. (2009). Energy-Efficient Action Potentials in Hippocampal Mossy Fibers. *Science, 325*(5946), 1405-1408. doi:10.1126/science.1174331

Arratia, R., Goldstein, L., & Gordon, L. (1990). Poisson approximation and the Chen-Stein method. *Statistical Science, 5*(4), 403-434.

Baird, R. A., Desmadryl, G., Fernandez, C., & Goldberg, J. M. (1988). THE VESTIBULAR NERVE OF THE CHINCHILLA .2. RELATION BETWEEN AFFERENT RESPONSE PROPERTIES AND PERIPHERAL INNERVATION PATTERNS IN THE SEMICIRCULAR CANALS. *Journal of Neurophysiology, 60*(1), 182-203.

Balasubramanian, V. (2015). Heterogeneity and Efficiency in the Brain. *Proceedings of the Ieee, 103*(8), 1346-1358. doi:10.1109/jproc.2015.2447016

Barbieri, R., Quirk, M. C., Frank, L. M., Wilson, M. A., & Brown, E. N. (2001). Construction and analysis of non-Poisson stimulus-response models of neural spiking activity. *Journal of Neuroscience Methods, 105*(1), 25-37. doi:10.1016/s0165-0270(00)00344-7

Basano, L., & Ottonello, P. (1975). THERMAL NOISE AS A SOURCE OF POISSON DISTRIBUTIONS. *American Journal of Physics, 43*(5), 452-453. doi:10.1119/1.9825

Bastian, A. J. (2011). Moving, sensing and learning with cerebellar damage. *Current Opinion in Neurobiology, 21*(4), 596-601. doi:10.1016/j.conb.2011.06.007

Baumann, O., Borra, R. J., Bower, J. M., Cullen, K. E., Habas, C., Ivry, R. B., . . . Sokolov, A. A. (2015). Consensus Paper: The Role of the Cerebellum in Perceptual Processes. *Cerebellum, 14*(2), 197-220. doi:10.1007/s12311-014-0627-7

Beck, J. M., Latham, P. E., & Pouget, A. (2011). Marginalization in Neural Circuits with Divisive Normalization. *Journal of Neuroscience, 31*(43), 15310-15319. doi:10.1523/jneurosci.1706-11.2011

Beck, J. M., Ma, W. J., Kiani, R., Hanks, T., Churchland, A. K., Roitman, J., . . . Pouget, A. (2008). Probabilistic Population Codes for Bayesian Decision Making. *Neuron, 60*(6), 1142-1152. doi:10.1016/j.neuron.2008.09.021

Bell, C. C., Han, V., & Sawtell, N. B. (2008). Cerebellum-like structures and their implications for cerebellar function *Annual Review of Neuroscience* (Vol. 31, pp. 1-24). Palo Alto: Annual Reviews.

Berger, J. O. (1985). *Statistical decision theory and Bayesian Analysis* (2 ed.). New York: Springer-Verlag.

Berger, T., & Levy, W. B. (2010). A Mathematical Theory of Energy Efficient Neural Computation and Communication. *Ieee Transactions on Information Theory, 56*(2), 852-874. doi:10.1109/tit.2009.2037089

Berger, T., Levy, W. B., & Jie, X. (2011, 28-30 Sept. 2011). *Energy efficient neurons with generalized inverse Gaussian interspike interval durations.* Paper presented at the Communication, Control, and Computing (Allerton), 2011 49th Annual Allerton Conference on.

Berniker, M., & Kording, K. (2011). Bayesian approaches to sensory integration for motor control. *Wiley Interdisciplinary Reviews-Cognitive Science, 2*(4), 419-428. doi:10.1002/wcs.125

Bolviken, E., Acklam, P. J., Christophersen, N., & Stordal, J. M. (2001). Monte Carlo filters for non-linear state estimation. *Automatica, 37*(2), 177-183. doi:10.1016/s0005-1098(00)00151-5

Boyle, R., & Highstein, S. M. (1990). RESTING DISCHARGE AND RESPONSE DYNAMICS OF HORIZONTAL SEMICIRCULAR CANAL AFFERENTS OF THE TOADFISH, OPSANUS-TAU. *Journal of Neuroscience, 10*(5), 1557-1569.

Brontestewart, H. M., & Lisberger, S. G. (1994). PHYSIOLOGICAL-PROPERTIES OF VESTIBULAR PRIMARY AFFERENTS THAT MEDIATE MOTOR LEARNING AND NORMAL PERFORMANCE OF THE VESTIBULOOCULAR REFLEX IN MONKEYS. *Journal of Neuroscience, 14*(3), 1290-1308.

Brown, E. N., Frank, L. M., Tang, D., Quirk, M. C., & Wilson, M. A. (1998). A statistical paradigm for neural spike train decoding applied to position prediction from ensemble firing patterns of rat hippocampal place cells. *J Neurosci, 18*(18), 7411-7425.

Carandini, M., & Heeger, D. J. (2012). Normalization as a canonical neural computation. *Nature Reviews Neuroscience, 13*(1), 51-62. doi:10.1038/nrn3136

Carriot, J., Jamali, M., Chacron, M. J., & Cullen, K. E. (2014). Statistics of the Vestibular Input Experienced during Natural Self-Motion: Implications for Neural Processing. *Journal of Neuroscience, 34*(24), 8347-8357. doi:10.1523/jneurosci.0692-14.2014

Chater, N., Oaksford, M., Hahn, U., & Heit, E. (2010). Bayesian models of cognition. *Wiley Interdisciplinary Reviews-Cognitive Science, 1*(6), 811-823. doi:10.1002/wcs.79

Chen, L. H. Y. (1975). Poisson Approximation for Dependent Trials. 534-545. doi:10.1214/aop/1176996359

Colombo, M., & Series, P. (2012). Bayes in the Brain-On Bayesian Modelling in Neuroscience. *British Journal for the Philosophy of Science, 63*(3), 697-723. doi:10.1093/bjps/axr043

Cromwell, R. L., Newton, R. A., & Carlton, L. G. (2001). Horizontal plane head stabilization during locomotor tasks. *Journal of Motor Behavior, 33*(1), 49-58.

Cullen, K. E. (2012). The vestibular system: multimodal integration and encoding of self-motion for motor control. *Trends in Neurosciences, 35*(3), 185-196. doi:10.1016/j.tins.2011.12.001

De Ridder, D., Vanneste, S., & Freeman, W. (2014). The Bayesian brain: Phantom percepts resolve sensory uncertainty. *Neuroscience and Biobehavioral Reviews, 44*, 4-15. doi:10.1016/j.neubiorev.2012.04.001

de Xivry, J. J. O., Coppe, S., Blohm, G., & Lefevre, P. (2013). Kalman Filtering Naturally Accounts for Visually Guided and Predictive Smooth Pursuit Dynamics. *Journal of Neuroscience, 33*(44), 17301-17313. doi:10.1523/jneurosci.2321-13.2013

Deneve, S. (2008). Bayesian spiking neurons I: Inference. *Neural Computation, 20*(1), 91-117. doi:10.1162/neco.2008.20.1.91

Doucet, A., De Freitas, N., & Gordon, N. (2001). *Sequential Monte Carlo methods in practice*. New York: Springer.

Doya, K. (2007). *Bayesian brain : probabilistic approaches to neural coding*. Cambridge, Mass.: MIT Press.

Eatock, R. A., & Songer, J. E. (2011). Vestibular Hair Cells and Afferents: Two Channels for Head Motion Signals. In S. E. Hyman, T. M. Jessell, C. J. Shatz, C. F. Stevens, & H. Y. Zoghbi (Eds.), *Annual Review of Neuroscience, Vol 34* (Vol. 34, pp. 501-534). Palo Alto: Annual Reviews.

Eliasmith, C., & Martens, J. (2011). Normalization for probabilistic inference with neurons. *Biological Cybernetics, 104*(4-5), 251-262. doi:10.1007/s00422-011-0433-y

England, J. L. (2013). Statistical physics of self-replication. *Journal of Chemical Physics, 139*(12). doi:10.1063/1.4818538

England, J. L. (2015). Dissipative adaptation in driven self-assembly. *Nature Nanotechnology, 10*(11), 919-923. doi:10.1038/nnano.2015.250

Faisal, A. A., White, J. A., & Laughlin, S. B. (2005). Ion-channel noise places limits on the miniaturization of the brain's wiring. *Current Biology, 15*(12), 1143-1149. doi:10.1016/j.cub.2005.05.056

Friston, K. (2010). The free-energy principle: a unified brain theory? *Nature Reviews Neuroscience, 11*(2), 127-138. doi:10.1038/nrn2787

Friston, K. (2012). A Free Energy Principle for Biological Systems. *Entropy, 14*(11), 2100-2121.

Friston, K. J. (2009). The free-energy principle: a rough guide to the brain? *Trends in Cognitive Sciences, 13*(7), 293-301. doi:10.1016/j.tics.2009.04.005

Friston, K. J., Samothrakis, S., & Montague, R. (2012). Active inference and agency: optimal control without cost functions. *Biological Cybernetics, 106*(8-9), 523-541. doi:10.1007/s00422-012-0512-8

Gelman, A., Carlin, J. B., Stern, H. S., Dunson, D. B., Vehtari, A., & Rubin, D. B. (2013). *Bayesian Data Analysis* (3 ed.): Chapman-Hall.

Gillespie, P. G., & Müller, U. (2009). Mechanotransduction by hair cells: models, molecules, and mechanisms. *Cell, 139*(1), 33-44. doi:10.1016/j.cell.2009.09.010

Goldberg, D. H., Sripati, A. P., & Andreou, A. G. (2003). Energy efficiency in a channel model for the spiking axon. *Neurocomputing, 52-4*, 39-44. doi:10.1016/s0925-2312(02)00770-1

Goldberg, J. M. (2000). Afferent diversity and the organization of central vestibular pathways. *Experimental Brain Research, 130*(3), 277-297. doi:10.1007/s002210050033

Goldberg, J. M., & Fernandez, C. (1971). PHYSIOLOGY OF PERIPHERAL NEURONS INNERVATING SEMICIRCULAR CANALS OF SQUIRREL MONKEY .3. VARIATIONS AMONG UNITS IN THEIR DISCHARGE PROPERTIES. *Journal of Neurophysiology, 34*(4), 676-&.

Goldberg, J. M., & Holt, J. C. (2013). Discharge regularity in the turtle posterior crista: comparisons between experiment and theory. *Journal of Neurophysiology, 110*(12), 2830-2848. doi:10.1152/jn.00195.2013

Goldberg, J. M., Smith, C. E., & Fernandez, C. (1984). RELATION BETWEEN DISCHARGE REGULARITY AND RESPONSES TO EXTERNALLY APPLIED GALVANIC CURRENTS IN VESTIBULAR NERVE AFFERENTS OF THE SQUIRREL-MONKEY. *Journal of Neurophysiology, 51*(6), 1236-1256.

Goldberg, J. M., Wilson, V. J., Cullen, K. E., Angelaki, D. E., Broussard, D. M., Buttner-Ennever, J. A., . . . Minor, L. B. (2012). *The vestibular system : a sixth sense*. Oxford ; New York: Oxford University Press.

Gordon, N. J., Salmond, D. J., & Smith, A. F. M. (1993). Novel approach to nonlinear/non-Gaussian Bayesian state estimation. *IEE Proceedings F (Radar and Signal Processing), 140*(2), 107-113. Retrieved from http://digital-library.theiet.org/content/journals/10.1049/ip-f-2.1993.0015

Grossman, G. E., Leigh, R. J., Abel, L. A., Lanska, D. J., & Thurston, S. E. (1988). FREQUENCY AND VELOCITY OF ROTATIONAL HEAD PERTURBATIONS DURING LOCOMOTION. *Experimental Brain Research, 70*(3), 470-476.

Haykin, S. (2001). *Kalman Filtering and Neural Networks*: Wiley.

Heil, P., Neubauer, H., Irvine, D. R. F., & Brown, M. (2007). Spontaneous activity of auditory-nerve fibers: Insights into Stochastic processes at ribbon synapses. *Journal of Neuroscience, 27*(31), 8457-8474. doi:10.1523/jneurosci.1512-07.2007

Herzfeld, D. J., & Shadmehr, R. (2014). Cerebellum estimates the sensory state of the body. *Trends in Cognitive Sciences, 18*(2), 66-67. doi:10.1016/j.tics.2013.10.015

Hoffman, L. F., & Honrubia, V. (2002). Fiber diameter distributions in the chinchilla's ampullary nerves. *Hearing Research, 172*(1-2), 37-52. doi:10.1016/s0378-5955(02)00390-8

Honrubia, V., Hoffman, L. F., Sitko, S., & Schwartz, I. R. (1989). Anatomic and Physiological Correlates in Bullfrog Vestibular Nerve. *Journal of Neurophysiology, 61*(4), 688-701.

Honrubia, V., Kuruvilla, A., Eichel, J. E., & Mamikunian, D. (1987). MORPHOLOGICAL ASPECTS OF THE VESTIBULAR NERVE OF THE SQUIRREL-MONKEY. *Laryngoscope, 97*(2), 228-238.

Honrubia, V., Sitko, S., Kimm, J., Betts, W., & Schwartz, I. (1981). PHYSIOLOGICAL AND ANATOMICAL CHARACTERISTICS OF PRIMARY VESTIBULAR AFFERENT NEURONS IN THE BULLFROG. *International Journal of Neuroscience, 15*(4), 197-206. doi:10.3109/00207458108985857

Howard, J., Roberts, W. M., & Hudspeth, A. J. (1988). MECHANOELECTRICAL TRANSDUCTION BY HAIR-CELLS. *Annual Review of Biophysics and Biophysical Chemistry, 17*, 99-124.

Huang, Y., & Rao, R. P. N. (2016). Bayesian Inference and Online Learning in Poisson Neuronal Networks. *Neural Computation*, 1-24. doi:10.1162/NECO_a_00851

Isler, K. (2013). Brain Size Evolution: How Fish Pay for Being Smart. *Current Biology, 23*(2), R63-R65. doi:http://dx.doi.org/10.1016/j.cub.2012.11.042

Itō, M. (1984). *The cerebellum and neural control*. New York: Raven Press.

Iyengar, S., & Liao, Q. M. (1997). Modeling neural activity using the generalized inverse Gaussian distribution. *Biological Cybernetics, 77*(4), 289-295. doi:10.1007/s004220050390

Jaynes, E. T., & Bretthorst, G. L. (2003). *Probability theory : the logic of science*. Cambridge, UK ; New York, NY: Cambridge University Press.

Kalluri, R., Xue, J. B., & Eatock, R. A. (2010). Ion Channels Set Spike Timing Regularity of Mammalian Vestibular Afferent Neurons. *Journal of Neurophysiology, 104*(4), 2034-2051. doi:10.1152/jn.00396.2010

Karmali, F., Chaudhuri, S. E., Yi, Y. W., & Merfeld, D. M. (2016). Determining thresholds using adaptive procedures and psychometric fits: evaluating efficiency using theory, simulations, and human experiments. *Experimental Brain Research, 234*(3), 773-789. doi:10.1007/s00221-015-4501-8

Kass, R. E., Eden, U. T., & Brown, E. N. (2014). *Analysis of neural data*.

Knill, D. C., & Pouget, A. (2004). The Bayesian brain: the role of uncertainty in neural coding and computation. *Trends in Neurosciences, 27*(12), 712-719. doi:http://dx.doi.org/10.1016/j.tins.2004.10.007

Koch, C., & Segev, I. (1989). *Methods in neuronal modeling : from synapses to networks*. Cambridge, Mass.: MIT Press.

Kording, K. P. (2014). Bayesian statistics: relevant for the brain? *Current Opinion in Neurobiology, 25*(0), 130-133. doi:http://dx.doi.org/10.1016/j.conb.2014.01.003

Kording, K. P., Beierholm, U., Ma, W. J., Quartz, S., Tenenbaum, J. B., & Shams, L. (2007). Causal Inference in Multisensory Perception. *PLoS One, 2*(9), 10. doi:10.1371/journal.pone.0000943

Kording, K. P., & Wolpert, D. M. (2004). Bayesian integration in sensorimotor learning. *Nature, 427*(6971), 244-247. doi:Doi 10.1038/Nature02169

Kording, K. P., & Wolpert, D. M. (2006). Bayesian decision theory in sensorimotor control. *Trends in Cognitive Sciences, 10*(7), 319-326. doi:DOI 10.1016/j.tics.2006.05.003

Koyama, S., Eden, U. T., Brown, E. N., & Kass, R. E. (2010). Bayesian decoding of neural spike trains. *Annals of the Institute of Statistical Mathematics, 62*(1), 37-59. doi:10.1007/s10463-009-0249-x

Landolt, J. P., & Correia, M. J. (1978). NEUROMATHEMATICAL CONCEPTS OF POINT PROCESS THEORY. *Ieee Transactions on Biomedical Engineering, 25*(1), 1-12. doi:10.1109/tbme.1978.326370

Laughlin, S. B. (2001). Energy as a constraint on the coding and processing of sensory information. *Current Opinion in Neurobiology, 11*(4), 475-480. doi:10.1016/s0959-4388(00)00237-3

Laughlin, S. B. (2004). The Implications of Metabolic Energy Requirements for the Representation of Information in Neurons. *Cognitive Neurosciences Iii, Third Edition*, 187-196.

Laughlin, S. B., van Steveninck, R. R. D., & Anderson, J. C. (1998). The metabolic cost of neural information. *Nature Neuroscience, 1*(1), 36-41. doi:10.1038/236

Lehky, S. R. (2010). Decoding Poisson Spike Trains by Gaussian Filtering. *Neural Computation, 22*(5), 1245-1271. doi:10.1162/neco.2009.07-08-823

Leiva, V., Tejo, M., Guiraud, P., Schmachtenberg, O., Orio, P., & Marmolejo-Ramos, F. (2015). Modeling neural activity with cumulative damage distributions. *Biological Cybernetics*. doi:10.1007/s00422-015-0651-9

Levy, W. B. (2006). *A Bayesian constraint on neural computation*. New York: Ieee.

Levy, W. B., & Baxter, R. A. (1996). Energy efficient neural codes. *Neural Computation, 8*(3), 531-543. doi:10.1162/neco.1996.8.3.531

Lewis, J. E., Gilmour, K. M., Moorhead, M. J., Perry, S. F., & Markham, M. R. (2014). Action Potential Energetics at the Organismal Level Reveal a Trade-Off in Efficiency at High Firing Rates. *Journal of Neuroscience, 34*(1), 197-201. doi:10.1523/jneurosci.3180-13.2014

Li, L., Paulin, M. G., Smith, J., Hullar, T., & Hoffman, L. F. (2016). *Head Kinematics in free-running chinchillas*. Paper presented at the ARO Winter Conference, San Diego, CA.

Liu, J. S., & Chen, R. (1998). Sequential Monte Carlo methods for dynamic systems. *Journal of the American Statistical Association, 93*(443), 1032-1044. doi:Doi 10.2307/2669847

Lochmann, T., & Deneve, S. (2011). Neural processing as causal inference. *Current Opinion in Neurobiology, 21*(5), 774-781. doi:10.1016/j.conb.2011.05.018

Loeb, G. E., & Fishel, J. A. (2014). Bayesian Action&Perception: Representing the World in the Brain. *Frontiers in Neuroscience, 8*. doi:10.3389/fnins.2014.00341

Louie, K., Khaw, M. W., & Glimcher, P. W. (2013). Normalization is a general neural mechanism for context-dependent decision making. *Proceedings of the National Academy of Sciences of the United States of America, 110*(15), 6139-6144. doi:10.1073/pnas.1217854110

Ma, W. J. (2010). Signal detection theory, uncertainty, and Poisson-like population codes. *Vision Research, 50*(22), 2308-2319. doi:10.1016/j.visres.2010.08.035

Manto, M., Bower, J. M., Conforto, A. B., Delgado-Garcia, J. M., da Guarda, S. N. F., Gerwig, M., . . . Timmann, D. (2012). Consensus Paper: Roles of the Cerebellum in Motor Control-The Diversity of Ideas on Cerebellar Involvement in Movement. *Cerebellum, 11*(2), 457-487. doi:10.1007/s12311-011-0331-9

Marr, D. (2010). *Vision : a computational investigation into the human representation and processing of visual information*. Cambridge, Mass.: MIT Press.

Merfeld, D. M. (2011). Signal detection theory and vestibular thresholds: I. Basic theory and practical considerations. *Experimental Brain Research, 210*(3-4), 389-405. doi:DOI 10.1007/s00221-011-2557-7

Miall, R. C., Christensen, L. O. D., Cain, O., & Stanley, J. (2007). Disruption of state estimation in the human lateral cerebellum. *Plos Biology, 5*(11), 2733-2744. doi:10.1371/journal.pbio.0050316

Miall, R. C., & King, D. (2008). State Estimation in the Cerebellum. *Cerebellum, 7*(4), 572-576. doi:10.1007/s12311-008-0072-6

Molinari, M., Restuccia, D., & Leggio, M. G. (2009). State Estimation, Response Prediction, and Cerebellar Sensory Processing for Behavioral Control. *Cerebellum, 8*(3), 399-402. doi:10.1007/s12311-009-0112-x

Monk, T., Paulin, M., & Green, P. (2015). Ecological constraints on the origin of neurones. *Journal of Mathematical Biology*, 1-26. doi:10.1007/s00285-015-0862-7

Niven, J. E., & Laughlin, S. B. (2008). Energy limitation as a selective pressure on the evolution of sensory systems. *Journal of Experimental Biology, 211*(11), 1792-1804. doi:10.1242/jeb.017574

Nixon, P. D., & Passingham, R. E. (2001). Predicting sensory events - The role of the cerebellum in motor learning. *Experimental Brain Research, 138*(2), 251-257. doi:10.1007/s002210100702

O'Reilly, J. X., Jbabdi, S., & Behrens, T. E. J. (2012). How can a Bayesian approach inform neuroscience? *European Journal of Neuroscience, 35*(7), 1169-1179. doi:10.1111/j.1460-9568.2012.08010.x

Oleary, D. P., Dunn, R. F., & Honrubia, V. (1974). FUNCTIONAL AND ANATOMICAL CORRELATION OF AFFERENT RESPONSES FROM ISOLATED SEMICIRCULAR CANAL. *Nature, 251*(5472), 225-227. doi:10.1038/251225a0

Oleary, D. P., & Honrubia, V. (1976). ANALYSIS OF AFFERENT RESPONSES FROM ISOLATED SEMICIRCULAR CANAL OF GUITARFISH USING ROTATIONAL ACCELERATION WHITE-NOISE INPUTS .2. ESTIMATION OF LINEAR-SYSTEM PARAMETERS AND GAIN AND PHASE SPECTRA. *Journal of Neurophysiology, 39*(3), 645-659.

Orbán, G., & Wolpert, D. M. (2011). Representations of uncertainty in sensorimotor control. *Current Opinion in Neurobiology, 21*(4), 629-635. doi:10.1016/j.conb.2011.05.026

Paulin, M. G. (1989). A Kalman filter theory of the cerebellum. In M. A. Arbib & S.-I. Amari (Eds.), *Dynamic Interactions in Neural Networks: Models and Data* (pp. 2239-2260). New York: Springer-Verlag.

Paulin, M. G. (1993). The Role of the Cerebellum in Motor Control and Perception. *Brain Behavior and Evolution, 41*(1), 39-50.

Pouget, A., Beck, J. M., Ma, W. J., & Latham, P. E. (2013). Probabilistic brains: knowns and unknowns. *Nature Neuroscience, 16*(9), 1170-1178. doi:10.1038/nn.3495

Rey, M. C. B., Clark, T. K., Wang, W., Leeder, T., Bian, Y., & Merfeld, D. M. (2016). Vestibular Perceptual Thresholds increase above the age of 40. *Frontiers in Neurology, 7*, 17. doi:10.3389/fneur.2016.00162

Rolfe, D. F. S., & Brown, G. C. (1997). Cellular energy utilization and molecular origin of standard metabolic rate in mammals. *Physiological Reviews, 77*(3), 731-758.

Sadeghi, S. G., Chacron, M. J., Taylor, M. C., & Cullen, K. E. (2007). Neural variability, detection thresholds, and information transmission in the vestibular system. *Journal of Neuroscience, 27*(4), 771-781. doi:10.1523/jneurosci.4690-06.2007

Schiff, S. J. (2009). Kalman Meets Neuron: The Emerging Intersection of Control Theory with Neuroscience *2009 Annual International Conference of the Ieee Engineering in Medicine and Biology Society, Vols 1-20* (pp. 3318-3321).

Schwartenbeck, P., FitzGerald, T., Dolan, R. J., & Friston, K. (2013). Exploration, novelty, surprise, and free energy minimization. *Frontiers in Psychology, 4*. doi:10.3389/fpsyg.2013.00710

Schwarz, W. (2001). The ex-Wald distribution as a descriptive model of response times. *Behavior Research Methods Instruments & Computers, 33*(4), 457-469. doi:10.3758/bf03195403

Selva, P., & Oman, C. M. (2012). Relationships between Observer and Kalman Filter models for human dynamic spatial orientation. *Journal of Vestibular Research-Equilibrium & Orientation, 22*(2-3), 69-80. doi:10.3233/ves-2012-0451

Sengupta, B., & Stemmler, M. B. (2014). Power Consumption During Neuronal Computation. *Proceedings of the Ieee, 102*(5), 738-750. doi:10.1109/jproc.2014.2307755

Sengupta, B., Stemmler, M. B., & Friston, K. J. (2013). Information and Efficiency in the Nervous System-A Synthesis. *Plos Computational Biology, 9*(7). doi:10.1371/journal.pcbi.1003157

Smith, C. E., & Goldberg, J. M. (1986). A STOCHASTIC AFTERHYPERPOLARIZATION MODEL OF REPETITIVE ACTIVITY IN VESTIBULAR AFFERENTS. *Biological Cybernetics, 54*(1), 41-51. doi:10.1007/bf00337114

Softky, W. R. (1995). Simple codes versus efficient codes. *Current Opinion in Neurobiology, 5*(2), 239-247. doi:http://dx.doi.org/10.1016/0959-4388(95)80032-8

Straka, H., & Dieringer, N. (2000). Convergence pattern of uncrossed excitatory and inhibitory semicircular canal-specific inputs onto second-order vestibular neurons of frogs - Organization of vestibular side loops. *Experimental Brain Research, 135*(4), 462-473. doi:DOI 10.1007/s002210000544

Straka, H., Holler, S., & Goto, F. (2002). Patterns of canal and otolith afferent input convergence in frog second-order vestibular neurons. *Journal of Neurophysiology, 88*(5), 2287-2301. doi:DOI 10.1152/jn.00370.2002

Trimmer, P. C., Houston, A. I., Marshall, J. A. R., Mendl, M. T., Paul, E. S., & McNamara, J. M. (2011). Decision-making under uncertainty: biases and Bayesians. *Animal Cognition, 14*(4), 465-476. doi:10.1007/s10071-011-0387-4

Wolpert, D. M. (2007). Probabilistic models in human sensorimotor control. *Human Movement Science, 26*(4), 511-524. doi:DOI 10.1016/j.humov.2007.05.005

Xing, J., Berger, T., Sungkar, M., & Levy, W. B. (2015). Energy Efficient Neurons With Generalized Inverse Gaussian Conditional and Marginal Hitting Times. *Ieee Transactions on Information Theory, 61*(8), 4390-4398. doi:10.1109/tit.2015.2444401

Young, L. R. (2011). Optimal estimator models for spatial orientation and vestibular nystagmus. *Experimental Brain Research, 210*(3-4), 465-476. doi:10.1007/s00221-011-2595-1

Young, L. R., & Oman, C. M. (1969). MODEL FOR VESTIBULAR ADAPTATION TO HORIZONTAL ROTATION. *Aerospace Medicine, 40*(10), 1076-&.

Zemel, R. S., Dayan, P., & Pouget, A. (1998). Probabilistic interpretation of population codes. *Neural Computation, 10*(2), 403-430. doi:10.1162/089976698300017818